5-14-2018 10:00 AM

Analysis and Tectonic Synthesis of the Multiscale Structures along the Shangdan Tectonic Zone in the Qinling Orogenic Belt, China

Mengmeng Qu
The University of Western Ontario

Supervisor
Jiang, Dazhi
The University of Western Ontario

Graduate Program in Geology
A thesis submitted in partial fulfillment of the requirements for the degree in Doctor of Philosophy

Recommended Citation

Qu, Mengmeng, "Analysis and Tectonic Synthesis of the Multiscale Structures along the Shangdan Tectonic Zone in the Qinling Orogenic Belt, China" (2018). *Electronic Thesis and Dissertation Repository*. 5383.
https://ir.lib.uwo.ca/etd/5383

Abstract

Geological structures occur on a vast range of scales in Earth's lithosphere. Because Earth's lithosphere is rheologically heterogeneous, a multiscale approach is necessary to relate these structures to the tectonic history of orogens. One such approach, called the multi-order power-law approach (MOPLA), has been developed recently. In this study, MOPLA is applied to the Shangdan tectonic zone (SDTZ) in the Qinling orogenic belt (QOB). The kinematics of the SDTZ and its relation to the country rock deformation are crucial questions for Qinling tectonics, having both been the subject of debate for decades. Detailed work is conducted along the SDTZ to address these two fundamental questions.

MOPLA treats a heterogeneous material as a continuum of rheologically distinct elements. The rheological properties of the material and the mechanical fields of the constituent elements are computed by solving the partitioning and homogenization equations self-consistently. The computation is based heavily on the numerical evaluation of Eshelby tensors. This thesis develops an optimal scheme for evaluating Eshelby tensors and implements the scheme in MATLAB to improve the computational efficiency of MOPLA.

Multiscale structural analysis is performed along the SDTZ. Three deformation events are identified in the SDTZ and its adjacent areas. D_1 deformation is a NE-SW shortening deformation and occurred between ca.385-355Ma. D_1 deformation is only observed to the north of the SDTZ in western Qinling. D_2 deformation is a strike-slip dominant deformation and occurred between ca.227-201Ma. In western Qinling, D_2

deformation is a dextral strike-slip along the SDTZ. In eastern Qinling, D_2 deformation is a sinistral strike-slip along the SDTZ and N-S shortening deformation in the Liuling Group that is south of the SDTZ. D_3 deformation is an along-orogen extension and occurred between ca.140-135Ma. D_3 deformation is only observed in the Liuling Group in eastern Qinling. D_2 deformation, the opposite shearing along the SDTZ and the N-S shortening deformation in the Liuling Group, was a response to the oblique convergence between the South China Block and the North China Block. The convergence angle is constrained to 20°~40° using MOPLA. The tectonic evolution of the QOB from the late Paleozoic to early Mesozoic is illustrated.

Keywords

Multiscale modeling, Flow partitioning, Structural analysis, Tectonic evolution, Shangdan tectonic zone, Qinling orogenic belt

Co-Authorship Statement

An earlier version of Chapter 2 in this thesis was published as a co-authored paper with my supervisor, Dr. Dazhi Jiang, and Lucy X. Lu (PhD student supervised by Dr. Dazhi Jiang).

Qu, M., Jiang, D., Lu, L.X. 2016. An optimal scheme for numerical evaluation of Eshelby tensors and its implementation in a MATLAB package for simulating the motion of viscous ellipsoids in slow flows. Computers & Geosciences 96 (2016): 98-108.

Dr. Jiang thoroughly edited the manuscript and L.X. Lu wrote some part of the MATLAB code in the paper.

Dedication

This work is dedicated to my parents, Qingxia Li and Lin Qu, for their love.

Acknowledgements

While working on the graduate program in Western University, I have benefited greatly from a large group of people.

First and foremost, I thank my supervisor, Dr. Dazhi Jiang, for the continuous support of my PhD research, for his immense knowledge on structural geology and tectonics, the never-ending enthusiasm and motivation in different research fields, caring and encouragement during my study at Western and my life in Canada. The accomplishment of this thesis would not be possible without his help.

Besides my supervisor, I thank the rest of my thesis committee: Dr. Richard Secco and Dr. Desmond Moser, for their encouragement, insightful suggestions, comments and questions during the comprehensive exam and the committee meeting. I also thank Dr. Desmond Moser for the extra help on the geochronological studies, and I thank Dr. Richard Secco for the suggestions and comments on the preliminary version of this thesis.

In addition, I thank Dr. Robert Shcherbakov and Dr. Colin Denniston for the two excellent courses that I have taken. One is 'Computer Modelling of Natural Processes' given by Dr. Robert Shcherbakov. During this course, I was surprised by the powerfulness of MATLAB, and thus motivated to move most of my programming work from MathCad to MATLAB. The other course is 'Scientific Computing' given by Dr. Colin Denniston in Applied Mathematics department. In this course, I have learned how efficient the computation could be in a parallel computing program. Although I do not have time to apply the parallel computing in my current research, I will definitely apply it into my future work.

My sincere thanks also go to my field assistants. In the order of their participation, they are Wenhang Liu, Yuanzhen Yang, Weiyin Chen, Lujun Lin, Teng Wang, Bo Zhang, Rui Yang in summers 2013-2016. I would like to thank Dr. Wei Li and Dr. Wentian Liang in Northwest University for the field guidance in east Qinling and west Qinling, respectively. Without their help, I would not have smoothly and happily conducted the field work during the summer times.

Finally, great thanks give to my family and friends for their love and supports in various aspects. Especially, I thank my colleague Rui Yang for performing the U-Pb dating of samples from the Shetang and Xinyang areas using a laser ablation inductively coupled plasma mass spectrometry at Northwest University. I thank Jiao Zhao for suggestions on processing U-Pb data. I thank Dr. Shuo Sun for the companion during the dark days. I thank my roommate and colleague Lucy Lu for the delicious food, great tea, encouraging words, good discussions and help on writing and debugging. I thank my parents for always trusting me, for giving me all their love and always being there for me.

Table of Contents

Abstract i

Co-Authorship Statement... iii

Dedication iv

Acknowledgements v

List of Tables xiii

List of Figures xiv

List of Appendices xix

Nomenclature xx

Chapter 1: Introduction 1

1.1. The multiscale problem in structural geology studies 1

1.2. MOPLA.. 3

1.2.1 The aim of MOPLA 4

1.2.2 The backbone theory of MOPLA 8

1.2.3 Homogenization systems in MOPLA 9

1.3. Application to the Shangdan tectonic zone in the Qinling orogenic belt 11

1.3.1 The problem in the QOB studies 11

1.3.2 The framework of the QOB 15

1.4. Objectives and methodology 16

1.5. Thesis outline 17

1.6. References 18

Chapter 2: An Optimal Scheme for Numerical Evaluation of Eshelby Tensors and Its Implementation in a MATLAB Package for Simulating the Motion of Viscous Ellipsoids in Slow Flows 25

2.1 Introduction 25

2.2 Numerical evaluation of Eshelby tensors 30

2.2.1 The Eshelby inclusion solutions and Eshelby tensors 30

2.2.2 Numerical evaluation of T_{ijkl} 33

2.3 An optimal scheme 37

2.4 A MATLAB package for simulating the motion of rigid and deformable inclusions 42

2.4.1 A brief summary of important equations for rigid and deformable ellipsoids 43

2.4.2 Verification and examples 44

2.4.3 Structure of the package 53

2.5 Summary and discussion 54

2.6 References 56

Chapter 3: Deformation of the Shangdan Tectonic Zone in the Eastern Qinling Orogenic Belt

Chapter 3: Deformation of the Shangdan Tectonic Zone in the Eastern Qinling Orogenic Belt 63

3.1 Introduction 63

3.2 The Shangdan tectonic zone 69

3.2.1 Geological setting 69

3.2.2 Structural geometry 71

3.2.2.1 The Heihe area 71

3.2.2.2 The Danfeng area 79

3.3 Theoretical modeling 84

3.3.1 Numerical model setup 85

3.3.2 Modeling results 88

3.3.3 Comparison of the simulation results with the field data 96

3.4 Deformation time of the SDTZ 97

3.4.1 The dominant strike-slip deformation along the SDTZ and D_1 deformation in the Liuling Group 97

3.4.2 D_2 deformation in the Liuling Group 99

3.5 Summary 100

3.6 References 101

Chapter 4: Deformation and Tectonic Implications of the Xinyang-Yuanlong Shear Zone in Western Qinling 106

4.1 Introduction 106

4.2 Field data 109

4.2.1 Geological setting 109

4.2.2 Structural geometric features 111

4.2.2.1 The Yuanlong area 111

4.2.2.2 The Shetang area 114

4.2.2.3 The Xinyang area 118

4.2.2.4 The Wushan area 129

4.3 Geochronology data 130

4.3.1 Sample descriptions 130

4.3.1.1 Samples from the Yuanlong area 130

4.3.1.2 Samples from the Shetang area 130

4.3.1.3 Samples from the Xinyang area 133

4.3.2 Analytical procedures 133

4.3.3 Geochronological results 135

4.4 Interpretations and summary 138

4.4.1 Xenocrystic ages from the samples 138

4.4.1.1 The Archean and Proterozoic age group (2623.6~646.3Ma, 213/377 analyses) 139

4.4.1.2 The Paleozoic age group (524.3~343.6Ma, 159/377 analyses) 141

4.4.1.3 The Mesozoic age group (234.5~121.7Ma, 5/377 analyses)142

4.4.2 Deformation time and kinematic interpretations of the Xinyang-Yuanlong shear zone 143

4.4.2.1 Deformation time in the Yuanlong area 143

4.4.2.2 Deformation time in the Xinyang area 144

(1) District 1, the Xiweizi valley 144

(2) District 2, the Moshi valley 144

(3) District 3, northeast of the Xiweizi and Moshi valleys 145

4.4.2.3 Deformation in the Shetang area 145

4.4.2.4 Deformation in the Wushan area 146

4.4.2.5 The kinematics of the Xinyang-Yuanlong shear zone 147

4.5 The deformation along the SDTZ in western Qinling 153

4.6 Tectonic implications 154

4.6.1 The importance of the strike-slip deformation in the QOB 154

4.6.2 The tectonic configuration of the QOB before the Triassic 156

4.6.3 Tectonic model of the QOB during Triassic 161

4.6.4 The Cretaceous E-W extension recorded in the Liuling Group 164

4.7 References 166

Chapter 5: Conclusions and Future Work 177

5.1 Contribution of this work 177

5.2 Future work 179

5.3 References 181

Appendices 183

Curriculum Vitae 269

List of Tables

Table E1 LA-ICP-MS U-Pb zircon dating results of the samples from the Yuanlong area 197

Table E2 LA-ICP-MS U-Pb zircon dating results of the samples from the Shetang area 200

Table E3 LA-ICP-MS U-Pb zircon dating results of the samples from the Xinyang area 206

Table E4. REE contents (ppm) of the samples from the Yuanlong area 209

Table E5. REE contents (ppm) of the samples from the Shetang area 212

Table E6. REE contents (ppm) of the samples from the Xinyang area 218

List of Figures

Figure 1.1 Spatial scales associated with the deformation of Earth's lithosphere....... 2

Figure 1.2 Heterogenous deformation throughout Earth's lithosphere 3

Figure 1.3 A multiscale approach to study natural deformation................................. 7

Figure 1.4 An Eshelby inclusion in an infinite linear elastic medium......................... 9

Figure 1.5 A conceptual diagram to show the two types of homogenization schemes in MOPLA 10

Figure 1.6 A simplified tectonic map of China showing the major tectonic units and central China orogenic belt 12

Figure 1.7 A geological map of Qinling orogenic belt and its adjacent areas 14

Figure 1.8 A satellite map to show the field work areas... 16

Figure 2.1 A conceptual diagram to illustrate three different scenarios of a clast-matrix system 28

Figure 2.2 Ellipsoid shape quantified by two parameters (R and Φ) in the Flinn space 38

Figure 2.3 The contour plot of computation time (s) with respect to R and Φ.......... 40

Figure 2.4 Optimal quadrature and associated node numbers for different shapes of the inclusion according to the iterative tests.. 42

Figure 2.5 An execution of SGLRGD 45

Figure 2.6 An isotropic ellipsoid embedded in a matrix with planar anisotropy....... 47

Figure 2.7 Comparison of the vorticity difference.. 50

Figure 2.8 Comparison of the strain rates differences 51

Figure 2.9 An example of using SGLRGD.. 51

Figure 2.10 An example of using SGLDEF... 53

Figure 3.1 Geological maps to show the Qinling orogenic belt and the eastern Qinling orogenic belt.. 67

Figure 3.2 Geological map showing the geological units in the Heihe area............. 70

Figure 3.3 Photos showing the deformed conglomerate at the Shaliangzi township 72

Figure 3.4 A diagram showing the concept of a fabric ellipsoid............................... 73

Figure 3.5 Fabric data from the deformed conglomerate 76

Figure 3.6 Photos showing shear-sense indicators in the Maanqiao shear zone 77

Figure 3.7 A conceptual block diagram summarizing the fabrics in the Heihe area. 78

Figure 3.8 Geological map showing the geological units in the Danfeng area 79

Figure 3.9 Photos and fabric data from the high-strain zones 81

Figure 3.10 Two-generation structures observed in the high-strain zones 82

Figure 3.11 Lower-hemisphere equal-area projection of stretching lineations and transposition foliations in the Liuling Group.. 82

Figure 3.12 Photos showing D2 deformation in the Liuling Group 83

Figure 3.13 A conceptual block diagram (not to scale) to illustrate the following idea 84

Figure 3.14 Numerical modeling diagram 88

Figure 3.15 Simulation results of lineations for different convergence angles (α) and dip angles (β) 93

Figure 3.16 Simulation results of poles to foliations for different convergence angles (α) and dip angles (β) 95

Figure 3.17 Field lineations and transposition foliations rotated to the model coordinate system 96

Figure 4.1 Maps showing the field work area 108

Figure 4.2 Photos and fabric data from the Yuanlong area 113

Figure 4.3 Geological map, photos and fabric data from the Shetang area 116

Figure 4.4 Geological map, photos and fabric data from the Xinyang area 117

Figure 4.5 Detailed mapping and photos from the Moshi valley 121

Figure 4.6 Detailed mapping and photos from unit 12 124

Figure 4.7 Detailed mapping and photos from unit 14 126

Figure 4.8 Detailed mapping and photos from unit 20 128

Figure 4.9 Photos and fabric data from the Huluhe Group 128

Figure 4.10 Photos and fabric data from the Wushan area 129

Figure 4.11 Field photos of granitic pegmatitic dykes from the Yuanlong area 131

Figure 4.12 Field photos of granitic pegmatitic dykes from the Shetang area 132

Figure 4.13 Field photos to show dykes from the Xinyang area 134

Figure 4.14 Age spectra from this study and previous studies 139

Figure 4.15 Paleozoic age spectra from this study and Paleozoic granitoids in the north Qinling belt 142

Figure 4.16 Distribution of granitoids with emphasis on Mesozoic granitoids in the Qinling orogenic belt 143

Figure 4.17 A conceptual diagram to show the interpretation of the fabric data from the Xinyang-Yuanlong shear zone 150

Figure 4.18 Transpression model in Jiang (2014) 151

Figure 4.19 Model predicted 'stretching lineations' patterns produced by different boundary conditions in Jiang (2014) 153

Figure 4.20 Forward modeling in van Staal et al. (1998) 155

Figure 4.21 The comparison of the tectonic evolution models from Dong and Santosh (2016, left) and Liu et al. (2016, right) of the QOB during 600~400Ma 160

Figure 4.22 Schematic cartoons showing the tectonic evolution of the Qinling orogenic belt during the Triassic 163

Figure 4.23 Geological map showing Neoproterozoic, Early Paleozoic, Late Triassic and Cretaceous magmatic intrusions in the Qinling orogenic belt 165

Figure E1 CL images and the REE pattern of TS1406 225

Figure E2 CL images and the REE pattern of TS1408-1 229

Figure E3 CL images and the REE pattern of TS1408-2 233

Figure E4 CL images and the REE pattern of ST1502 236

Figure E5 CL images and the REE pattern of ST1510-1 239

Figure E6 CL images and the REE pattern of ST1510-2 242

Figure E7 CL images and the REE pattern of ST1511 245

Figure E8 CL images and the REE pattern of ST1515 249

Figure E9 CL images and the REE pattern of ST1512 251

Figure E10 CL images and the REE pattern of ST1513 255

Figure E11 Concordia diagrams and weighted mean ages of TS1512 and TS1513, respectively 256

Figure E12 CL images and the REE patterns of XY1605 259

Figure E13 CL images and the REE patterns of XY1601A. 262

Figure E14 CL images and the REE patterns of XY1601B.................................... 264

Figure E15 CL images and the REE patterns of XY1602 267

List of Appendices

Appendix A: Empirical functions for the domain boundaries in Fig.2.4................. 183

Appendix B: The MATLAB package instruction in Chapter 2.............................. 184

Appendix C: Download link for the MATLAB package in Chapter 2................... 185

Appendix D: The $R_f - \varphi$ data from the deformed conglomerate in Chapter 3...... 186

Appendix E: The geochronological results in Chapter 4.. 195

Nomenclature

Symbol quantities

a_1, a_2, a_3, a_i	the semi-axes of an ellipsoid (first, second, third, general)
$\mathbf{A}$	strain-rate partitioning tensor (fourth order) for linear materials or strain partitioning tensor for elastic materials
α	boundary convergence angle of a transpression zone
$\mathbf{B}$	stress partitioning tensor (fourth order) for linear materials
β	dip angle of a transpression zone or a high-strain zone
$\mathbf{C}$	elastic moduli or viscous stiffness tensor (fourth order)
$\mathbf{C}$	linearized viscous stiffness tensor
$\overline{\mathbf{C}}$	HEM viscous stiffness tensor
δ	microscale characteristic length
δ_{ij}	Kronecker delta
δt	time step for numerical computation
d	mesoscale characteristic length
D	macroscale characteristic length
$\mathscr{D}$	characteristic length of the whole deformation body
$\mathbf{e}$	elastic strain tensor in the ellipsoid)

$\mathbf{E}$	elastic strain or viscous strain-rate tensor in the far-field matrix or HEM (symmetric part of $\mathbf{L}$ in viscous case)
$\boldsymbol{\varepsilon}$, $\tilde{\boldsymbol{\varepsilon}}$	viscous strain-rate tensor (general or in the ellipsoid), strain-rate difference between the ellipsoid and the far-field matrix
$\mathbf{F}$	position gradient tensor (second order)
$\mathbf{J}^{\mathbf{D}}$, $\mathbf{J}^{A}$	4th order deviatoric and anti-symmetric identity tensors
$\mathbf{L}$	velocity gradient tensor of matrix flow (second order)
λ	fluctuation length of boundary loading or velocity conditions
m	the strength of the anisotropy
$\mathbf{Q}$	transformation matrix defined by the orientation of an ellipsoid
$\overline{\boldsymbol{\Theta}}$	angular velocity tensor of an ellipsoid
n	power law stress exponent
η_n , η_{s}	foliation-normal viscosity, foliation-parallel viscosity
r , r_{eff} , r_0	viscosity ratio between ellipsoid and matrix medium (Newtonian, effective where one or both the ellipsoid and the matrix medium are power law, effective at the matrix medium strain-rate state)
$\boldsymbol{\sigma}$, $\boldsymbol{\sigma}$, $\boldsymbol{\sigma}^0$	Cauchy stress tensor (general or in the ellipsoid), stress difference between the ellipsoid and the far-field

	matrix, pre-stress term in a linearized constitutive relation
$\boldsymbol{\Sigma}$, $\boldsymbol{\Sigma}^0$	Cauchy stress tensor in the far-field matrix or HEM, pre-stress term in a linearized rheological relation for the far-field matrix or HEM
$\mathbf{S}$	symmetric Eshelby tensor for incompressible viscous materials
$\boldsymbol{\Pi}$	anti-symmetric Eshelby tensor for incompressible viscous materials
$\mathbf{T}$	Green interaction tensor for incompressible viscous materials
$\mathbf{w}$, $\mathbf{w}$	vorticity, vorticity difference between the ellipsoid and the far-field matrix medium
$\mathbf{W}$	vorticity of the far-field matrix or HEM, anti-symmetric part of $\mathbf{L}$
$\boldsymbol{\omega}$	elastic rotation tensor

Super- or sub-script labelling

E	ellipsoid
eff	effective

K	the k-th element
M	matrix
tan	tangent
sec	secant

Acronyms

BXDS	Bikou-Xiaomoling-Douling subduction zone
CCOB	Central China orogenic belt
HEM	Homogeneous effective medium
KPS	Kuanping suture
LLWF	Lingbao-Lushan-Wuyang fault
MBXF	Mianlue-Bashan-Xiangguang fault
MHS	Micangshan-Huangling subduction zone
MLS	Mianlue suture
MOPLA	Multi-order power-law approach
NCB	North China block
NQB	North Qinling belt

N-SCB	Northern South China block
QOB	Qinling orogenic belt
RDP	Rheologically Distinct Phase
RVE	Representative Volume Element
SCB	South China Block
SDS	Shangdan suture
SDTZ	Shangdan tectonic zone
SFF	Shangyang-Fengzhen fault
S-NCB	Southern North China block
SQB	South Qinling block
VPSC	self-consistent viscoplastic formulation
XYSZ	Xinyang-Yuanlong shear zone

Chapter 1: Introduction

1.1. The multiscale problem in structural geology studies

Classical continuum models have been well studied and applied to structural analysis to interpret the relationship between fabrics and flow fields in homogeneous rock units (e.g., Ramsay, 1967; Ramsay and Graham, 1970; Ramberg, 1975; Passchier and Trouw, 1996). To identify the structural geometries and kinematics of a deformation zone, one conducts detailed structural analysis and geochronological studies in key areas and then in most cases, attempts to deduce the tectonic evolution of the zone. Field studies generally begin with observations of features at outcrop scale (i.e., a scale of a few millimeters to several meters). Studies then may proceed 'downscale' to observations made at the microscopic or even electron-microscopic level of microns, or 'upscale' to regional observations on a scale of hundreds to thousands of kilometers (Fig.1.1, Bruce and Ord, 2015). However, when one must analyze structures for a wide range of characteristic lengths in a single problem, the rheological heterogeneities of the lithosphere cause flow partitioning (Lister and Williams, 1983; Jiang, 2014). Structural geology studies on relatively small-scale features ('minor structures' in Jiang, 2013) are disconnected from large-scale tectonic synthesis. This scale problem has been recognized for many decades in structural geology studies (e.g., Lister and Williams, 1979, 1983; Jiang, 1994a,b; Jiang and White, 1995; Jiang and Williams, 1999). During the deformation of the lithosphere, the 'bulk' or 'regional' flow is partitioned into different small-scale rheologically distinct domains, and the final structures and fabrics are produced directly by the partitioned flow fields in 'local' domains (Fig.1.2). 'Partitioning' is generally used as a qualitative concept to, sometimes, 'explain' observations that do not fit the predictions of simple models, or, at other times, critique simple-minded extrapolations from small-scale observations to large-scale processes. The use of small structures to infer tectonic processes is impeded if ‘partitioning’ is not considered quantitatively. Classical single-scale models cannot effectively address the heterogeneous deformation (Jiang, 2014). Therefore, a multiscale approach is necessary to link small-scale geological observations to large-scale tectonic synthesis.

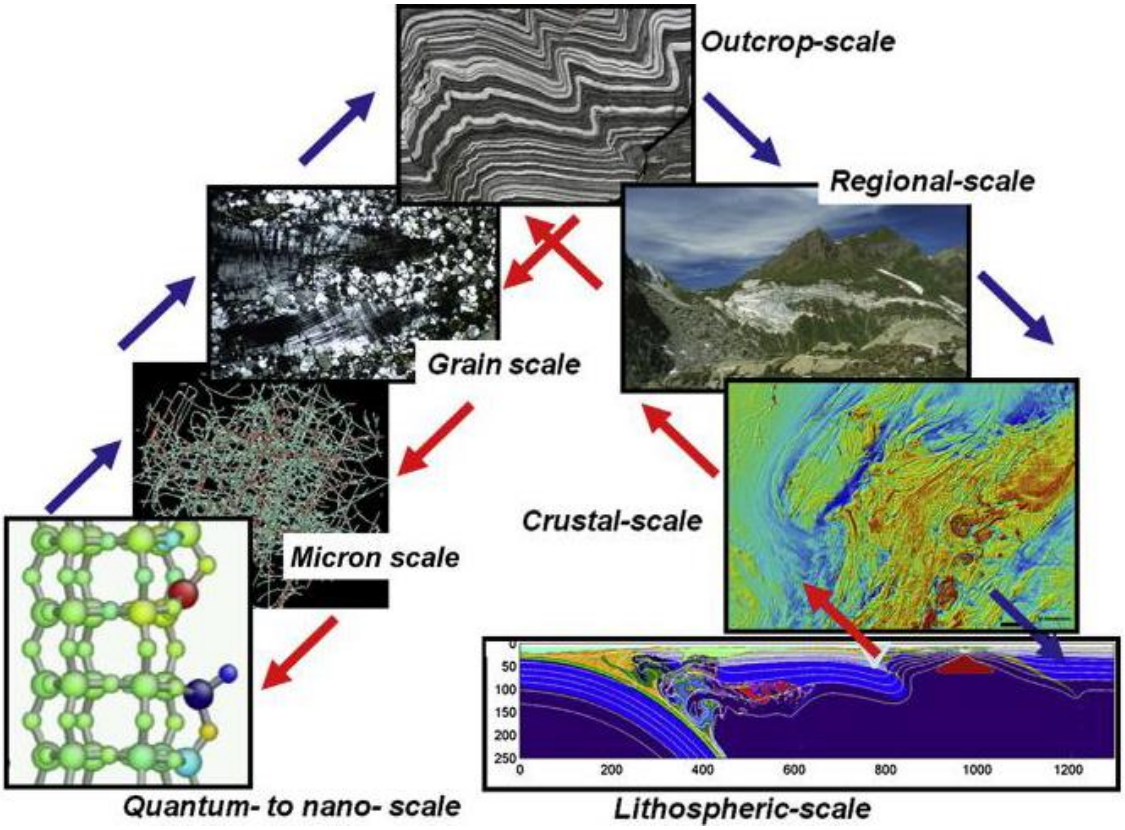

Figure 1.1 Spatial scales associated with the deformation of Earth’s lithosphere. The blue arrows show the ‘upscale’ processes, the red arrows show the ‘downscale’ processes (Bruce and Ord, 2015).

Recently, Jiang and Bentley (2012) and Jiang (2013, 2014) have developed a multiscale approach, called the multi-order power-law approach (MOPLA), based on micromechanics to quantitatively deal with ‘partitioning’ and bridge the scale gap between small-scale structures and large-scale tectonic synthesis.

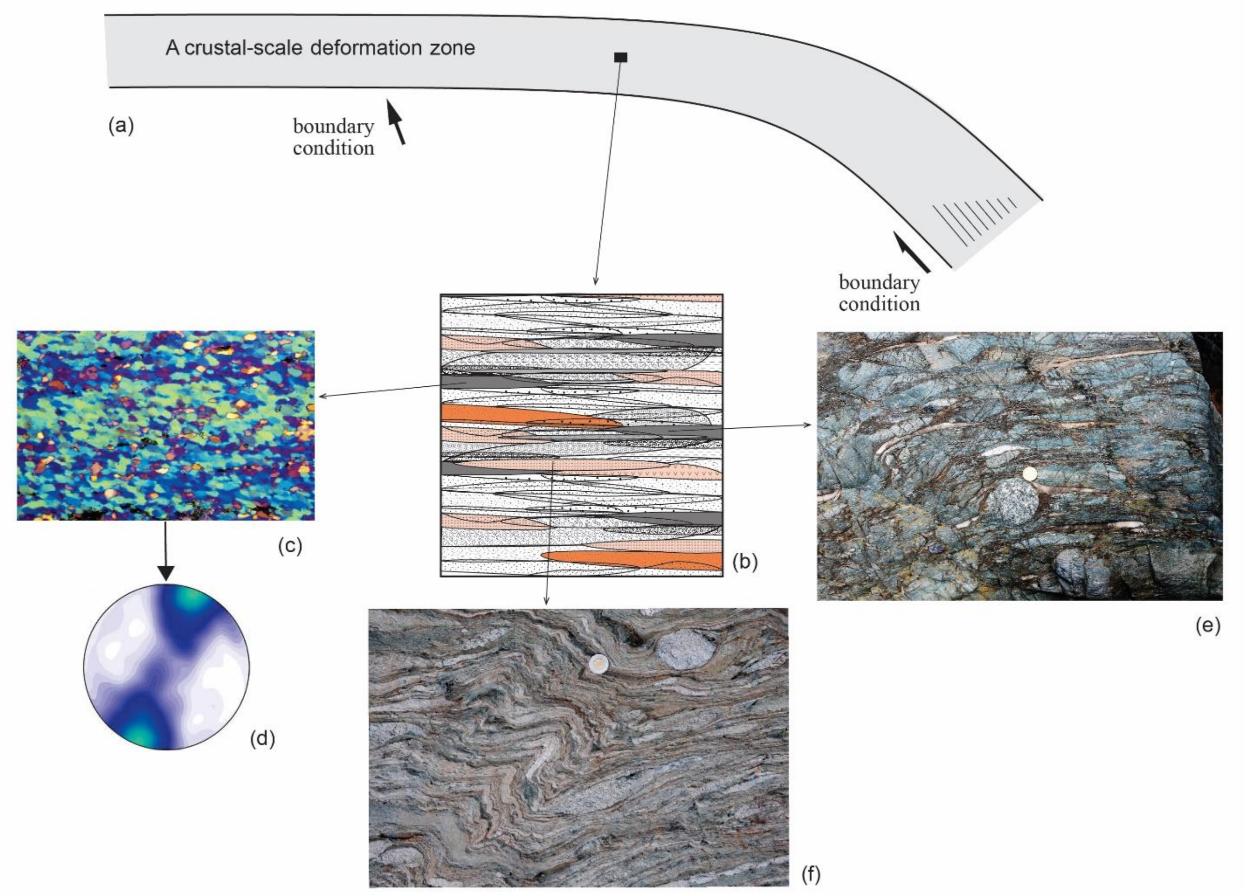

Figure 1.2 Heterogenous deformation throughout Earth’s lithosphere (modified after Jiang, 2014). (a) illustrates a crustal-scale deformation zone. (b) is a small region in the deformation zone and composed of transposed deformation domains. (e) and (f) are variable structures that are observed on outcrops. (c) and (d) are the microstructures observed under microscopes. (c)-(f) are directly produced by the ‘local’ flow fields in each domain in (b).

1.2. MOPLA

MOPLA stands for the multi-order power-law approach. MOPLA was built up to effectively address the heterogeneous deformation throughout the rheologically heterogeneous lithosphere. MultiOrder means that with the idea of 'elements within elements', one can investigate rheological elements with multiple characteristic lengths, from relatively large (lower-order) elements (e.g., a deformed geological unit) to small (high-order) elements (e.g., fabric-defining elements inside the deformed geological unit) using MOPLA. Power-Law indicates that MOPLA considers deformed rocks as power-law viscous materials that reflect the rheological behavior of rocks for ductile deformation (Tullis et al., 1991; Kohlstedt et al., 1995). The theoretical formulations of MOPLA have been fully developed in Jiang (2014, 2016), and the algorithms are implemented in MathCad and MATLAB.

1.2.1 The aim of MOPLA

The aim of MOPLA is to effectively investigate the heterogeneous deformation that is mainly caused by the rheological heterogeneities in Earth's lithosphere and to bridge the scale gap between the small-scale observations to large-scale tectonic synthesis.

The idea of MOPLA is illustrated in Fig.1.3. Fig.1.3 considers three different scales, and they are, from large to small, the *macroscale*, the *mesoscale* and the *microscale*. According to the nature of a problem, one can consider more scales if necessary. There are many orders of magnitude differences among the characteristic lengths of the three scales, and the absolute lengths depend on exact problems. In Fig.1.3, the deformation in a crustal-scale zone is regarded as the macroscale deformation (Fig.1.3a) with a characteristic length of $\mathcal{D}$. The statistically homogenous macroscale fields ('regional' stress, strain-rate and vorticity fields) are defined in terms of a Representative Volume Element (RVE) at every location (X) with a characteristic length of D (Fig.1.3b). If a neighbor location (X' in Fig.1.3b) is considered, the RVE is slightly shifted but most parts overlap with the previous RVE. The RVE is a large enough volume element containing a representative assemblage of all Rheologically Distinct Phases (RDPs) with a characteristic length of d (Fig.1.3c). D, the size of the RVE, represents the macroscale characteristic length. D must be sufficiently smaller than the characteristic dimensions $\mathscr{D}$ of the whole deformation zone, and smaller than the fluctuation length λ of the boundary loading. Namely, $D \ll \mathscr{D}$ and $D \ll \lambda$.

The mesoscale fields ('local' stress, strain-rate and vorticity fields) are regarded as the field quantities in individual rheological heterogeneities. Rheological heterogeneities may vary in size, but one can always divide larger rheological heterogeneities into smaller units, so that in a single problem, all RDPs have similar sizes with a characteristic length, d, in a macroscale RVE, and $\mathrm{d} \ll D$. We assume d is small enough that the deformation fields inside each RDP are uniform. The shape of an RDP is approximated by an ellipsoid (Fig.1.3d). An RDP interacts with a Homogeneous Effective Medium (HEM) that is the homogenized medium on the RVE (Fig.1.3d).

The microscale features with a characteristic length of δ can be considered as the structures and fabric elements within mesoscale RDPs. They can be structures that are directly observed on outcrops (Fig.1.3e), or they can be the microstructural shape and lattice fabrics under microscope (Fig.1.3f, g) if the deformation in an RDP is homogeneous down to the microscopic scale. The condition, $\delta \ll \mathrm{d}$, is assumed so that the microscale elements do not break the assumption that the mesoscale deformation inside each RDP is uniform.

In summary, the scale gaps among the microscale, the mesoscale and the macroscale can be expressed as $\delta \ll \mathrm{d} \ll D \ll \mathscr{D},\ D \ll \lambda$. This scale separation condition is the basis to regard mesoscale RDPs as Eshelby inhomogeneities in a macroscale deforming RVE and microscale fabrics as inclusions in partitioned fields in RDPs. The characteristic length scale description is not rigorous. The same method is used at different length scales if the material at the smallest scale is still a continuum body (i.e., micron scale and above in Fig.1.1). For a scale lower than microns, a discrete particle system made of atoms or molecules, and molecular dynamics (MD) and quantum mechanics are used to study the behavior of the material (e.g., Ollila et al., 2013).

As we assume that the deformation fields within mesoscale RDPs are uniform, microscale and mesoscale field quantities are the same for each RDP. The macroscale field quantities can be related to microscale field quantities by definition (Hill, 1963; 1967; Jiang, 2014):

$$\boldsymbol{\Sigma}\left(\mathbf{X}\right)=\frac{1}{V}\int_{V}\boldsymbol{\sigma}\left(\mathbf{x}\right)dV=\left\langle\boldsymbol{\sigma}\right\rangle \tag{1.1a}$$

$$\dot{\mathbf{E}}\left(\mathbf{X}\right)=\frac{1}{V}\int_{V}\dot{\boldsymbol{\varepsilon}}(\mathbf{x})dV=\left\langle\dot{\boldsymbol{\varepsilon}}\right\rangle \tag{1.1b}$$

$$\mathbf{W}\left(\mathbf{X}\right)=\frac{1}{V}\int_{V}\mathbf{w}(\mathbf{x})dV=\left\langle\mathbf{w}\right\rangle \tag{1.1c}$$

where $\boldsymbol{\Sigma}$, $\dot{\mathbf{E}}$ and $\mathbf{W}$ are respectively macroscale stress, strain-rate, and vorticity; $\boldsymbol{\sigma}$, $\dot{\boldsymbol{\varepsilon}}$ and $\mathbf{w}$ are respectively microscale stress, strain-rate and vorticity; $\mathbf{X}$ and $\mathbf{x}$ represent the macroscale and microscale locations respectively; V is the volume of the RVE, and the operator $\left\langle\bullet\right\rangle$ indicates the volume average value over the RVE.

The inverse relations of the Eqs.1.1 are to obtain the partitioned mesoscale flow fields within RDPs from imposed macroscale fields and can quantitively solve the flow partitioning problem caused by the rheological heterogeneities of the lithosphere (Lister and Williams, 1983). The extended Eshelby theory is used to solve the partitioned fields in MOPLA and will be introduced in the next section.

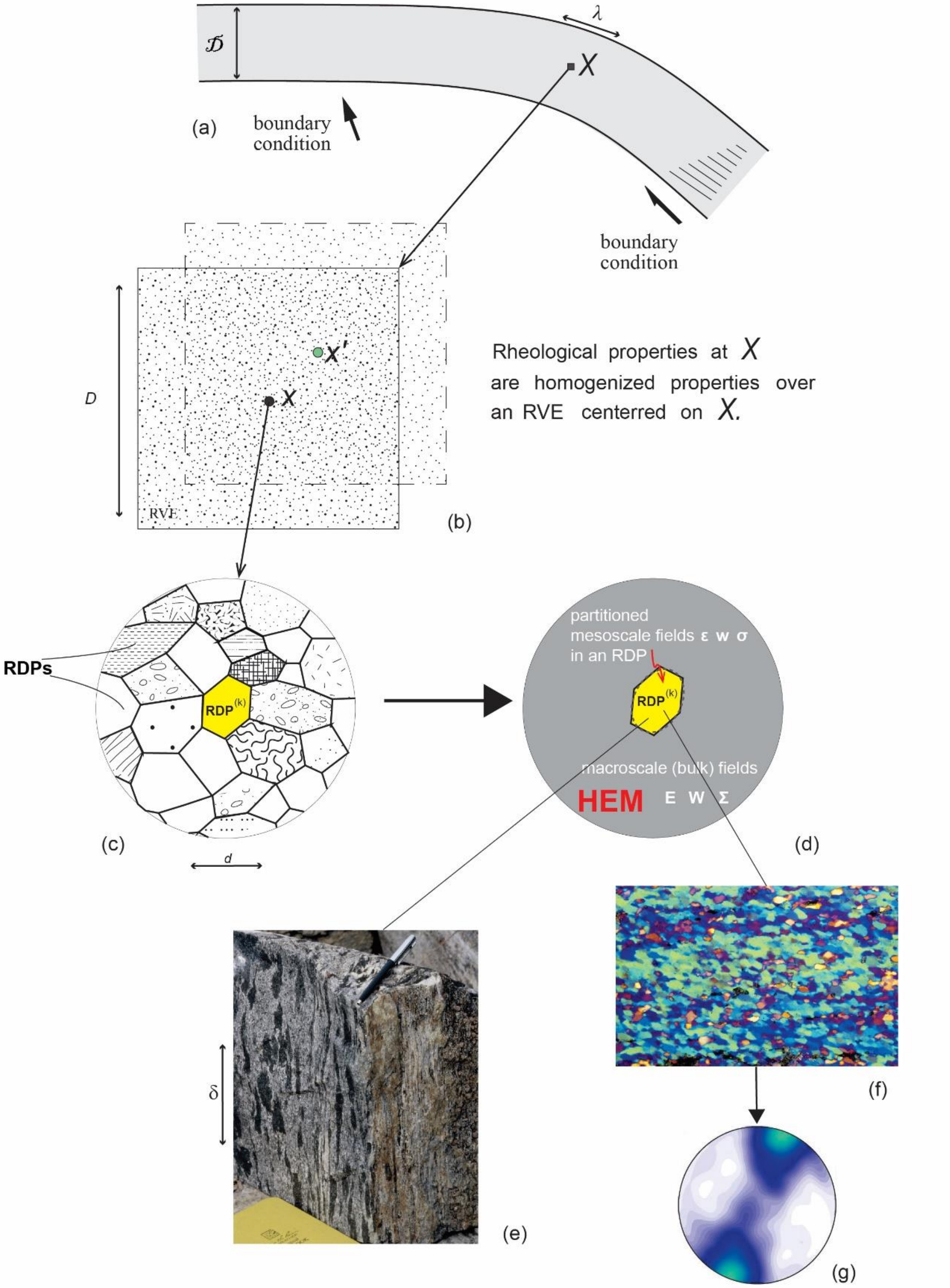

Figure 1.3 A multiscale approach to study natural deformation (modified after Jiang, 2014). See text for detailed explanation.

1.2.2 The backbone theory of MOPLA

The backbone theory of MOPLA is the extended Eshelby formalism for power-law viscous materials (Jiang and Bentley, 2012; Jiang, 2013, 2014). The classical Eshelby inclusion problem deals with an elastic ellipsoidal inclusion embedded in an infinite uniform elastic medium. Eshelby (1957, 1959) gave the expressions of the mechanical fields inside the inclusion (the interior fields) and around the inclusion (the exterior fields) in terms of the far-field mechanical fields. Eshelby (1957) solved the problem by proceeding a thought experiment on the possible mechanical fields in a linear elastic medium containing an inclusion. He considered the situation where the inclusion has undergone a transformation and correspondingly needed to change shape and size to accommodate the transformation, but the change is restricted due to the surrounding material (Fig.1.4). Eshelby (1957) used a ‘sequence of imaginary cutting, straining and welding operations’ and found that the resulting elastic field can be obtained.

Mura (1987) summarized Eshelby’s work of an inhomogeneity inclusion inside a matrix. The general solution of an elastic inhomogeneity problem is expressed by the following set of equations (Jiang 2014, his Eqs.9):

$$\mathbf{e} = \mathbf{A} : \mathbf{E} \ , \ \ \mathbf{A} = \left[\mathbf{J}^{s} + \mathbf{S} : \left(\mathbf{C}_{\mathbf{M}}^{-1} : \mathbf{C}_{\mathbf{E}} - \mathbf{J}^{\mathbf{S}} \right) \right]^{-1} \tag{1.2a}$$

$$\boldsymbol{\omega}^{\mathbf{E}} = \boldsymbol{\omega}^{\mathbf{M}} + \boldsymbol{\Pi} : \mathbf{S}^{-1} : \left(\mathbf{e} - \mathbf{E} \right) \tag{1.2b}$$

$$\boldsymbol{\sigma} = \mathbf{B} : \boldsymbol{\Sigma} \ , \ \ \mathbf{B} = \mathbf{C}_{\mathbf{E}} : \mathbf{A} : \mathbf{C}_{\mathbf{M}}^{-1} \tag{1.2c}$$

where $\mathbf{e}$, $\boldsymbol{\omega}^{\mathrm{E}}$, and $\boldsymbol{\sigma}$ are strain, rotation and stress fields inside inhomogeneity, respectively; $\mathbf{E}$, $\boldsymbol{\omega}^{\mathbf{M}}$ and $\boldsymbol{\Sigma}$ are corresponding macroscale fields in infinite matrix; $\mathbf{C}^{\mathrm{E}}$ and $\mathbf{C}^{\mathbf{M}}$ represent the elastic stiffness inside inhomogeneity and matrix, respectively; $\mathbf{A}$ and $\mathbf{B}$ are respectively strain partitioning tensor and stress partitioning tensor; $\mathbf{S}$ and $\boldsymbol{\Pi}$ are two 4th order Eshelby tensors.

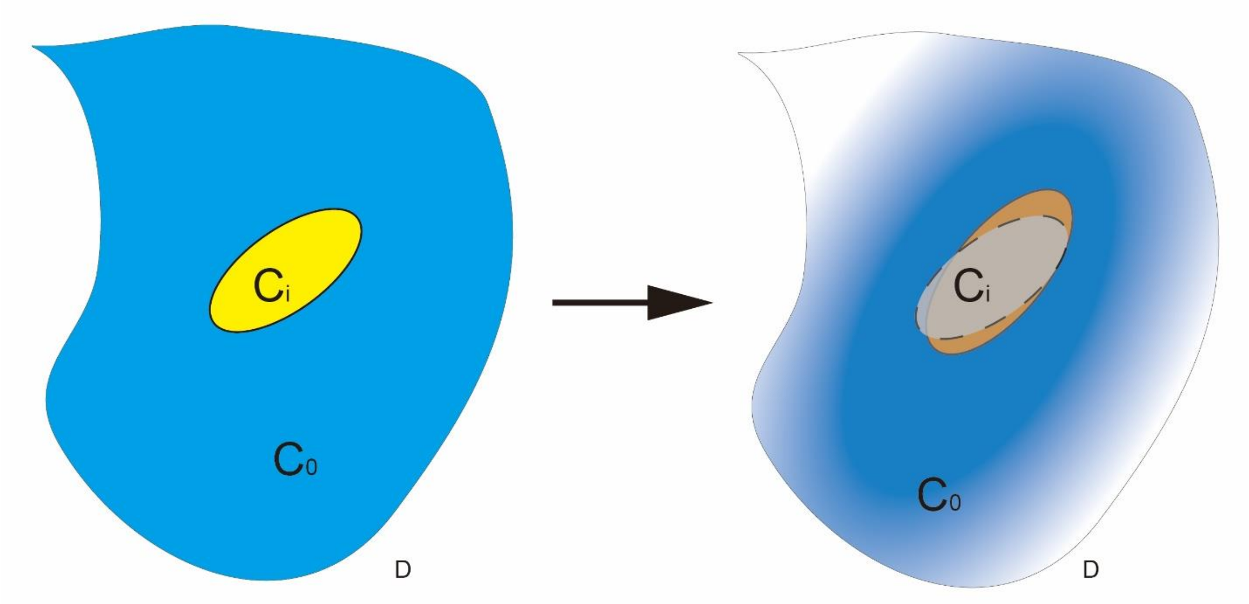

Figure 1.4 An Eshelby inclusion in an infinite linear elastic medium. The stiffness tensor of the medium is C_0, and the stiffness tensor of the inclusion is C_i. A transformation strain changes the shape and orientation of the inclusion. The matrix is with the characteristic length of D that is much larger than the size of the inclusion.

The above solutions have been extended to isotropic Newtonian viscous materials (Bilby et al., 1975; Bilby and Kolbuszewski, 1977) and to nonlinear viscous power-law materials through the linearization approach (e.g., Hutchinson, 1976; Molinari et al., 1987; Lebensohn and Tomé, 1993; Masson et al., 2000; Lebensohn et al., 2003, 2004; Jiang 2013, 2014).

1.2.3 Homogenization systems in MOPLA

The above extended Eshelby theory for power-law viscous materials is for an isolated Eshelby inhomogeneity embedded in an infinite homogeneous matrix. In MOPLA, every mesoscale RDP is treated as an Eshleby inhomogeneity embedded in an effective Homogeneous Effective Medium (HEM, Figs. 1.3d, 1.5), and the calculation of the mesoscale field quantities of RDPs from the macroscale field quantities is the partitioning process. The rheological properties of HEM are represented by the overall rheological properties of the RVE. The process to calculate the rheological properties of HEM from the overall properties of the RVE is called homogenization. The homogenization process is based on the extended Eshleby theory as well (Jiang, 2014).

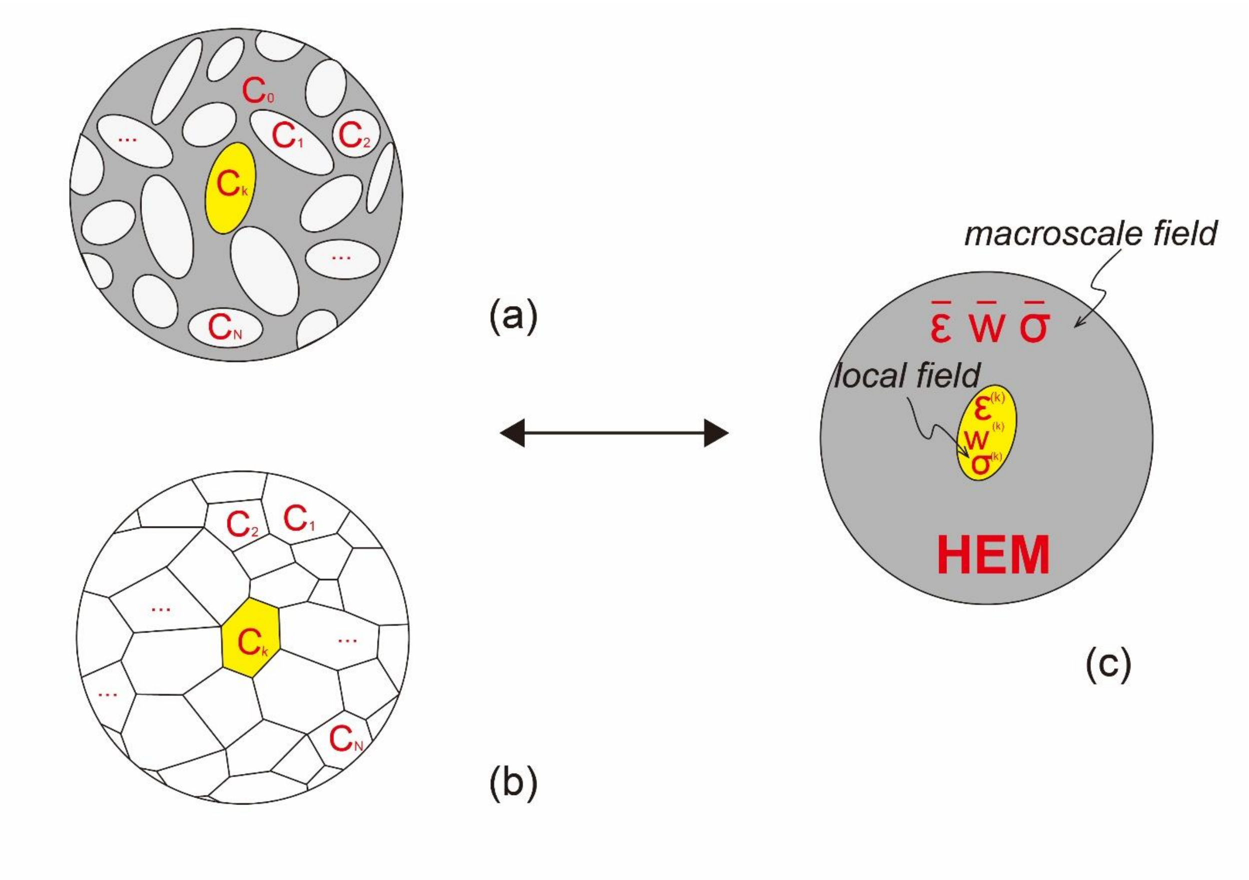

Figure 1.5 A conceptual diagram to show the two types of homogenization schemes in MOPLA (modified after Qu et al., 2016). (a) The Mori-Tanaka homogenization scheme is used for a composite material with crowed inclusions embedded in a connected matrix representing. (b) The self-consistent homogenization scheme is used for a continuum of poly-elements without a matrix phase. (c) The rheological properties of the homogeneous effective medium (HEM) are the 'average' from all the constituent elements in (a) or (b).

An RVE can be considered as a composite material, and there are two ways to proceed homogenization in MOPLA. One is the self-consistent system (Fig.1.5b) (Jiang, 2014), and the another is the Mori-Tanaka system (Fig.1.5a) (Mori and Tanaka, 1973). For composite materials such as polycrystalline materials without a distinct matrix phase, the self-consistent homogenization scheme is used. For a composite material with inclusions embedded in a connected matrix, especially the concentration of the matrix phase should be around 25%-30%, the Mori-Tanaka homogenization method (Mori and Tanaka, 1973; Mercier and Molinari, 2009) is adopted.

In both systems, the partitioning and homogenization processes run in a self-consistent fashion. The initial rheological properties of RDPs are known, but, as the power-law viscous materials are considered, the actual viscous compliances (or stiffnesses) in RDPs are unknown until the mesoscale stress or strain-rate fields in RDPs obtained. Simultaneously, to calculate the partitioned mesoscale field quantities in RDPs, the rheological properties of HEM that are from the instantaneous viscous compliance (or stiffness) are required (Fig.1.5). The detailed equations are in Jiang (2014).

1.3. Application to the Shangdan tectonic zone in the Qinling orogenic belt

So far, MOPLA has only been applied to the Cascade Lake shear zone in the eastern Sierra Nevada region of California (Jiang and Bentley, 2012; Jiang, 2014), and more work is needed to explore possible fabric patterns for different sets of boundary conditions and model parameters. In this thesis, MOPLA is applied to the data-rich Shangdan tectonic zone (SDTZ) in the Qinling orogenic belt (QOB) to investigate the tectonic evolution of the QOB.

1.3.1 The problem in the QOB studies

The QOB separates China into the North China Block (NCB) and the South China Block (SCB), and it links the Kunlun, Qilian orogens in the west and the Dabie orogen in the east. The

Kunlun, Qilian, Qinling and Dabie orogens together are called the Central China Orogenic Belt (Fig.1.6, Dong et al., 2015).

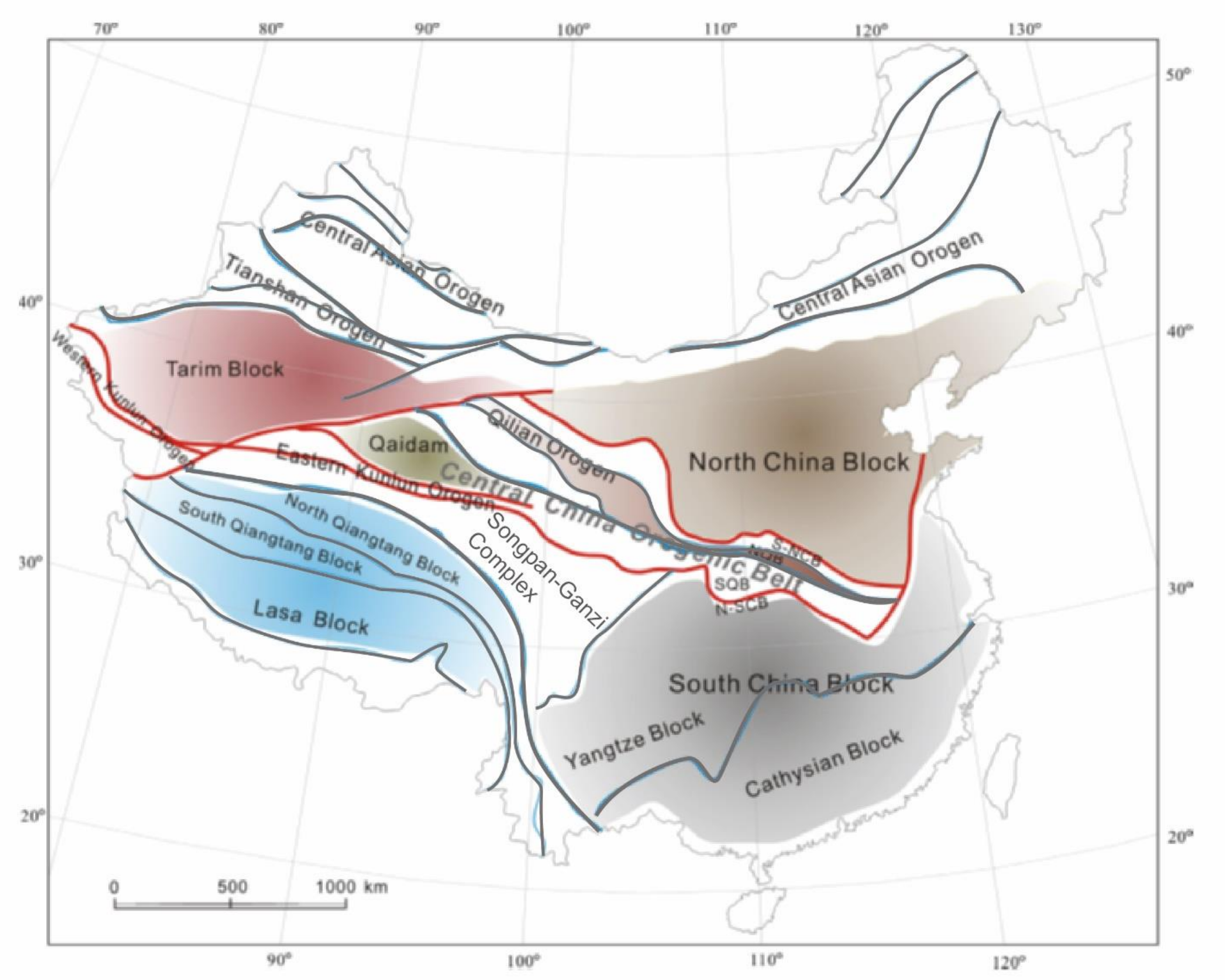

Figure 1.6 A simplified tectonic map of China showing the major tectonic units and central China orogenic belt (the red-line area) (modified after Dong et al., 2015).

The main morphology of the QOB resulted from the final Triassic collision between the NCB and SCB, and the Cenozoic extension across China, but the QOB is a long-lived orogen and has experienced accretional and collisional processes since the Precambrian (Dong and Santosh, 2016 and references therein). The QOB is divided into two major belts, the North Qinling Belt (NQB) and the South Qinling Belt (SQB), by the Shangdan suture (Fig1.7). The Shangdan suture is Paleozoic and marked by discontinuously exposed ophiolite mélange, clastic sedimentary rocks and carbonates (Zhang et al., 2001; Dong et al., 2011a,b; Dong and Santosh, 2016). The Shangdan suture and its adjacent areas are referred to as the Shangdan tectonic zone (SDTZ) in this work. Because the western and eastern parts of the QOB show distinctive features (Zhang et al., 2001), the QOB is roughly divided into the western Qinling belt and the eastern Qinling belt by ~108°E (Fig1.7, Zhang et al., 2001).

In eastern Qinling, sub-vertical foliations and sub-horizontal stretching lineations with sinistral shear-sense indicators have been observed in mylonites along the SDTZ (Mattauer et al., 1985; Xu et al., 1986; Zhang et al., 1989; Reischmann et al., 1990; Wang et al., 2005), and the fabrics indicate a sinistral strike-slip deformation. However, the age of this deformation and how it is related to the tectonic evolution of the QOB are still unclear. The detailed field work is conducted along the SDTZ in eastern Qinling in order to investigate the above questions.

In western Qinling, the NQB and Shangdan suture are not well established, and the structural features are unclear due to the cover of the Quaternary. With the guidance of Dr.Wentian Liang at Northwest University, we were able to find a shear zone, called the Xinyang-Yuanlong shear zone, in western Qinling. This shear zone was recognized in 2004 during a 1:250,000 regional geological mapping project and mapped as the boundary between the QOB and the Qilian orogen. It is also suggested as the western extension of the SDTZ by some researchers. The Xinyang-Yuanlong shear zone is studied in detail to address the following questions: what the geometric structures and kinematics of the zone and the corresponding deformation time are; how this shear zone relates to the deformation in eastern Qinling; whether this shear zone is the SDTZ in western Qinling.

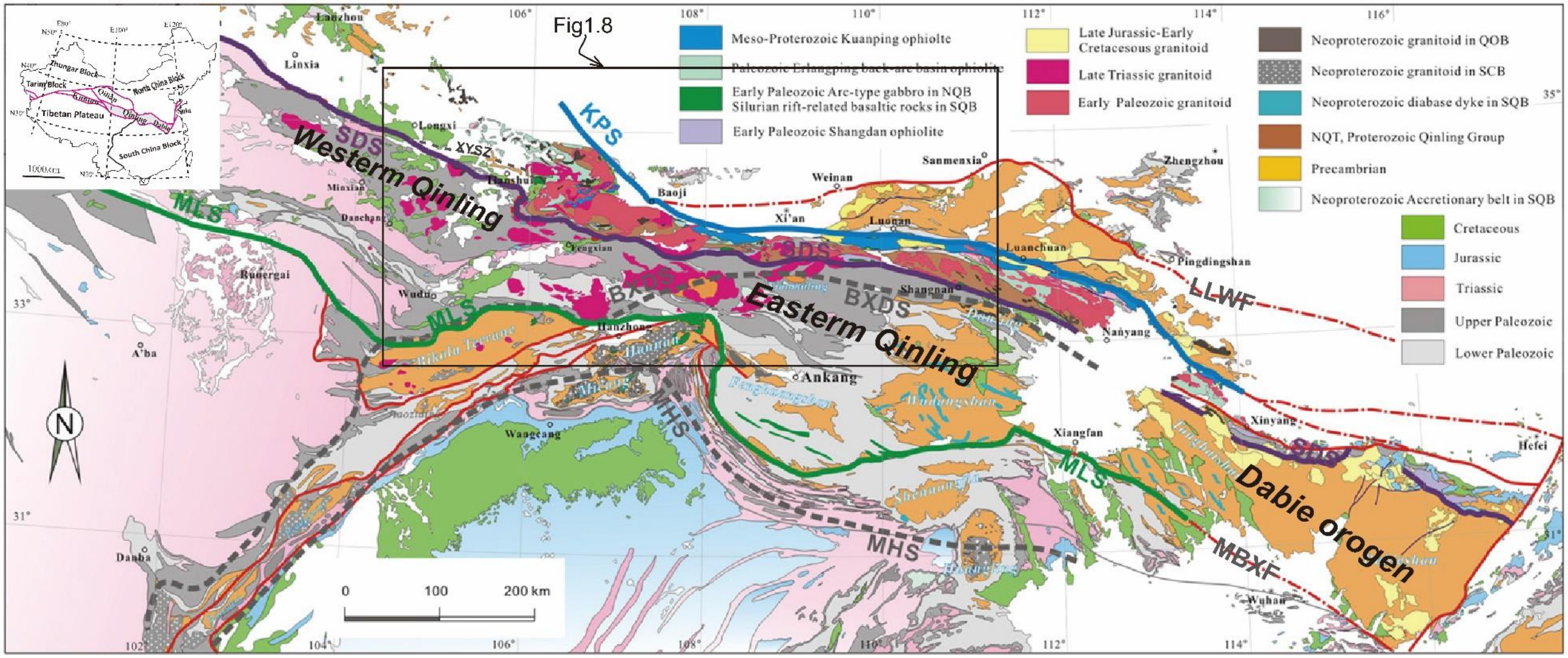

Figure 1.7 A geological map of Qinling orogenic belt and its adjacent areas. KPS: the Neoproterozoic Kuanping suture; SDS: the Paleozoic Shangdan suture; MLS: the Triassic Mianlue suture; BXDS: the Neoproterozoic Bikou-Xiaomoling-Douling subduction zone; MHS: the Neoproterozoic Micangshan-Huangling subduction zone; LLWF: the Lingbao-Lushan-Wuyang fault; MBXF: the Mianlue-Bashan-Xiangguang fault; XYSZ: the Xinyang-Yuanlong shear zone. The grey part in the left-up-corner map showing the location of the Qinling-Dabie orogen in China (Dong and Santosh, 2016).

Overall, in this thesis, the detailed field work and geochronological studies are conducted along the SDTZ in the western and eastern QOB, and the outcrop-scale fabrics are used to extrapolate the tectonic-scale boundary conditions by applying MOPLA to the field work areas.

1.3.2 The framework of the QOB

The first recorded study in the Qinling Mountain was a field investigation from Baoji to Hanzhong by F. Von Richthofen, a German, in the year of 1866 (Zhang et al., 2001). Since then, a lot of route surveys and preliminary geological inquiries were carried out in the Qinling Mountain (Zhao and Huang, 1931 as cited in Zhang et al., 2001). Since the 1950s, regional geological surveys were started in the Qinling Mountain. In the early 1980s, the first geological map of the Qinling Mountains on a scale of 1:200000 was completed, and several geochemical and geophysical studies were carried out (Zhang et al., 2001).

Over the past three decades, many studies have shown that the QOB was produced by the collisions among the micro-continents between the NCB and the SCB and the terminal collision of the NCB and the SCB (e.g., Mattatuer et al., 1985; Zhang et al., 1989; Enkin et al., 1992; Ames et al., 1996; Hacker et al., 1998; Meng and Zhang, 1999, 2000; Faure et al., 2001; Zhang et al., 2001; Ratschbacher et al., 2003, 2006; Dong et al., 2011a,b,c, 2012; Bader et al., 2013a,b; Dong and Santosh, 2016). At present, the Qinling orogen is bounded by the Lingbao-Lushan-Wuyang fault (LLWF) in the north and the Mianlue-Bashan-Xiangguang fault (MBXF) in the south (Fig1.7). It extends more than 1500km from west to east across central China, and it links Dabie

Mountains in the east and Qilian and Kunlun Mountains in the west. The QOB is generally divided into four tectonic belts that are the Southern North China Block (S-NCB), the North Qinling Belt (NQB), the South Qinling Belt (SQB) and the Northern South China Block (N-SCB) by 3 major sutures (i.e., the Neoproterozoic Kuanping suture, the Paleozoic Shangdan suture and the Triassic Mianlue suture) from north to south (Meng and Zhang, 2000; Zhang, et al., 2001; Dong et al., 2011a).

1.4. Objectives and methodology

The main objective of this thesis is to investigate the tectonic evolution of the SDTZ and to refine existing tectonic models for the QOB. Considering the distinctive features of western Qinling and eastern Qinling, the field study of the SDTZ in this thesis is correspondingly divided into the eastern part and the western part (Figs1.7,1.8).

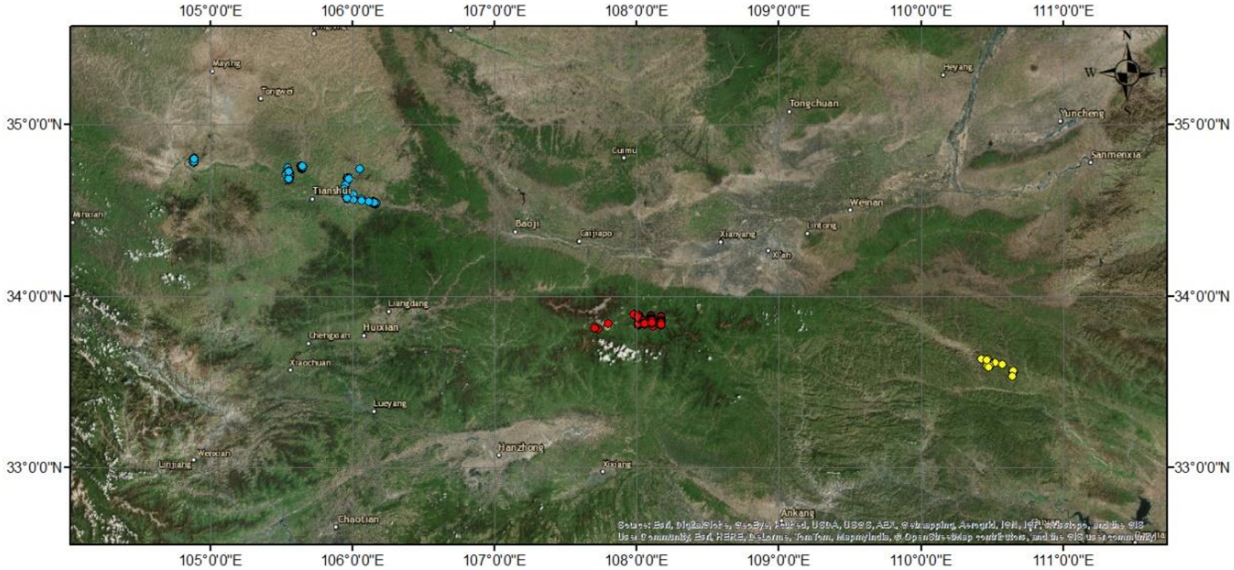

Figure 1.8 A satellite map to show the field work areas. Red and yellow dots are the traces along the SDTZ in eastern Qinling, and the blue dots are the footprints along the Xinyang-Yuanlong shear zone in western Qinling.

The detailed structural mapping is conducted to reveal the spatial changes of fabrics using a Trimble Yuma differential Global Position System (GPS) with 1-to-2-meter accuracy. To relate the deformation with the tectonic evolution of the QOB, the deformation time is constrained by regional structural correlation and geochronology studies. U-Pb Laser Ablation Inductively Coupled Plasma Mass Spectrometry (LA-ICP-MS) Zircon dating of the deformation-related dykes is used for the geochronological studies in this thesis. MOPLA is applied to research areas and used to simulate fabrics produced by partitioned flow fields, in order to infer the tectonic-scale boundary conditions.

1.5. Thesis outline

This thesis investigates the deformation of the SDTZ in eastern Qinling and the Xinyang-Yuanlong shear zone in western Qinling using MOPLA. There are six chapters. Chapter 1 provides a general introduction to this thesis. Chapter 2 develops an optimal scheme to efficiently evaluate the Eshleby tensors and implements the scheme into a MATLAB package to improve the computational efficiency of MOPLA. Chapter 3 studies the deformation of the SDTZ in eastern Qinling. Chapter 4 studies the deformation of the Xinyang-Yuanlong shear zone in western Qinling and integrates the previous results in eastern Qinling (i.e., Chapter 3) and discusses the tectonic synthesis of the deformation along the SDTZ in the QOB. Chapter 5 summarizes the contribution of this work and the future work of this study.

1.6. References

Ames, L., Gaozhi, Z. and Baocheng, X., 1996. Geochronology and isotopic character of ultrahigh-pressure metamorphism with implications for collision of the Sino-Korean and Yangtze cratons, central China. Tectonics, 15(2), pp.472-489.

Bader, T., Ratschbacher, L., Franz, L., Yang, Z., Hofmann, M., Linnemann, U. and Yuan, H., 2013a. The heart of China revisited, I. Proterozoic tectonics of the Qin mountains in the core of supercontinent Rodinia. Tectonics, 32(3), pp.661-687.

Bader, T., Franz, L., Ratschbacher, L., Capitani, C., Webb, A.A.G., Yang, Z., Pfänder, J.A., Hofmann, M. and Linnemann, U., 2013b. The Heart of China revisited: II Early Paleozoic (ultra) high-pressure and (ultra) high-temperature metamorphic Qinling orogenic collage. Tectonics, 32(4), pp.922-947.

Bilby, B.A., Eshelby, J.D. and Kundu, A.K., 1975. The change of shape of a viscous ellipsoidal region embedded in a slowly deforming matrix having a different viscosity. Tectonophysics, 28(4), pp.265-274.

Bilby, B.A. and Kolbuszewsk, M.L., 1977. The finite deformation of an inhomogeneity in two-dimensional slow viscous incompressible flow. In Proc. R. Soc. Lond. A, 355(1682), pp.335-353.

Dong, Y. and Santosh, M., 2016. Tectonic architecture and multiple orogeny of the Qinling Orogenic Belt, Central China. Gondwana Research, 29(1), pp.1-40.

Dong, Y., Zhang, G., Neubauer, F., Liu, X., Genser, J. and Hauzenberger, C., 2011a. Tectonic evolution of the Qinling orogen, China: review and synthesis. Journal of Asian Earth Sciences, 41(3), pp.213-237.

Dong, Y., Zhang, G., Hauzenberger, C., Neubauer, F., Yang, Z. and Liu, X., 2011b. Palaeozoic tectonics and evolutionary history of the Qinling orogen: evidence from geochemistry and geochronology of ophiolite and related volcanic rocks. Lithos, 122(1-2), pp.39-56.

Dong, Y., Genser, J., Neubauer, F., Zhang, G., Liu, X., Yang, Z. and Heberer, B., 2011c. U-Pb and 40Ar/39Ar geochronological constraints on the exhumation history of the North Qinling terrane, China. Gondwana Research, 19(4), pp.881-893.

Dong, Y., Liu, X., Zhang, G., Chen, Q., Zhang, X., Li, W. and Yang, C., 2012. Triassic diorites and granitoids in the Foping area: Constraints on the conversion from subduction to collision in the Qinling orogen, China. Journal of Asian Earth Sciences, 47, pp.123-142.

Dong, Y., Zhang, X., Liu, X., Li, W., Chen, Q., Zhang, G., Zhang, H., Yang, Z., Sun, S. and Zhang, F., 2015. Propagation tectonics and multiple accretionary processes of the Qinling Orogen. Journal of Asian Earth Sciences, 104, pp.84-98.

Enkin, R.J., Yang, Z., Chen, Y. and Courtillot, V., 1992. Paleomagnetic constraints on the geodynamic history of the major blocks of China from the Permian to the present. Journal of Geophysical Research: Solid Earth, 97(B10), pp.13953-13989.

Eshelby, J.D., 1957. The determination of the elastic field of an ellipsoidal inclusion, and related problems. In Proc. R. Soc. Lond. A, 241(1226), pp.376-396.

Eshelby, J.D., 1959. The elastic field outside an ellipsoidal inclusion. In Proc. R. Soc. Lond. A, 252(1271), pp.561-569.

Eshelby, J.D., 1961. Elastic inclusions and inhomogeneities. Progress in Solid Mechanics, 2(1), pp.89-140.

Faure, M., Lin, W. and Le Breton, N., 2001. Where is the North China–South China block boundary in eastern China?. Geology, 29(2), pp.119-122.

Hacker, B.R., Ratschbacher, L., Webb, L., Ireland, T., Walker, D. and Shuwen, D., 1998. U/Pb zircon ages constrain the architecture of the ultrahigh-pressure Qinling–Dabie Orogen, China. Earth and Planetary Science Letters, 161(1-4), pp.215-230.

Hill, R., 1963. Elastic properties of reinforced solids: some theoretical principles. Journal of the Mechanics and Physics of Solids, 11(5), pp.357-372.

Hill, R., 1967. The essential structure of constitutive laws for metal composites and polycrystals. Journal of the Mechanics and Physics of Solids, 15(2), pp.79-95.

Hobbs, B.E. and Ord, A., 2015. Structural geology: the mechanics of deforming metamorphic rocks. Elsevier.

Hutchinson, J.W., 1976. Bounds and Self-Consistent Estimates for Creep of Polycrystalline Materials. Proceedings of the Royal Society of London. A. Mathematical and Physical Sciences, 348(1652): 101-127.

Jiang, D., 1994a. Flow variation in layered rocks subjected to bulk flow of various kinematic vorticities: theory and geological implications. Journal of Structural Geology, 16(8), pp.1159-1172.

Jiang, D., 1994b. Vorticity determination, distribution, partitioning and the heterogeneity and non-steadiness of natural deformations. Journal of Structural Geology, 16(1), pp.121-130.

Jiang, D., 2013. The motion of deformable ellipsoids in power-law viscous materials: Formulation and numerical implementation of a micromechanical approach applicable to flow partitioning and heterogeneous deformation in Earth's lithosphere. Journal of Structural Geology, 50, pp.22-34.

Jiang, D., 2014. Structural geology meets micromechanics: A self-consistent model for the multiscale deformation and fabric development in Earth's ductile lithosphere. Journal of Structural Geology, 68, pp.247-272.

Jiang, D. and Bentley, C., 2012. A micromechanical approach for simulating multiscale fabrics in large-scale high-strain zones: Theory and application. Journal of Geophysical Research: Solid Earth, 117(B12).

Jiang, D. and White, J.C., 1995. Kinematics of rock flow and the interpretation of geological structures, with particular reference to shear zones. Journal of Structural Geology, 17(9), pp.1249-1265.

Jiang, D. and Williams, P.F., 1999. A fundamental problem with the kinematic interpretation of geological structures. Journal of Structural Geology, 21(8-9), pp.933-937.

Kohlstedt, D.L., Evans, B. and Mackwell, S.J., 1995. Strength of the lithosphere: Constraints imposed by laboratory experiments. Journal of Geophysical Research: Solid Earth, 100(B9), pp.17587-17602.

Lebensohn, R.A. and Tomé, C.N., 1993. A self-consistent anisotropic approach for the simulation of plastic deformation and texture development of polycrystals: application to zirconium alloys. Acta Metallurgica et Materialia, 41(9), pp.2611-2624.

Lebensohn, R. A., Dawson, P. R., Kern, H. M., and Wenk, H. R., 2003. Heterogeneous deformation and texture development in halite polycrystals: comparison of different modeling approaches and experimental data. Tectonophysics, 370(1), 287-311.

Lebensohn, R. A., Tomé, C. N., and Maudlin, P. J., 2004. A selfconsistent formulation for the prediction of the anisotropic behavior of viscoplastic polycrystals with voids. Journal of the Mechanics and Physics of Solids, 52(2), 249-278.

Lister, G.S. and Williams, P.F., 1979. Fabric development in shear zones: theoretical controls and observed phenomena. Journal of Structural Geology, 1(4), pp.283-297.

Lister, G.S. and Williams, P.F., 1983. The partitioning of deformation in flowing rock masses. Tectonophysics, 92(1-3), pp.1-33.

Masson, R., Bornert, M., Suquet, P., and Zaoui, A., 2000. An affine formulation for the prediction of the effective properties of nonlinear composites and polycrystals. Journal of the Mechanics and Physics of Solids, 48(6), 1203-1227.

Mattauer, M., Matte, P., Malavieille, J., Tapponnier, P., Maluski, H., Qin, X.Z., Lun, L.Y. and Qin, T.Y., 1985. Tectonics of the Qinling belt: build-up and evolution of eastern Asia. Nature, 317(6037), p.496.

Meng, Q.R. and Zhang, G.W., 1999. Timing of collision of the North and South China blocks: controversy and reconciliation. Geology, 27(2), pp.123-126.

Meng, Q.R. and Zhang, G.W., 2000. Geologic framework and tectonic evolution of the Qinling orogen, central China. Tectonophysics, 323(3-4), pp.183-196.

Mercier, S., and Molinari, A., 2009. Homogenization of elastic–viscoplastic heterogeneous materials: Self-consistent and Mori-Tanaka schemes. International Journal of Plasticity, 25(6), 1024-1048.

Molinari, A., Canova, G.R. and Ahzi, S., 1987. A self consistent approach of the large deformation polycrystal viscoplasticity. Acta Metallurgica, 35(12), pp.2983-2994.

Mori, T., and Tanaka, K., 1973. Average stress in matrix and average elastic energy of materials with misfitting inclusions. Acta Metallurgica, 21(5), 571-574.

Mura, T., 1987. Micromechanics of defects in solids. Martinus Nijhoff Publishers, Dordrecht/Boston/Lancaster, 587 pp.

Ollila, S.T., Smith, C.J., Ala-Nissila, T. and Denniston, C., 2013. The Hydrodynamic Radius of Particles in the Hybrid Lattice Boltzmann--Molecular Dynamics Method. Multiscale Modeling & Simulation, 11(1), pp.213-243.

Passchier, C.W. and Trouw, R.A.J., 1996. Microtectonics. Springer.

Qu, J. and Cherkaoui, M., 2006. Fundamentals of micromechanics of solids (pp. 226-240). Hoboken: Wiley.

Ramberg, H., 1975. Particle paths, displacement and progressive strain applicable to rocks. Tectonophysics, 28(1-2), pp.1-37.

Ramsay, J., 1967. Folding and fracturing of rocks. McGraw-Hill, New York.

Ramsay, J.G. and Graham, R.H., 1970. Strain variation in shear belts. Canadian Journal of Earth Sciences, 7(3), pp.786-813.

Ratschbacher, L., Hacker, B.R., Calvert, A., Webb, L.E., Grimmer, J.C., McWilliams, M.O., Ireland, T., Dong, S. and Hu, J., 2003. Tectonics of the Qinling (Central China): tectonostratigraphy, geochronology, and deformation history. Tectonophysics, 366(1-2), pp.1-53.

Ratschbacher, L., Franz, L., Enkelmann, E., Jonckheere, R., Porschke, A., Hacker, B.R., Dong, S. and Zhang, Y., 2006. The Sino-Korean-Yangtze suture, the Huwan detachment, and the Paleozoic-Tertiary exhumation of (ultra) high-pressure rocks along the Tongbai-Xinxian-Dabie Mountains. Special Papers-Geological Society of America, 403, p.45.

Reischmann, T., Altenberger, U., Kröner, A., Zhang, G., Sun, Y. and Yu, Z., 1990. Mechanism and time of deformation and metamorphism of mylonitic orthogneisses from the Shagou shear zone, Qinling Belt, China. Tectonophysics, 185(1-2), pp.91-109.

Tullis, J., 2002. Deformation of granitic rocks: experimental studies and natural examples. Reviews in Mineralogy and Geochemistry, 51(1), pp.51-95.

Wang, T., Pei, X.Z., Wang, X.X., Hu, N.G., Li, W.P. and Zhang, G.W., 2005. Orogen-parallel westward oblique uplift of the Qinling basement complex in the core of the Qinling orogen (China): an example of oblique extrusion of deep-seated metamorphic rocks in a collisional orogen. The Journal of Geology, 113(2), pp.181-200.

Xu, Z.Q., Lun, L.Y., Tang, Y.Q., Mattauer, M., Matte, P., Malavieille, J., Tapponnier, P. and Maluski, H., 1986. Deformation and tectonic evolution of the eastern Qinling orogenic belt. Acta Geologica Sinica, 60(3), pp.237-247 (in Chinese).

Zhang, G.W., Yu, Z.P., Sun, Y., Cheng, S.Y., L., T.H., Xue, F. and Zhang, C.L., 1989. The major suture zone of the Qinling orogenic belt. Journal of Southeast Asian Earth Sciences, 3(1-4), pp.63-76.

Zhang, G.W., Zhang, B.R., Yuan, X.C., Xiao, Q.H., 2001. Qinling Orogenic Belt and Continental Dynamics. Science Press, Beijing, pp. 1–855 (in Chinese with English abstract).

Chapter 2: An Optimal Scheme for Numerical Evaluation of Eshelby Tensors and Its Implementation in a MATLAB Package for Simulating the Motion of Viscous Ellipsoids in Slow Flows

2.1 Introduction

The motion of a heterogeneous inclusion dispersed in a continuous matrix has been the subject of research for over a century (e.g., Einstein, 1896, 1911, as cited by Jeffery 1922; Jeffery, 1922; Eshelby, 1957; Goldsmith and Mason, 1967; Mura, 1987; Jiang 2013, 2014). The theories and their various modified versions have been widely applied to natural rock deformation and fabric development in the geological literature (e.g., Flinn, 1956; Ramsay, 1967; Gay, 1968; Dunnet, 1969; Bilby et al., 1975; Ferguson, 1979; Fry, 1979; Lisle, 1985; Freeman, 1985; Ježek et al., 1996; Jiang, 2007a,b; Meng et al., 2012; Xiang and Jiang; 2013; Chen et al., 2014). A brief history of this theoretical development is summarized below. Jeffery (1922) first derived equations for the angular velocity of a rigid ellipsoid embedded in an infinite isotropic Newtonian material undergoing far-field homogeneous flow. As many natural rocks resemble the system of a matrix containing rigid or nearly rigid inclusions, Jeffery's theory has been found many applications in geology (e.g., Passchier and Simpson, 1986; Simpson and De Paor, 1993; Vigneresse and Tikoff, 1999; Mancktelow et al., 2002; Johnson et al., 2009; Griera et al., 2013). For the more general case involving deformable inclusions, Bilby et al. (1975) and Bilby and Kolbuszewski (1977) extended Eshelby’s (1957) pioneering work on an isotropic elastic ellipsoid embedded in an infinite isotropic elastic solid undergoing far-field homogeneous deformation to isotropic Newtonian viscous materials. However, the general equations of Jeffery (1922), Bilby et al. (1975), and Bilby and Kolbuszewski (1977) do not have analytical solutions. For the Jeffery equations, analytical solutions have been found so far only for spheroids in monoclinic flows (e.g., Jeffery, 1922; Ježek et al., 1996; Jiang, 2007a). For viscous deformable inclusions, closed-form solutions have only been found for some simple and two-dimensional flows (e.g., Eshelby 1957; Bilby and Kolbuszewski, 1977). In general, Jeffery's and Eshelby's equations must be solved numerically. Freeman (1985) first numerically investigated the possible rotational behaviors of a rigid ellipsoid using Jeffery's theory for a variety of flow fields. He (Freeman, 1987) was also the first to use the equations of Bilby and Kolbuszewski (1977) to numerically analyze the motion of deformable ellipsoids in pure and simple shearing. Ježek (1994) developed FORTRAN programs to calculate the rotational path of individual rigid ellipsoids in any given flow field as well as the rotation and preferred orientation development for a system of multiple, but non-interacting, rigid ellipsoids. Jiang (2007a,b) developed algorithms and MathCad worksheets to numerically calculate the rotational path of individual rigid and deformable ellipsoids and the fabric evolution in a system of multiple non-interacting rigid or deformable ellipsoids. In his algorithms, a set of spherical angles (similar to plunge direction and plunge angle of a line in geology) was used to define the orientation of the ellipsoid instead of the Euler angles used in previous studies. Jiang (2012) further simplified the algorithms by using a single differential equation for rotation: $d\mathbf{Q}/dt = -\overline{\mathbf{\Theta}}\mathbf{Q}$ (where $\overline{\mathbf{\Theta}}$ is the angular velocity and $\mathbf{Q}$ the matrix for the orientation of the ellipsoid). This is different from using a set of three coupled differential equations for Euler angles in previous works (e.g., Ježek 1994). The use of a single differential equation greatly improves the computational efficiency. For dilute inclusions dispersed in a uniform matrix (Figs.2.1a, b) where the non-interaction assumption is valid, the numerical approach of Jiang (2012) provides an efficient and accurate means of numerical simulation.

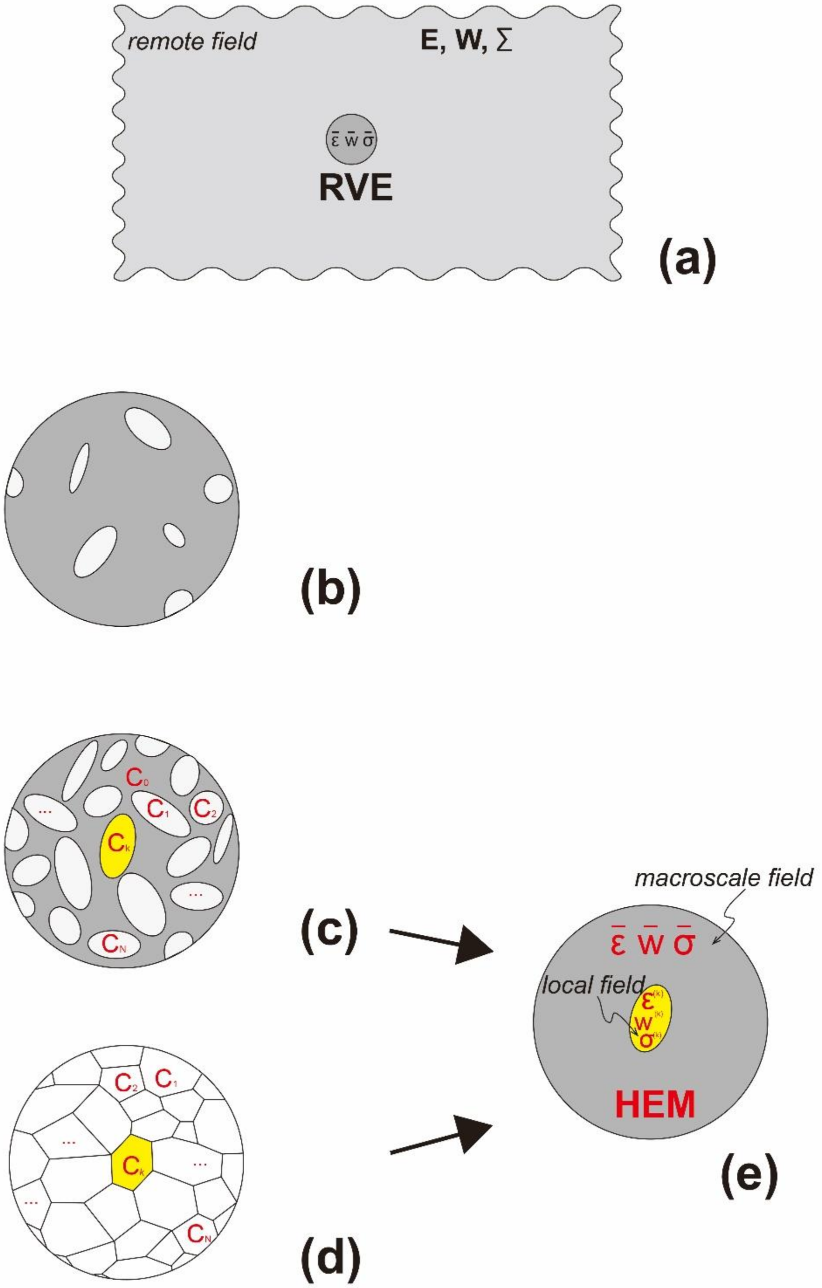

Figure 2.1 A conceptual diagram to illustrate three different scenarios of a clast-matrix system. (a) An infinite medium subjected to a remote motion with strain rate E, vorticity W, and stress $\sum$. The macroscale deformation is defined, at every point, in terms of a Representative Volume Element (RVE) with strain rate $\bar{\boldsymbol{\varepsilon}}$, vorticity $\bar{\mathbf{w}}$, and stress $\bar{\boldsymbol{\sigma}}$. (b), (c) and (d) are the magnified illustrations of an RVE to show three different scenarios. (b) In the scenario, the inclusions are dispersed far apart from each other in a matrix; this is the dilute inclusion scenario in which the macroscale fields are similar to the infinite fields. (c) A composite material with more crowded inclusions embedded in a connected matrix: the matrix phase (C_0) is adopted as a reference medium to solve for the partitioned fields ($\boldsymbol{\varepsilon}^{(k)}, \mathbf{w}^{(k)}, \boldsymbol{\sigma}^{(k)}$) in each clast ($C_k$) (i.e., Mori-Tanaka scheme). The rheological properties of C_0 are the same as the Homogeneous Effective Medium (HEM) in (e). (d) An inclusion is in a polyelement continuum system without a matrix phase: HEM in (e) is adopted as a reference medium which has the macroscopic response of the material ($\bar{\boldsymbol{\varepsilon}}, \bar{\mathbf{w}}, \bar{\boldsymbol{\sigma}}$) and its rheological properties are the homogenized result of all the constituent elements in an RVE.

Eshelby's inclusion theory has also been extended to nonlinear viscous power-law materials through the so-called 'linearization approach' (e.g., Hutchinson, 1976; Molinari et al., 1987; Lebensohn and Tomé, 1993; Masson et al., 2000; Lebensohn et al., 2003, 2004; Jiang 2013, 2014). This extension forms the basis of the viscoplastic self-consistent (VPSC) theory (Molinari et al., 1987; Lebensohn and Tomé, 1993; Tomé and Lebensohn, 2008; Lebensohn et al., 2011) for simulating lattice preferred orientation fabrics in polycrystalline materials. Recently, the extended Eshelby theory has also been used in a self-consistent MultiOrder Power-Law Approach (MOPLA, Jiang and Bentley 2012; Jiang 2014) to address the multiscale heterogeneous deformation characteristic of Earth's lithosphere (Fig.2.1). In the latter, a macroscale field variable at every point is represented by the average of the variable over a Representative Volume Element (RVE) (Fig.2.1a), which contains many rheologically distinct power-law viscous elements (Fig.2.1d). The mechanical fields in a constituent element (treated as an Eshelby inhomogeneity) are related to the macroscale fields by the extended Eshelby theory and the mechanical fields in constituent elements are used to model the development of small-scale fabrics within the elements (Jiang, 2014). To apply the extended Eshelby theory, the macroscale polyelement continuum is represented rheologically by a Homogeneous Effective Medium (HEM, Fig.2.1e), which is used as a reference medium for homogenization – the procedure to obtain the effective rheological properties of HEM. Self-consistent homogenizations (e.g., Molinari 2002) make use of the consistency conditions (macroscale compatibility and equilibrium) which require that the average of the local fields (within elements) over the representative volume of the polyelement be equal to those imposed at the macroscale ($\bar{\boldsymbol{\varepsilon}}$, $\bar{\mathbf{w}}$, $\bar{\boldsymbol{\sigma}}$ in Fig.2.1e). The one-site self-consistent approach (or the mean-field theory, Lebensohn and Tomé, 1993; Lebensohn et al., 1998) assumes that HEM is rheologically uniform. Local fields are partitioned fields of the macroscale field. The partitioned fields then dictate the fabric development in individual elements, and this constitutes the multiscale simulation of Jiang (2014). In the case where there is a clearly identified matrix phase (Fig.2.1c), the matrix can be considered a reference medium instead of HEM and the Mori-Tanaka (Mori and Tanaka, 1973) approach can be used for the homogenization (e.g., Mercier and Molinari, 2009).

One can appreciate that a self-consistent approach, such as MOPLA, is computationally intensive, because the partitioning calculation (to obtain local fields from the macroscale field) and the homogenization calculation (to obtain HEM rheological properties from instantaneous local fields and constituent rheological properties) (Fig.2.1) must be performed self-consistently and this requires large numbers of iterative calculations, each involving a large number (for all constitutive elements) of evaluations of the Eshelby tensors. As deformation proceeds, the constituent elements become more elongated and/or flattened, and the HEM also becomes rheologically more anisotropic, both rendering the accurate evaluation of the Eshelby tensors for these elements ever more time-consuming. Therefore, an efficient scheme to evaluate Eshelby tensors is critical for self-consistent modeling. The main purpose of this paper is to develop an efficient scheme for evaluating Eshelby tensors. We also apply the efficient scheme to develop a MATLAB package for simulating the motion of single and multiple ellipsoids, upgrading the MathCad package of Jiang (2007a,b, 2012).

2.2 Numerical evaluation of Eshelby tensors

In this section, we first summarize the Eshelby inclusion solutions in order to introduce the Eshelby tensors. We then discuss numerical methods to evaluate the Eshelby tensors.

2.2.1 The Eshelby inclusion solutions and Eshelby tensors

The general Eshelby formalism for a viscous ellipsoidal inclusion (Molinari et al., 1987; Lebensohn et al., 1998) relates the local uniform fields inside a linear viscous ellipsoid (strain rate $\boldsymbol{\varepsilon}$, vorticity $\mathbf{w}$, and deviatoric stress $\boldsymbol{\sigma}$, all second-order tensors) to their far-field counterparts in the matrix (namely, the strain rate $\mathbf{E}$, vorticity $\mathbf{W}$, and deviatoric stress $\mathbf{\Sigma}$) by the following set of relations (Fig.2.1) (e.g., Jiang, 2014, Eq.11 there, for incompressible materials):

$$\tilde{\boldsymbol{\varepsilon}} = \left(\mathbf{J^D} - \mathbf{S^{-1}}\right)^{-1} : \mathbf{C_M^{-1}} : \tilde{\boldsymbol{\sigma}} \tag{2.1a}$$

$$\tilde{\mathbf{w}} = \mathbf{\Pi} : \mathbf{S^{-1}} : \tilde{\boldsymbol{\varepsilon}} \tag{2.1b}$$

$$\tilde{\boldsymbol{\sigma}} = \mathbf{C_M} : \left(\mathbf{J^D} - \mathbf{S^{-1}}\right) : \tilde{\boldsymbol{\varepsilon}} \tag{2.1c}$$

where the tilde above a quantity stands for the difference between the local field and that at infinity (e.g., $\tilde{\boldsymbol{\varepsilon}} = \boldsymbol{\varepsilon} - \mathbf{E}$), $\mathbf{C_M}$ is the 4th-order viscous stiffness tensor of the matrix, $\mathbf{J^D}$ is the 4th-order deviatoric identity tensor, as used in Jiang (2013, 2014), defined by $J^D_{ijkl} = \frac{1}{2}\left(\delta_{ik}\delta_{jl} + \delta_{jk}\delta_{il}\right) - \frac{1}{3}\delta_{ij}\delta_{kl}$ with $\delta_{ij} = \begin{cases} 1 & i = j \\ 0 & i \neq j \end{cases}$, and $\mathbf{S}$ and $\mathbf{\Pi}$ are, respectively, the symmetric and antisymmetric Eshelby tensors. The sign "**:**" stands for the double-index contraction operation between tensors (see Jiang 2013, 2014 for more details).

The set of Eqs.(2.1) is an exact solution for linear viscous materials. For nonlinear materials, there is no such exact solution. However, Eqs.(2.1) can be used as an approximate solution if the material's nonlinear behavior is replaced by a linearized behavior, using the well-known linearization approach (e.g., Molinari et al., 1987; Lebensohn and Tomé, 1993). Through linearization, one can write the constitutive equations for the matrix and inclusion in approximate linear forms: $\mathbf{\Sigma} = \hat{\mathbf{C}}_\mathbf{M} : \mathbf{E} + \mathbf{\Sigma^0}$, $\boldsymbol{\sigma} = \hat{\mathbf{C}}_\mathbf{E} : \boldsymbol{\varepsilon} + \boldsymbol{\sigma}^\mathbf{0}$, where $\hat{\mathbf{C}}_\mathbf{M}$ and $\hat{\mathbf{C}}_\mathbf{E}$ are, respectively, the linearized viscous stiffness for the matrix and the inclusion; $\mathbf{\Sigma^0}$ and $\boldsymbol{\sigma}^\mathbf{0}$ are associated pre-stress terms (see Molinari et al., 1987; Lebensohn and Tomé 1993; Tomé and

Lebensohn, 2008; Lebensohn et al., 2011; Jiang, 2013, 2014 for details). Eqs.(2.1) can be used as a set of approximate solutions, e.g., $\tilde{\boldsymbol{\varepsilon}} = \left(\mathbf{J}^{\mathbf{D}} - \mathbf{S}^{-1}\right)^{-1} : \mathbf{C}_{\mathbf{M}}^{-1} : \tilde{\boldsymbol{\sigma}}$, for nonlinear viscous materials. A variety of linearization approaches have been proposed (e.g., Hutchinson, 1976; Molinari et al., 1987; Lebensohn and Tomé, 1993; Masson et al., 2000; Lebensohn et al., 2003, 2004; Jiang 2013, 2014). A well-known one is the tangent linearization, in which $\hat{\mathbf{C}}$ is (e.g., Jiang, 2014, Eq.22 there)

$$\hat{\mathbf{C}} = \mathbf{C}^{(\mathbf{tan})} = \frac{1}{n}\mathbf{C}^{(\mathbf{sec})} \tag{2.2}$$

where $\mathbf{C}^{(\mathbf{tan})}$ and $\mathbf{C}^{(\mathbf{sec})}$ are the tangent and secant viscous stiffness tensors of a power-law material, and n is the power-law stress exponent for the material. The secant stiffness is also known as the effective viscosity (Ranalli, 1995, p.78).

The key to evaluating Eqs.(2.1) lies in the evaluation of the two Eshelby tensors ($\mathbf{S}$ and $\mathbf{\Pi}$). For isotropic materials, this can be done using closed-form expressions or expressions involving the simple complete elliptic integrals of the first type and second type (Eshelby 1957; Mura 1987, p.77). For anisotropic materials, which are common in natural deformation and must be accounted for in self-consistent models such as MOPLA, VPSC or any self-consistent homogenization (e.g., Molinari, 2002; Molinari and Mercier, 2004; Mercier and Molinari, 2009), Eshelby tensors can only be evaluated numerically.

The two Eshelby tensors can be defined in terms of an auxiliary fourth order tensor $\mathbf{T}$, called the Green interaction tensor by Lebensohn et al. (1998). For incompressible materials, $\mathbf{T}$ can be expressed as (e.g., Lebensohn et al., 2004; Jiang, 2014):

$$T_{ijkl} = \frac{a_1 a_2 a_3}{4\pi} \int_{|\xi|=1} \frac{\xi_j \xi_l A_{ik}(\boldsymbol{\xi})}{\left[\left(a_1\xi_1\right)^2 + (a_2\xi_2)^2 + \left(a_3\xi_3\right)^2\right]^{\frac{3}{2}}} d\boldsymbol{\xi} \tag{2.3a}$$

$$\mathbf{S} = \mathbf{J^D} : \mathbf{T} : \mathbf{C_M} \tag{2.3b}$$

$$\mathbf{\Pi} = \mathbf{J^A} : \mathbf{T} : \mathbf{C_M} \tag{2.3c}$$

where a_1, a_2, a_3 are the three semi-axes of the ellipsoid, $\boldsymbol{\xi}$ is the unit vector variable, $\widehat{\mathrm{A}}_{ik}(\boldsymbol{\xi})$ is a symmetric 3×3 matrix related to the viscous stiffness of the matrix medium and is a function of $\boldsymbol{\xi}$ (see Lebensohn et al., 2004 and Jiang, 2014 for more details), and $\mathbf{J^A}$ is the 4th-order anti-symmetric identity tensor with $J^A_{ijkl} = \frac{1}{2}\left(\delta_{ik}\delta_{jl} - \delta_{jk}\delta_{il}\right)$ as used in Jiang (2013, 2014).

2.2.2 Numerical evaluation of T_{ijkl}

Calculating the Eshelby tensors boils down to evaluating the integral in Eq.(2.3a) efficiently. The integral can be expressed in terms of spherical angles using the substitution $\boldsymbol{\xi} = \begin{pmatrix} \cos\theta\sin\phi \\ \sin\theta\sin\phi \\ \cos\phi \end{pmatrix}$:

$$T_{ijkl} = \frac{a_1 a_2 a_3}{4\pi} \int_0^{2\pi} \left\{ \int_0^{\pi} \left[\mathrm{f}(\theta,\phi)\right]_{ijkl} \sin\phi d\phi \right\} d\theta \tag{2.4a}$$

where

$$\left[\mathrm{f}(\theta,\phi)\right]_{ijkl} = \frac{\xi_j \xi_l A_{ik}(\boldsymbol{\xi})}{\left[\left(a_1\xi_1\right)^2 + (a_2\xi_2)^2 + \left(a_3\xi_3\right)^2\right]^{\frac{3}{2}}} \tag{2.4b}$$

Jiang (2013, 2014) in his MathCad worksheets used the following product Gaussian quadrature for Eq.(2.4a):

$$T_{ijkl} \approx \frac{a_1 a_2 a_3}{4\pi} \sum_{q=1}^{n} \sum_{p=1}^{n} w_p w_q \left[\mathrm{f}\left(\phi_q, \theta_p\right) \right]_{ijkl} sin\phi_q \tag{2.5}$$

where $\left(\phi_q, \theta_p\right)$ are Gauss-Legendre grid nodes, w_p are the Gauss-Legendre weights within [-1, 1], and n is the number of nodes and weights. The total number of grid nodes used in Eq.(2.5) is thus n^2. Atkinson (1982) presented a slightly different product Gaussian quadrature. Instead of discretizing both ϕ_p in [0, π] and θ_p in [0, 2π] according to the Gauss-Legendre method as in Jiang (2013, 2014), in Atkinson (1982), the grid nodes $\left(\phi_q, \theta_p\right)$ are generated by discretizing $(\cos\phi)_p$ in [-1, 1] based on the Gauss-Legendre formula while θ_p is evenly spaced within [0, 2π]. In this scheme T_{ijkl} is approximated by the following expression:

$$T_{ijkl} \approx \frac{a_1 a_2 a_3}{4n} \sum_{q=1}^{2n} \sum_{p=1}^{n} w_p \left[\mathrm{f}\left(\phi_p, \theta_q\right) \right]_{ijkl} \tag{2.6}$$

where w_p are weights in [-1, 1] using the Gauss-Legendre formula and the total node number is $2n^2$. We compared these two quadrature schemes in MATLAB for different ellipsoid shapes and found that the approximation of Eq.(2.5) consistently outperforms that of Eq.(2.6). Therefore, we shall use Eq.(2.5) when we adopt a product Gaussian quadrature and do not consider Eq.(2.6) any further in this paper.

A less well-known scheme for numerical integration over a unit sphere such as Eq.(2.3a) is the Lebedev quadrature (Lebedev, 1977) in which Eq.(2.4a) is approximated by:

$$T_{ijkl} \approx a_1 a_2 a_3 \sum_{p=1}^{N} w_p \left[\mathrm{f}\left(\phi_p, \theta_p \right) \right]_{ijkl} \tag{2.7}$$

where the nodes and their associated weights are determined by the Lebedev quadrature rules. It is beyond the scope of this paper to describe the mathematical details of the Lebedev quadrature. Interested readers may refer to Lebedev (1977). Basically, the quadrature obtains spherical harmonics that are invariant under the octahedral group with inversion and yields exact integration for all spherical harmonics up to a given order (Lebedev, 1977). Geometrically, the Lebedev grid nodes correspond to the vertices of a geometric polyhedron with octahedral rotation and inversion symmetry, and all nodes from the same geometric polyhedron share the same weight defined below (similar to Lebedev, 1977, Eq.2.2 there):

$$\begin{aligned} T_{ijkl}^{N}(\mathrm{f}) \approx a_1 a_2 a_3 \Bigg\{ & w^{\left(A^1\right)} \sum_{p=1}^{6} \left[\mathrm{f}\left(A_p^1 \right) \right]_{ijkl} + w^{\left(A^2\right)} \sum_{p=1}^{12} \left[\mathrm{f}\left(A_p^2 \right) \right]_{ijkl} + w^{\left(A^3\right)} \sum_{p=1}^{8} \left[\mathrm{f}\left(A_p^3 \right) \right]_{ijkl} + \\ & \sum_{q=1}^{N_1} w^{\left(B^q\right)} \sum_{p=1}^{24} \left[\mathrm{f}\left(B_p^q \right) \right]_{ijkl} + \sum_{q=1}^{N_2} w^{\left(C^q\right)} \sum_{p=1}^{24} \left[\mathrm{f}\left(C_p^q \right) \right]_{ijkl} + \sum_{q=1}^{N_3} w^{\left(D^q\right)} \sum_{p=1}^{48} \left[\mathrm{f}\left(D_p^q \right) \right]_{ijkl} \Bigg\} \end{aligned} \tag{2.8}$$

where N is the total number of nodes generated, $A^1, A^2, A^3, B^q, C^q, D^q$ are different sets of nodes associated with different geometric polyhedrons, and $w^{\left(A^1\right)}, w^{\left(A^2\right)}, w^{\left(A^3\right)}, w^{\left(B^q\right)}, w^{\left(C^q\right)}, w^{\left(D^q\right)}$ are their corresponding weights. The total number of nodes generated in Eq.(2.8) is $N = 26 + 24 \times \left(N_1 + N_2 \right) + 48 \times N_3$. For example, the smallest set of Lebedev nodes is 6, corresponding to the vertices of a regular octahedron (A^1), and can be expressed by polar coordinates, $(1, \phi, \theta)$. The weight for these 6 nodes is the same (i.e., $w^{\left(A^1\right)}$).

By selecting the set of (w, ϕ and θ) simultaneously in a double integral, rather than discretizing ϕ and θ integrals separately as in the product Gaussian quadrature described above, Lebedev quadrature is more economic computationally. According to our MATLAB tests, the evaluation of T_{ijkl} [Eq.(2.4a)] using the Lebedev quadrature always outperforms the product Gaussian quadrature using Eq.(2.5) significantly, especially for elongate prolate-like ellipsoids. It would seem to suggest that one should always use the Lebedev quadrature to evaluate T_{ijkl}. However, the maximum of nodes and weights now available for the Lebedev quadrature is 5810 because of difficulties (Lebedev, 1975, 1976, 1977, 1995; Lebedev and Skorokhodov, 1992; Lebedev and Laikov, 1999) encountered when the order of spherical harmonics gets high. This limits the use of the Lebedev quadrature. Where even the maximum nodes and weights of the Lebedev quadrature cannot allow for accurate evaluation of T_{ijkl}, we must still use the product quadrature. There is an online library providing MATLAB code for computing Lebedev nodes and weights (Saff and Kuijlaars, 1997). We make use of this library and incorporate the Lebedev quadrature as an option to numerically evaluate Eq.(2.4a).

The error associated with evaluating Eq.(2.4a) using the product quadrature or the Lebedev quadrature with a given node number is unknown, *a priori*. One can easily build in an error estimate in either quadrature as follows: prescribing a tolerance and evaluating the integral iteratively, starting with a lower node number and progressively increasing the node number until the outputs converge within the prescribed tolerance. Alternatively, one can use an adaptive algorithm to evaluate Eq.(2.4a) in which a fixed number of nodes is applied on refined subintervals of the integration domain, and the subintervals are partitioned into successively finer subdivisions until the prescribed tolerance is reached (e.g., Davis and Rabinowitz, 1975; Krommer, 1994; Quarteroni et al., 2010). Both the iterative and the adaptive approaches involve repetitive calculations. Because the adaptive approach selects the number of nodes based on local integrand behaviors, it is more economical than the iterative approach in general. To save computational resources, one would like to avoid any repetitive calculations if it is at all practical by prescribing, *a priori*, the node number of the product quadrature or the Lebedev quadrature to evaluate Eq.(2.4a). Our motivation in developing an optimal scheme in the following section is to avoid repetitive calculations as much as possible.

2.3 An optimal scheme

We note that it takes longer to evaluate Eq.(2.4a) as an ellipsoid becomes more elongate or flattened. In order to quantify this dependence, we use the Flinn parameters in structural geology (e.g., Ramsay, 1967; Hobbs et al., 1976) to quantify the shape of ellipsoids below and investigate how the computational time required to evaluate Eq.(2.4a) depends on the ellipsoid's Flinn parameters.

As shown in Fig.2.2, in the Flinn space, an ellipsoid shape is represented uniquely by two coordinates, $R=\sqrt{ln^2\left(a_1/a_2\right)+ln^2\left(a_2/a_3\right)}$ and $\Phi=\arctan\left(\frac{\ln\left(a_1/a_2\right)}{\ln\left(a_2/a_3\right)}\right)$. *R* measures quantitatively the degree of elongation/flatness of an ellipsoid and Φ measures the oblateness and prolateness of an ellipsoid. A sphere is plotted at the origin (*R* = *0*), an oblate object on the abscissa ($\Phi = 0^\circ$), and a prolate object on the ordinate ($\Phi = 90^\circ$). A general triaxial ellipsoid is plotted in the quadrant between the two. The $\Phi = 45^\circ$ line separates prolate-like objects from oblate-like ones (Fig.2.2).

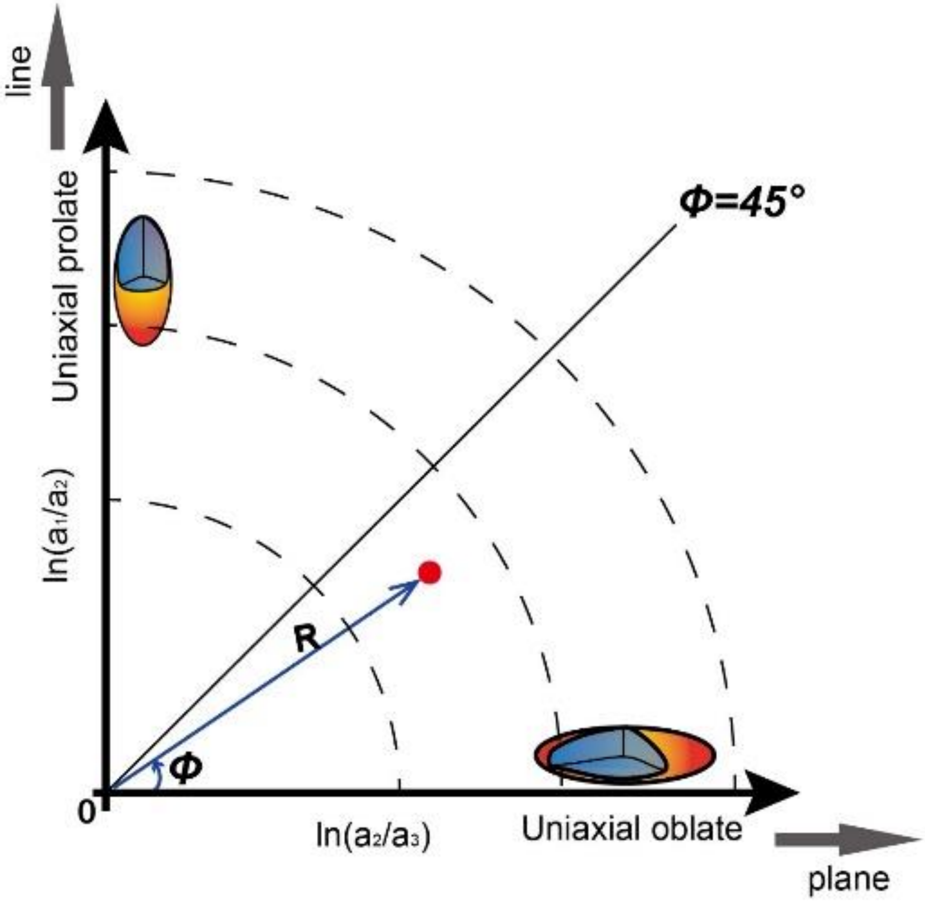

Figure 2.2 Ellipsoid shape quantified by two parameters (R and Φ) in the Flinn space. Any ellipsoid is plotted as a point on the diagram. R measures the deviation of the ellipsoid from a sphere and Φ measures its oblateness and prolateness of the ellipsoid.

In order to find out how the computational time depends on R and Φ, we ran numerical calculations using the adaptive product Gaussian quadrature to evaluate Eq.(2.4a) for an isotropic matrix. The range of Φ is [0˚, 90˚] to cover all types of prolate-like and oblate-like ellipsoids. Natural deformations can reach extremely high strains. Therefore, in principle, the shapes of constituent elements can reach very high aspect ratios. We could have selected any R as the upper limit for our numerical tests. We have arbitrarily chosen $a_1 : a_3 = 100 : 1$ as the upper limit ($R=4.7;\ ln100 \approx 4.605$) in this paper. We believe that, for elements with even higher aspect ratios, treating them as ellipsoids becomes questionable as the uniform field assumption within such elements is unrealistic. We have also limited the matrix to be isotropic because we want to reveal the dependence of computation time solely on ellipsoid shape. There is an infinite number of possible choices if the matrix is anisotropic. We discuss this point further in Section 2.5. The numerical runs were carried out using MATLAB (version is R2015a) on an HP z820 Workstation with Intel Xeon E5-2690 CPU and 192GB RAM in a Windows 7 system.

Fig.2.3 is a contoured map showing the dependence of the computational time to numerically evaluate Eq.(2.4a) on ellipsoid shape using the adaptive product Gaussian quadrature. For each given ellipsoid (Φ and R), the time in Fig.2.3 represents the total time needed to evaluate Eq.(2.4a) 100 times. We use 100 times of evaluation to reduce system turbulence effect on the computational time. Fig.2.3 shows clearly that the computational time increases with Φ and R in general, confirming the known observation that more elongate/flattened ellipsoids require longer computation to get their Eshelby tensors. The red dashed lines in Fig.2.3 are a_1-isolines. For example, the ‘ a_1= 100’ isoline represents ellipsoids with three semi-axes being 100 : a_2: 1, where a_2 varies from 1 (Φ = 90˚) to 100 (Φ = 0˚).

In principle, the contour lines in Fig.2.3 can be used as criteria to assign node numbers according to ellipsoid shapes. However, these lines are rather irregular, so we generate smoother curves empirically to mimic the contour lines in Fig.2.3 and use these curves as criteria to assign proper node numbers. These curves are $R = f_1(\Phi)$, $R = f_2(\Phi)$, $R = f_3(\Phi)$, $R = f_4(\Phi)$ in Fig.2.4 and they divide the shape space (Fig.2.3) into five domains (Fig.2.4). The mathematical expressions of the curves are given in Appendix A. The computational time in Fig.2.3, which is based on the

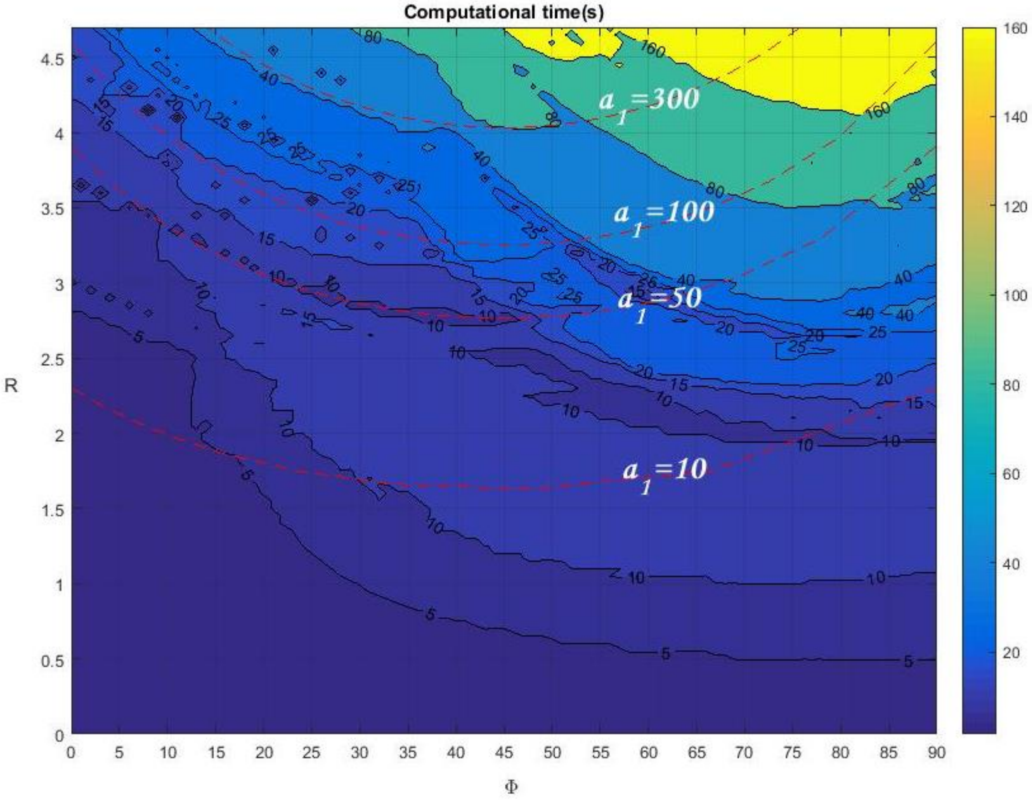

Figure 2.3 The contour plot of computation time (s) with respect to R and Φ. Contour levels are 5, 10, 15, 20, 25, 40, 80 and 160s from low to high values of the computation time. Red dashed lines are a_1- isolines (a_1= 10, a_1= 50, a_1= 100, a_1= 300, details refer to the text).

adaptive product Gaussian quadrature, reflects the behaviour of the integrand in Eq.(2.4a) and the required node number: a longer computational time means more recursions, which suggests that more nodes are needed for the Lebedev quadrature and product Gaussian quadrature, and vice versa. We wish to find an optimal quadrature (i.e., product Gaussian quadrature or Lebedev quadrature) and corresponding node number for each domain using iterative tests. The optimal quadrature and corresponding node numbers for Domains A, B, C, D are based on the iterative tests of $R = f_1(\Phi)$, $R = f_2(\Phi)$, $R = f_3(\Phi)$, $R = f_4(\Phi)$, respectively. For example, in order to set the quadrature and its corresponding node number for Domain A, we evaluate Eq.(2.4a) iteratively for all ellipsoids with R and Φ on f_1 and choose the largest node number as the node number for Domain A to guarantee the accuracy. As explained in Section 2.2, the Lebedev quadrature is the best option to evaluate Eq.(2.4), and when the maximum node number of the Lebedev quadrature (5810) is not sufficient accurately evaluate Eq.(2.4a), we use the product Gaussian quadrature. In one domain, such as Domain A, the Lebedev quadrature generally requires fewer nodes for prolate-like ellipsoids than oblate-like ellipsoids, so we further divide one domain into two subdomains according to Φ and set a more appropriate node number for each subdomain. For Domain E, the required node number for the product Gaussian quadrature is 650^2 (i.e., PGQ(650^2)). This would require more computational time than the adaptive product Gaussian quadrature. Therefore, for ellipsoids fall in Domain E, an adaptive product Gaussian quadrature is the best choice. In summary, the optimal scheme works as follows: According to the instantaneous three axes of an ellipsoid, we can calculate its Φ and R, based on which the domain for the ellipsoid is decided. If the ellipsoid falls in Domain E, the adaptive product Gaussian quadrature is used to evaluate Eq.(2.4a), otherwise its Φ value is used to decide further what subdomain the ellipsoid is in. The optimal quadrature and associated node number are then selected for the ellipsoid to evaluate Eq.(2.4a).

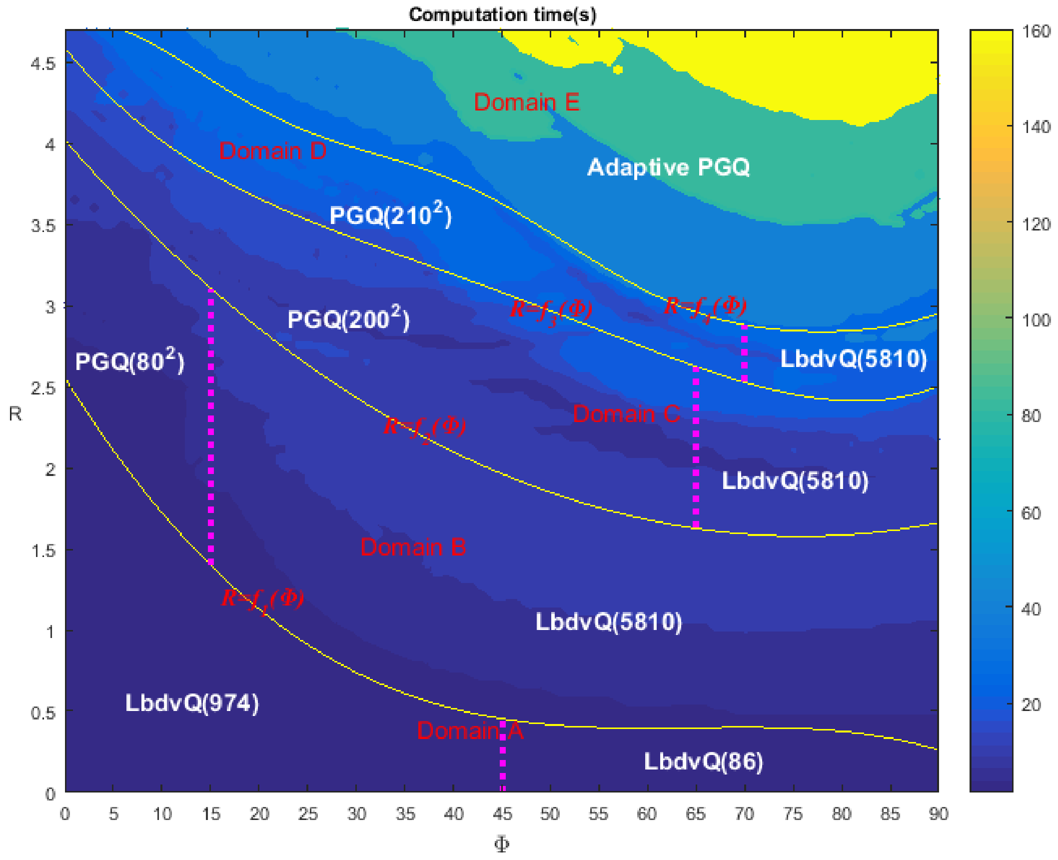

Figure 2.4 Optimal quadrature and associated node numbers for different shapes of the inclusion according to the iterative tests. ‘LbdvQ’ stands for the Lebedev Quadrature and ‘PGQ’ stands for the Product Gaussian Quadrature.

2.4 A MATLAB package for simulating the motion of rigid and deformable inclusions

The optimal scheme developed above can be applied in any model that involves the numerical integration of Eq.(2.4a). As a demonstration of its use, we implement it in a MATLAB package for the motion of rigid and deformable ellipsoids in ductile flows.

2.4.1 A brief summary of important equations for rigid and deformable ellipsoids

The rotation of a rigid or deformable ellipsoid in ductile flows is described by the following differential equation (Jiang, 2012):

$$\frac{d\mathbf{Q}}{dt} = -\bar{\boldsymbol{\Theta}}\mathbf{Q} \tag{2.9}$$

For deformable ellipsoids, the shape evolution with time is governed by

$$\frac{d\mathbf{a}}{dt} = \mathbf{D}^{\mathbf{axis}}\mathbf{a} \tag{2.10}$$

where $\mathbf{a} = \begin{pmatrix} a_1 \\ a_2 \\ a_3 \end{pmatrix}$ and $\mathbf{D}^{\text{axis}}$ is a diagonal matrix for the strain rates along the current semi-axes, $D_{ij}^{axis} = \begin{cases} 0, & if\ i \neq j \\ \varepsilon_{ij}, & if\ i = j \end{cases}$. The angular velocity, $\bar{\boldsymbol{\Theta}}$, in Eq.(2.9) is determined by the vorticity in an ellipsoid (Eq.(2.1b)) and a shear spin, $\mathbf{w}^{\text{s}}$ (Jiang, 2012, 2013, 2014): $\bar{\boldsymbol{\Theta}} = \mathbf{W} + \boldsymbol{\Pi} : \mathbf{S}^{\mathbf{-1}} : \tilde{\boldsymbol{\varepsilon}} - \mathbf{w}^{\mathbf{s}}$, where $w_{ij}^{s} = \begin{cases} \dfrac{a_i^2 + a_j^2}{a_i^2 - a_j^2}\varepsilon_{ij} & a_i \neq a_j \\ w_{ij} & a_i = a_j \end{cases}$ $(no\ sum)$. For a rigid ellipsoid, $\tilde{\boldsymbol{\varepsilon}} \equiv \mathbf{-E}$ ($\varepsilon_{ij} \equiv 0$) and $w_{ij}^{s} \equiv 0$, the angular velocity is $\bar{\boldsymbol{\Theta}}_{(rigid)} = \mathbf{W} - \boldsymbol{\Pi} : \mathbf{S}^{-1} : \mathbf{E}$, which is a generalization of Jeffery’s (1922) equation to a general anisotropic viscous matrix. $\boldsymbol{\varepsilon}$ (i.e., $\mathbf{D}^{\text{axis}}$ in Eq.(2.10)) can be obtained from Eq.(2.1a) by using the general constitutive equations for the matrix and the inclusion (i.e., $\boldsymbol{\Sigma} = \mathbf{C_M} : \mathbf{E}$ and $\boldsymbol{\sigma} = \mathbf{C_E} : \boldsymbol{\varepsilon}$): $\boldsymbol{\varepsilon} = \left[\mathbf{J^D} - \mathbf{S} + \mathbf{S} : \mathbf{C_E} : \mathbf{C_M^{-1}}\right]^{\mathbf{-1}} : \mathbf{E}$.

Eqs.(2.9) and (2.10) can be solved numerically by using the Runge-Kutta method (Jiang, 2012), the Rodrigues approximation (Jiang, 2013), or a combination of both (Jiang 2014). We apply the tangent linearization (i.e., Eq.(2.2)) in the MATLAB package, so the package can be used for power-law viscous materials. The package is written in MATLAB generally. For better performance, we have written part of the numerical integration of Eq.(2.4a) in C language and compiled the part using MATLAB's built-in *mex* function and the Microsoft Visual C++ 2015 compiler (Altman, 2014).

2.4.2 Verification and examples

For isotropic materials, results (Fig.2.5) obtained from the package for rigid spheroids in an isotropic matrix reproduce perfect "Jeffery orbits" obtained from analytical solutions (e.g., Jeffery, 1922; Freeman, 1985; Ježek, 1994; Jiang, 2007a). In Fig.2.5, the rotation paths follow Jeffery orbits even when the shear strain reaches 100. For deformable ellipsoids in an isotropic matrix, results from the package are identical to those obtained from the MathCad worksheets of Jiang (2007b, 2012) in which the Eshelby tensors are calculated from the closed-form expressions.

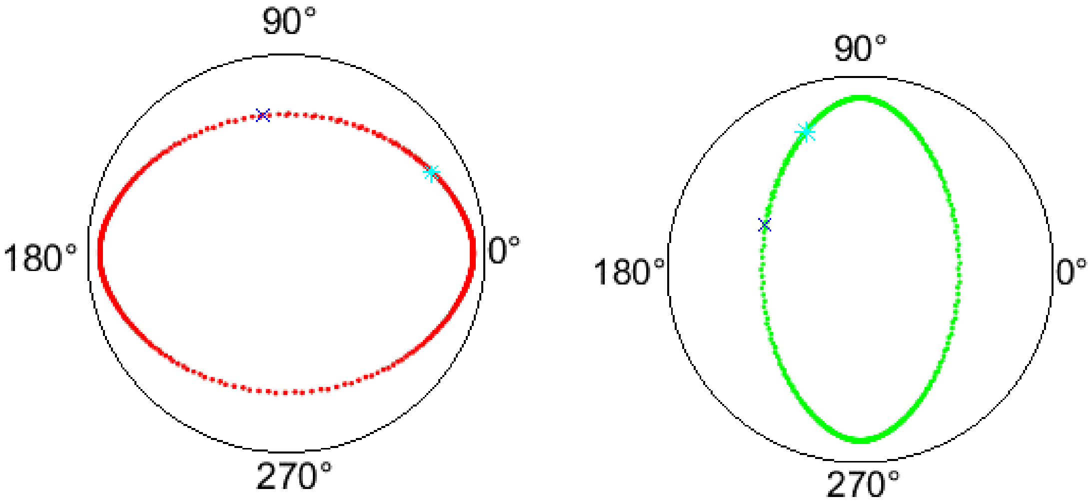

(a) (b)

Figure 2.5 An execution of SGLRGD. The rotation paths for the rigid ellipsoids embedded in an isotropic matrix in simple shearing flows plotting on equal-area projections. Red and green color symbols are, respectively, hemispheres associated with positive x_3 and negative x_3 half-spaces. '×' represents the initial state, and '*' represents the final state. Input parameters are $L = \begin{pmatrix} 0 & 1 & 0 \\ 0 & 0 & 0 \\ 0 & 0 & 0 \end{pmatrix}$ for simple shearing flow field, ang = $\begin{pmatrix} 100 \\ 60 \\ 30 \end{pmatrix}$, tincr = 0.01, steps = 10000, (a) is the rotation path of a prolate ellipsoid $a = \begin{pmatrix} 5 \\ 1 \\ 1 \end{pmatrix}$, and (b) is the rotation path of an oblate ellipsoid $a = \begin{pmatrix} 5 \\ 5 \\ 1 \end{pmatrix}$. Perfect Jeffery orbits are produced in excellent agreement with analytic solutions of Jeffery (1922), Freeman (1985), Ježek (1994), Jiang (2007a).

For inclusions in an incompressible anisotropic material, to our knowledge, there is no 3D analytical solution available. To verify the package for anisotropic materials, we compare our numerical results for an extremely elongate ellipsoid (to approximate an elliptical cylinder) in a plane-straining flow with the 2D analytical solutions of Fletcher (2009) for an ellipse in a homogeneous incompressible viscous matrix with planar anisotropy under plane-straining flows. The imposed velocity gradient tensor **L** is:

$$\mathbf{L} = \begin{pmatrix} \varepsilon & \gamma & 0 \\ 0 & -\varepsilon & 0 \\ 0 & 0 & 0 \end{pmatrix} \tag{2.11}$$

where ε and γ are the pure shearing strain rate and simple shear rate, respectively. We use an extremely elongate ellipsoid with its a_3 semi-axis parallel to the vorticity (the x_3 axis) of the flow (Fig.2.6a) to approximate an elliptic cylinder in 2D flows. The specific anisotropic matrix considered by Fletcher (2004, 2009) is one with a planar anisotropy. The corresponding viscous stiffness tensor **C** with the anisotropy plane (i.e., “foliation”) normal to the x_2 axis (Figs.2.6) can be written in a block matrix form (see Jiang, 2016) as follows:

$$C_{ijkl} = 2\eta_n \begin{pmatrix} J^D_{11kl} & \frac{1}{m} J^D_{12kl} & J^D_{13kl} \\ \frac{1}{m} J^D_{12kl} & J^D_{22kl} & \frac{1}{m} J^D_{23kl} \\ J^D_{13kl} & \frac{1}{m} J^D_{23kl} & J^D_{33kl} \end{pmatrix} \tag{2.12}$$

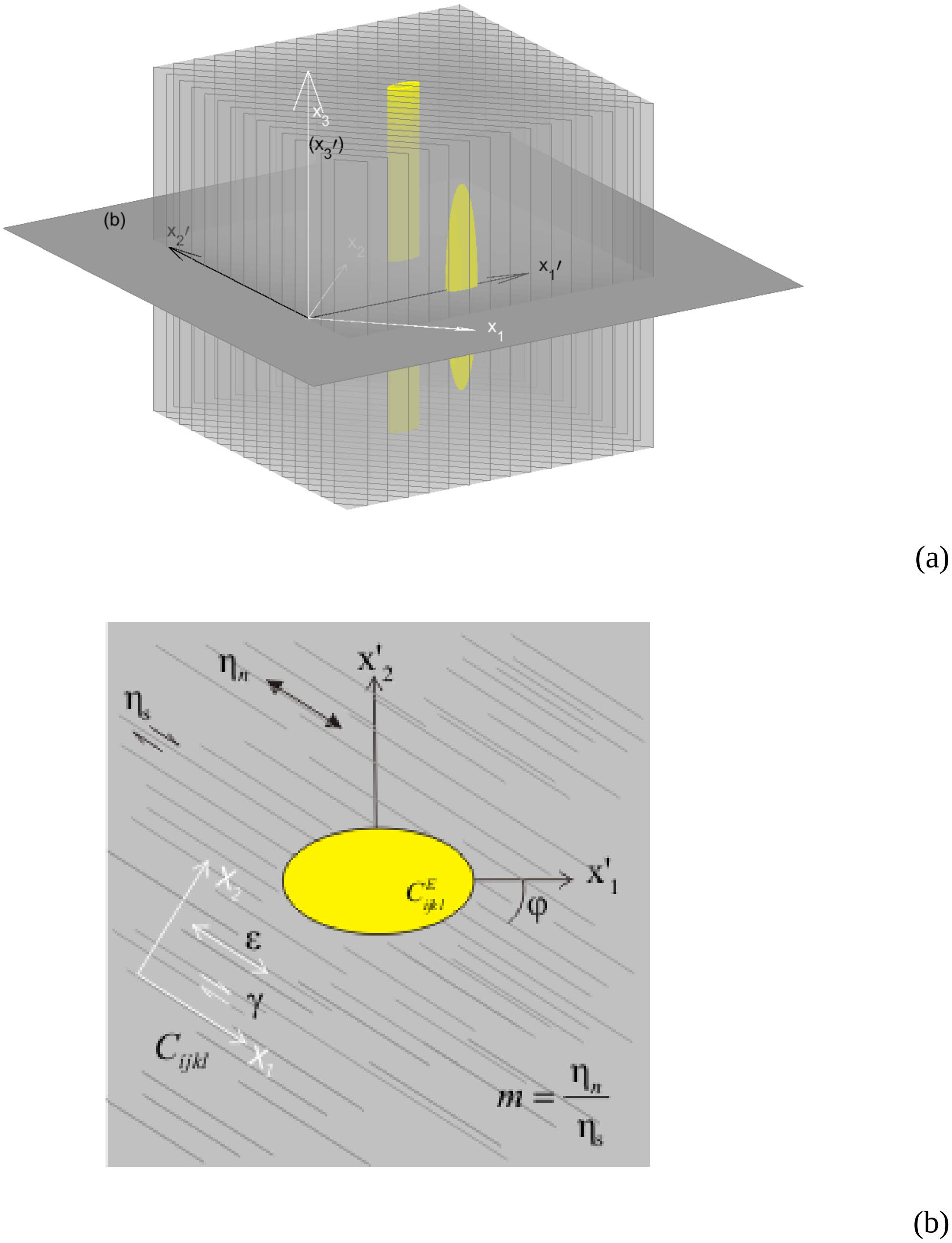

Figure 2.6 An isotropic ellipsoid embedded in a matrix with planar anisotropy. The matrix rheology is defined by η_n and η_s. $m = {}^{\eta_n}\!/_{\eta_s}$ indicates the strength of the anisotropy. The imposed plane-straining general shear flow (ε is the pure shearing strain rate and γ is simple shear rate) is defined in the x (white) coordinate system. The ellipsoid's principal axes define x' (black) coordinate system at angle φ.

where $\mathbf{J}^{\mathbf{D}}$ is the same as defined in Eqs.(2.1), and η_n is the foliation-normal viscosity measuring the resistance of the matrix to pure shearing along and perpendicular to the anisotropy plane, $m = {}^{\eta_n}\!/_{\eta_s}$ with η_s being the foliation-parallel viscosity measuring the resistance to shearing parallel to the anisotropy plane (Fig.2.6b). The parameter m indicates the strength of the anisotropy (Treagus, 2002; Fletcher 2004, 2009; Chen et al., 2014).

The analytic solutions in Fletcher (2009, his Eqs.14&15) can be rewritten in the following forms (Jiang, 2016):

$$\tilde{\varepsilon}_{11} = \frac{2\sqrt{m}R}{R^2 + 2r\sqrt{m}R + 1}\left[-r\left(\varepsilon\cos 2\varphi + \frac{\gamma}{2}\sin 2\varphi\right) + \left(\varepsilon\cos 2\varphi + \frac{\gamma}{2m}\sin 2\varphi\right)\right]$$

(2.13a)

$$\tilde{\varepsilon}_{12} = \frac{\sqrt{m}\left(R^2+1\right)}{r\sqrt{m}\left(R^2+1\right) + 2R}\left[-r\left(-\varepsilon\sin 2\varphi + \frac{\gamma}{2}\cos 2\varphi\right) + \left(-\varepsilon\sin 2\varphi + \frac{\gamma}{2m}\cos 2\varphi\right)\right]$$

(2.13b)

$$\tilde{w}_{12} = \frac{R^2-1}{R^2+1}\tilde{\varepsilon}_{12} = \frac{\sqrt{m}\left(R^2-1\right)}{r\sqrt{m}\left(R^2+1\right) + 2R}\left[-r\left(-\varepsilon\sin 2\varphi + \frac{\gamma}{2}\cos 2\varphi\right) + \left(-\varepsilon\sin 2\varphi + \frac{\gamma}{2m}\cos 2\varphi\right)\right]$$

(2.13c)

where the tilde above a quantity stands for the difference in the quantity between the inclusion and matrix (e.g., $\tilde{w}_{12} = w_{12} - W_{12}$), $R = {}^{a_1}\!/_{a_2}$ indicates the shape of an ellipse, r is the ratio of the inclusion viscosity to the matrix η_n, and φ is the angle between the ellipse a_1 semi-axis and the anisotropy plane (Fig.2.6b). For a rigid inclusion (i.e., $r \to \infty$), Eq.(2.13c) becomes (Eq.17 in Fletcher (2009))

$$\tilde{w}_{12rigid} = -\frac{R^2 - 1}{R^2 + 1}\left(-\varepsilon \sin 2\varphi + \frac{\gamma}{2}\cos 2\varphi \right) \tag{2.14}$$

Fig.2.7 presents the results for a rigid inclusion (R = 10) in plane-strain general shear ($\varepsilon = 0.5$ and $\gamma = 1$) obtained from the MATLAB package and those calculated directly using Eq.(2.14). In Fig.2.7, a_3 is set to 5, 15, 50 and 100. When $a_3 = 100$, the results from the package agree with the 2D analytical results. Fig.2.8 presents the results for a deformable inclusion (R = 5, r = 10, and m = 25) in plane-strain general shear ($\varepsilon = 0.5$ and $\gamma = 1$). In Fig.2.8, $a_3 = 100$, the numerical results agree with the analytical ones perfectly.

The package applies to 3D flows of course. Figs.2.9 and 2.10 are examples of a rigid triaxial ellipsoid (5:3:1) embedded in a planar anisotropic matrix (m = 25) and a deformable (r = 2) triaxial ellipsoid (5:3:1) embedded in a planar anisotropic matrix (m = 10), respectively. Detailed inputs are in figure captions.

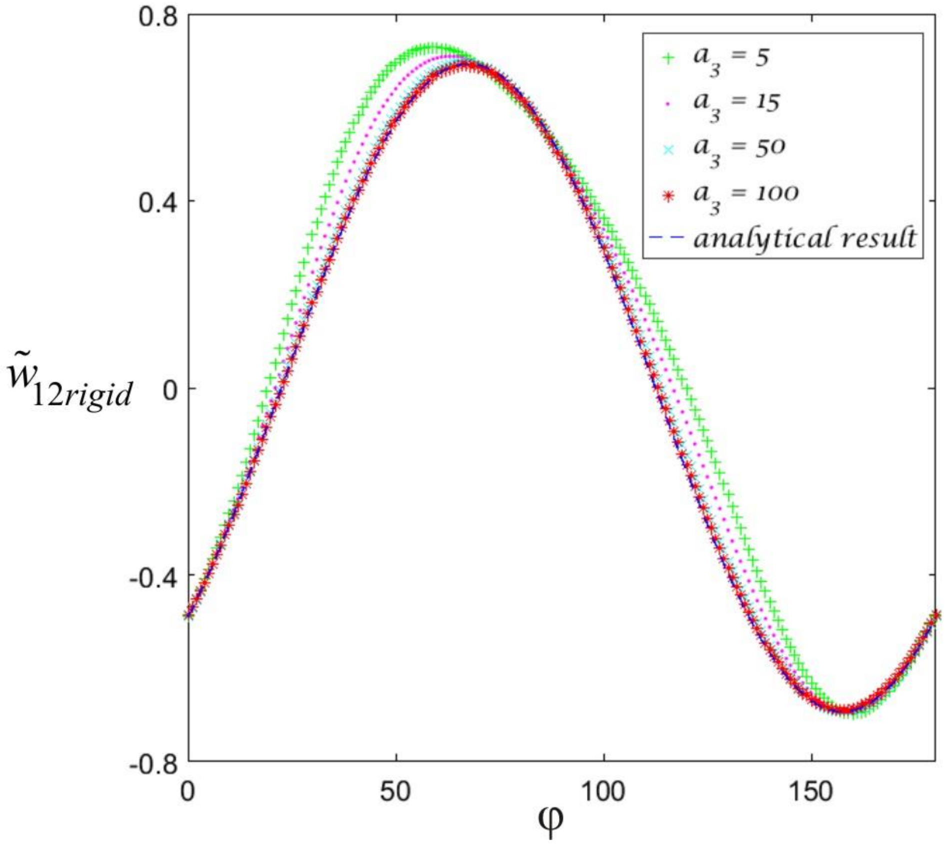

Figure 2.7 Comparison of the vorticity difference $\tilde{w}_{12}$ of a rigid inclusion (R = 10) in plane-strain general shear ($\varepsilon = 0.5$ and $\gamma = 1$) calculated from the MATLAB package (green markers: $a_3 = 5$, magenta markers: $a_3 = 15$, cyan markers: $a_3 = 50$, red markers: $a_3 = 100$) with the results calculated with Fletcher's analytical solutions (dashed line). The figure shows that the result from the package converges to the 2D analytical result with the increase of a_3. When $a_3 = 100$, the result from the package is undistinguishable from the 2D analytical result.

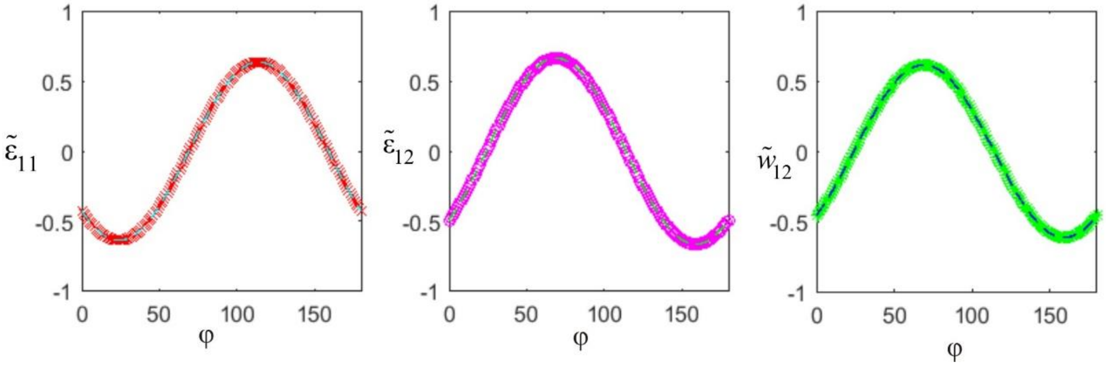

Figure 2.8 Comparison of the strain rates differences, $\tilde{\varepsilon}_{11}$ and $\tilde{\varepsilon}_{12}$, and the vorticity difference $\tilde{w}_{12}$ of a deformable inclusion (R = 5, r = 10, and m = 25) in plane-strain general shear ($\varepsilon = 0.5$ and $\gamma = 1$) calculated from the MATLAB package (cross markers, $a_3 = 100$) with the results calculated with Fletcher's analytical solutions (dashed lines).

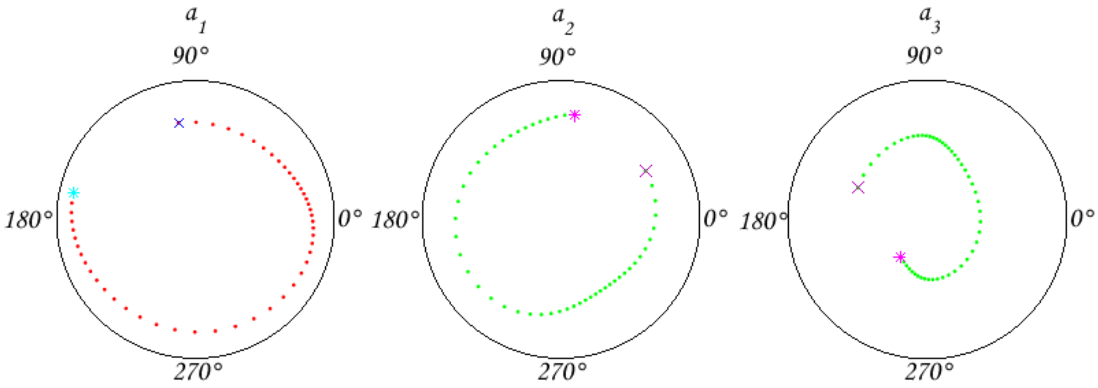

Figure 2.9 An example of using SGLRGD. Rotational paths of three semi-axes on equal-area projections. Red and green color symbols are, respectively, hemispheres associated with positive x_3 and negative x_3 half-spaces. '×' represents the initial state, and '*' represents the final state.

Input parameters are $\mathbf{L} = \begin{pmatrix} 0 & 1 & 0 \\ 0 & 0 & 0 \\ 0 & 0 & 0 \end{pmatrix}$**, for simple shearing flow field,**

ang = $\begin{pmatrix} 100 \\ 60 \\ 30 \end{pmatrix}$**, a =** $\begin{pmatrix} 5 \\ 3 \\ 1 \end{pmatrix}$ **, tincr = 0.01, steps = 1000, m=25.**

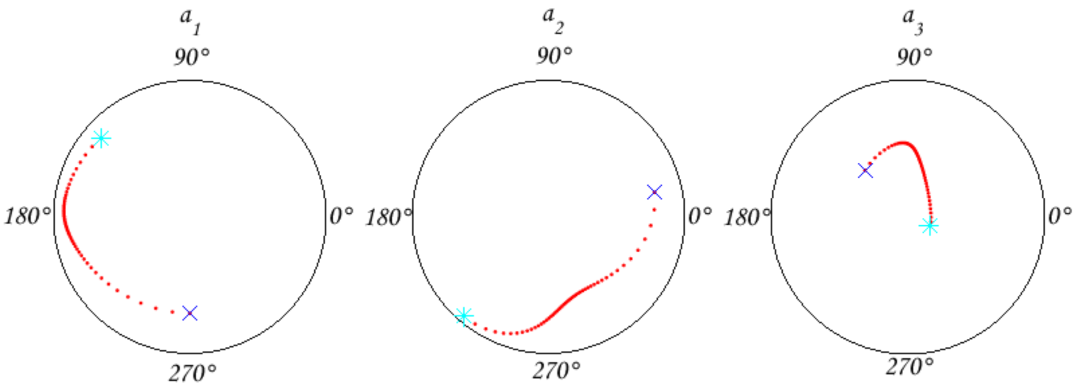

(a)

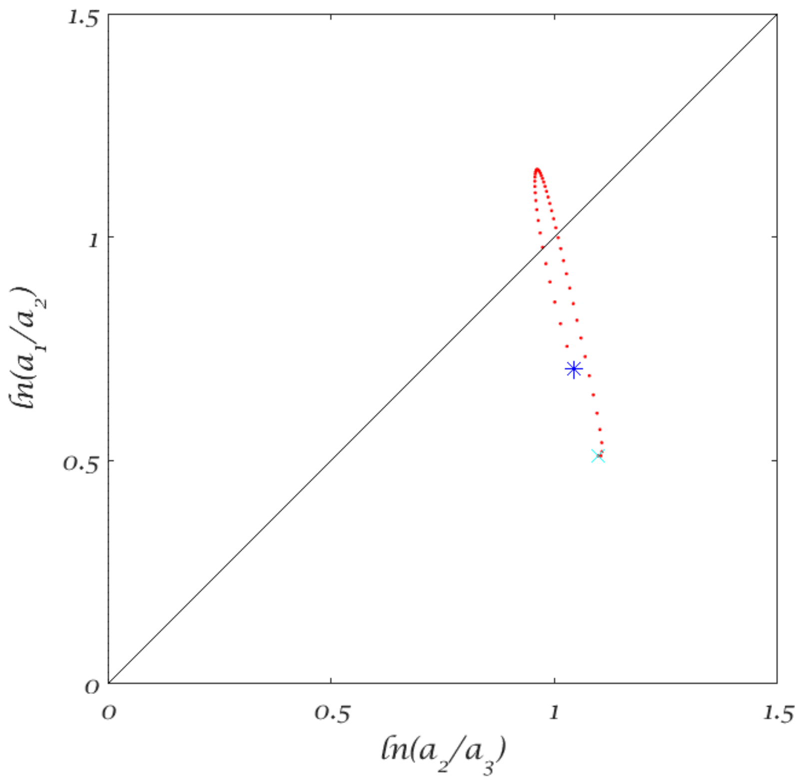

(b)

Figure 2.10 An example of using SGLDEF. (a) Rotational paths of three semi-axes on equal-area projections. (b) Shape evolution on the Flinn diagram. '×' represents the initial state, and '*' represents the final state.

2.4.3 Structure of the package

The package contains the following four MATLAB functions that one can run directly:

SGLRGD is for the simulation of a single rigid inclusion;

SGLDEF is for the simulation of a single deformable inclusion;

MLTRGD is for the simulation of multiple non-interacting rigid inclusions;

MLTDEF is for the simulation of multiple non-interacting deformable inclusions.

The folder *Routines* contains all the functions called in the above four executable functions. The optimal scheme to compute the 4th-order Green interaction tensor **T** is named *"TGreen.m"*. *"partTGL.mexw64"* and *"partTLeb.mexw64"* are two MEX (MATLAB Executable) files, written in C and compiled using the MATLAB's built-in *mex* function and the Microsoft Visual C++ 2015 compiler on the Win64 platform using MATLAB version R2016a. The subfolder, *C codes*, contains C source codes (*"partTGL.c"* and *"partTLeb.c"*) for *"partTGL.mexw64"* and *"partTLeb.mexw64"*. The subfolder, *Lebedev*, is taken from the library of Saff and Kuijlaars (1997) to generate nodes and weights following the Lebedev quadrature rules.

The validations in this paper are stored in the *Validations* folder (i.e., *RGDval* and *DEFval*). One can run the two functions in the folder to obtain Figs.2.7 and 2.8.

For power-law viscous deformable inclusions (i.e., *SGLDEF* and *MLTDEF*), $\boldsymbol{\varepsilon} = \left[\mathbf{J^D} + \mathbf{S} : (n_M \mathbf{C}_\mathbf{E}^{\mathbf{(sec)}} : \mathbf{C}_\mathbf{M}^{\mathbf{(sec)}-1} - \mathbf{J^D}) \right]^{-1} : \left[\mathbf{J^D} + (n_M - 1)\mathbf{S} \right] : \mathbf{E}$ (Eq.23 in Jiang, 2014). The linearized viscous stiffness is not a material constant but depends on the current state of deviatoric stresses (or strain rates). If the ellipsoidal inclusion is isotropic, we input an initial effective viscosity (η_{eff}^E) defined at a given reference strain rate for the ellipsoid and use calculated $\boldsymbol{\varepsilon}$ to update the effective viscosity (Ranalli, 1995; Mancktelow, 2011; Jiang, 2013) iteratively until the new calculated effective viscosity converges within the prescribed tolerance (*"Ed.m"* in *Routines*). If the inclusion is anisotropic, the input of a full constitutive relation (e.g., $\varepsilon_{ij} = g_{ij}(\sigma'_{kl})$) for the inclusion is necessary to update the linearized viscous stiffness, and the equation $\boldsymbol{\varepsilon} = \left[\hat{\mathbf{C}}_\mathbf{M} : (\mathbf{S^{-1}} - \mathbf{J^D}) + \hat{\mathbf{C}}_\mathbf{E} \right]^{-1} : \hat{\mathbf{C}}_\mathbf{M} : \mathbf{S^{-1}} : \mathbf{E} + \left[\hat{\mathbf{C}}_\mathbf{M} : (\mathbf{S^{-1}} - \mathbf{J^D}) + \hat{\mathbf{C}}_\mathbf{E} \right]^{-1} : (\mathbf{\Sigma^0} - \boldsymbol{\sigma}^\mathbf{0})$ (Eq.17 in Jiang, 2014) can be used to calculate $\boldsymbol{\varepsilon}$.

For the detailed implementation of the package, one can refer to Appendix B, the *"ReadMe.txt"* and comment lines in the package.

2.5 Summary and discussion

In this work, we have proposed an optimal numerical integration scheme (Fig.2.4) to efficiently evaluate Eshelby tensors. We have implemented this scheme in a MATLAB package to simulate the evolution of a single ellipsoid or dilute multiple ellipsoids embedding in a viscous material. The MATLAB package is applicable for general anisotropic incompressible viscous materials.

The optimal scheme in Fig.2.4 captures the effect of the inclusion's shape on the integrand in Eq.(2.4a). This scheme is based on isotropic matrix rheology. Clearly, the computational effort to evaluate Eq.(2.4a) is also affected by the viscous stiffness tensor of the matrix ($\mathbf{C_M}$) if the material is anisotropic. There is an infinite number of possible anisotropic $\mathbf{C_M}$, and it is impossible to address their effect on computation time generally. In principle, the anisotropic effect of $\mathbf{C_M}$ can be investigated case by case and a diagram similar to Fig.2.4 can be constructed once a specific type of $\mathbf{C_M}$ is given. We have applied our optimal scheme (based on the isotropic matrix) to a planar anisotropic matrix in the validation section. For a very high degree (m = 25) of anisotropy, our numerical results agree with the analytical solutions (Fig.2.8) perfectly. Based on this, we tentatively conclude that the effect of anisotropic $\mathbf{C_M}$ on the computational time of Eq.(2.4a) is insignificant compared to an ellipsoid shape. This may suggest that the optimal scheme in Fig.2.4 is generally applicable to general anisotropic matrices. Nevertheless, planar anisotropy is among the most common in natural deformed rocks.

To further speed up the MATLAB package, one can call BLAS (Basic Linear Algebra Subprograms) to perform matrix operations in the C source codes, and use open source libraries (e.g., MPI (Message Passing Interface)) or GPU programming (e.g., CUDA (Compute Unified Device Architecture)) to make the calculations on each node carried out simultaneously during the computation.

2.6 References

Altman, Y.M., 2014. Accelerating MATLAB Performance: 1001 tips to speed up MATLAB programs. CRC Press.

Atkinson, K., 1982. Numerical integration on the sphere. The Journal of the Australian Mathematical Society. Series B. Applied Mathematics, 23(03), 332-347.

Bilby, B.A., Eshelby, J.D., and Kundu, A.K., 1975. The change of shape of a viscous ellipsoidal region embedded in a slowly deforming matrix having a different viscosity: Tectonophysics, v. 28, p. 265-274.

Bilby, B.A., Kolbuszewski, M.L., 1977. The finite deformation of an inhomogeneity in two-dimensional slow viscous incompressible flow. Proceedings of the Royal Society of London, A355, 335-353.

Chen, Y., Jiang, D., Zhu, G., and Xiang, B., 2014. The formation of micafish: a modeling investigation based on micromechanics. Journal of Structural Geology, 68, 300-315.

Davis, P. J., and Rabinowitz, P., 1975. Methods of Numerical Integration. Academic, New York.

Dunnet, D., 1969. A technique of finite strain analysis using elliptical particles. Tectonophysics, 7(2), 117-136.

Eshelby, J. D., 1957. The determination of the elastic field of an ellipsoidal inclusion, and related problems: Proceedings of the Royal Society of London, v. A241, p. 376-396.

Ferguson, C.C., 1979. Rotations of elongate rigid particles in slow non-Newtonian flows. Tectonophysics, 60(3), 247-262.

Fletcher, R.C., 2004. Anisotropic viscosity of a dispersion of aligned elliptical cylindrical clasts in viscous matrix. Journal of Structural Geology, *26*(11), 1977-1987.

Fletcher, R.C., 2009. Deformable, rigid, and inviscid elliptical inclusions in a homogeneous incompressible anisotropic viscous fluid. Journal of Structural Geology, 31(4), 382-387.

Flinn, D. , 1956, On the deformation of the Funzie conglomerate, Fetlar, Shetland. The Journal of Geology, 480-505.

Freeman, B. 1985. The motion of rigid ellipsoidal particles in three-dimensional slow flows: implications for geological strain analysis. Tectonophysics, 113, 163-183.

Freeman, B. 1987. The behavior of deformable ellipsoidal particles in three-dimensional slow flows: implications for geological strain analysis. Tectonophysics, 132, 297-309.

Fry, N. , 1979. Random point distributions and strain measurement in rocks. Tectonophysics, 60(1), 89-105.

Gay, N.C., 1968. The motion of rigid particles embedded in a viscous fluid during pure shear deformation of the fluid. Tectonophysics 5, 81-88.

Goldsmith, H.L., Mason, S.G., 1967. The microrheology of dispersions. Rheology: theory and applications. Vol 4, 86-250.

Griera, A., Llorens, M. G., Gomez-Rivas, E., Bons, P. D., Jessell, M. W., Evans, L. A., and Lebensohn, R., 2013. Numerical modelling of porphyroclast and porphyroblast rotation in anisotropic rocks. Tectonophysics, 587, 4-29.

Hobbs, B.E., Means, W.D., and Williams, P.F., 1976. An Outline of Structural Geology. John Wiley & Sons.

Hutchinson, J.W., 1976. Bounds and Self-Consistent Estimates for Creep of Polycrystalline Materials. Proceedings of the Royal Society of London. A. Mathematical and Physical Sciences, 348(1652): 101-127.

Jeffery, G.B., 1922, The motion of ellipsoidal particles immersed in a viscous fluid: Proceedings of the Royal Society of London, v. A102, p. 161-179.

Ježek, J. ,1994. Software for modeling the motion of rigid triaxial ellipsoidal particles in viscous flow. Computers & Geosciences, 20(3), 409-424.

Ježek, J., Schulmann, K., Segeth, K., 1996. Fabric evolution of rigid inclusions during mixed coaxial and simple shear flows. Tectonophysics, 257, 203-221.

Jiang, D., 2007a. Numerical modeling of the motion of rigid ellipsoidal objects in slow viscous flows: A new approach. Journal of Structural Geology, 29(2): 189-200.

Jiang, D., 2007b. Numerical modeling of the motion of deformable ellipsoidal objects in slow viscous flows. Journal of Structural Geology, 29(3): 435-452.

Jiang, D., 2012. A general approach for modeling the motion of rigid and deformable objects in ductile flows. Computers & Geosciences 38, 52-61.

Jiang, D., 2013. The motion of deformable ellipsoids in power-law viscous materials: Formulation and numerical implementation of a micromechanical approach applicable to flow partitioning and heterogeneous deformation in Earth's lithosphere. Journal of Structural Geology 50, 22-34.

Jiang, D., 2014. Structural geology meets micromechanics: a self-consistent model for the multiscale deformation and fabric development in Earth's ductile lithosphere. Journal of Structural Geology 68, 247-272.

Jiang, D., 2016. Viscous inclusions in anisotropic materials: Theoretical development and perspective applications. Tectonophysics, 693, pp.116-142.

Johnson, S.E., Lenferink, H.J., Price, N.A., Marsh, J.H., Koons, P.O., West Jr., D.P., Beane, R., 2009. Clast-based kinematic vorticity gauges: the effects of slip at matrix/clast interfaces. Journal of Structural Geology 31, 1322-1339.

Krommer, A. R., 1994. Numerical Integration: On Advanced Computer Systems (Vol. 848). Springer Science & Business Media.

Lebedev, V. I., 1975. Values of the nodes and weights of quadrature formulas of Gauss-Markov type for a sphere from the ninth to seventeenth order of accuracy that are invariant with respect to an octahedron group with inversion. Zhurnal Vychislitel'noi Matematiki i Matematicheskoi Fiziki, 15(1), 48-54.

Lebedev, V. I., 1976. Quadratures on a sphere. USSR Computational Mathematics and Mathematical Physics, 16(2), 10-24.

Lebedev, V. I., 1977. Spherical quadrature formulas exact to orders 25–29. Siberian Mathematical Journal, 18(1), 99-107.

Lebedev, V. I., 1995. A quadrature formula for the sphere of 59th algebraic order of accuracy. Russian Academy of Sciences-Doklady Mathematics-AMS Translation, 50(2), 283-286.

Lebedev, V. I., and Laikov, D. N., 1999. A quadrature formula for the sphere of the 131st algebraic order of accuracy. In Doklady. Mathematics (Vol. 59, No. 3, pp. 477-481). MAIK Nauka/Interperiodica.

Lebedev, V. I., and Skorokhodov, A. L., 1992. Russian Acad. Sci. In Dokl. Math (Vol. 45, p. 587).

Lebensohn, R. A., Dawson, P. R., Kern, H. M., and Wenk, H. R., 2003. Heterogeneous deformation and texture development in halite polycrystals: comparison of different modeling approaches and experimental data.Tectonophysics, 370(1), 287-311.

Lebensohn, R. A., Rollett, A. D., and Suquet, P., 2011. Fast Fourier transform-based modeling for the determination of micromechanical fields in polycrystals. Jom, 63(3), 13-18.

Lebensohn, R.A., and Tomé, C.N., 1993. A self-consistent anisotropic approach for the simulation of plastic deformation and texture development of polycrystals: Application to zirconium alloys: Acta Metallurgica et Materialia, 41, 2611-2624.

Lebensohn, R. A., Tomé, C. N., and Maudlin, P. J., 2004. A selfconsistent formulation for the prediction of the anisotropic behavior of viscoplastic polycrystals with voids. Journal of the Mechanics and Physics of Solids, 52(2), 249-278.

Lebensohn, R.A., Turner, P.A., Signorelli, J.W., Canova, G.R. and Tomé, C.N., 1998. Calculation of intergranular stresses based on a large-strain viscoplastic self-consistent polycrystal model. Modeling and Simulation in Materials Science and Engineering, 6(4): 447-465.

Lisle, R. J., 1985. The use of the orientation tensor for the description and statistical testing of fabrics. Journal of Structural Geology, 7(1), 115-117.

Mancktelow, N.S., 2011. Deformation of an elliptical inclusion in two-dimensional incompressible power-law viscous flow. Journal of Structural Geology, 33(9), 1378-1393.

Mancktelow, N.S., Arbaret, L., Pennacchioni, G., 2002. Experimental observations on the effect of interface slip on rotation and stabilization of rigid particles in simple shear and a comparison with natural mylonites. Journal of Structural Geology 24, 567-585.

Masson, R., Bornert, M., Suquet, P., and Zaoui, A., 2000. An affine formulation for the prediction of the effective properties of nonlinear composites and polycrystals. Journal of the Mechanics and Physics of Solids, 48(6), 1203-1227.

Meng, C., Heltsley, W., and Pollard, D. D., 2012. Evaluation of the Eshelby solution for the ellipsoidal inclusion and heterogeneity. Computers & Geosciences, 40, 40-48.

Mercier, S., and Molinari, A., 2009. Homogenization of elastic–viscoplastic heterogeneous materials: Self-consistent and Mori-Tanaka schemes. International Journal of Plasticity, 25(6), 1024-1048.

Molinari, A., 2002. Averaging models for heterogeneous viscoplastic and elastic-viscoplastic materials. Journal of Engineering Materials and Technology, 124(1), 62-70.

Molinari, A., Canova, G.R., and Ahzi, S., 1987, A self-consistent approach of the large deformation polycrystal viscoplasticity. Acata Mettalurigica, v. 35, 2983-2994.

Molinari, A., and Mercier, S. 2004. Homogenization of viscoplastic materials. In: Ahzi, S., et al. (eds.), Multiscale Modeling and Characterization of Elastic-Inelastic Behavior of Engineering Materials, 113-124.

Mori, T., and Tanaka, K., 1973. Average stress in matrix and average elastic energy of materials with misfitting inclusions. Acta Metallurgica, 21(5), 571-574.

Mura, T., 1987. Micromechanics of defects in solids. Martinus Nijhoff Publishers, Dordrecht/Boston/Lancaster, 587 pp.

Passchier, C.W., and Simpson, C., 1986. Porphyroclast systems as kinematic indicators. Journal of Structural Geology 8, 831-843.

Quarteroni, A., Sacco, R., and Saleri, F., 2010. Numerical mathematics (Vol. 37). Springer Science & Business Media.

Ramsay, J.G., 1967. Folding and fracturing of rocks. McGraw-Hill, New York.

Ranalli, G., 1995. Rheology of the Earth. Springer Science & Business Media.

Saff, E.B., and Kuijlaars, A.B., 1997. Distributing many points on a sphere. The mathematical intelligencer, 19(1), 5-11 Available at https://people.sc.fsu.edu/~jburkardt/f_src/sphere_lebedev_rule/sphere_lebedev_rule.html (accessed Feb. 2015).

Simpson, C. and De Paor, D. G., 1993. Strain and kinematic analysis in general shear zones. Journal of Structural Geology, 15(1), 1-20.

Tomé, C. N., and Lebensohn, R. A., 2008. Manual for code viscoplastic self-consistent (Version 7). Available at: http://public.lanl.gov/lebenso/VPSC7c_manual.pdf (accessed Feb. 2015).

Treagus, S.H., 2002. Modeling the bulk viscosity of two-phase mixtures in terms of clast shape. Journal of Structural Geology, 24(1), 57-76.

Vigneresse, J. L. and Tikoff, B., 1999. Strain partitioning during partial melting and crystallizing felsic magmas. Tectonophysics, 312(2), 117-132.

Xiang, B. and Jiang D., 2013. Small-scale ductile shear zones as transposed rheologically weak domains: A numerical modeling investigation and practical application. Journal of Structural Geology 54: 184-198

Chapter 3: Deformation of the Shangdan Tectonic Zone in the Eastern Qinling Orogenic Belt

3.1 Introduction

The Qinling Orogenic Belt (QOB) extends more than ~1000km from west to east across central China and links Dabie Mountains in the east and Qilian and Kunlun Mountains in the west (Fig.3.1a, Dong et al., 2011a). It is commonly accepted that the QOB was as a result of episodic subductions and collisions of microcontinental fragments prior to the Triassic continent-continent collision between the North China Block (NCB) and the South China Block (SCB) (e.g., Zhang et al., 2001; Dong et al., 2011a,b; Wu and Zheng, 2013; Dong and Santosh, 2016). The Shangdan suture separates the QOB into the North Qinling Belt (NQB) and the South Qinling Belt (SQB) and is defined by the discontinuously exposed Danfeng Complex that consists of ophiolitic mélange (Fig.3.1b, Zhang et al., 2001; Dong et al., 2011a,b; Dong and Santosh, 2016). The deformation documented in the Shangdan suture and its adjacent areas is important to investigate the tectonic boundary conditions during the deformation and thus to understand the tectonic evolution of the QOB.

Along the Shangdan suture, sub-vertical foliations and sub-horizontal stretching lineations with sinistral shear-sense indicators have been observed in mylonites (Mattauer et al., 1985; Xu et al., 1986; Zhang et al., 1989; Reischmann et al., 1990; Wang et al., 2005), and the set of fabrics indicates a conspicuous sinistral strike-slip deformation along the Shangdan tectonic zone. Mattauer et al. (1985)

proposed that the displacement of the strike-slip deformation is at least 100km. However, the age of this deformation is still in dispute. Mattatuer et al. (1985) and Xu et al. (1986) obtained a biotite ^{39}Ar-^{40}Ar plateau age of 314±6 Ma in mica schist with subvertical foliation and E-W stretching lineation along the Shangdan zone, and they (Mattatuer et al., 1985; Xu et al., 1986) interpreted this age as the start of the sinistral strike-slip deformation. Wang et al. (2005) correlated this deformation along the Shangdan suture to a deformation zone (the Zhuxia zone) in the Qinling Complex and interpreted the biotite ^{39}Ar-^{40}Ar plateau age of 314±6 Ma in Mattatuer et al. (1985) as the late stage of the sinistral strike-slip deformation. Reischmann et al. (1990) obtained a U-Pb zircon age of 211±8 Ma from a mylonitic pluton in the Shagou shear zone, a segment of the Shangdan tectonic zone. Along with a Sm/Nd garnet-whole rock age of 126±9 Ma, Reischmann et al. (1990) proposed that the sinistral ductile deformation happened between 211Ma and 126Ma. According to a Rb-Sr whole-rock isochron age of 219Ma and a U-Pb zircon age of 211±8 Ma from a mylonite along the Shangdan tectonic zone, Zhang et al. (1989) proposed that the ductile deformation along Shangdan tectonic zone was at the late Triassic resulting from the ultimate convergence of the NCB and the SCB.

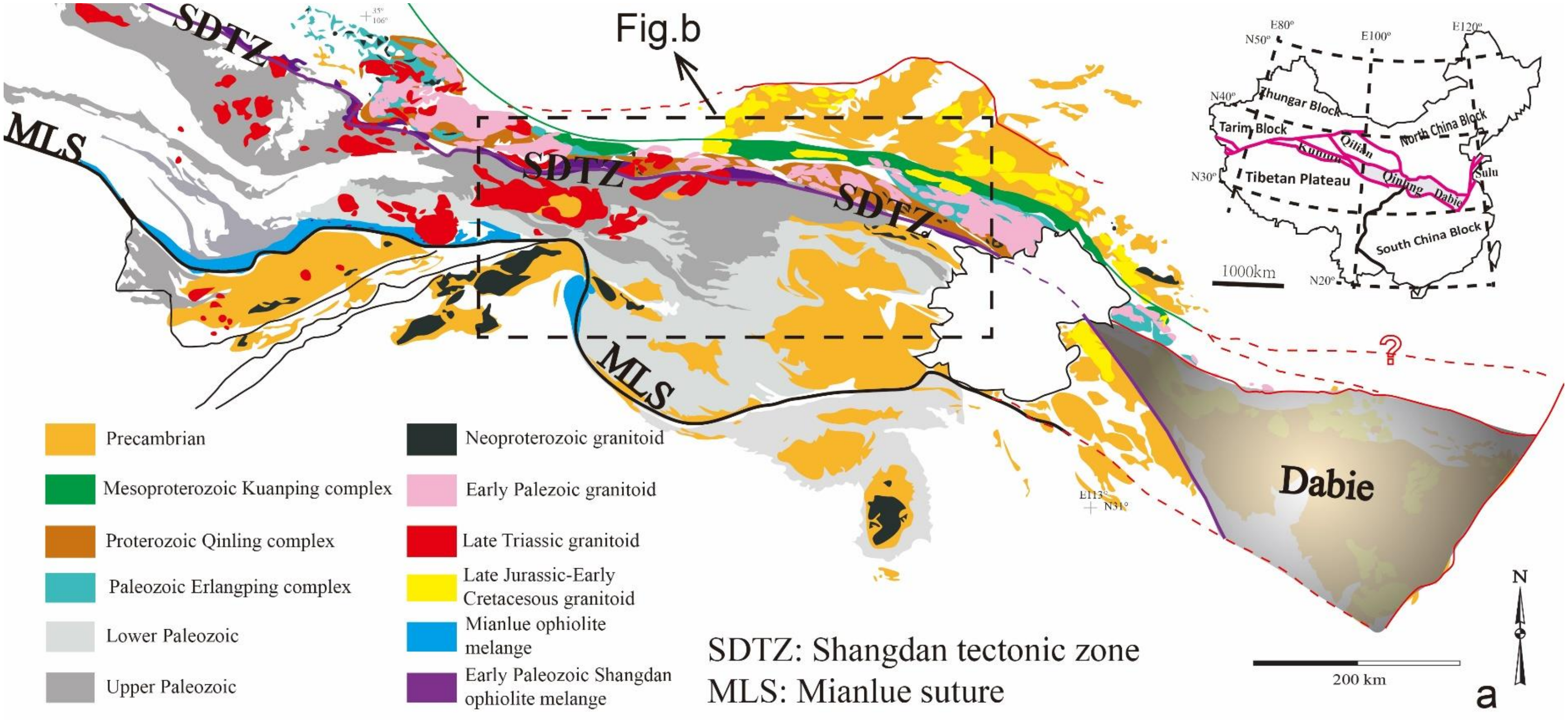SDTZ
MLS
35°
106°
Fig.b
SDTZ
SDTZ
MLS
?
E113°
N31°
Dabie
E80°
N50°
E100°
E120°
N40°
Zhungar Block
Tarim Block
North China Block
Qilian
Kunlun
N30°
Tibetan Plateau
Qinling
Dabie
Sulu
South China Block
1000km
N20°
Precambrian
Mesoproterozoic Kuanping complex
Proterozoic Qinling complex
Paleozoic Erlangping complex
Lower Paleozoic
Upper Paleozoic
Neoproterozoic granitoid
Early Palezoic granitoid
Late Triassic granitoid
Late Jurassic-Early Cretacesous granitoid
Mianlue ophiolite melange
Early Paleozoic Shangdan ophiolite melange
SDTZ: Shangdan tectonic zone
MLS: Mianlue suture
200 km
N
a

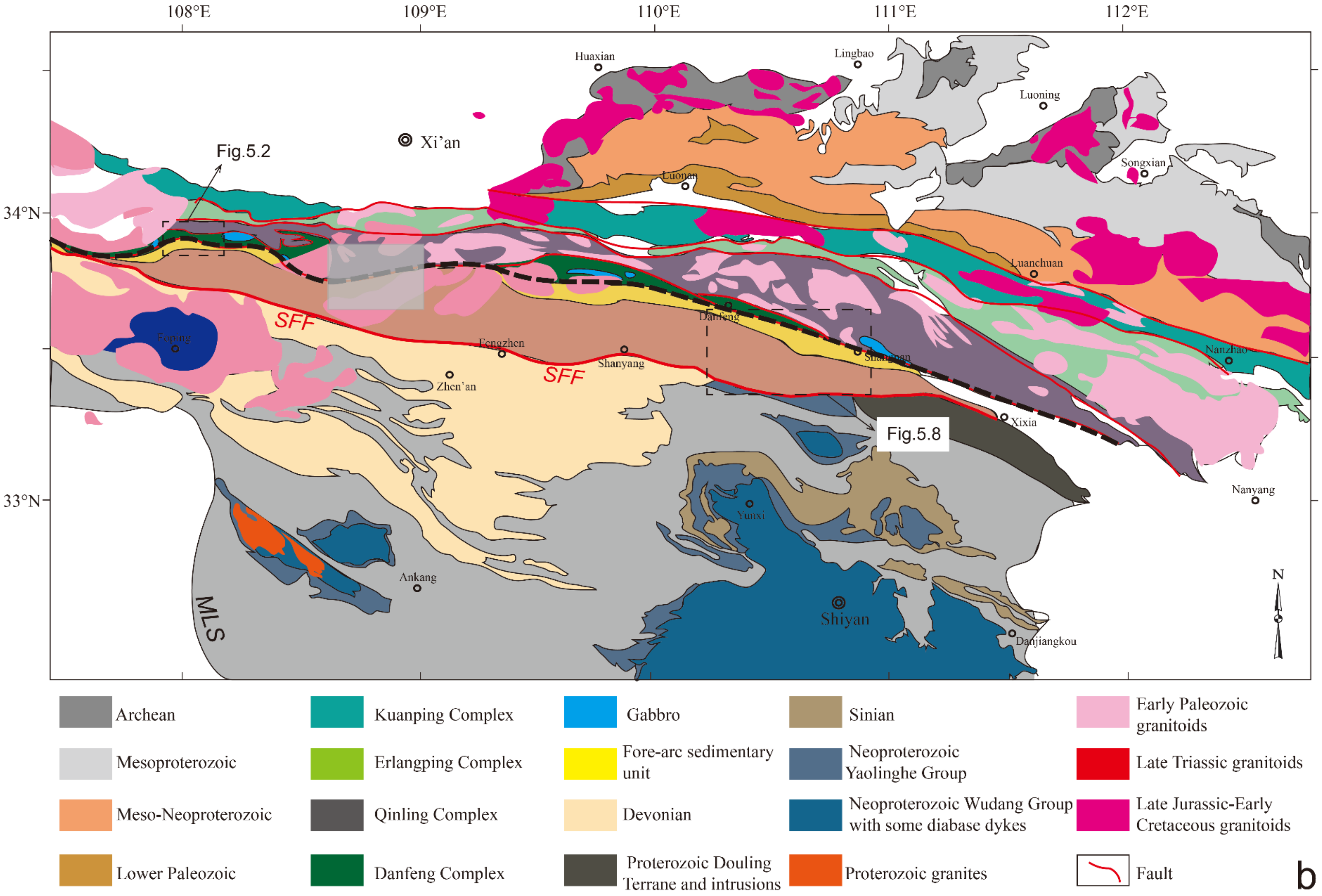
108°E
109°E
110°E
111°E
112°E
34°N
33°N
Huaxian
Lingbao
Luoning
Songxian
Xi'an
Fig.5.2
Luonan
Luanchuan
Danfeng
Foping
SFF
Fengzhen
Shanyang
Zhen'an
SFF
Shangnan
Nanzhao
Xixia
Fig.5.8
Nanyang
Yunxi
Ankang
MLS
Shiyan
Danjiangkou
N
Archean
Mesoproterozoic
Meso-Neoproterozoic
Lower Paleozoic
Kuanping Complex
Erlangping Complex
Qinling Complex
Danfeng Complex
Gabbro
Fore-arc sedimentary unit
Devonian
Proterozoic Douling Terrane and intrusions
Sinian
Neoproterozoic Yaolinghe Group
Neoproterozoic Wudang Group with some diabase dykes
Proterozoic granites
Early Paleozoic granitoids
Late Triassic granitoids
Late Jurassic-Early Cretaceous granitoids
Fault
b

Figure 3.1 Geological maps to show the Qinling orogenic belt and the eastern Qinling orogenic belt. (a).Geological map showing the location and composition of the Qinling orogenic belt and its adjacent areas (Dong and Santosh, 2016). The map in the upper right corner shows the location of the Qinling orogenic belt in China. (b). Geological map of the eastern Qinling belt showing the major geological units and field work areas (the Heihe area and the Danfeng area) (Dong et al., 2013; Liao et al., 2017). SSF: Shanyang-Fengzhen fault.

The Paleozoic Shangdan suture contain ultramafic and mafic rocks that have characteristics of N-MORB, E-MORB, boninite and island-arc basalts were formed during 534-500Ma (Dong et al., 2011b; Liu et al., 2016). Cambrian-Ordovician radiolarians and conodonts were found in the Danfeng Complex (Cui et al., 1995; Ding et al. 2004). Subduction-related volcanic and sedimentary rocks are in the range of ca.530-470Ma (Dong and Santosh, 2016). Although the exact deformation time along the Shangdan suture and its vicinity is still unclear, it is either during the early Mesozoic in response to the collision between the SQB and the SCB or during the Paleozoic after the assemblage of the SQB and the NQB. In both processes, the predominant strike-slip deformation along the Shangdan tectonic zone was not compatible with the compressional tectonic boundary during the collisional process.

An orogenic belt, especially as the QOB that contains different geological units and has experienced a long time of evolution (thus involved numerous structures, fluids, new minerals, etc.), is a very complicated region and consists of omnipresent rheological heterogeneities. Ubiquitous rheological heterogeneities throughout a deformation zone can cause significant flow-field partitioning (Lister and Williams, 1983), and hence the deformation demonstrated in different geological domains may show different characteristics over a wide range of observational scales (e.g., outcrops, thin-sections). Thereupon, in a tectonic-scale transpressional zone, such as the Shangdan tectonic zone, small-scale structural features (e.g., stretching lineations, shear-sense indicators) on outcrops or in thin sections are directly related to the 'local' partitioned flow fields but not to the 'bulk' tectonic-scale boundary conditions (Jiang, 2014). Recently, Jiang and Bentley (2012) and Jiang (2013, 2014) have proposed a robust multi-scale approach to handle flow-field partitioning that has been introduced in Chapter 1 and Chapter 2, and we apply this approach to understand the deformation of the Shangdan tectonic zone.

In this work, we conduct detailed structural analysis along the Shangdan suture and its adjacent areas, collectively referred to as the Shangdan tectonic zone (SDTZ) in this paper, to investigate the deformation history and deformation time of the SDTZ along with previous geochronological works. In addition, we apply the recently developed multiscale approach (Jiang and Bentley, 2012; Jiang, 2013, 2014) to the study area and connect small-scale fabrics in distinct rheological domains to large-scale tectonic synthesis and to infer the tectonic-scale boundary conditions of the SDTZ.

3.2 The Shangdan tectonic zone

3.2.1 Geological setting

The Shangdan suture zone divides the QOB into the NQB and the SQB. One can refer to Dong and Santosh (2016) for the detailed geological descriptions of each geological unit in the QOB. Here, only the geological units that are involved in the field work areas are introduced. The field work is conducted in two regions along the SDTZ (i.e., the Heihe area and the Danfeng area, Fig.3.1b, Fig.3.2, Fig.3.8).

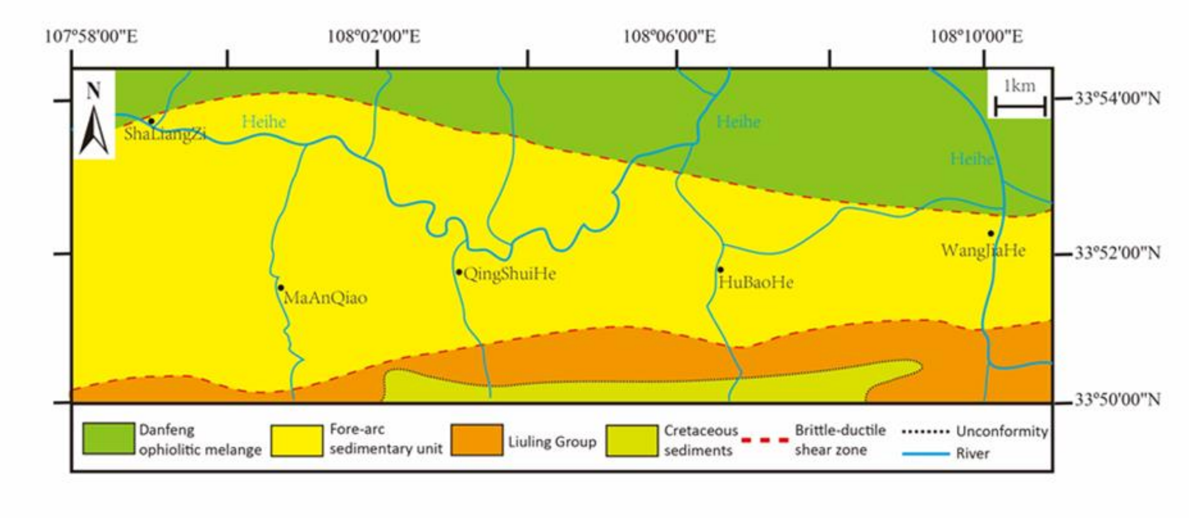

Figure 3.2 Geological map showing the geological units in the Heihe area (modified from 1:200000 regional geological map). The Shaliangzi township is on the upper left corner of the map.

In Heihe, the field work is conducted in a sedimentary unit (the yellow area in Fig.3.2). The unit is characterized by the metamorphosed conglomerate, sandstone, shale and carbonate from bottom to top (Meng et al.,1994; Yu and Meng, 1995; Dong et al., 2013). This unit is interpreted as a fore-arc sedimentary prism according to the investigation of the conglomerates outcropping as two intercalations within sandstones and volcanic rocks (Meng et al., 1994, 1997; Yu and Meng, 1995). The depositional age of the sedimentary unit is bracketed in the range of ca.455-435Ma by the youngest detrital zircon (ca.455Ma) and the magmatic zircons (435±7Ma, MSWD=4.1) from a mafic dyke that intruded in the sedimentary unit (Dong et al., 2013). The comparison of the detrital zircon age populations from the sedimentary unit with the known ages from the NQB and the SQB suggests that the sedimentary provenance is attributed to the NQB (Dong et al., 2013).

In Danfeng, the field work is mainly conducted in the Danfeng Complex, the Wuguan Complex and the Liuling Group (Fig.3.8). *Danfeng Complex* is discontinuously exposed and composed of ophiolitic assemblages, arc-related volcanic rocks and sedimentary rocks (Zhang et al., 1995; Zhang et al., 2001; Dong et al., 2011a, b). The rocks underwent greenschist to lower amphibolite metamorphic facies, and the formation age of these rocks was constrained by zircon U-Pb ages of ca.534-470Ma from mafic rocks of the ophiolitic assemblages and subduction-related rocks (Dong and Santosh, 2016 and reference therein). The Danfeng Complex marks the Shangdan suture. *Wuguan Complex* is composed of quartz schists, marbles and amphibolites (Pei, 1997). The depositional age of the Wuguan Complex is in the range of ca.389-330 Ma according to the detrital zircon age analyses (Yan et al., 2016). *Liuling Group* consists of the several kilometers thick turbidite sequences and has been further divided into the Niuerchuan formation, Chigou formation, Qingshiya formation, Xiadonggou formation, and Tongyusi formation from the lower to the upper strata (Zhang et al., 2001). According to the youngest detrital zircon (400Ma) data (Dong et al., 2013) and the crystallization age (373.8Ma) of a pegmatitic dyke, the depositional age of the Liuling Group is constrained to 373.8-400Ma (Shi, 2016).

3.2.2 Structural geometry

3.2.2.1 The Heihe area

A highly deformed meta-conglomerate is found at the Shaliangzi township on Fig.3.2, and the rest of the deformed rocks are mainly meta-sandstone, meta-pelite and marble.

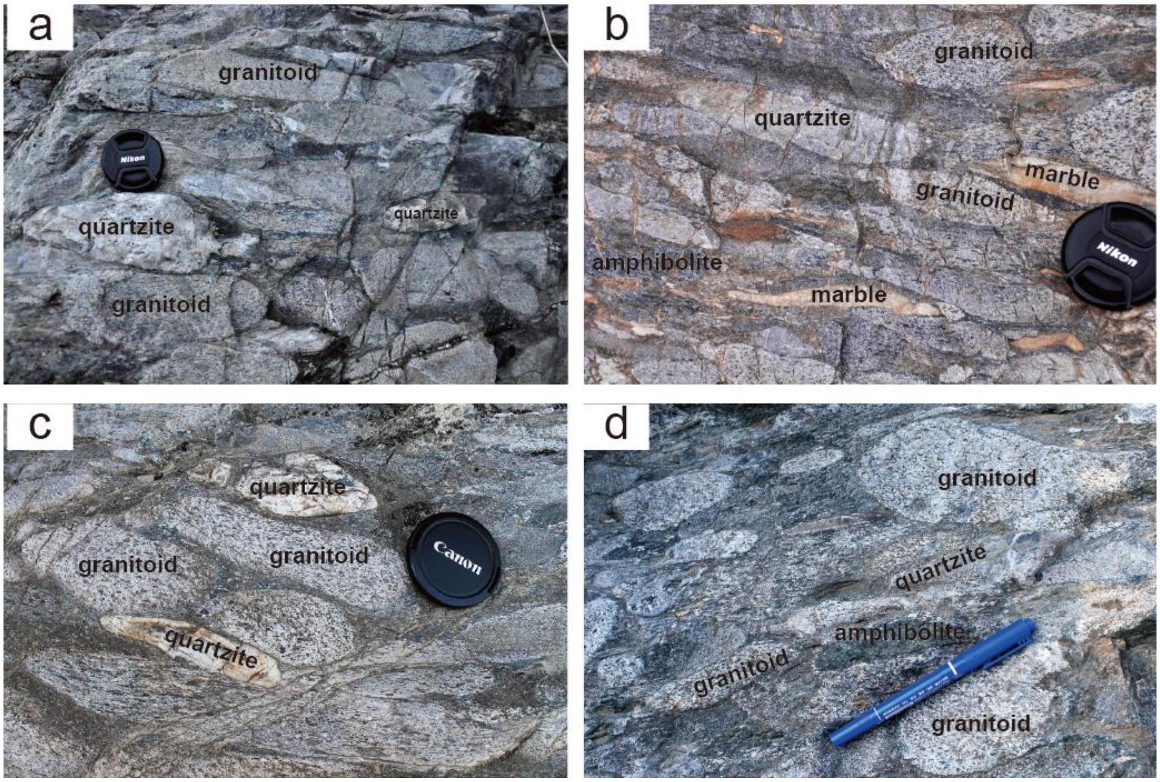

Figure 3.3 Photos showing the deformed conglomerate at the Shaliangzi township. The conglomerate is clast-supported and contains granitoid pebbles, quartzite pebbles, amphibolite pebbles and marble pebbles.

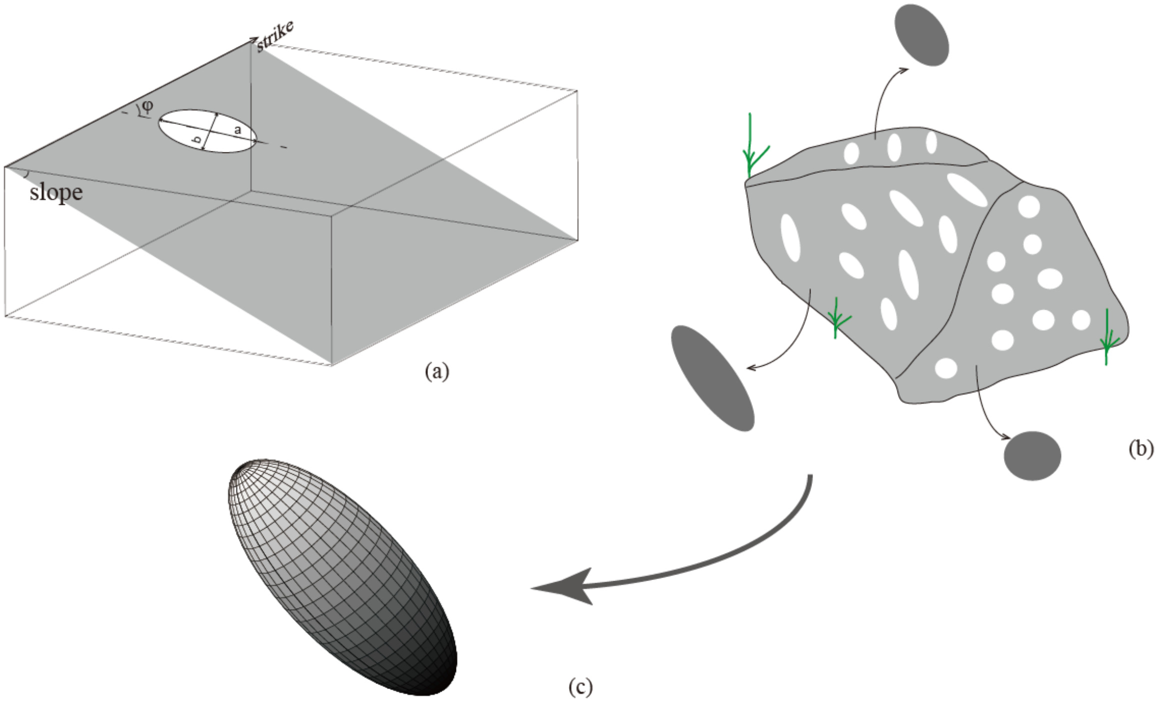

Figure 3.4 A diagram showing the concept of a fabric ellipsoid. (a). On an arbitrary planer section, a deformed pebble is exposed as an ellipse. $R_f = \frac{a}{b}$ ($R_f \geq 1$) represents the shape, and φ ($0^\circ \leq \varphi < 180^\circ$) describes the orientation. (b). On an outcrop, 2D fabric data are measured from planar sections, and a best-fit ellipse from each section can be calculated (modified after Giorgis and Tikoff, 2004). (c). A best-fit 3D fabric ellipsoid can be obtained from 2D best-fit ellipses.

The apparent thickness of the conglomerate is up to 50m (Dong et al., 2013), and the matrix of the conglomerate is greywacke and recorded greenschist to amphibolite metamorphic facies indicated by the existence of new grown amphibole and biotite. The deformed conglomerate is clast-support, and the percentages of clast and matrix are 80% and 20%, respectively. The deformed conglomerate contains polymictic pebbles including granitoid (~40%), quartzite (~30%), amphibolite (~20%) and marble (~10%), and sizes of pebbles are in the range between 3cm and 30cm (Fig.3.3).

Deformed conglomerates are important strain markers compared with other strain markers (such as deformed fossils), as they are widely distributed in deformed rocks and easy to be recognized after intense deformation and high-grade metamorphism and able to indicate the total strain since their deposition (Ramsey, 1967; Lisle, 1979). One way to extract the information that deformed conglomerates hold is to collect fabric data (shape and orientation of deformed pebbles) on planar sections and summarize the results into a fabric ellipsoid (Fig.3.4). On a planar section, the shape of a deformed pebble can be represented by $R_f = \frac{long\ axis}{short\ axis}$ (a and b in Fig.3.4a) and the pitch of the long axis (φ in Fig.3.4a) can represent the orientation of the deformed pebble. According to the solutions in Robin (2002), after measuring sufficient fabric data of deformed pebbles on a planar section, a best-fit sectional ellipse is found (Fig.3.4b). After best-fit sectional ellipses are obtained from $N\left(N \geq 3\right)$ planar sections, together with the orientations of the planar sections, a best-fit 3D fabric ellipsoid can be obtained (Fig.3.4c, Robin, 2002).

The aspect ratio (R_f) and the orientation of the long axis (φ) of each pebble on 15 field exposed sections are measured. Best-fit fabric ellipsoids of granitoid, quartzite, amphibolite and marble pebbles are obtained. The measured data are in Appendix D. The shape of the fabric ellipsoids is plotted in the Flinn diagram (Fig.3.5a) to investigate the deformation of the conglomerate. Four fabric ellipsoids are all plotted in constrictional deformation on the Flinn diagram. According to the distance from the origin to the points, the strain magnitudes reflected from four fabric ellipsoids are marble > quartzite > amphibolite ≈ granite, and thus the competence sequence of the four types of pebbles is in reverse. The longest axis of the fabric ellipsoid is comparable with the stretching lineations, and the longest axes of the fabric ellipsoids from four types of pebbles are plotted on a lower-hemisphere equal-area projection (Fig.3.5b). Although four types of pebbles show distinct competence, the longest axes of their fabric ellipsoids are all sub-horizontally. The orientation is coincident with the stretching lineations (Fig.3.7) throughout the Heihe area.

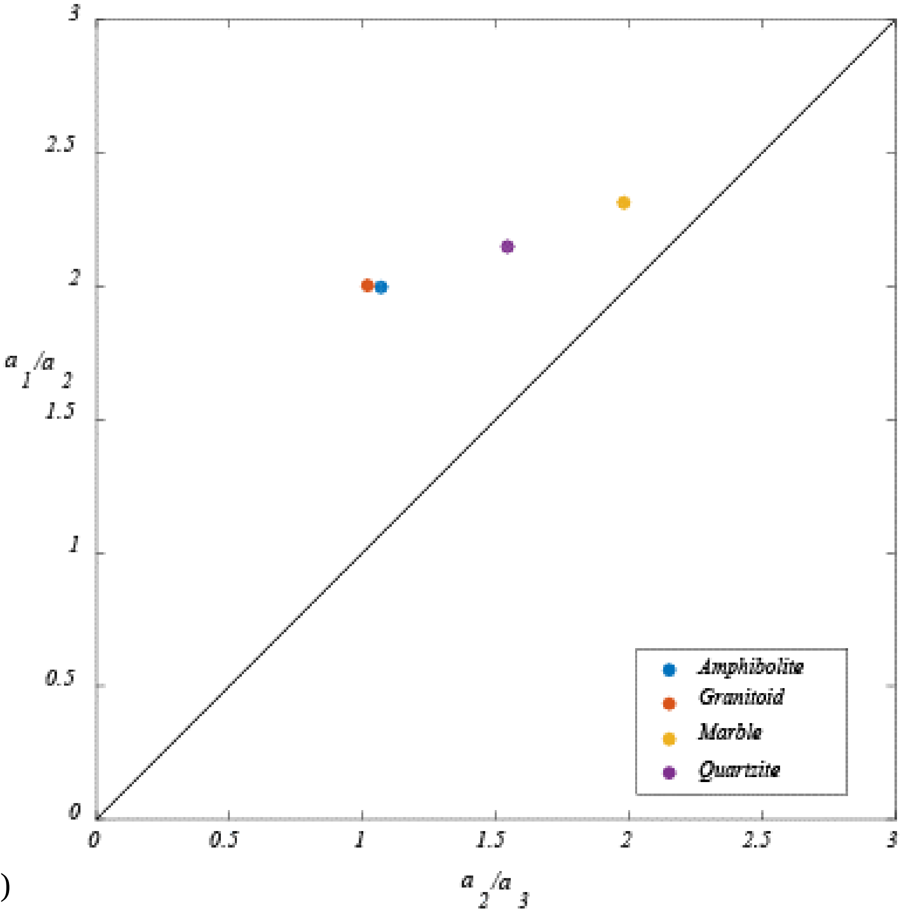

(a)

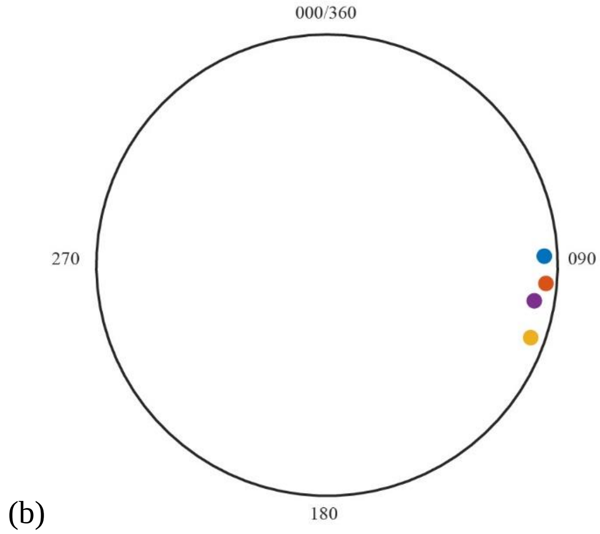

Figure 3.5 Fabric data from the deformed conglomerate. (a). the Flinn diagram of the amphibolite, granitoid, marble and quartzite fabric ellipsoids. a_1, a_2, a_3 are three semi-axes of a fabric ellipsoid ($a_1 > a_2 > a_3$). (b). Lower-hemisphere equal-area projection of the longest axes of the four fabric ellipsoids.

The rest of this region are highly transposed metamorphic tectonites (meta-sandstone and meta-pelite). Sub-vertical foliations and horizontal lineations are developed in S>L tectonites. Foliations are mainly slaty cleavage in meta-pelite and schistosity in meta-sandstone, and the rocks show a very strong preferred orientation under microscope. Lineations are mineral stretching lineations defined by elongate mineral aggregates on outcrops, and the aggregate is mainly composed of quartz and mica. Shear sense indicators (including S-C-C', S-C fabrics and rotated porphyroclasts) are well developed on sub-horizontal sections on outcrops and in thin sections showing a sinistral sense of shear (Fig.3.6).

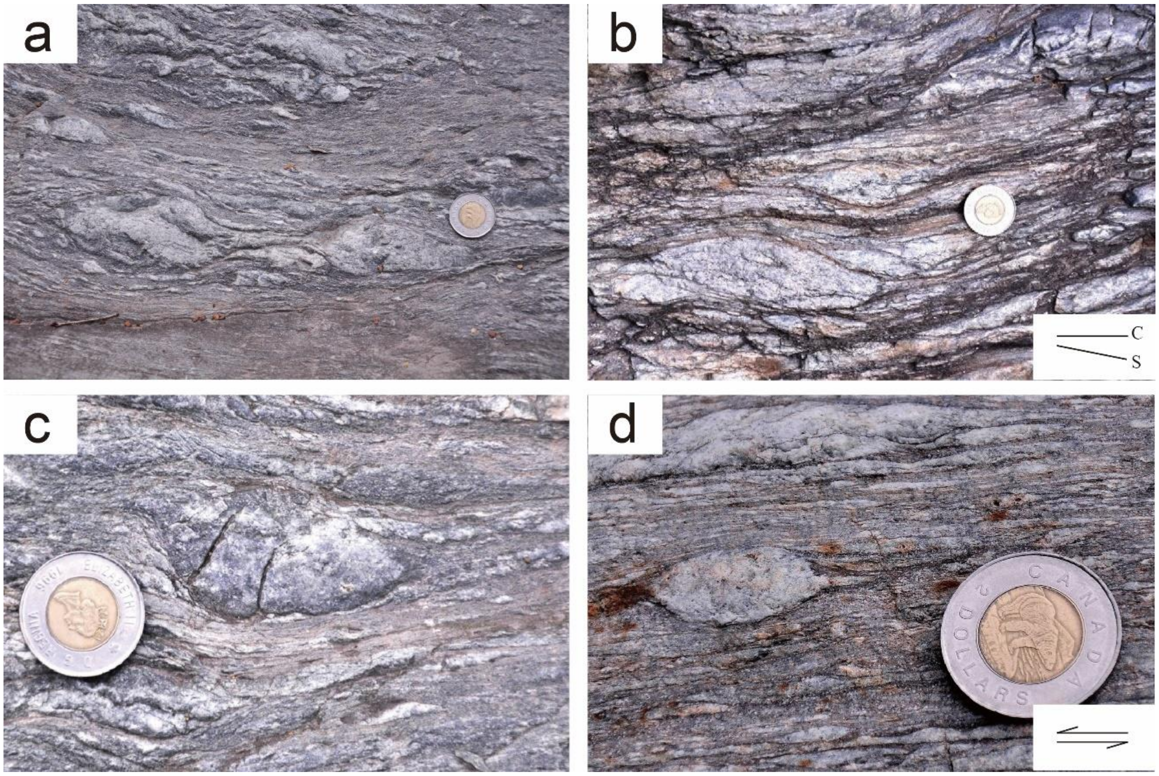

Figure 3.6 Photos showing shear-sense indicators in the Maanqiao shear zone (southern part of the fore-arc sedimentary unit). (a) and (b) present S-C fabric in metamorphic sandstones on the outcrop, and sense of shear is sinistral. (c) and (d) show tails of deformed quartzite pebbles in outcrop, reflecting sinistral shear. The photos are taken on sub-horizontal planes.

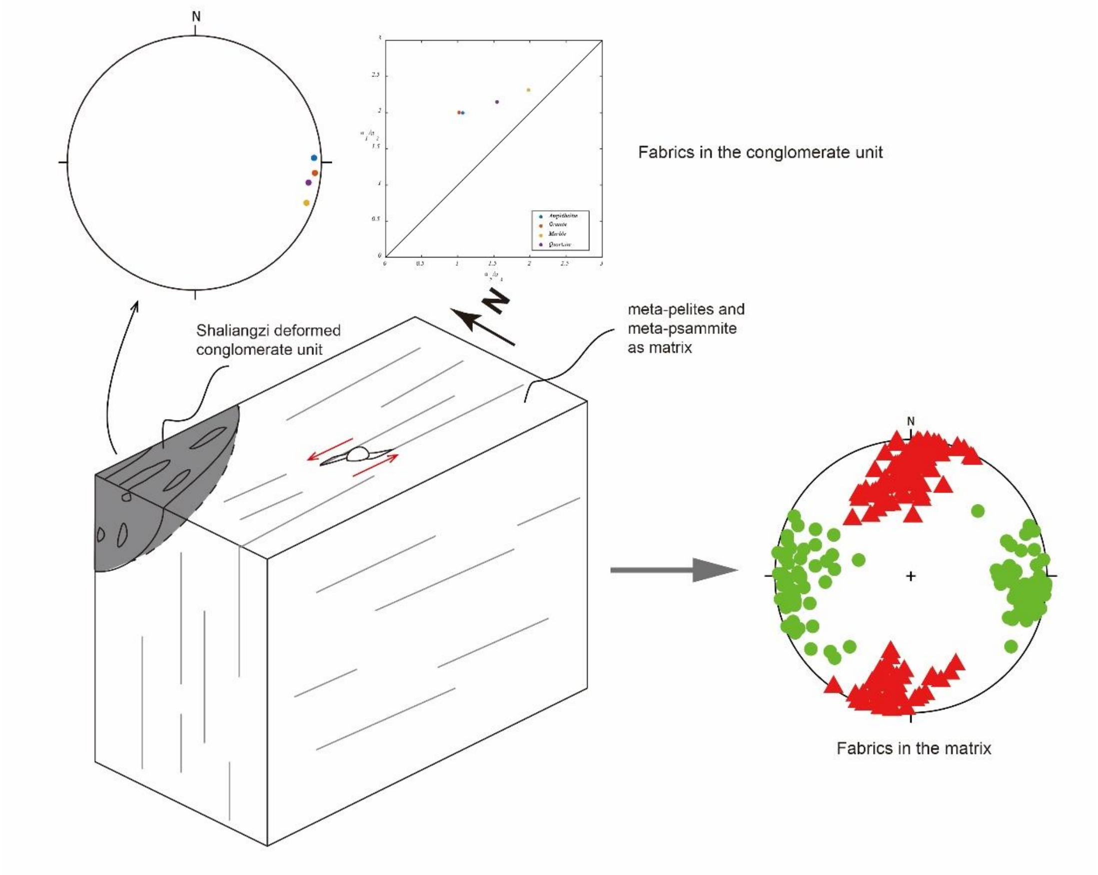

Figure 3.7 A conceptual block diagram summarizing the fabrics in the Heihe area. The right corner plot is a lower-hemisphere equal area projection of stretching lineations and poles to foliation throughout the tectonites in the Heihe area. Green dots are stretching lineations, and red triangles are poles to transposition foliations.

In brief, the fabric data in the Heihe area can be summarized as a conceptual block diagram in Fig.3.7. The structural geometry in Fig.3.7 shows a sinistral strike-slip dominated transpressional deformation (Lin et al., 1998; Jiang and Williams, 1998). The constrictional deformation shown in the deformed conglomerate can be explained by the heterogeneity of the deformed rocks. Generally, in a strong domain, under a transpressional deformation, the deformed rocks tend to show a constrictional deformation (Freeman and Lisle, 1986; Chen, 2014), so the deformed conglomerate is more competent than the surrounding matrix (i.e., the meta-sandstone and meta-pelite).

3.2.2.2 The Danfeng area

In the Danfeng area (Fig.3.8), four outcrop-scale high-strain zones are observed along the SDTZ, and two generations of deformation can be recognized in the Liuling Group.

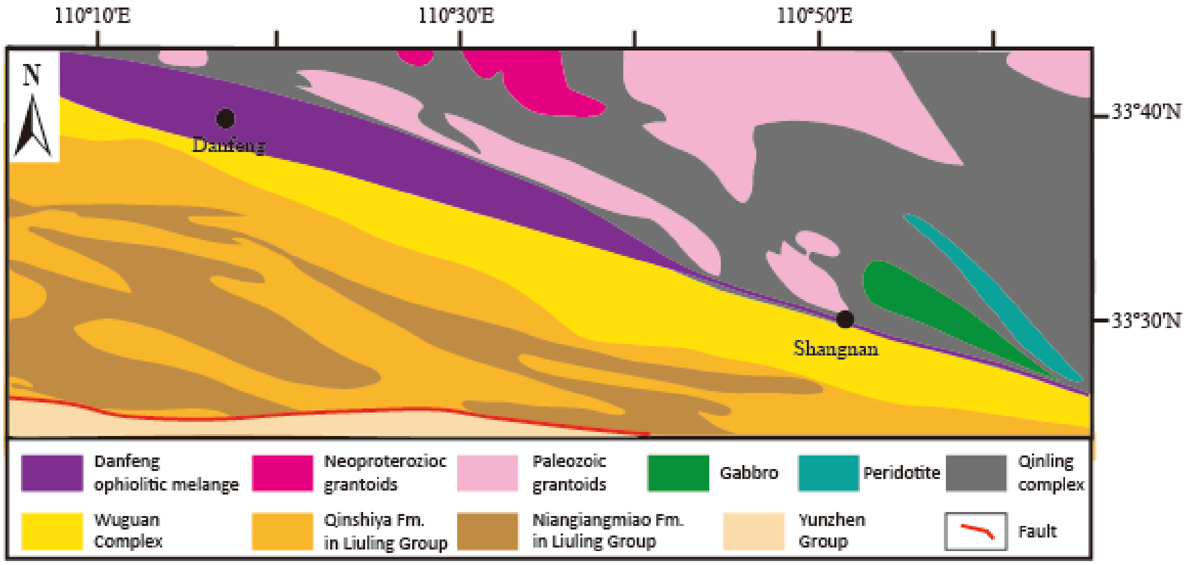

Figure 3.8 Geological map showing the geological units in the Danfeng area (modified from 1:200000 regional geological map and Dong et al., 2013).

Outcrop-scale high strain zones are observed along the SDTZ in the Wuguan Complex and the Danfeng Complex. Sub-vertical foliations and horizontal stretching lineations (Fig.3.9e) are developed in mylonites and highly transposed metamorphic tectonites. Shear-sense indicators are well developed on sub-horizontal sections on outcrops and in thin sections showing a sinistral sense of shear (Figs.3.9a-d). Two generations of deformation can be observed on the outcrops in Qingyouhe and Mianyuzui. As the second generation is at the same scale of the first generation and they both show the same geometric features, the two generations of deformation are interpreted as the different stages of one progressive deformation event (Fig.3.10).

Field geometries indicate two generations of deformation in the Liuling Group. These two generations of deformation in the Liuling Group are referred to as D_1 deformation and D_2 deformation in this paper. The significant structures of D_1 deformation are isoclinal folds (F_1) that are associated with the occurrence of transposition foliation or crenulation cleavage (S_1) and mineral lineations (Fig.3.11). F_1 folds can be recognized from the geological map (Fig. 3.8) of the Liuling Group. D_2 deformation is represented by recumbent (F_2) folds with crenulation cleavage (S_2) parallel to F_2 axial planes (Fig.3.12). L-tectonite, which is generated by D_2 deformation, is defined by F_2 hinge lines (Fig.3.12). The distinctive D_2 structures are observed in the Liuling Group only. The overprinting relationship between D_1 fabrics and D_2 fabrics can be recognized on the outcrops. The structures developed by D_2 deformation are heterogeneous spatially. D_2 deformation can be well recognized in the southern part of the Maoligang and the Zhulinguan areas. Only a few D_2 fabrics can be observed in the southernmost of the Lishangou and the Laopenggou areas. Namely, D2 deformation becomes weaker northward where D1 deformation is well preserved.

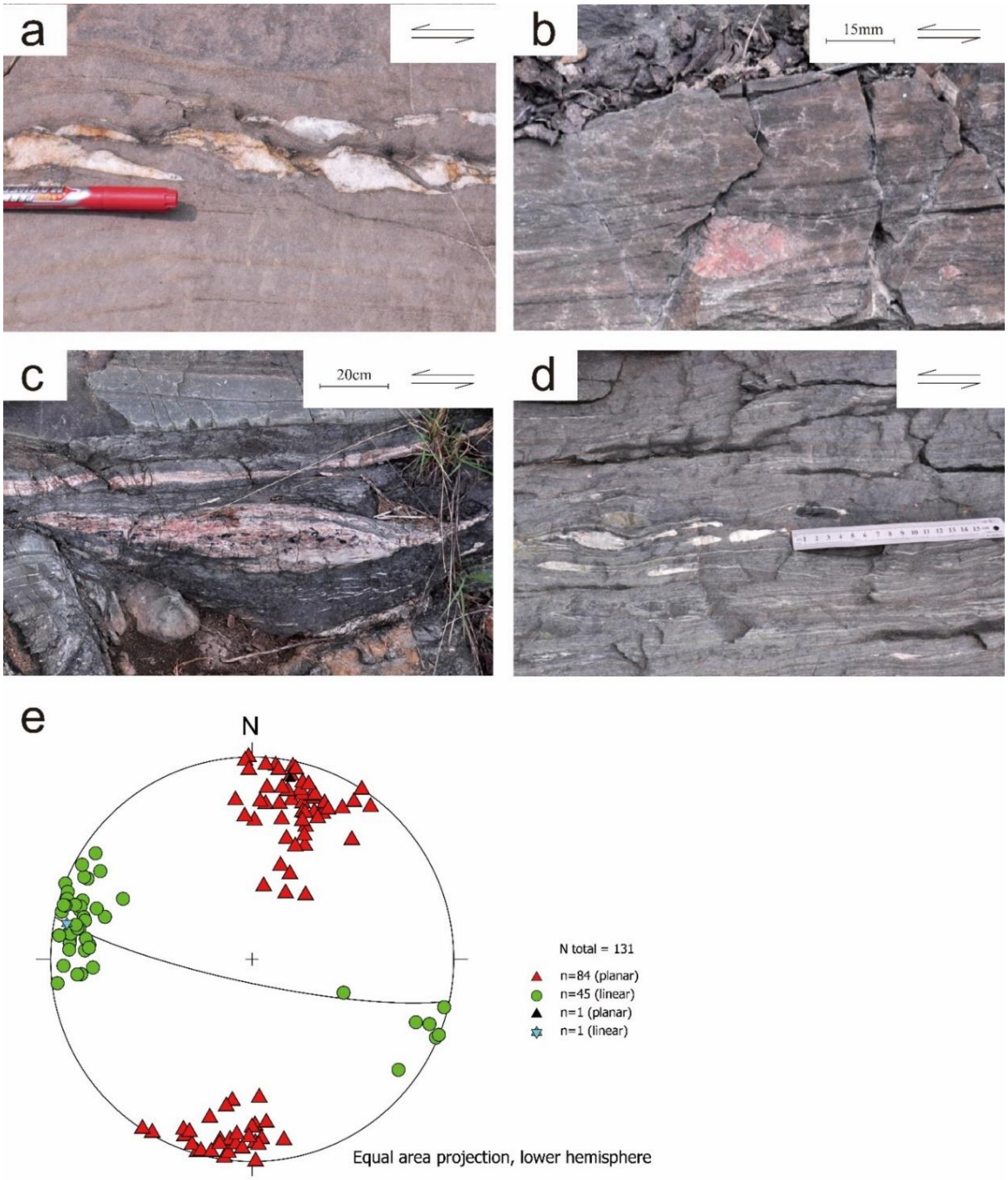

Figure 3.9 Photos and fabric data from the high-strain zones. (a-d) Photos showing shear-sense indicators on outcrops in the high-strain zones. All photos are taken on sub-horizontal surfaces. (e) Lower-hemisphere equal-area projection of stretching lineations and transposition foliations in high-strain zones. Green dots are stretching lineations, and red triangles are poles to transposition foliations. The black great circle is the average of the foliations, and

the light blue star is the average of the lineations (close to horizontal and covered by green dots).

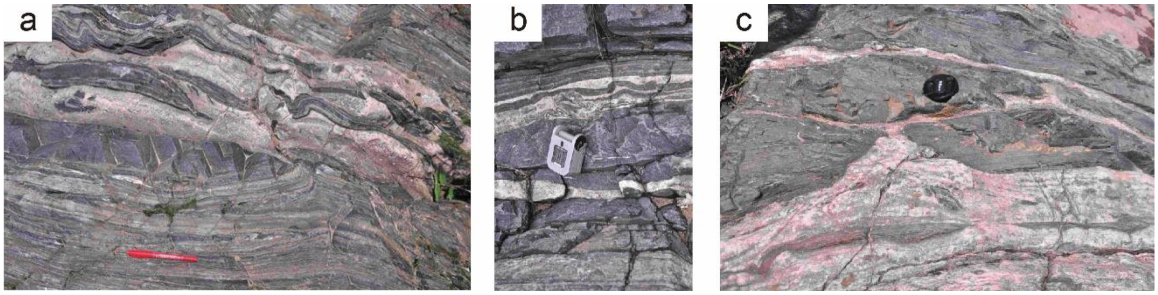

Figure 3.10 Two-generation structures observed in the high-strain zones.

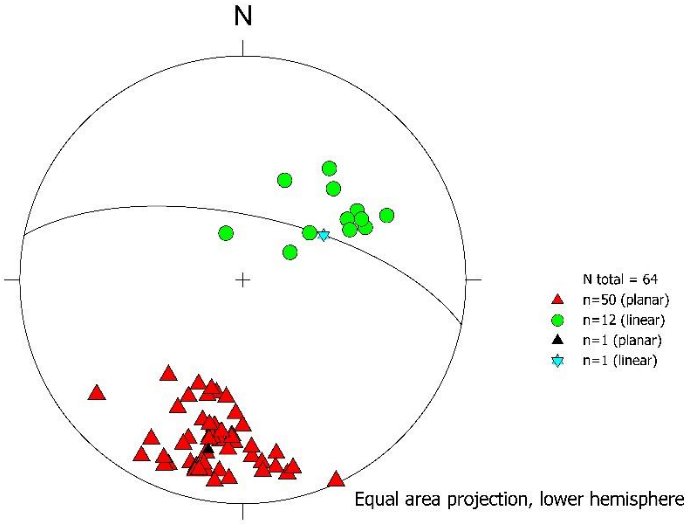

Figure 3.11 Lower-hemisphere equal-area projection of stretching lineations and transposition foliations in the Liuling Group. Green dots are stretching lineations, and red triangles are poles to transposition foliations. The black great circle is the average of the foliations, and the light blue star is the average of the lineations.

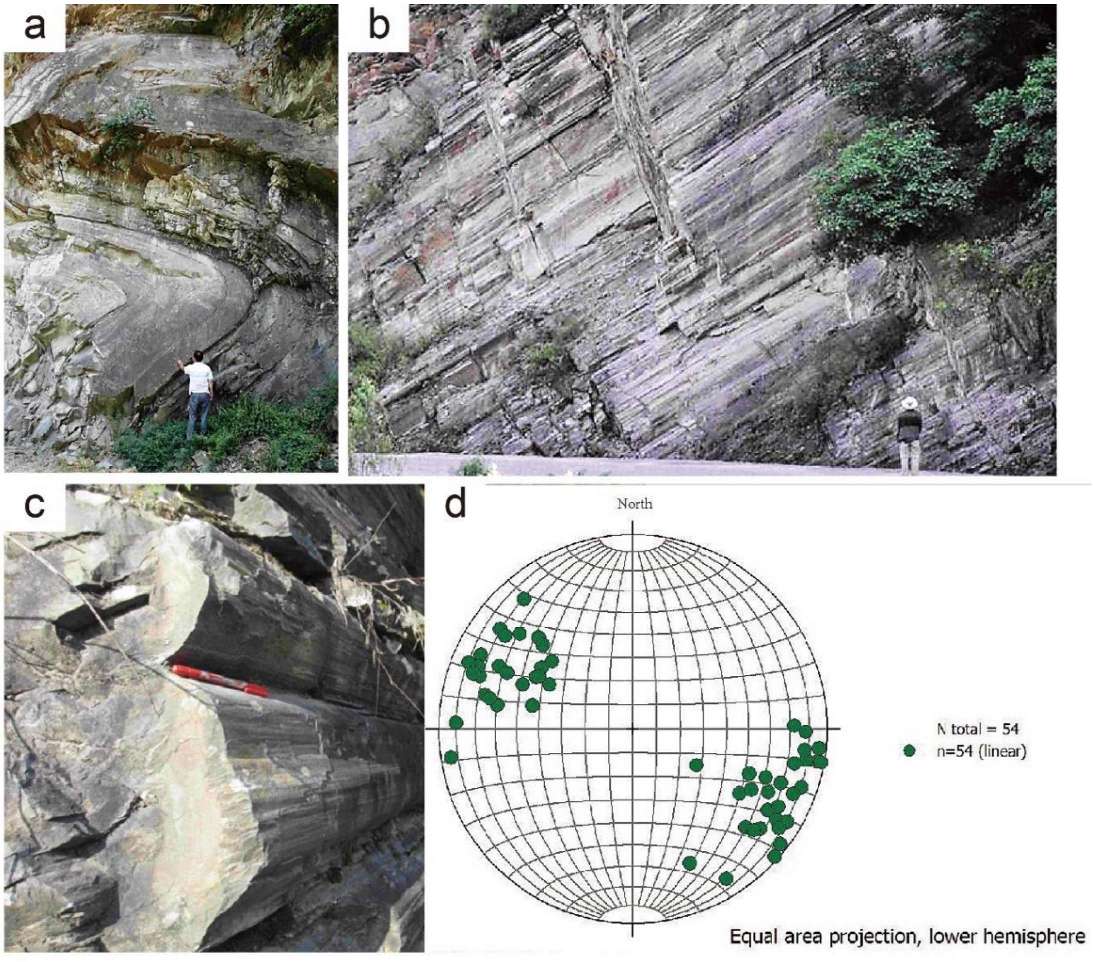

Figure 3.12 Photos showing D2 deformation in the Liuling Group. The lower-hemisphere projection of the recumbent fold hinge lines and L-tectonites (Shi, 2016).

3.3 Theoretical modeling

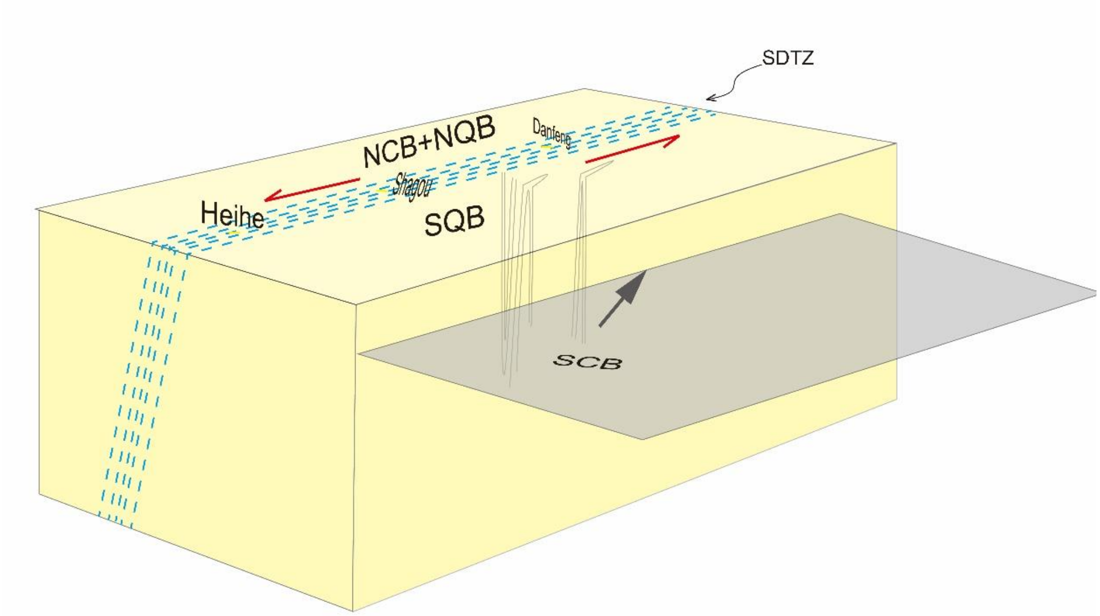

Figure 3.13 A conceptual block diagram (not to scale) to illustrate the following idea: the sinistral strike-slip deformation is concentrated in a weak domain along the SDTZ, together with the F_1 Folding in the Liuling Group, resulting from the oblique convergence between the SCB and the NCB.

If D_2 deformation in Liuling group is removed, the fabric data in the Heihe area, fabrics in high-strain zones and the D_1 fabrics in the Liuling Group can be summarized into a conceptual block diagram (Fig.3.13). We think that this set of fabrics (sinistral shearing along the SDTZ and F_1 Folding) was mainly produced by the oblique convergence between the SCB and the NCB in the Triassic. The detailed discussion on the deformation time is in the next section. As the Shangdan suture was developed during Paleozoic, the high strain zone along the SDTZ was an existing weak zone during the Triassic.

The theoretical modeling is used to test the above idea. The tectonic-scale boundary condition is an oblique convergence with the convergence angle α

(Fig.3.14a). The SDTZ is considered as a weak Eshelby inclusion in the transpressional zone and the Liuling group is the matrix that is near the inclusion (Fig.3.14c). Different far-field tectonic boundary conditions (i.e., α) are tested, and simulated fabrics are compared with the measured results to further constrain the tectonic boundary condition.

The 'SGLDEF' MATLAB program in Chapter 2 is used to model the deformation inside the inclusion and in the bulk matrix.

3.3.1 Numerical model setup

The tectonic boundary condition is constrained by plate motions. Here, we consider an oblique convergence between the SCB and the NCB. The convergence angle is, and a monoclinic transpressional deformation is modeled (Fig.3.14a). The velocity gradient tensor is

$$\mathbf{L} = \begin{bmatrix} 0 & -\cos\alpha & 0 \\ 0 & -\sin\alpha & 0 \\ 0 & 0 & \sin\alpha \end{bmatrix} \varepsilon_v$$

where α is the convergence angle and ε_v is the average deformation rate of the zone. Since we consider the fabric is the final product of the progressive deformation and the absolute rate will not affect the final product, the average deformation rate ε_v is simply set to 1. The time increment for computation is $\delta t = 0.01$ to ensure that every step of the computation corresponds to an infinitesimal increment of deformation.

The SDTZ is a deformation concentration zone and modeled as a weak Eshelby inclusion (Fig.3.14c). The shape of the zone is represented by an ellipsoid. Three semi-axes of the ellipsoid are set to 50:5:1. The longest axis represents the length of the zone, the mediate axis represents the depth of the zone, and the shortest axis is the width of the zone. The longest axis of the ellipsoid or the strike of the zone is parallel to the tectonic boundary. As the Shangdan suture was produced by the northward subduction of the Shangdan oceanic plate under the NQB (Dong and Santosh, 2016), before the deformation in the Triassic, the weak zone was dipping to the north, and the dip angle is β. According to current subduction zones, β is tested from 90° to 50° (Zoback et al., 1987; Davey et al., 1995; Norris and Cooper, 2000).

All materials considered in the model are assumed to be power-law viscous with stress exponent equals to 3. The choices of the viscosity of the materials are rather arbitrary based on an incomplete understanding of rheological contrasts in rocks (e.g., Treagus, 2002; Czeck et al., 2009). The relative effective viscosity of the high-strain zone is set to 0.1 defined at the macroscale strain-rate state to represent a weak domain.

To estimate the foliation and lineations inside the high-strain zone and in the matrix, we assume that the high-strain zone is a homogeneous domain and so as the matrix. We use the position gradient tensor, $\mathbf{F}$, to represent the deformation of a continuous body (Jiang, 2010). For the bulk deformation, $\mathbf{F}(t)=\exp(\mathbf{L}t)$, where t is the deformation time (Eq.35 in Jiang, 2010). For the deformation inside the high-strain zone where the deformation is not steady, $\mathbf{F}$ is updated after every step. Principal stretch axes can be calculated from $\mathbf{F}$ (Truesdell, 1991). The maximum principal stretch axis represents stretching lineations, and the minimum principal stretch axis represents poles to the foliations (Lin et al., 1998; Jiang and Williams, 1998).

$STEPS = 300$ is taken for all simulations to illustrate the evolution of lineations and foliations inside the high-strain zone and in the bulk matrix.

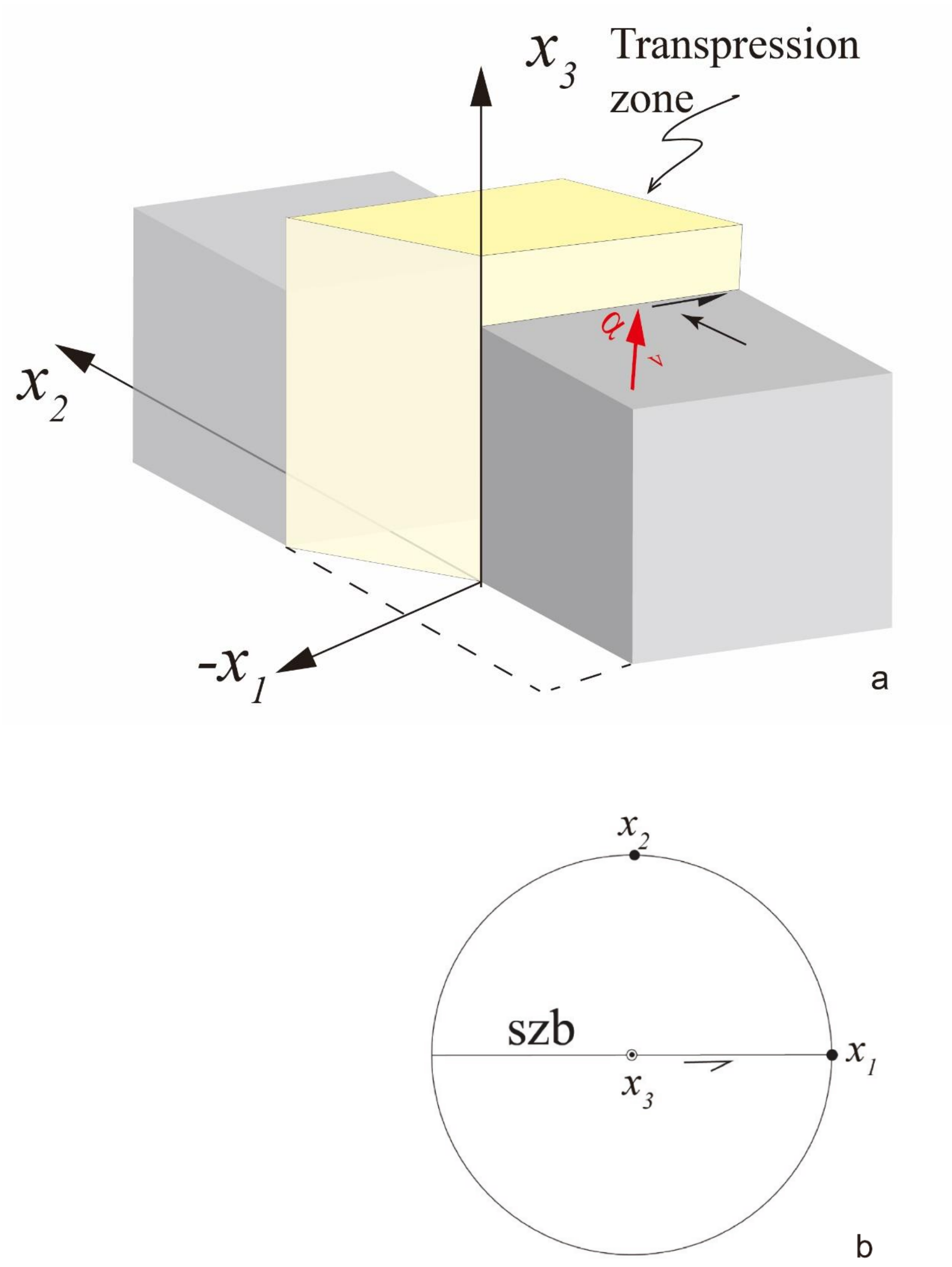

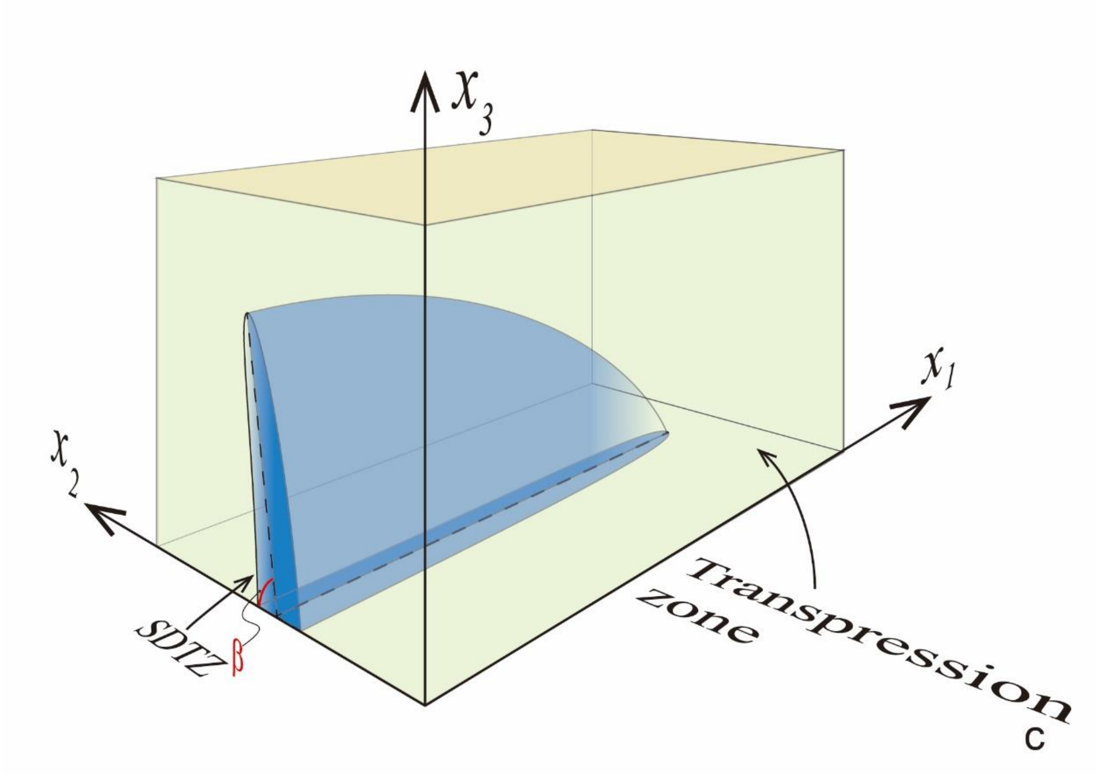

Figure 3.14 Numerical modeling diagram. (a). Transpression model for the macroscale deformation of the SDTZ. As the boundary condition is produced by the plate motion and the SDTZ is far from the plate margin, the deformation resulted from the oblique convergence with a convergence angle α in the transpression zone is monoclinic. Therefore, in the modeling, a vertical instead of an inclined transpression zone is considered, and different convergence angles (α) are simulated. (b). The coordinate system for the equal-area projections of the simulation results. (c). The SDTZ is modeled as an Eshelby ellipsoid inside the transpression zone. Different initial dip angles (β) of the SDTZ are tested.

3.3.2 Modeling results

We systematically test different α and β, and output the evolution of foliation and lineation inside the high-strain zone and in the bulk matrix. The comparison between the simulation results and the field measurements is used to constrain the tectonic-scale deformation boundary conditions. The evolution of the orientations of stretching lineations (the maximum strain axis is interpreted as the stretching lineation) inside the high-strain zone (dark blue) and in the bulk matrix (light blue) for different convergence angle and dip angles are presented in Fig.3.15. The evolution of the transposition foliation (the minimum strain axis is interpreted as the pole to the transposition foliation) is plotted in Fig.3.16.

All results in Fig.3.16 represents the evolution of the foliations inside the high-strain zone and in the bulk matrix. The transposition foliations show similar patterns, and hence the transposition foliations are not sensitive to the change of convergence angles and dip angles. This is consistent with single-scale kinematic transpression models (e.g., Jiang and Williams, 1998; Jiang, 2007) and the multiscale model that considers fabric elements to define the transposition foliation (Jiang, 2014). The transposition foliations in the bulk matrix and in the high-strain zone tend to rotate to the transpressional deformation zone boundary, and the transposition foliation in the high-strain zone rotates faster. This phenomenon may because that there is more simple-shearing component partitioned in the high-strain zone (Xiang and Jiang, 2013) and the strains accumulated faster in the high-strain zone than in the bulk matrix. For different dip angles especially for small convergence angles, the intersection angle between the transposition foliation inside the high-strain zone and the transposition foliation in the bulk matrix is slightly different, but this difference is too small to be observed in the field.

The evolution of lineations is extremely sensitive to the change of the dip angles and convergence angles.

In simple shearing flow or flow with a small convergence angle ($\alpha = 0° \, or \, 10°$), the evolution of the lineation inside the high-strain zone and in the bulk matrix is along the strike of the foliations. This is consistent with single-scale kinematic transpression models (e.g., Jiang and Williams, 1998).

For vertical weak domains ($\beta = 90°$), the lineation inside the zone is numb to the change of the convergence angle: for $\alpha = 0° \sim 50°$, the lineation in the vertical weak zones is invariably horizontal.

For intermediate and slightly large convergence angles ($\alpha = 20° \sim 50°$), the dip of the weak domain plays a key role to affect the evolution of the lineation inside the domain. For steeply dipping domains ($\beta = 70° \sim 80°$) under intermediate convergence angles ($\alpha = 20° \sim 40°$), although the bulk lineations are down-dip, lineations inside the weak domain are still horizontal or sub-horizontal, while for gently dipping domains ($\beta = 50° \sim 60°$), the lineations are oblique. In the case of $\alpha = 50°$ and $\beta = 50°$, the lineation inside the weak domain is close to the lineation in the bulk matrix. It seems that the decrease of the dip angle and the increase of the convergence angle show the similar effects on the development of the lineation inside the weak domain. They both tend to produce steep lineations inside the weak domain.

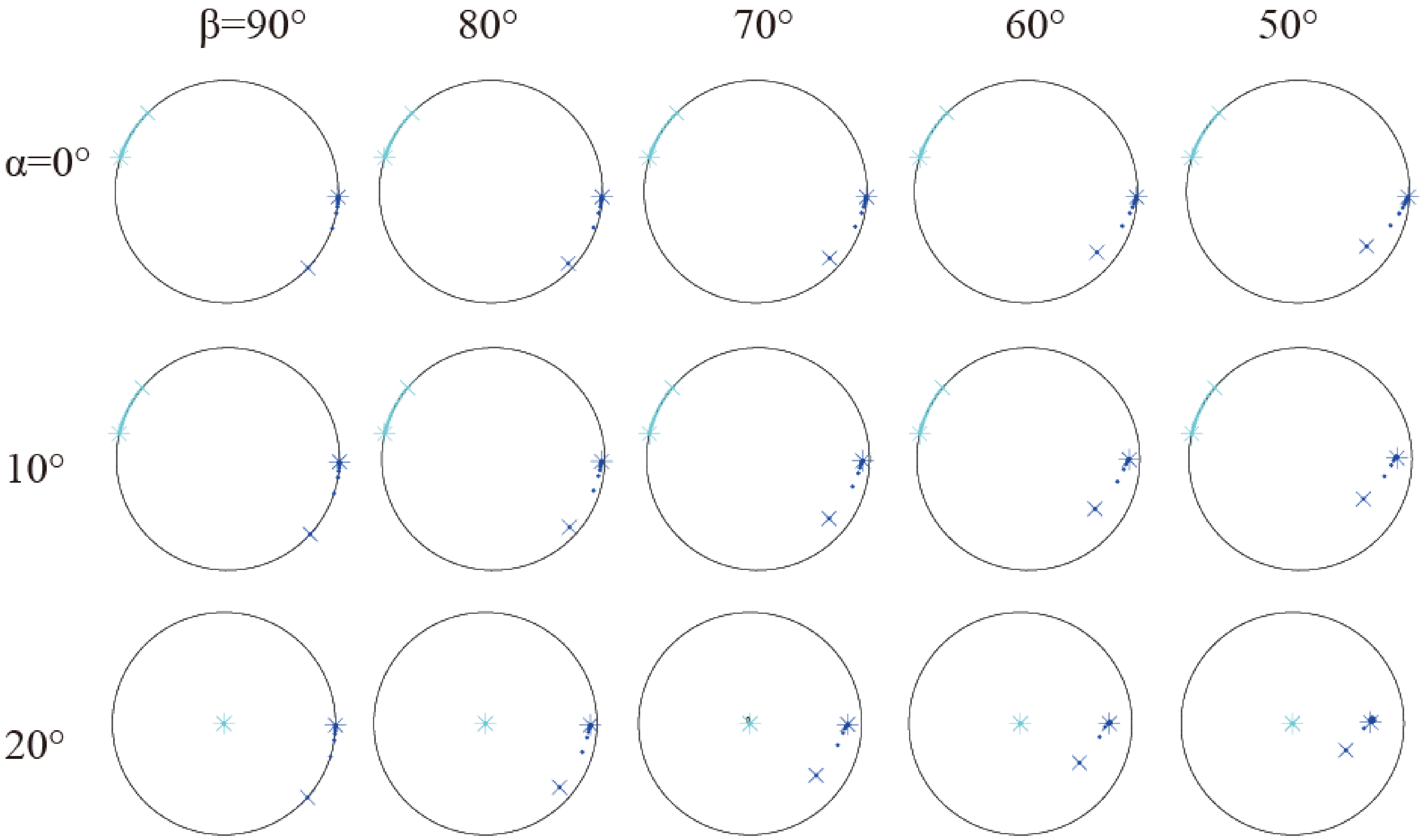
β=90°
80°
70°
60°
50°
α=0°
10°
20°

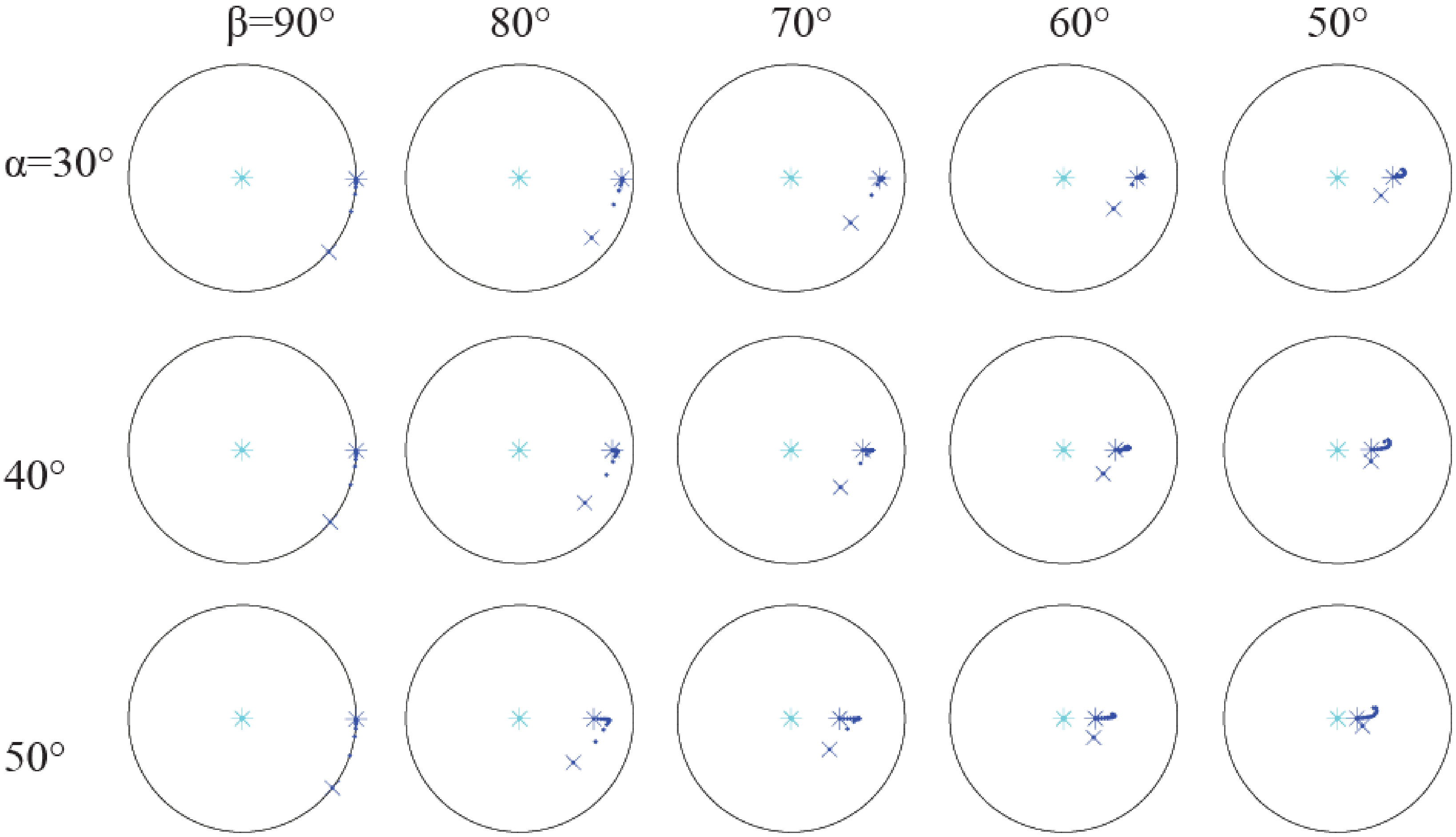
β=90°
80°
70°
60°
50°
α=30°
40°
50°

Figure 3.15 Simulation results of lineations for different convergence angles (α) and dip angles (β). The projection is $x_3 - positive$ hemisphere equal-area projection. Light blue dots are the evolution of the lineation in the bulk matrix, and dark blue dots are the evolution of the lineation in the high-strain zone. 'x' is the starting dot, and '*' is the end dot.

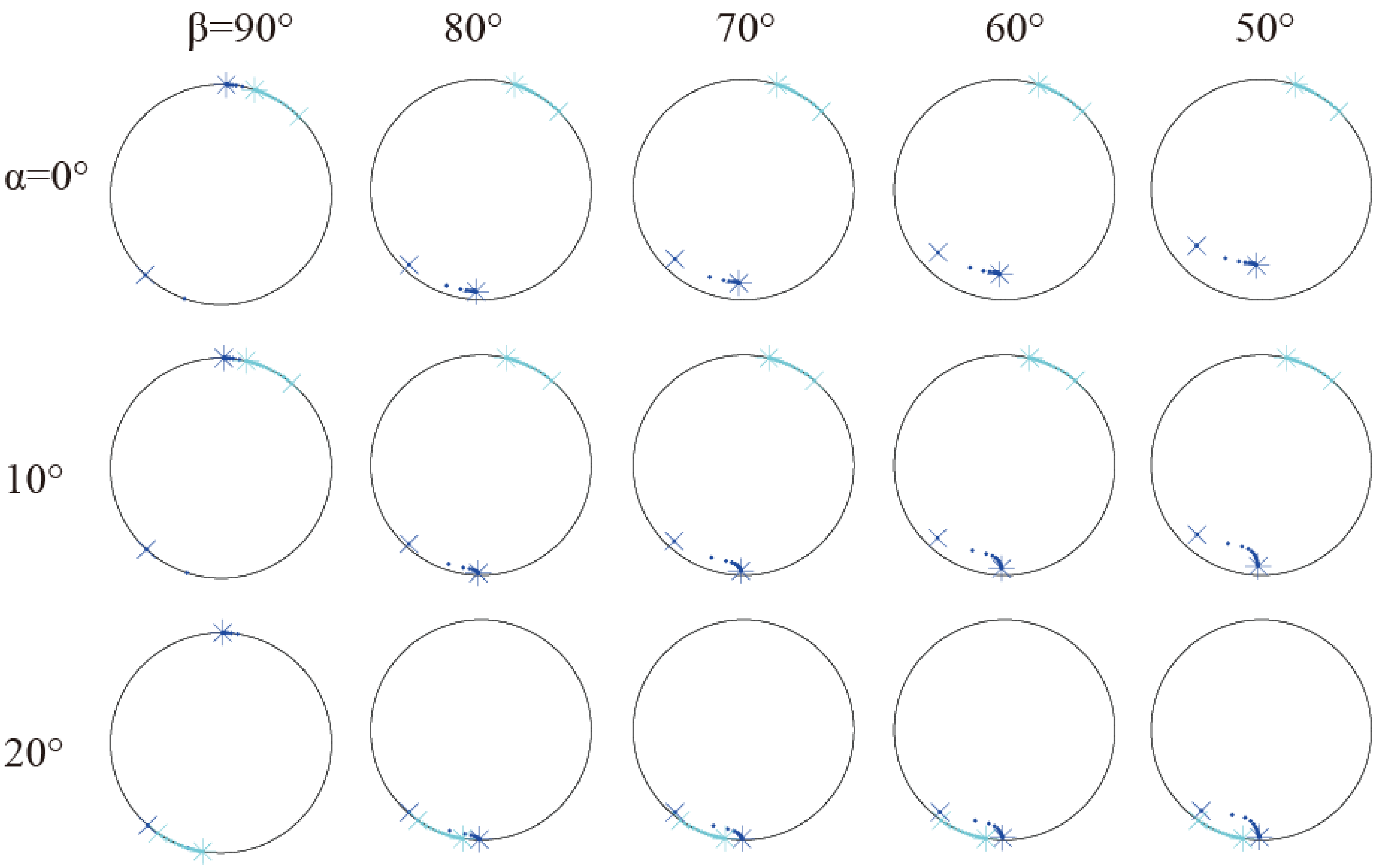
β=90°
80°
70°
60°
50°
α=0°
10°
20°

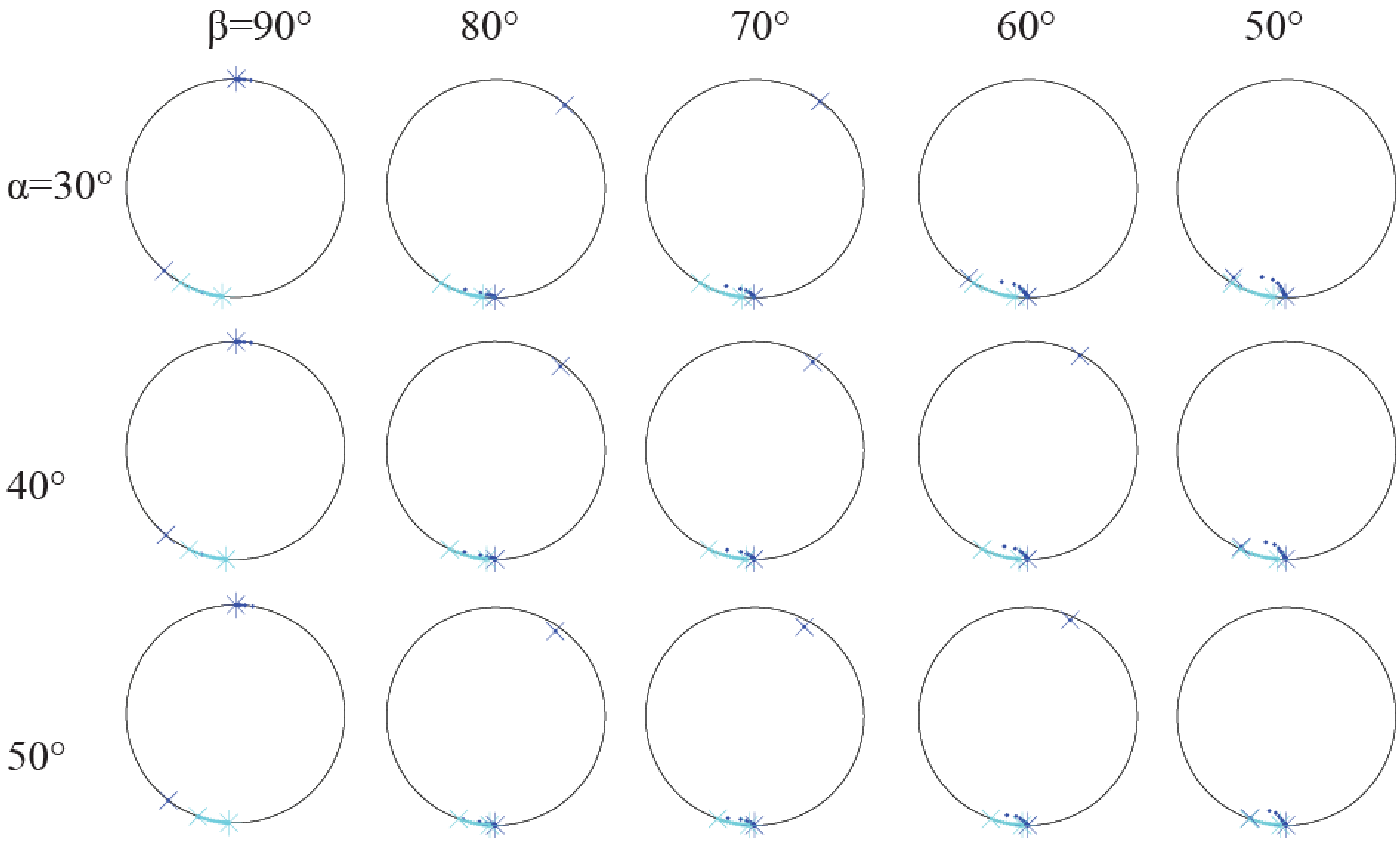

Figure 3.16 Simulation results of poles to foliations for different convergence angles (α) and dip angles (β).

3.3.3 Comparison of the simulation results with the field data

The field data that are rotated to the model coordinate system are shown in Fig.3.17. The fabrics are characterized by the lineations along the strike of the foliations in the SDTZ and the lineations oblique to the strike of the foliations in the nearby Liuling Group (Fig.3.17).

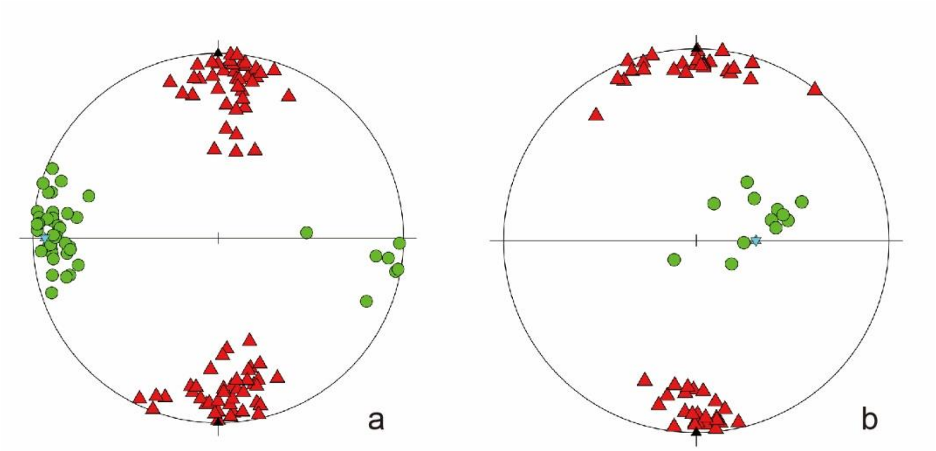

Figure 3.17 Field lineations and transposition foliations rotated to the model coordinate system. (a) Fabric data in high-strain zones. (b) Fabric data in the Liuling Group. The blue stars are the average of the lineations, and the black great circles are the average of the foliations.

Because the Liuling Group is neighboring to the SDTZ, the D_1 fabrics in the Liuling Group were influenced by the far-field tectonic oblique convergence as well as the existence of the SDTZ. The fabrics in the Liuling Group cannot be directly used to compare with the predicted fabrics in the bulk matrix, but they can be used to constrain the initial dip angle of the SDTZ. As for $\beta = 90°$, fabrics inside the weak domain are independent of the convergence angle and consistently show horizontal lineations, together with the monoclinic tectonic boundary conditions, so the symmetry of the entire system is monoclinic, and the exterior fields of the weak domain should produce monoclinic fabrics. However, the lineations in the Liuling Group are oblique on the foliation (Fig.3.17) which should result from a triclinic flow (Lin et al., 1998; Jiang and Williams, 1998). Therefore, the initial SDTZ is not vertical. If the initial dip angle of the SDTZ is relatively shallow ($\beta = 50^\circ \sim 60^\circ$), the convergence angle is constrained to $\alpha = 20^\circ \sim 30^\circ$ to produce horizontal lineations inside the SDTZ. If the initial dip angle of the SDTZ is steep ($\beta = 70^\circ \sim 80^\circ$), the convergence angle could be $\alpha = 20^\circ \sim 40^\circ$. To further extrapolate the convergence angle, the simulation of the exterior fields of the SDTZ is needed. The predicted fabrics in the exterior fields can be used to compare with the fabrics in the Liuling Group to constrain the convergence angle range.

3.4 Deformation time of the SDTZ

3.4.1 The dominant strike-slip deformation along the SDTZ and D_1 deformation in the Liuling Group

Recently, Li et al. (2017) have done some detailed work in the Shagou shear zone (the grey square in Fig.3.1b). After comparing the foliation, lineation and kinematic indicators in Li et al. (2017), we think that the deformation shown in the Shagou shear zone is same as the deformation in the Heihe area and in high-strain zones in the Danfeng area (Fig.3.13). Therefore, the deformation time of the Shagou shear zone should be the same as the deformation of the SDTZ.

In the Shagou area, LA-ICP-MS zircon U-Pb analyses of the granitic mylonites in the Shagou shear zone have been done in Li et al. (2017). The measured $^{206}Pb/^{238}U$ ages of the metamorphic zircon rims are concordant and yielded a weighted mean age of 210.3±1.5 Ma (MSWD=0.13), and zircons with clearly visible oscillatory zoning yield a mean $^{206}Pb/^{238}U$ age of 220.8±1.3 Ma (MSWD=0.19) representing the age for the protolith of the granitic mylonite (Sample MD01 in Li et al.,2017). Li et al.(2017) dated a syntectonic granitic vein (SG02 in Li et al., 2017), and the crystallization age 200.7±1.3 Ma represents the forming time of this syntectonic granitic vein. They (Li et al., 2017) proposed that the transpressional deformation in Shagou area was last from ca.221Ma to 201Ma.

Therefore, we think that the dominant strike-slip deformation along the SDTZ and D_1 deformation in the Liuling Group occurred during 221Ma~201Ma (the late Triassic).

Besides the support of geochronology data in Li et al. (2017), D_1 deformation in the Liuling Group can be related to the collision between the SQB and N-SCB (late Triassic) due to their similar structural geometries. Shortening structures, such as isoclinal folds and transposition foliation, are produced by D_1 deformation in the Liuling Group. Additionally, similar structures including tight folds, foliations, and faults, have been documented in various locations in the SQB (Mattauer et al., 1985; Xu et al., 1986; Dong et al., 2011a, 2016). The sketched cross-section (Fig.1b in Dong et al., 2016) generally illustrates shortening structures across the SQB, and the trending of the fold-thrust structures is parallel to the orogenic belt. According to previous studies, these tight fold-thrust structures were produced by the collision between the SQB and the SCB. Therefore, D_1 deformation in the Liuling Group resulted from the collision of the SQB and the N-SCB.

The Shangdan suture is a Paleozoic suture and very likely to be deformed since the Paleozoic. However, we propose that the dominant strike-slip deformation recorded in the SDTZ was mainly produced during the late Triassic. Because as an existent weak zone in the late Triassic, under a transpressional boundary condition, the SDTZ was easy to accommodate the strike-slip deformation component, and thus we can observe the dominant strike-slip deformation along the SDTZ. The shortening deformation has been preserved in the Liuling Group and the SQB.

3.4.2 D_2 deformation in the Liuling Group

D_2 deformation in the Liuling Group is characterized by the recumbent folds and the L-tectonite and can be produced by an orogen-parallel extension. An orogenic scale L-tectonite has been reported in the Tongbai orogenic belt (Liu et al., 2017). L-tectonite in the Taibaiding region of Tongbai mountain is defined by well-developed mineral lineation with weakly developed foliation. The trend of this mineral lineation is parallel to the orogenic belt with a sub-horizontally plunging angle (1° to 20°). The orientation is similar to the L-tectonite and the recumbent fold hinge lines (Fig.3.12) produced by D_2 deformation in the Liuling Group. Both fabrics can be interpreted as an orogen-parallel extension that is developed by the crustal thinning. In addition, the Tongbai-Dabie orogenic belt associated with the QOB is considered as the Central China Orogenic Belt (Fig.3.1a). The location of the L-tectonite in Tongbai can be lined up with the D_2 deformation in the Liuling Group paralleled with the extension direction of the orogenic belt where the Nanyang Basin cut across. Hence, the extensional deformation occurred in the Liuling Group was produced at the same time with the L-tectonite recorded in the Tongbai mountain. According to Liu et al. (2017), the extensional deformation event occurred during the intra-continental orogeny from 140 to 135Ma based on geochronological data.

Therefore, D_2 deformation in the Liuling Group could be placed into the Early Cretaceous extensional event.

3.5 Summary

The deformations along the SDTZ and the Liuling Group were mainly caused by the collision of the SCB and the SQB in the late Triassic.

According to the numerical modeling results, the collision is obliquely convergent, and the convergence angle is in the range of $\alpha = 20^\circ \sim 40^\circ$.

D_2 deformation in the Liuling Group can be related to the L-tectonites in the Tongbai mountain and indicates extensional tectonism in the early Cretaceous.

3.6 References

Chen, W., 2014. The Development of L-tectonites in High-strain Zone Settings: A Multiscale Modeling Investigation. (Master thesis http://ir.lib.uwo.ca/etd/2307/).

Cui, Z.L., Sun, Y., Wang, X.R., 1995. Discovery of radiolarias from the Danfeng ophiolite zone, North Qinling, and their geologic significance. Chin. Sci. Bull. 40, 1686–1688 (in Chinese).

Czeck, D.M., Fissler, D.A., Horsman, E. and Tikoff, B., 2009. Strain analysis and rheology contrasts in polymictic conglomerates: an example from the Seine metaconglomerates, Superior Province, Canada. Journal of Structural Geology, 31(11), pp.1365-1376.

Davey, F.J., Henyey, T., Kleffmann, S., Melhuish, A., Okaya, D., Stern, T.A., Woodward, D.J. and Transect, S.I.G., 1995. Crustal reflections from the Alpine Fault zone, South Island, New Zealand.

Ding, S.P., Pei, X.Z., Li, Y., Hu, B., Zhao, X., Guo, J.F., 2004. Analysis of the disintegration and tectonic setting of the “Liziyuan group” in the Tianshui area, western Qinling. Geol. Bull. China 23 (12), 1209–1214 (in Chinese).

Dong, Y. and Santosh, M., 2016. Tectonic architecture and multiple orogeny of the Qinling Orogenic Belt, Central China. Gondwana Research, 29(1), pp.1-40.

Dong, Y., Zhang, G., Neubauer, F., Liu, X., Genser, J. and Hauzenberger, C., 2011a. Tectonic evolution of the Qinling orogen, China: review and synthesis. Journal of Asian Earth Sciences, 41(3), pp.213-237.

Dong, Y., Zhang, G., Hauzenberger, C., Neubauer, F., Yang, Z. and Liu, X., 2011b. Palaeozoic tectonics and evolutionary history of the Qinling orogen: evidence from geochemistry and geochronology of ophiolite and related volcanic rocks. Lithos, 122(1), pp.39-56.

Dong, Y., Liu, X., Neubauer, F., Zhang, G., Tao, N., Zhang, Y., Zhang, X. and Li, W., 2013. Timing of Paleozoic amalgamation between the North China and South China Blocks: evidence from detrital zircon U–Pb ages. Tectonophysics, 586, pp.173-191.

Dong, Y., Yang, Z., Liu, X., Sun, S., Li, W., Cheng, B., Zhang, F., Zhang, X., He, D. and Zhang, G., 2016. Mesozoic intracontinental orogeny in the Qinling Mountains, central China. Gondwana Research, 30, pp.144-158.

Freeman, B. and Lisle, R.J., 1987. The relationship between tectonic strain and the three-dimensional shape fabrics of pebbles in deformed conglomerates. Journal of the Geological Society, 144(4), pp.635-639.

Giorgis, S. and Tikoff, B., 2004. Constraints on kinematics and strain from feldspar porphyroclast populations. Geological Society, London, Special Publications, 224(1), pp.265-285.

Jiang, D., 2007. Sustainable transpression: an examination of strain and kinematics in deforming zones with migrating boundaries. Journal of Structural Geology, 29(12), pp.1984-2005.

Jiang, D., 2010. Flow and finite deformation of surface elements in three dimensional homogeneous progressive deformations. Tectonophysics, 487(1-4), pp.85-99.

Jiang, D., 2013. The motion of deformable ellipsoids in power-law viscous materials: Formulation and numerical implementation of a micromechanical approach applicable to flow partitioning and heterogeneous deformation in Earth’s lithosphere. Journal of Structural Geology 50, 22-34.

Jiang, D., 2014. Structural geology meets micromechanics: a self-consistent model for the multiscale deformation and fabric development in Earth’s ductile lithosphere. Journal of Structural Geology 68, 247-272.

Jiang, D. and Bentley, C., 2012. A micromechanical approach for simulating multiscale fabrics in large-scale high-strain zones: Theory and application. Journal of Geophysical Research: Solid Earth, 117(B12).

Jiang, D. and Williams, P.F., 1998. High-strain zones: a unified model. Journal of Structural Geology, 20(8), pp.1105-1120.

Li, Y., Liang, W., Zhang, G., Jiang, D. and Wang, J., 2017. Tectonic setting of the Late Triassic magmatism in the Qinling Orogen: New constraints from the interplay between granite emplacement and shear zone deformation in the Shagou area. Geological Journal, 52(S1), pp.250-271.

Lin, S., Jiang, D. and Williams, P.F., 1998. Transpression (or transtension) zones of triclinic symmetry: natural example and theoretical modeling. Geological Society, London, Special Publications, 135(1), pp.41-57.

Lisle, R.J., 1979. Strain analysis using deformed pebbles: the influence of initial pebble shape. Tectonophysics, 60(3-4), pp.263-277.

Lister, G.S. and Williams, P.F., 1983. The partitioning of deformation in flowing rock masses. Tectonophysics, 92(1-3), pp.1-33.

Liu, L., Liao, X., Wang, Y., Wang, C., Santosh, M., Yang, M., Zhang, C. and Chen, D., 2016. Early Paleozoic tectonic evolution of the North Qinling Orogenic Belt in Central China: Insights on continental deep subduction and multiphase exhumation. Earth-Science Reviews, 159, pp.58-81.

Liu, H., Lin, S., Song, C. and Wu, M., 2017. Structure and geochronology of the Tongbai complex and their implications for the evolution of the Tongbai orogenic belt, central China. International Geology Review, 59(4), pp.470-483.

Mattauer, M., Matte, P., Malavieille, J., Tapponnier, P., Maluski, H., Qin, X.Z., Lun, L.Y. and Qin, T.Y., 1985. Tectonics of the Qinling belt: build-up and evolution of eastern Asia. Nature, 317(6037), pp.496-500.

Meng, Q.R., Xue, F. and Zhang, G.W., 1994. Conglomerate Sedimentation and its Tectonic Implication, Heihe Area Within Shangdan Zone of the Qinling [J]. Acta Sedimentologica Sinica, 3.

Meng, Q.R., Yu, Z. and Mei, Z., 1997. Sedimentation and Development of the forearc basin at southern margin of North Qinling. Scientia Geologica Sinica, 32(2), pp.136-145.

Norris, R.J. and Cooper, A.F., 2001. Late Quaternary slip rates and slip partitioning on the Alpine Fault, New Zealand. Journal of Structural Geology, 23(2-3), pp.507-520.

Pei, X.Z. (Ed.), 1997. Composition and Tectonic Evolution of the Shangdan Structural Zone in the East Qinling, China. Cartographic Publishing House, Xi'an, pp. 1–184 (in Chinese with English abstract).

Ramsay, J., 1967. Folding and fracturing of rocks. McGraw-Hill, New York.

Reischmann, T., Altenberger, U., Kröner, A., Zhang, G., Sun, Y. and Yu, Z., 1990. Mechanism and time of deformation and metamorphism of mylonitic orthogneisses from the Shagou shear zone, Qinling Belt, China. Tectonophysics, 185(1), pp.91-109.

Robin, P.Y.F., 2002. Determination of fabric and strain ellipsoids from measured sectional ellipses—theory. Journal of Structural Geology, 24(3), pp.531-544.

Shi, J., 2016. An Investigation of Multi-Generation Folds in Liuling Group south of the Shangdan Suture Zone in the Qinling Belt (Master thesis https://ir.lib.uwo.ca/etd/4169/).

Treagus, S.H., 2002. Modeling the bulk viscosity of two-phase mixtures in terms of clast shape. Journal of Structural Geology, 24(1), 57-76.

Truesdell, C.A., 1991. 2nd edition. A first course in rational continuum mechanics, vol. 1. Academic Press, Inc, Boston.

Wang, T., Pei, X.Z., Wang, X.X., Hu, N.G., Li, W.P. and Zhang, G.W., 2005. Orogen-parallel westward oblique uplift of the Qinling basement complex in the core of the Qinling orogen (China): an example of oblique extrusion of deep-seated metamorphic rocks in a collisional orogen. The Journal of Geology, 113(2), pp.181-200.

Wu, Y.B. and Zheng, Y.F., 2013. Tectonic evolution of a composite collision orogen: an overview on the Qinling–Tongbai–Hong'an–Dabie–Sulu orogenic belt in central China. Gondwana Research, 23(4), pp.1402-1428.

Xiang, B. and Jiang, D., 2013. Small-scale ductile shear zones as transposed rheologically weak domains: A numerical modeling investigation and practical application. Journal of Structural Geology, 54, pp.184-198.

Xu, Z., Lu, Y., Tang, Y., Mattauer, M., Matte, P., Malavieille, J., Tapponnier, P. and Maluski, H., 1986. The deformation and tectonic evolution of the east Qinling orogenic belt. Acta Geologica Sinica, 60(3), pp.237-247.

Yan, Z., Fu, C., Wang, Z., Yan, Q., Chen, L. and Chen, J., 2016. Late Paleozoic subduction–accretion along the southern margin of the North Qinling terrane, central China: evidence from zircon U-Pb dating and geochemistry of the Wuguan Complex. Gondwana Research, 30, pp.97-111.

Yu, Z.P. and Meng, Q.R., 1995. Late Paleozoic sedimentary and tectonic evolution of the Shangdan suture zone, eastern Qinling, China. Journal of Southeast Asian Earth Sciences, 11(3), pp.237-242.

Zhang, G.W., Yu, Z.P., Sun, Y., Cheng, S. Y., Li, T.H., Xue, F. and Zhang, C.L., 1989. The major suture zone of the Qinling orogenic belt. Journal of Southeast Asian Earth Sciences, 3(1-4), pp.63-76.

Zhang, G., Meng, Q. and Lai, S., 1995. Tectonics and structure of Qinling orogenic belt. Science in China (Scienctia Sinica) Series B, 11(38), pp.1379-1394.

Zhang, G.W., Zhang, B.R., Yuan, X.C. and Xiao, Q.H., 2001. Qinling orogenic belt and continental dynamics. Sci. Press, Beijing, pp.1-806 (in Chinese).

Zoback, M.D., Zoback, M.L., Mount, V.S., Suppe, J., Eaton, J.P., Healy, J.H., Oppenheimer, D., Reasenberg, P., Jones, L., Raleigh, C.B. and Wong, I.G., 1987. New evidence on the state of stress of the San Andreas fault system. Science, 238(4830), pp.1105-1111.

Chapter 4: Deformation and Tectonic Implications of the Xinyang-Yuanlong Shear Zone in Western Qinling

4.1 Introduction

The Qinling orogenic belt (QOB) is the boundary between the North China block (NCB) and the South China block (SCB) and produced by the collision of the NCB and the SCB (Zhang et al., 2001). The Shangdan suture zone is a Paleozoic suture and marked by the discontinuously exposed Danfeng Complex that consists of ophiolitic mélange (Dong and Santosh, 2016). The Shangdan suture separates the QOB into the north Qinling belt (NQB) and the south Qinling belt (SQB). The QOB is divided into western Qinling and eastern Qinling (Fig.4.1) (Zhang et al., 2001). In eastern Qinling, the Shangdan tectonic zone (SDTZ) is clearly marked by the Danfeng Complex and its adjacent areas. However, as the tectonic units in western Qinling are not as clear as them in eastern Qinling and most areas are covered by the Quaternary, the questions of how the SDTZ extends to the west and what geometric features and the corresponding kinematics along the SDTZ in western Qinling are still unclear.

The Xinyang-Yuanlong shear zone is a ductile shear zone that has been recognized during a regional geological mapping project in 2004. The whole zone extends from WNW to ESE about 80 km, and the width of the shear zone can reach 2-3km. Most parts of the shear zone are not well exposed (Ding et al., 2009). However, the Xingyang-Yuanlong shear zone is considered to separate the western Qinling orogenic belt and the Qilian orogen, and it is argued to be the west extension of the

SDTZ. Before the year of 2000, previous studies generally combined the Qilian orogen and north Qinling orogen in this area and considered them as a unitary tectonic belt (Zhang et al., 1994). After the year of 2000, a lot of geochemical and petrological studies were conducted in this area, and these studies provided a basic framework of this area (Ding et al., 2004; Dong et al., 2007b; Pei et al., 2007a,b), and suggested that the Shangdan suture locates at the purple areas in Fig.4.1c. However, the kinematics of the shear zone, the deformation of the shear zone and how the deformation related to the deformation of the SDTZ in the QOB are still unclear. In addition, as the boundary of the QOB and the Qilian orogen, the Xinyang-Yuanlong shear zone locates at a key area to investigate the relationship among different tectonic units (i.e., Qilian orogen, QOB, and NCB) in central China.

We conduct detailed structural analysis and geochronological studies in this zone and try to identify the geometric features, the deformation time, and the kinematics of the zone.

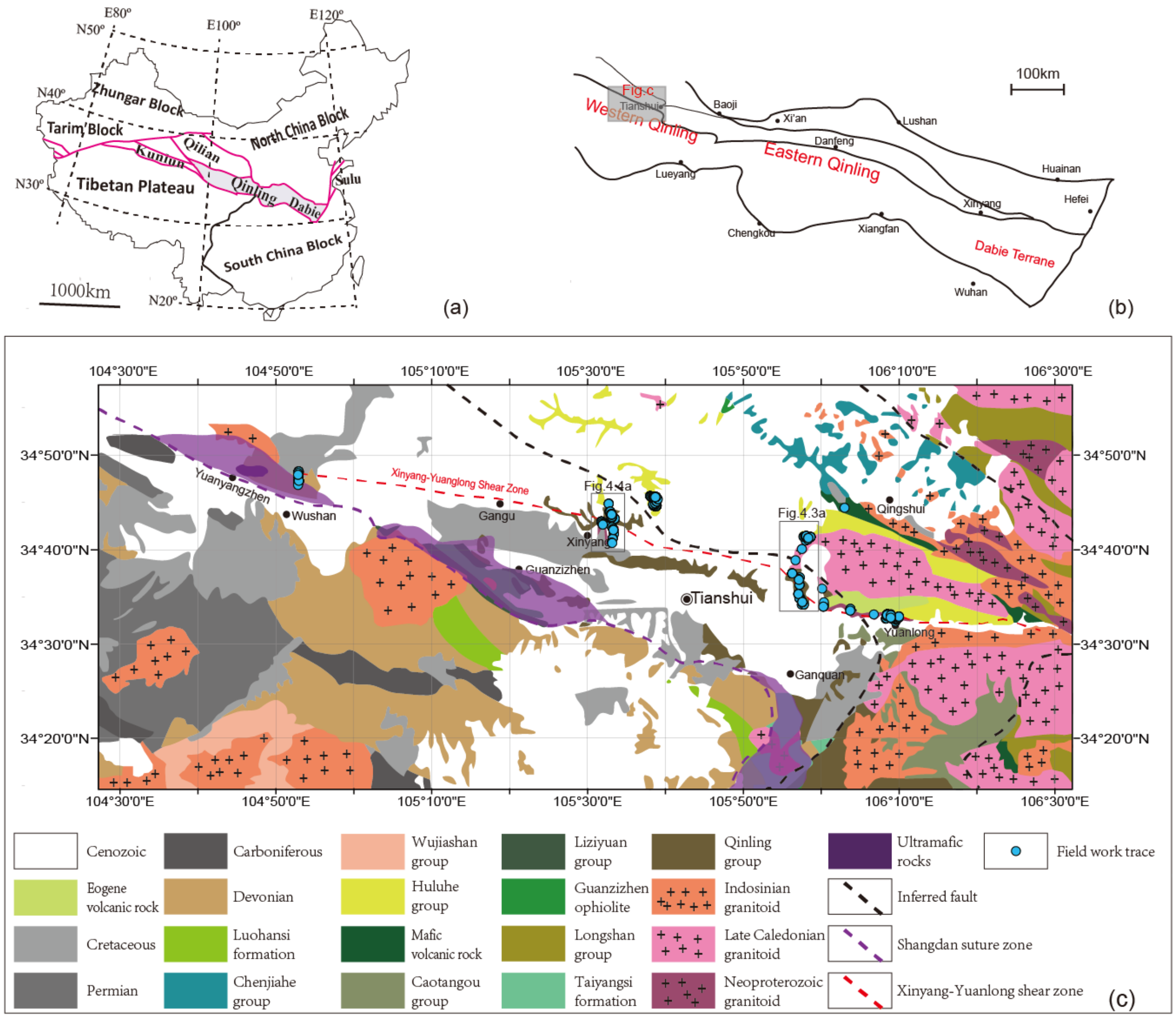

Figure 4.1 Maps showing the field work area. (a) The location of the Qinling orogenic belt in China. (b) Simplified tectonic map of the Qinling orogenic belt. (c) Detailed geological map of the field work area in western Qinling (Modified from Liang et al., 2017; Pei et al.2009; Lu, 2008; Dong et al., 2007).

4.2 Field data

4.2.1 Geological setting

The Xinyang-Yuanlong shear zone is the boundary between the QOB and Qilian orogen. The geological units, involved in the shear zone, are the Qinling Complex belonging to the QOB and the Huluhe Group belonging to the Qilian orogen.

Qinling Complex

The Qinling Complex is the main part of the NQB. The Qinling Complex is predominantly made of highly deformed and metamorphosed Precambrian basements and represents the North Qinling terrane (NQT). It was proposed that the NQT was originally the southern part of the NCB and separated from the NCB during the spreading the Proterozoic Kuanping back-arc basin (Zhang and Zhang, 1995; Dong et al., 2008) or the Paleozoic Erlangping back-arc basin (Zhang et al., 1994; Zhang et al., 1995; Meng and Zhang, 1999; Zhang et al., 2001; Dong et al., 2011a,b). However, the geochemical features and metamorphic events recorded in the NQT (Zhang et al., 1996; Zhu, 2001) are different from that are recorded in the NCB (Zhao and Zhai, 2013; Zhai, 2014; Yang and Santosh, 2015) suggesting that the NQT can be regarded as a micro-continent that is independent of the NCB (Dong and Santosh, 2016). Therefore, the tectonic affinity of the NQT is still in dispute.

The metamorphic ages from the Qinling Complex are in the range of 1.2~0.9Ga (Dong and Santosh, 2016 and references therein). The Qinling Complex consists of gneisses, schists, amphibolites, marble and calc-silicate rocks (You et al., 1991). Previous studies (You et al., 1991; Zhang et al., 1994, 1995, 2001) suggested that the sedimentary protoliths in the complex were deposited during the Paleoproterozoic. Recent studies proposed that the Qinling Complex was mainly formed during late Mesoproterozoic to early Neoproterozoic (Yang et al., 2003; Lu et al., 2009; Yang et al., 2010; Diwu et al., 2014) or during early Neoproterozoic (Shi et al., 2009; Wan et al., 2011). In addition, early Neoproterozoic granitoids (979–911 Ma) (e.g. Dehe, Zhaigen, and Niujiaoshan granitic plutons; Lu et al., 2003; Chen et al., 2004; Zhang et al., 2004; Wang et al., 2013) and Paleozoic granitoids (ca.500, 450, and 420–400 Ma; Wang et al., 2009; Wang et al., 2013; Zhang et al., 2013) have been found in this complex.

Huluhe Group

The Huluhe Group locates at the southeastern margin of the Qilian orogen and north to the Wei River. The Huluhe Group mainly contains meta-sedimentary rocks and has been further divided into two formations. The lower formation mainly distributes in the Houchuan-Zhengchuan county and the Qingshui county and includes grey to dark grey schists and meta-quartz sandstones. This unit is highly deformed and experienced a higher metamorphic grade compared with the upper formation, and the metamorphic facies can reach lower-amphibolite metamorphic facies. The primary depositional layering can barely be observed in this unit. The upper formation is in the Zhengchuan-Yangjiasi area extending east to the Qingshui county. The upper formation contains purple-grey to dark grey biotite quartz schists, phyllites, pelites, and the protolith is clastic rocks including sandstone and greywacke. The schistosity is developed, but some primary depositional layering is preserved. According to the youngest detrital zircons age group in the Huluhe Group and the crystallization age of a granitoid dyke that was intruded into the Huluhe Group (Pei et al.,2012), the depositional time of the Huluhe Group is constrained to ca.447-434Ma and the depositional sources include the Qilian orogen, the northern margin of the western QOB, and the basement of the NCB.

4.2.2 Structural geometric features

Field work has been carried out into four areas throughout the Xinyang-Yuanlong shear zone. From east to west, they are Yuanlong, Shetang, Xinyang, and Wushan (Fig.4.1c). Outcrop-scale structures and fabrics are identified and measured in the four areas. For some complicated area (i.e., Xinyang), the detailed structural mapping is conducted.

4.2.2.1 The Yuanlong area

In the Yuanlong area, the shear zone is developed in granitic and felsic gneisses. In addition, there are some mafic dykes and granitoid pegmatitic dykes intruded in the deformed rocks and parallel to the foliations, but there is no deformation-related fabric inside the dykes (Figs.4.2a,b). Fig4.2c shows the lower-hemisphere equal-area projection of transposition foliations and mineral lineations throughout this area. The overall average foliation is steeply dipping and strikes WNW-ESE, and the corresponding lineations trend to SE plunging 9°~50° (white-filled dots, Fig.4.2c,d). Well-developed shear-sense indicators can be observed on the sections that are subparallel to the lineations and perpendicular to the foliations (Figs.4.2f-j) showing a dextral sense of shear.

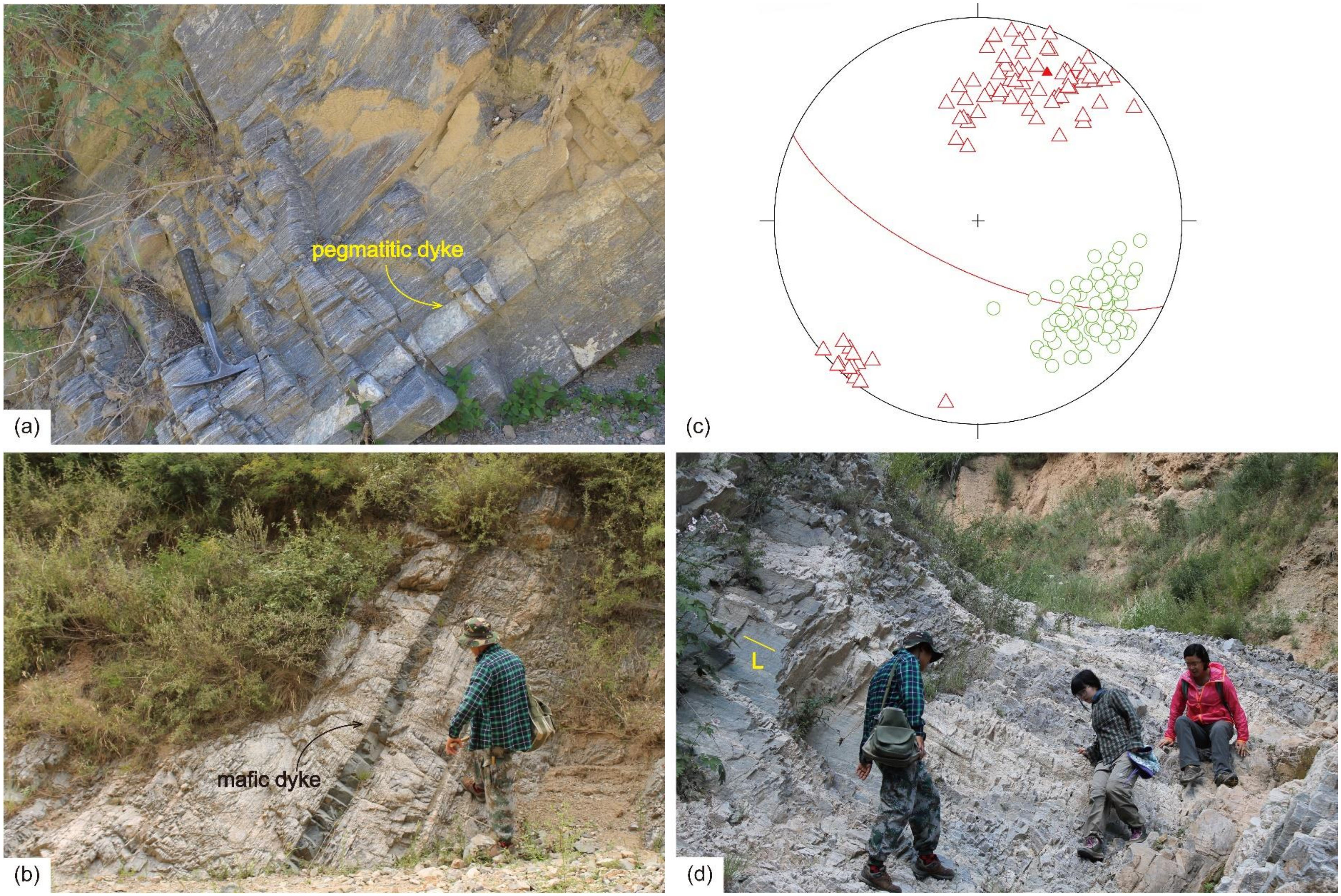
(a)
pegmatitic dyke
(c)
(b)
mafic dyke
(d)
L

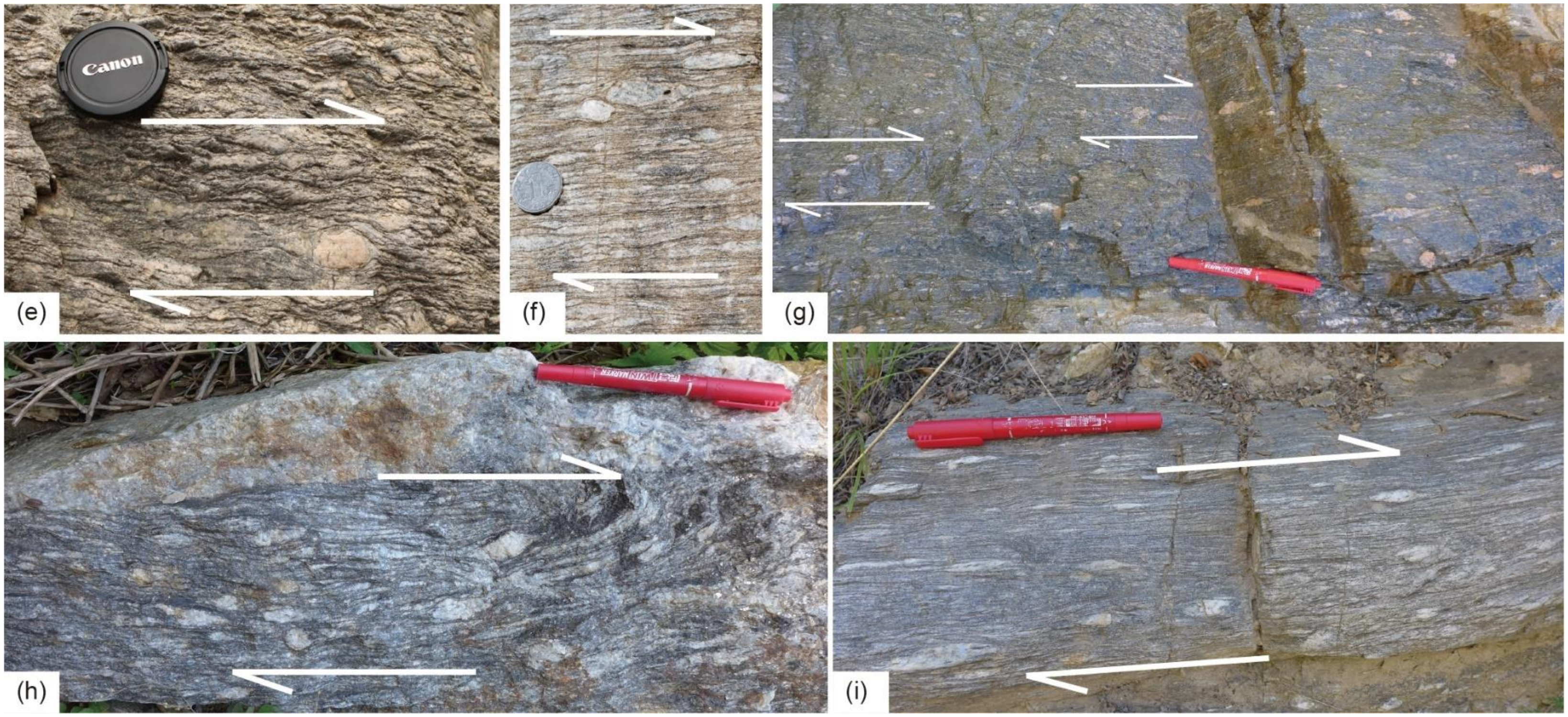

Figure 4.2 Photos and fabric data from the Yuanlong area. Pictures to show granitic pegmatitic dyke and mafic dyke (a,b), mineral lineations (d) and shear-sense indicators (e-i) in the Yuanlong are; (c) is the equal-area lower-hemisphere projection of the transposition foliations and mineral lineations in the Yuanlong area: triangles are the poles to the foliations and dots represent the lineations. Shear-sense indicators are all observed on sub-horizontal surfaces, and the sub-vertical sections do not show good shear-sense indicators.

4.2.2.2 The Shetang area

In the Shetang area, the shear zone is developed in granitic gneiss, meta-pelites, and calc-silicates from the Qinling Complex (Fig.4.3a). There are some mafic dykes that intruded into the calc-silicates, and the mafic dykes are parallel to the transposition foliations in the calc-silicates (Fig.4.3d). To the north of the highly deformed rocks, there is a granitoid pluton and no deformation-related fabric in the granitoids (Fig.4.3a). To the north of the pluton, the Huluhe Group is well exposed (Figs.4.3e-g). The foliation in this area is defined by schistosity, and the highly deformed quartz veins can be observed along the layers (Figs.4.3f,g). Fig.4.3c and Fig.4.3b are the equal-area projections of transposition foliations and stretching lineations from the Qinling Complex, and schistosity and mineral lineations from the Huluhe Group, respectively.

The foliation and lineation data in Fig.4.3c are divided into two groups: In the 1st group, the foliations (blue great circles) are shallowly dipping to the SE and SW (dip angles ~20°-30°), and the corresponding lineations (blue-filled dots) are oblique to the strike of the foliations (pitch ~10°-70°); In the 2nd group, the foliations steeply strike WNW-ESE with lineations (green circles) along the strike or oblique to the strike. The dashed-line area in the Qinling Complex in Fig.4.3a contains meta-pelites and calc-silicate with the fabrics in the 2nd group. The rest of the Qinling Complex in the Shetang area is mainly composed of granitic gneiss. Schistosity in the Huluhe group (Fig.4.3b) is shallowly dipping to NE with lineations oblique on foliations.

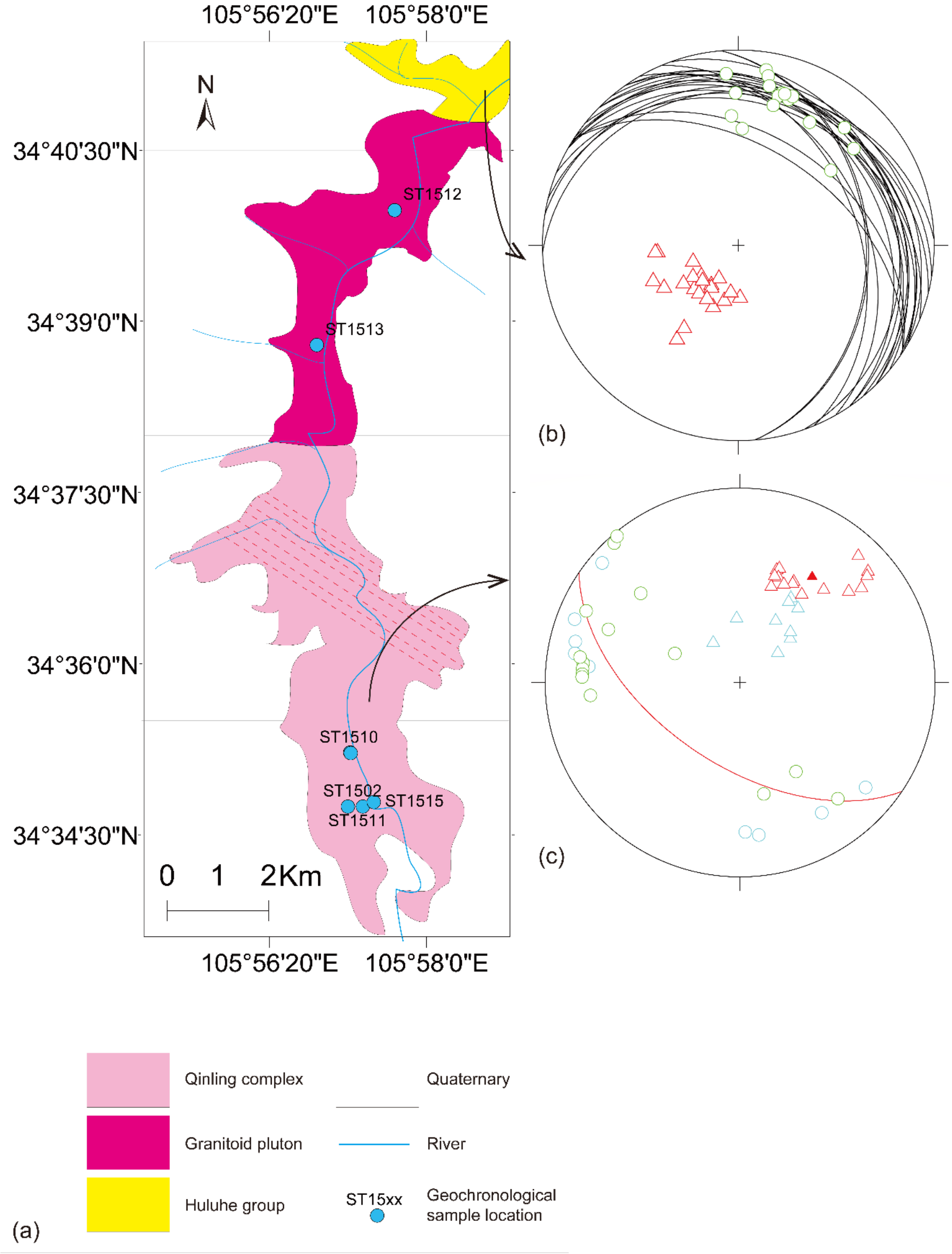
105°56'20"E
105°58'0"E
N
34°40'30"N
34°39'0"N
34°37'30"N
34°36'0"N
34°34'30"N
ST1512
ST1513
ST1510
ST1502
ST1515
ST1511
0 1 2Km
(b)
(c)
Qinling complex
Granitoid pluton
Huluhe group
Quaternary
River
ST15xx
Geochronological sample location
(a)

Figure 4.3 Geological map, photos and fabric data from the Shetang area. (a) A detailed map of the Shetang area. (b) and (c) are lower-hemisphere equal-area projections of the schistosity & mineral lineations in the Huluhe Group and transposition foliations & stretching lineations in the Qinling Complex, respectively. Triangles are the poles to the foliations and dots represent the lineations. (d) The picture to show the mafic dykes southern part of the Shetang area. The country rocks are highly deformed calc-silicates, and the dykes are parallel to the transposition foliations. The scale of the picture is a stone wall at the bottom of the picture, and its height is ~1.5m. (e-g) are the deformed Huluhe Group in the northern edge of (a). The scale of (e) is the height (~0.5m) of the white stakes on the road.

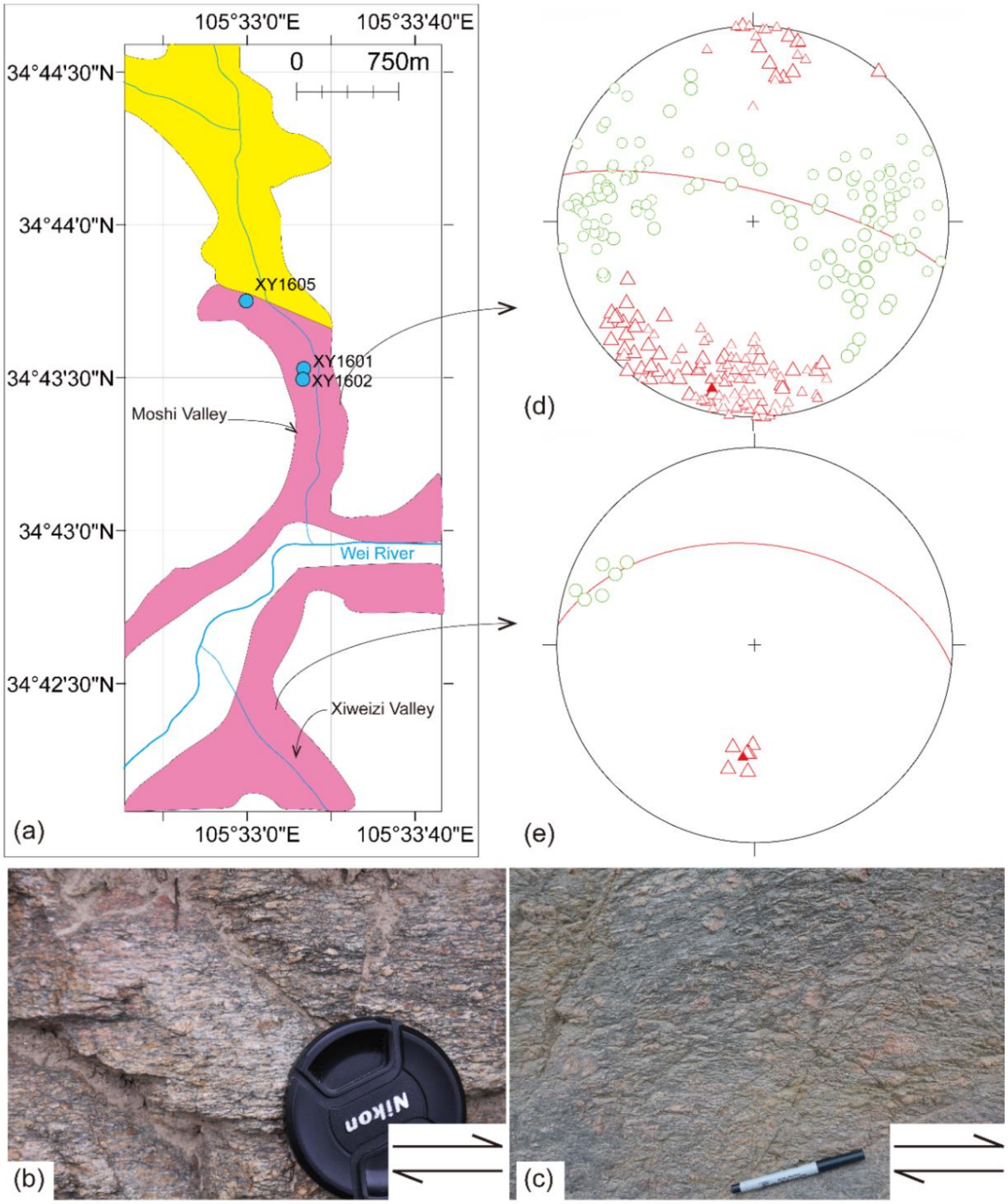

Figure 4.4 Geological map, photos and fabric data from the Xinyang area. (a) A geological map to show the Moshi valley and Xiweizi valley in the Xinyang area. (b,c) Shear-sense indicators on sub-horizontal surfaces in the Xiweizi valley to show a dextral sense of shear. (d,e) The equal-area lower-hemisphere projections of the transposition foliations and mineral lineations in the Moshi valley and Xiweizi valley, respectively: triangles are the poles to the foliations and dots represent the lineations.

4.2.2.3 The Xinyang area

In the Xinyang area, the deformed rocks are separated by the Wei River (Fig.4.4a). To the south of the river (the Xiweizi Valley), the deformed rocks are granitic gneiss where rotated clasts and trails are observed on sub-horizontal planes indicating a dextral sense of shear (Figs.4.4b,c). The transposition foliation steeply strikes E-W and mineral lineations gently plunge to WSW (Fig.4.4e).

To the north of the river, deformed rocks are more heterogeneous, consisting of meta-pelite, calc-silicate, marble, metamorphosed diabase and meta-basalt. Meta-sedimentary units are mostly deformed with well-developed transposition foliations and stretching lineations. Generally, the diabase has no recognizable fabrics, and the meta-basalt has a weak lineation and foliation. The equal-area lower-hemisphere projections of foliations and lineations in the Moshi Valley are shown in Fig.4.4d. The foliations strike WNW-ESE steeply dipping, and lineations form a broad girdle along the average transposition foliation. As we think that the variation of the lineation is due to the heterogeneity of the deformed rocks, a detailed structural mapping in this area is carried out, and we try to divide rocks into different units and map the fabrics in each unit (Figs.4.5-4.8).

The whole Moshi Valley is divided into 22 units according to the lithology and structural variations (Fig.4.5a). The metamorphosed diabase and meta-basalt units are labeled by green numbers (e.g., units 2, 4, 6), and the black numbers represent meta-sedimentary rock units (e.g., units 1, 3, 5). There are three units that contain various structures and lithologies, and a more detailed mapping of each unit is conducted (i.e., units 12, 14, 20).

The metamorphosed diabase units generally show no deformation-related fabrics inside the units (Fig.4.5b). For example, Fig.4.5b shows the boundary between unit 4 and unit 5. The left side in Fig.4.5b is unit 4, and it is a metamorphized diabase. Except for some fractures, there is no fabric inside the diabase (i.e., transposition foliations or mineral lineations), but the whole unit strikes NW-SE. The right side in Fig.4.5b is unit 5, and it contains calc-silicates and meta-pelites. The foliations and lineations are well-developed inside unit 5. The meta-sedimentary units are generally highly transposed (Figs.4.5b,c).The shear-sense indicators can be observed on sub-horizontal sections and consistently show a dextral sense of shear (Figs.4.5e-h). As in units 12, 14 and 20, the mafic dykes are too small to be mapped on Fig.4.5a, and the structures are more complicated than structures in other units, we conduct more detailed mappings in these three units.

Fig.4.6a is the detailed mapping of unit 12. Fig.4.6c shows that a deformed meta-basalt (sub-unit 12-4) was boudinaged and the country rocks are calc-silicates. Some isoclinal folds can be observed in unit 12 (Fig.4.6d), and they are intra-folia and should be developed during the formation of the transposition foliation. Fig.4.6b (12-14) represents a projection of the isoclinal fold axial plane and hinge line (orange dot and great circle), and the orientation is similar to the transposition foliation and mineral lineations in the unit. Sub-unit 12-15 is a mafic rock unit. It contains undeformed mafic rocks and highly transposed rocks (Fig.4.6e). The highly transposed rocks contain massive quartz veins, and the quartz veins are transposed (right side of Fig.4.6e).

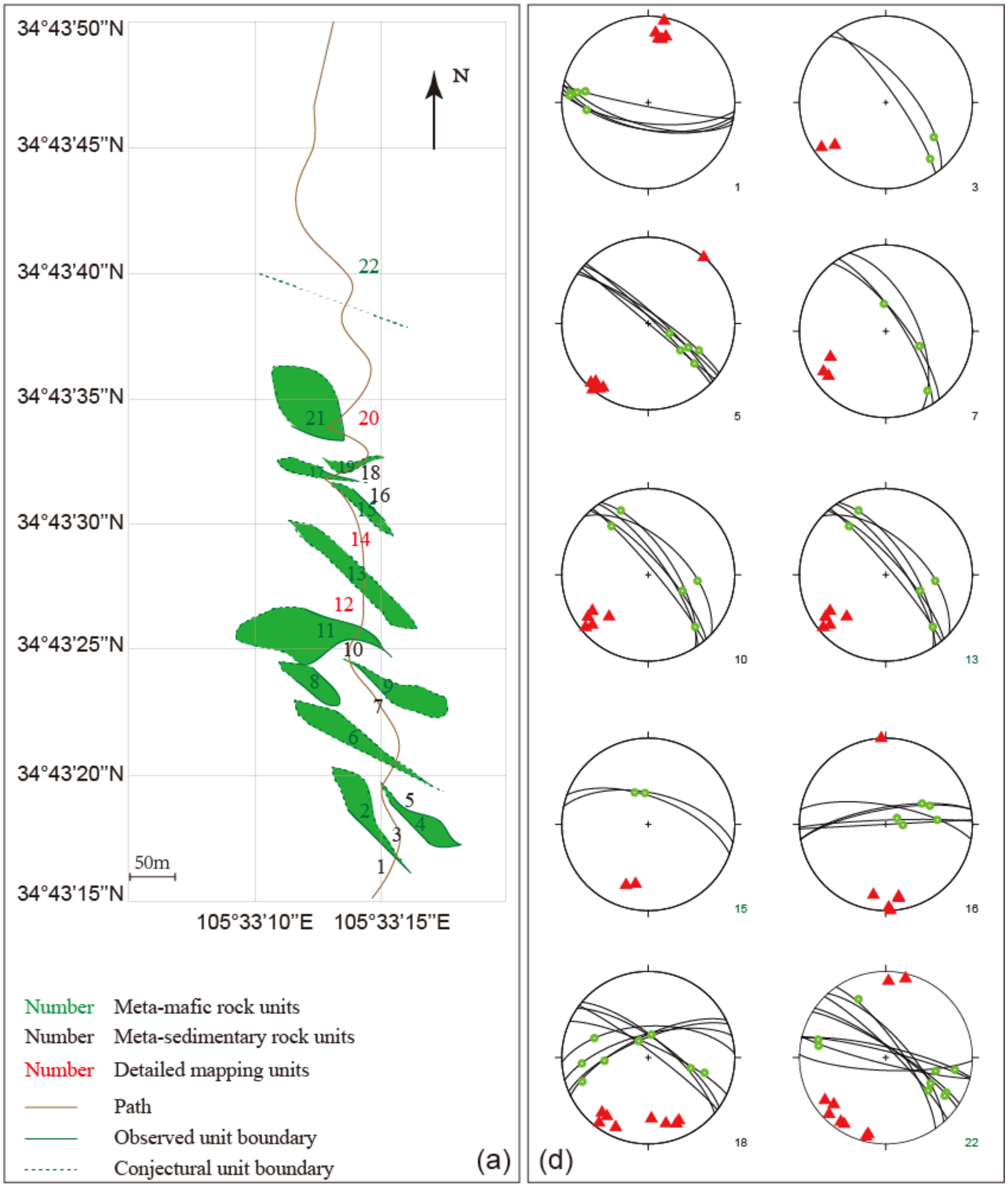

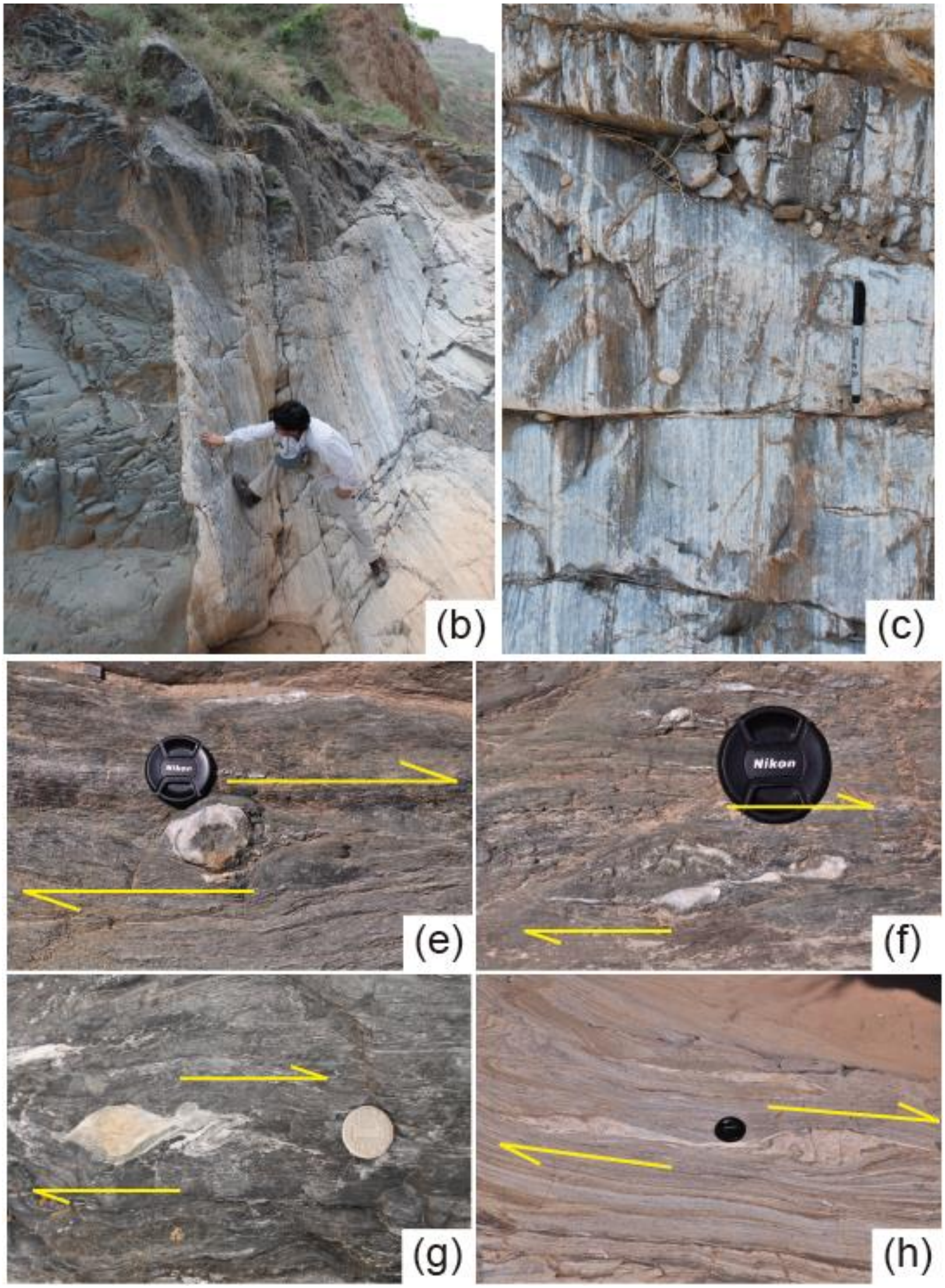

Figure 4.5 Detailed mapping and photos from the Moshi valley. (a) Detailed mapping of the Moshi valley. (b) A photo to show the boundary between unit 4 (left side) and unit 5 (right side): unit 5 is highly deformed, but unit 4 has no internal fabrics. (c) A photo to show the highly transposed calc-silicates in unit 1

(sub-horizontal surface). (d) Transposition foliations and mineral lineations of each unit (note that the mafic rock units generally do not show fabrics except for units 13, 15, 22). (e-f) Photos to show shear-sense indicators on sub-horizontal surfaces. They consistently show a dextral sense of shear.

Fig.4.7a is the detailed mapping of unit 14. Intra-folia folds are widespread in unit 14. There are two generations of intra-folia folds (F_{1a} and F_{1b}). In some outcrops, we can observe the overprinting relationships (Figs.4.7c-f) between F_{1a} and F_{1b}, and thus we can distinguish between F_{1a} and F_{1b}. In most cases, we cannot distinguish between them (Fig.4.7g), so the intra-folia folds are labeled as $F_{1a/b}$.

Fig.4.8a is the detailed mapping of unit 20. In this unit, F_1 folds are widely distributed (Figs.4.8c-i). In addition, F_2 folds can be observed (Figs.4.8i-l). The transposition foliations that were developed during $F_{1a/b}$ are folded. However, F_2 folds are only observed in this unit, and the orientations of their fold axial planes are close to the transposition foliation (S_t) and the axial planes of F_1. Additionally, asymmetric F_2 folds consistently show a dextral sense of shear. Thus, we think that F_2 folds were developed during the later deformation process but not another deformation event.

Well exposed Huluhe Group is northeast of the Xinyang mapping area (Fig.4.1c). Schistosity is well-developed in meta-pelite and meta-sandstone. There is no lineation on schistosity, but the abundant rootless folds of quartz veins are in the deformed rocks (Figs.4.9a-d) indicating that this rock unit is highly deformed. The hinge line of the intra-folia folds and the schistosity are plotted on lower-hemisphere equal-area projection (Fig.4.9e).

Unit12

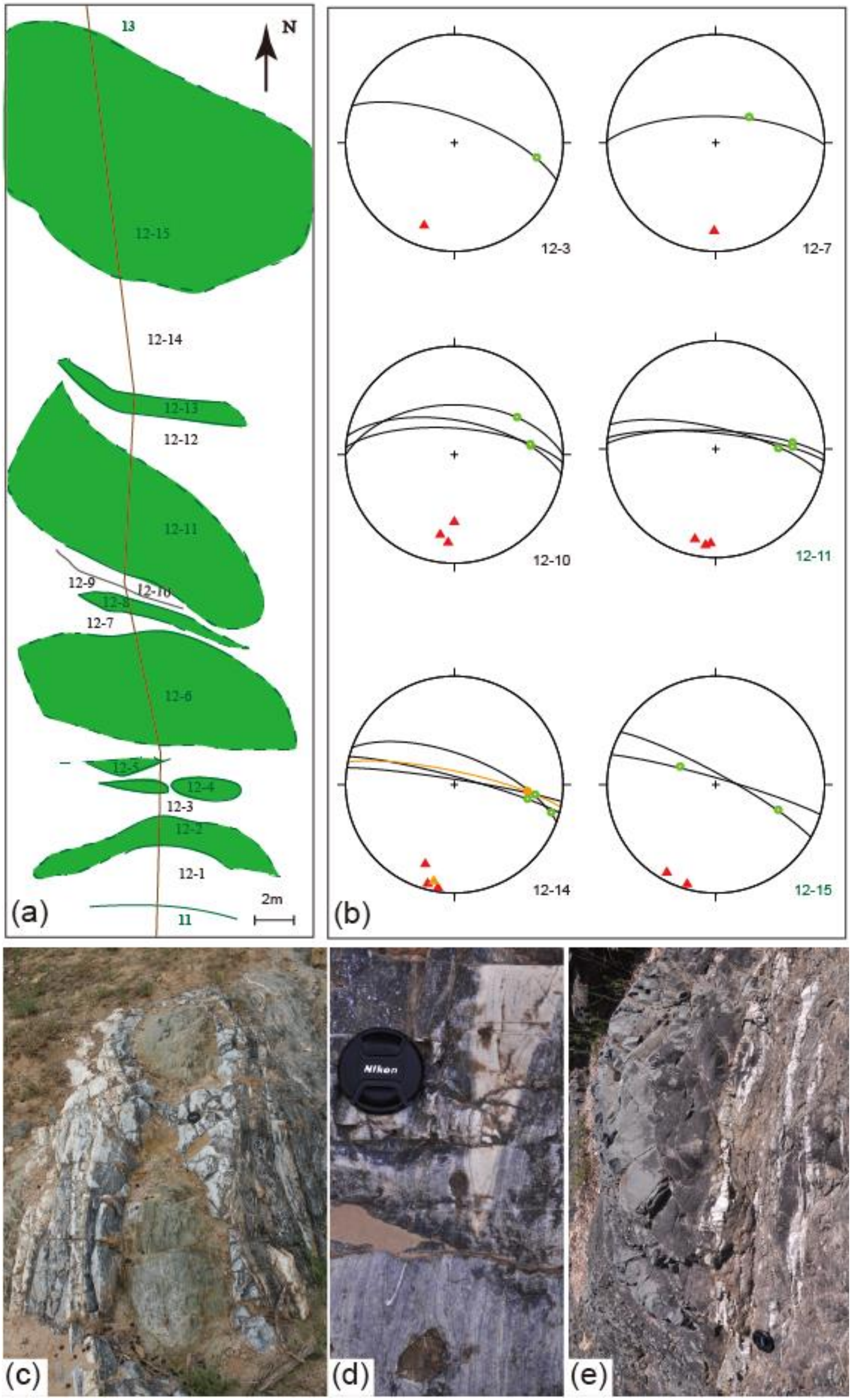
13
N
12-15
12-14
12-13
12-12
12-11
12-9
12-10
12-8
12-7
12-6
12-5
12-4
12-3
12-2
12-1
2m
11
(a)
12-3
12-7
12-10
12-11
12-14
12-15
(b)
(c)
Nikon
(d)
(e)

Figure 4.6 Detailed mapping and photos from unit 12. (a) A more detailed mapping of unit 12. (b) Transposition foliations (red triangles and black great circles) and mineral lineations (green dots) of each sub-unit (note that sub-unit 12-14 contains a plot of fold hinge line (orange dot) and axial plane (orange triangle and great circle)). (c) A photo (sub-unit 12-4) to show the bondinaged meta-basalt. The boudins are meta-basalts, and country rocks are calc-silicates. Both meta-basalts and calc-silicates show well-developed foliations. (d) A photo to show the parasitic folds in sub-unit 12-14. (e) A photo (sub-unit 12-15) to show undeformed diabase and highly transposed mafic rocks (note that there are voluminous quartz veins in the deformed rocks).

Unit14

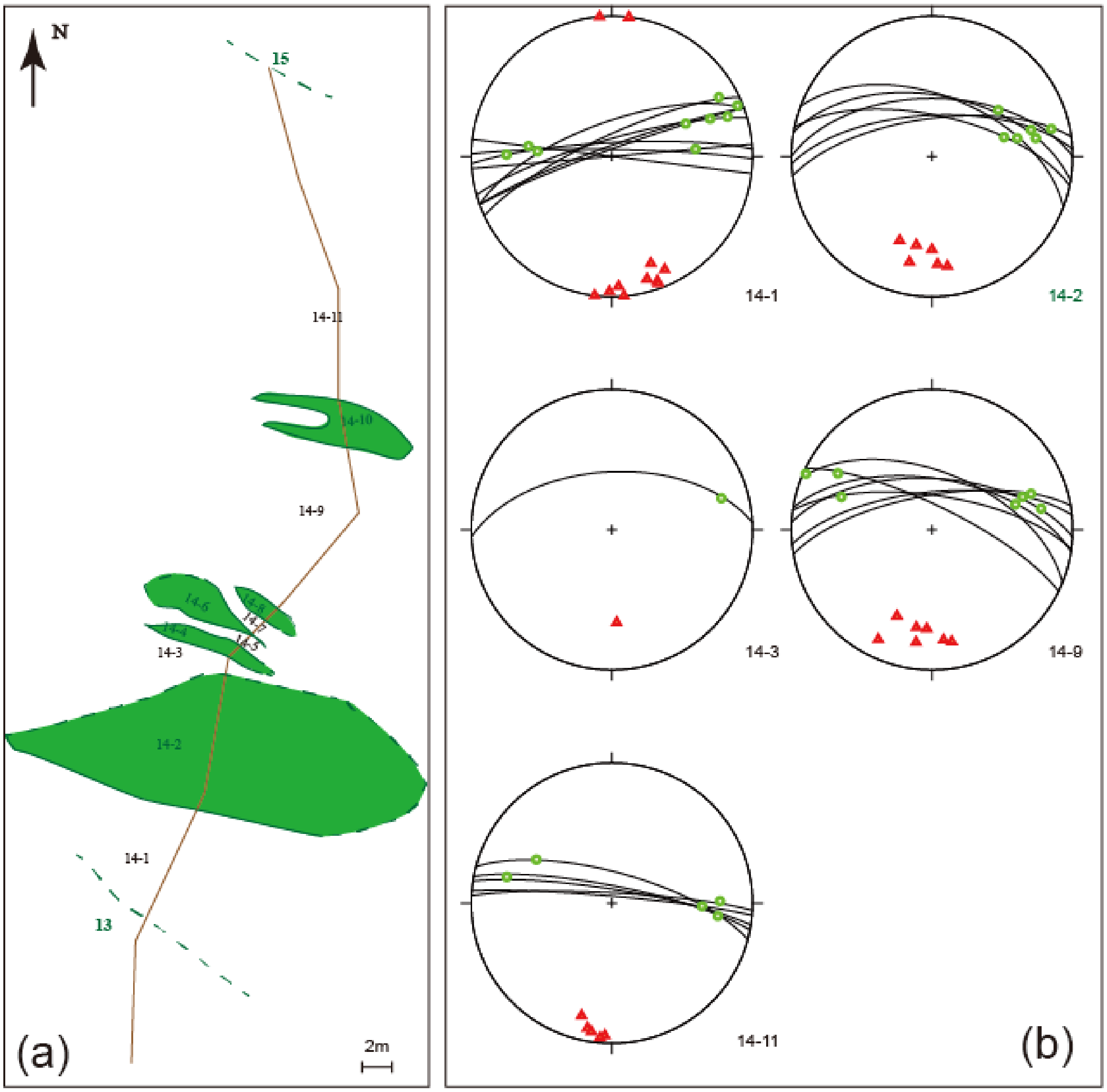

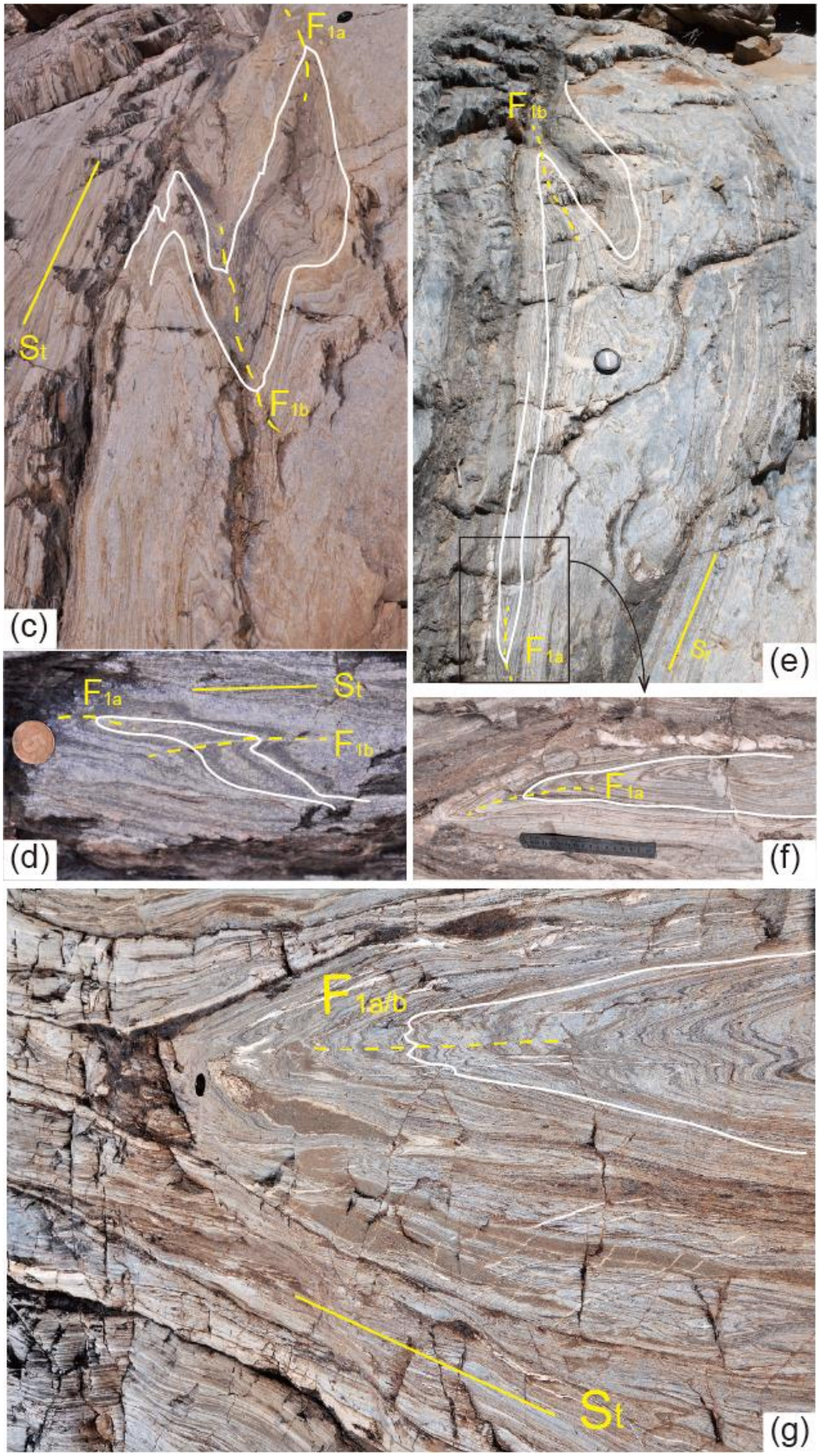
F1a
St
F1b
(c)
F1b
F1a
St
(e)
F1a
St
F1b
(d)
F1a
(f)
F1a/b
St
(g)

Figure 4.7 Detailed mapping and photos from unit 14. (a) A more detailed mapping of unit 14. (b) Transposition foliations (red triangles and black great circles) and mineral lineations (green dots) of each sub-unit. (c-g) Photos to show two generations of folds (F_{1a} and F_{1b}) in unit 14.

Unit20

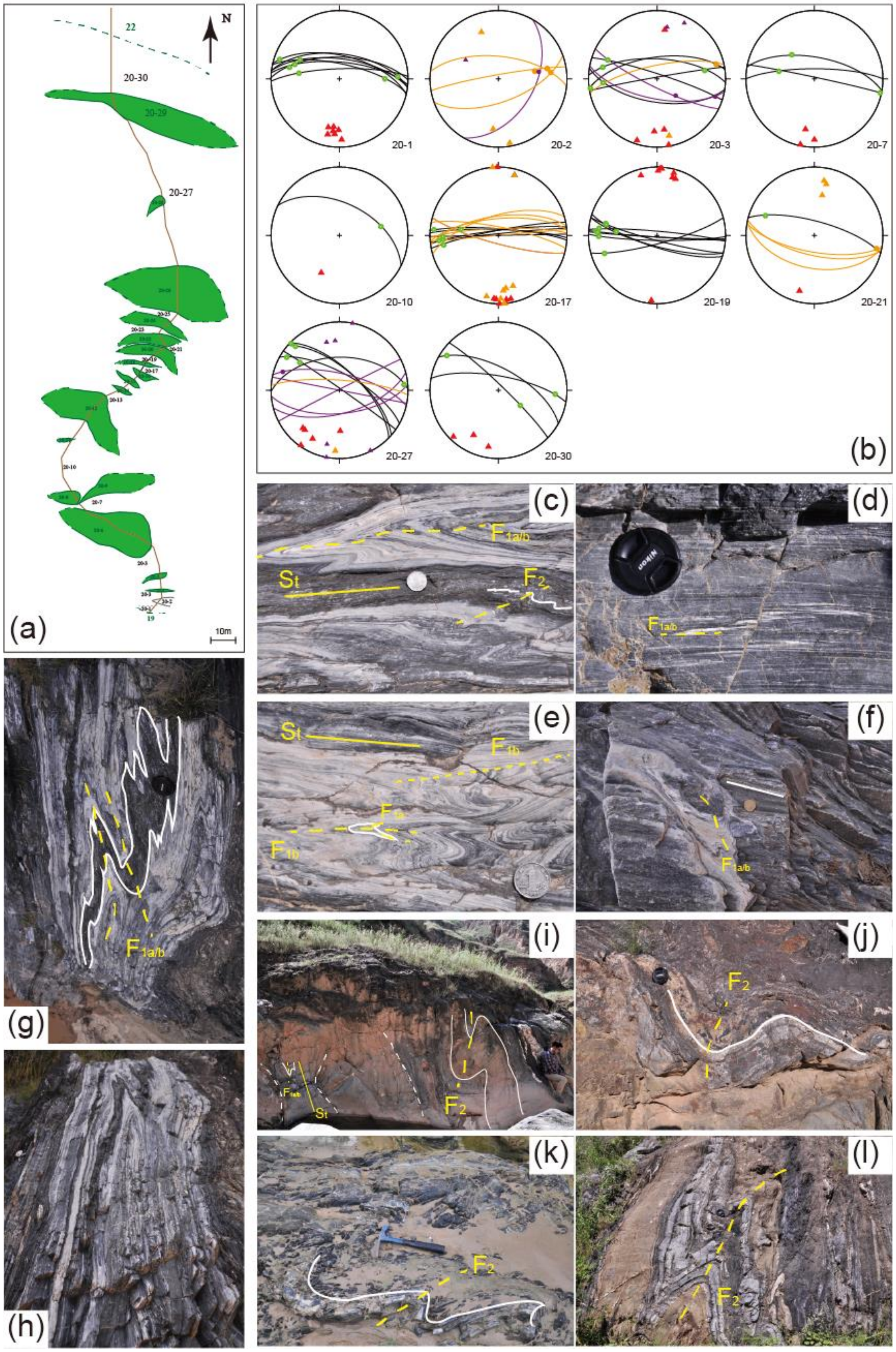
22
N
20-30
20-29
20-27
20-25
20-23
20-21
20-19
20-17
20-13
20-12
20-10
20-7
20-5
20-3
20-2
19
(a)
10m
20-1
20-2
20-3
20-7
20-10
20-17
20-19
20-21
20-27
20-30
(b)
(c)
F1a/b
St
F2
(d)
F1a/b
(e)
St
F1b
F1a
F1b
(f)
F1a/b
(g)
F1a/b
(h)
(i)
F1a/b
St
F2
(j)
F2
(k)
F2
(l)
F2

Figure 4.8 Detailed mapping and photos from unit 20. (a) A more detailed mapping of unit 20. (b) Transposition foliations (red triangles and black great circles) and mineral lineations (green dots) of each sub-unit. Fold hinge lines (orange dots) and axial planes (orange triangle and great circles) of $F_{1a/b}$ in each sub-unit. Fold hinge lines (purple dots) and axial planes (purple triangles and great circles) of F_2 in each sub-unit. (c-l) Photos to show $F_{1a/b}$ and F_2.

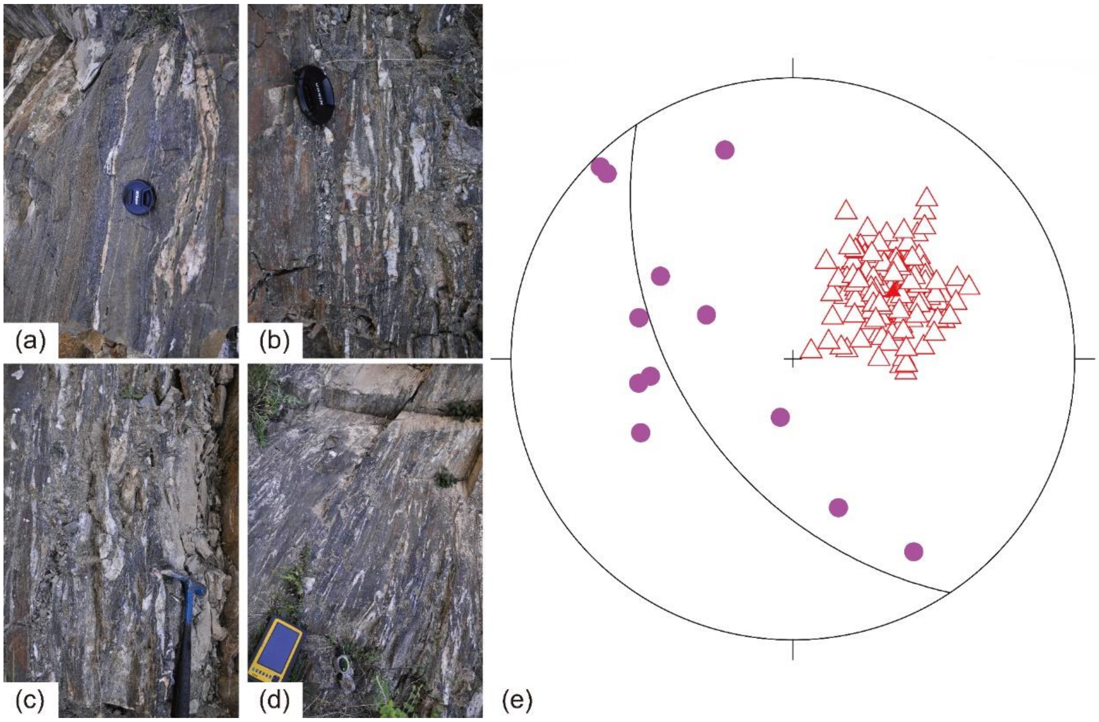

Figure 4.9 Photos and fabric data from the Huluhe Group. (a-d) Photos to show the deformed Huluhe Group that is southeast of the Xinyang mapping area (note that the highly transposed quartz veins). (e) Lower-hemisphere equal-area projection of the schistosity (red triangles and black great circles) and the hinge lines of the intra-folia folds defined by quartz veins (purple dots).

4.2.2.4 The Wushan area

In the Wushan area, well-developed lineations and foliations are found in a deformed diabase outcrop and metapelites, and dextral shear-sense indicators are observed on horizontal planes (Figs.4.10a,b). The equal-area lower-hemisphere projections of lineations and foliations are shown in Fig.4.10c. Most of the stretching lineations are along the strike of the foliations. The foliations are steeply dipping and striking NW-SE.

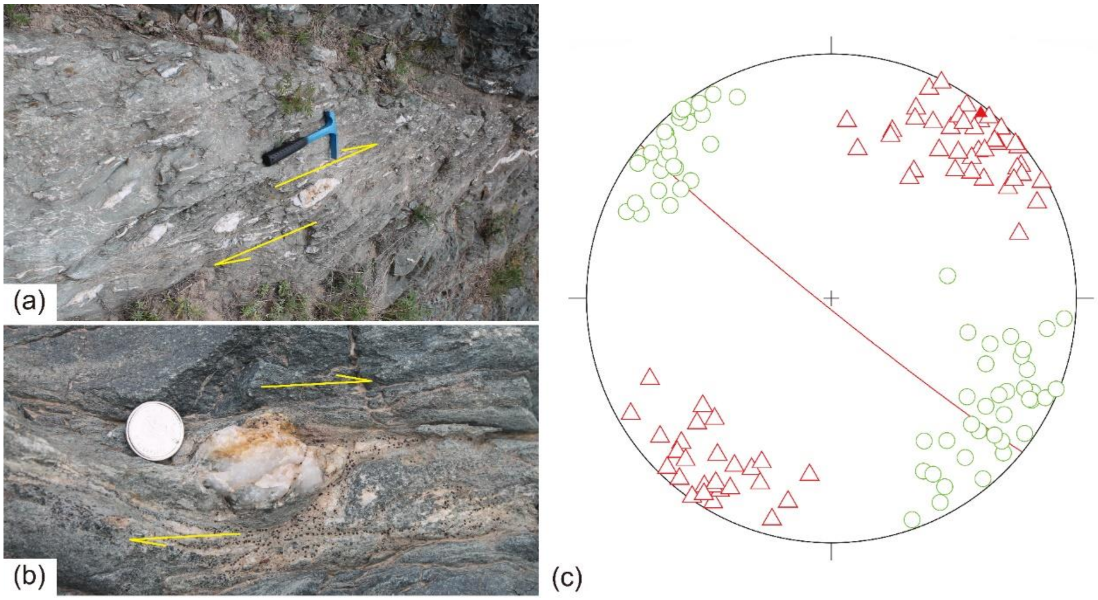

Figure 4.10 Photos and fabric data from the Wushan area. (a,b) Photos on sub-horizontal surfaces to show a dextral sense of shear in Wushan. (c) Lower-hemisphere equal-area projection of transposition foliations and mineral lineations in Wushan.

4.3 Geochronology data

There are several dykes in the shear zone. Zircon dating of these dykes is used to constrain the deformation time.

4.3.1 Sample descriptions

4.3.1.1 Samples from the Yuanlong area

In the Yuanlong area, there are several granitoid pegmatite dykes. These dykes are intruded in the granitic and felsic mylonites. Although these dykes are undeformed, the dykes are all subparallel to the foliations, and in addition, there are flanking structures around the dykes (Fig.4.11). Therefore, we suspect that these dykes intruded into the mylonites before the deformation, and the crystallization age of these dykes can be used to limit the time before the deformation.

These samples are TS1406, TS1408-1, TS1408-2.

4.3.1.2 Samples from the Shetang area

In the Shetang area, several granitoid pegmatitic dykes have been found in the deformed Qinling Complex. These dykes were intruded in the deformed rocks (Fig.4.12). There are two circumstances regarding the relation between the dykes and the deformation: 1) the dykes could be boundinaged during the deformation, and the inner boundin parts were not deformed; 2) the dykes could intrude into the deformed rocks after the deformation. It is hard to distinguish between these two circumstances.

These dykes are ST1502, ST1510-1, ST1510-2, ST1511, ST1515.

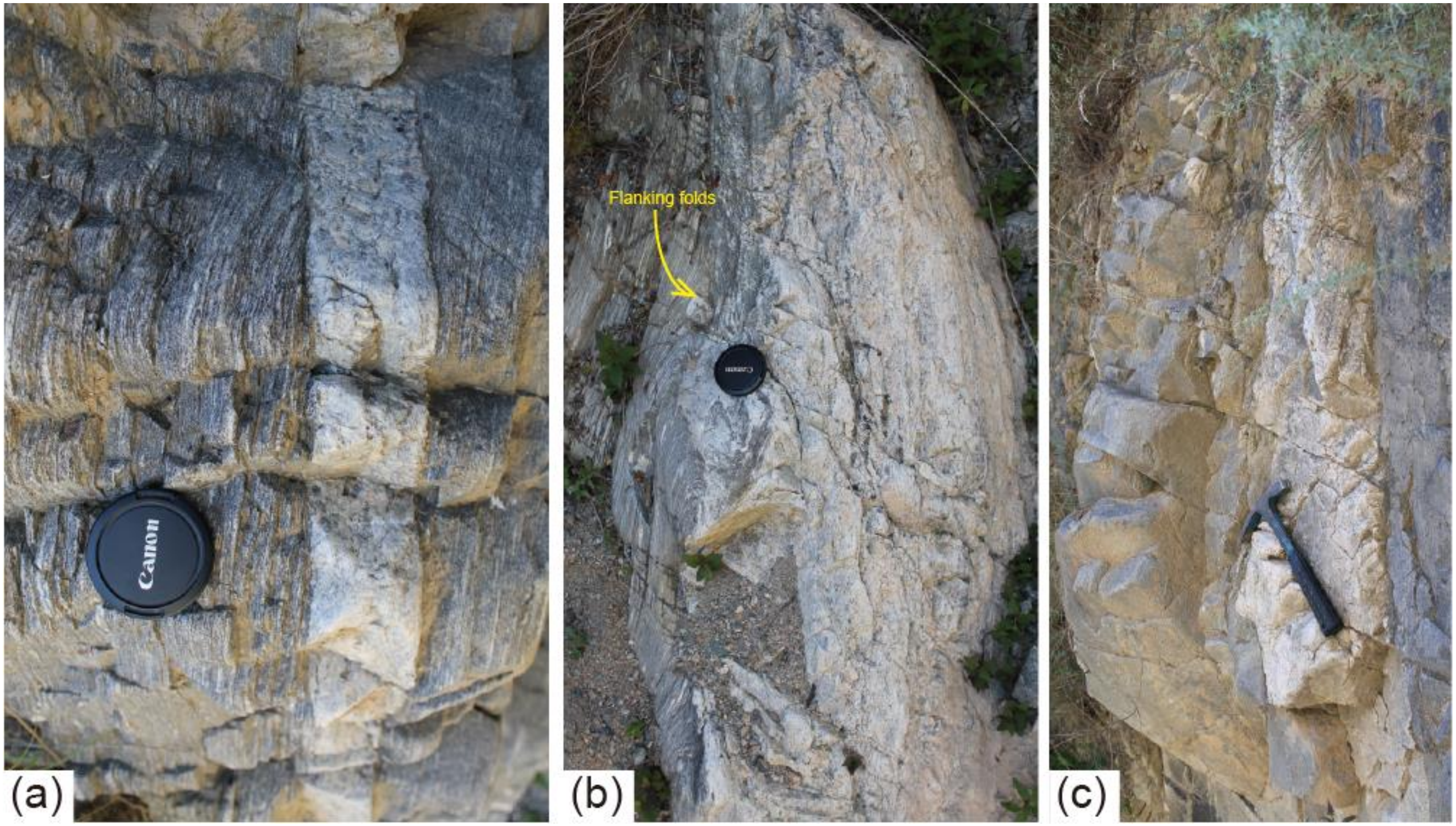

Figure 4.11 Field photos of granitic pegmatitic dykes from the Yuanlong area. (a) TS1406, (b) TS1408-1, (c)TS1408-2. Note the flanking structures beside the pegmatitic dyke.

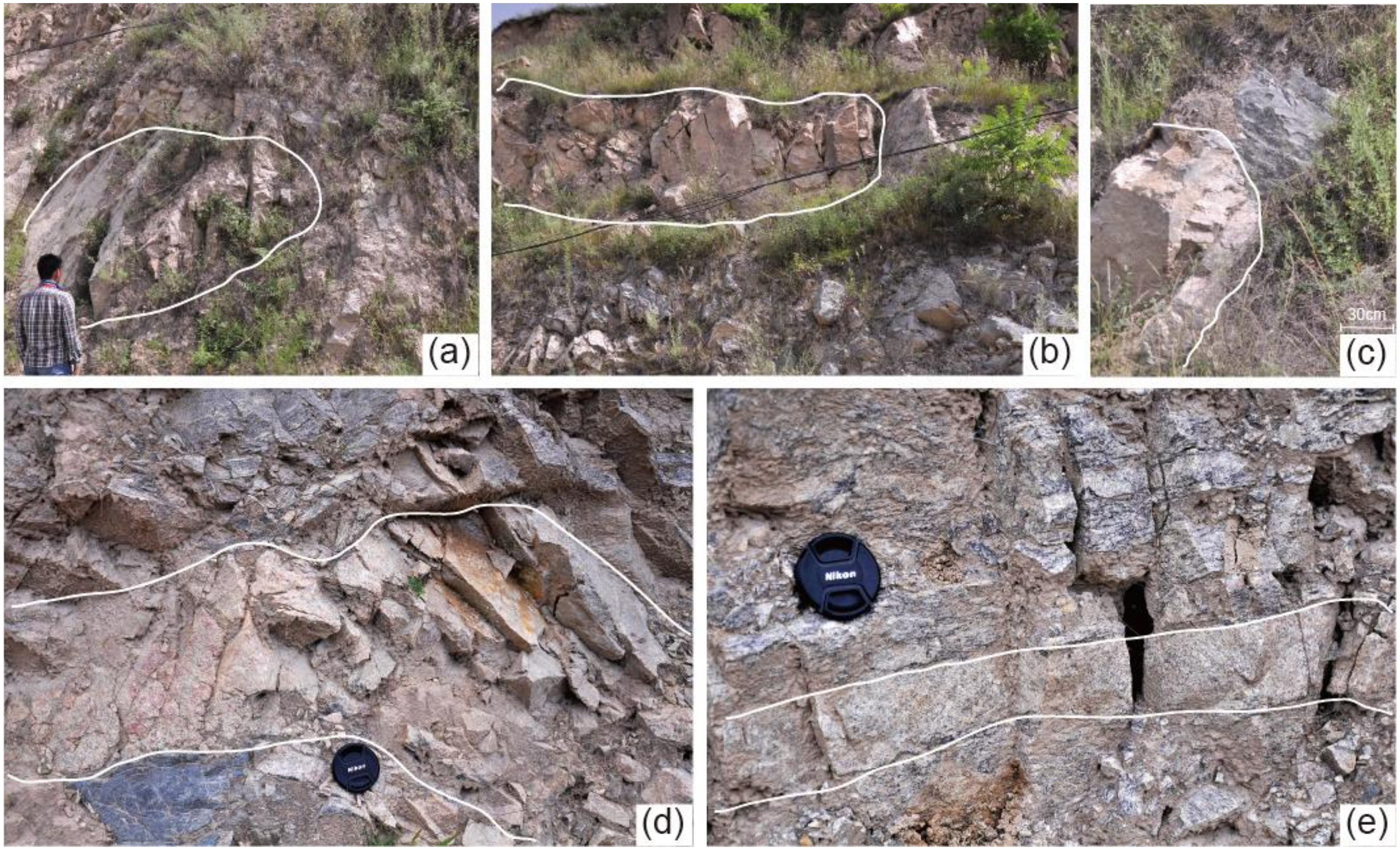

Figure 4.12 Field photos of granitic pegmatitic dykes from the Shetang area. (a) ST1502, (b) ST1511, (c) ST1515, (d) ST1510-1, (e) ST1510-2. Their locations are on Fig.4.3a. The black wire in (b) is served as a scale and about 5 meters in length.

To the north of the deformation zone, there is an undeformed granitoid body. Two samples are collected from this granitoid body, and they are ST1512, ST1513 (Fig.4.3a).

4.3.1.3 Samples from the Xinyang area

In the Xinyang area, there is a syn-deformation dyke: the body of the dyke cut the foliation, and the two tails of the dyke were deformed along the foliation (Fig.4.13c). Thus, the crystallization age of this dyke can constrain the deformation time. This dyke is XY1605. This dyke is a syenite dyke and highly weathered.

There are other highly deformed dykes in this region (Figs.4.13a,b). They are XY1601A, XY1601B, XY1602. XY1601A and XY 1602 are two meta-mafic dykes, and XY1602B is a granitoid dyke.

4.3.2 Analytical procedures

Zircon separation and morphology: Zircons are selected by crushing, initial heavy liquid separation techniques and subsequent magnetic separation handpicked and mounted. The mounts are ground and polished to half of the zircons' thickness. Zircons are photographed in transmitted and reflected light for further analysis. Cathodoluminescence (CL) imaging of zircons is conducted to reveal their internal structures. The CL imaging is performed by using a Quanta 400FEG environmental scanning electron microscope equipped with an Oxford energy dispersive spectroscopy system and a Gatan CL3+ detector. This process is completed at Xi'an Lucky-stone Geological Service, China.

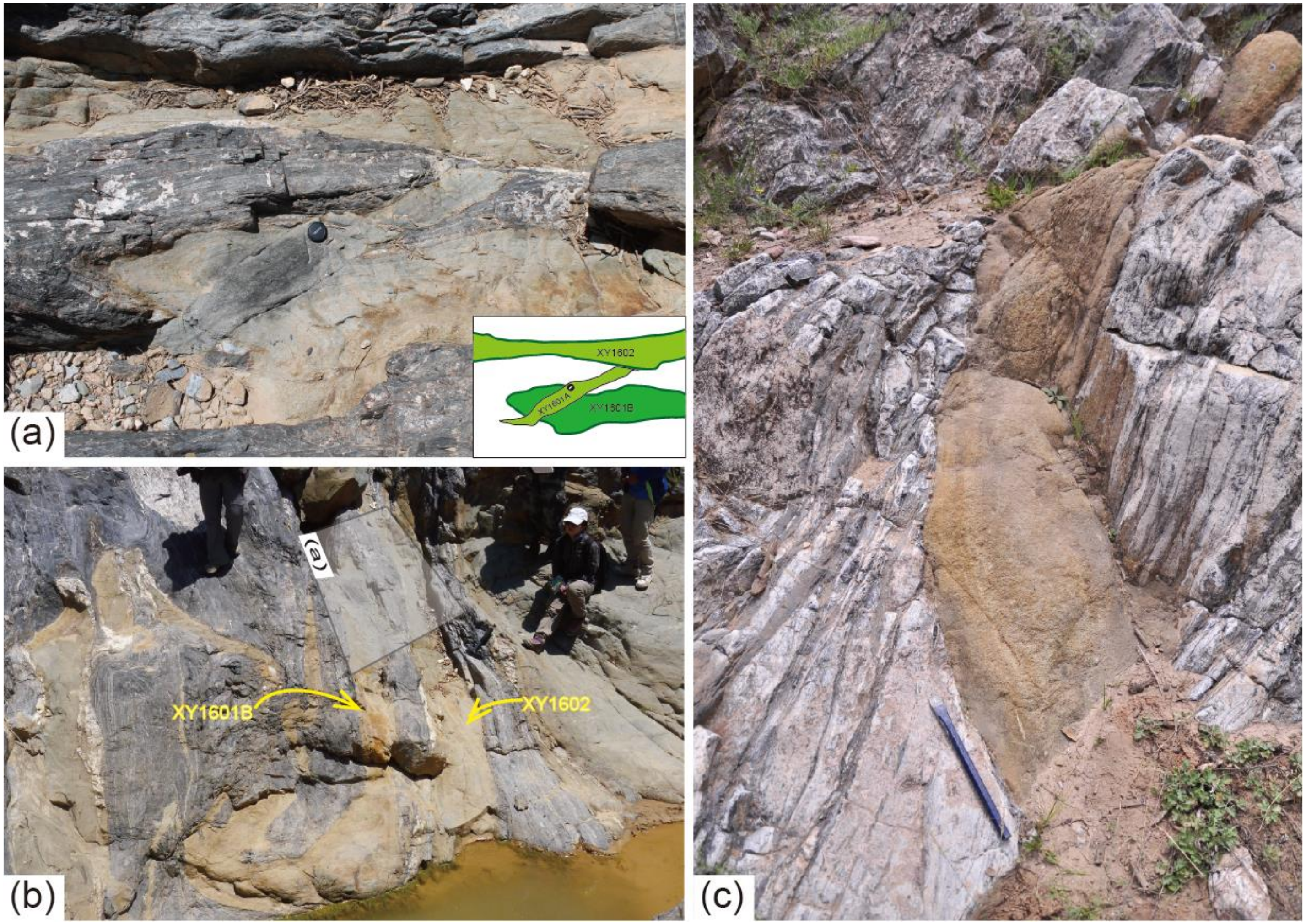

Figure 4.13 Field photos to show dykes from the Xinyang area. (a,b) XY1601A, XY1601B, XY1602, (c) XY1605 (syenite, the body cuts the transposition foliation, and the tail is deformed along the transposition foliation).

LA-ICP-MS U-Pb dating: U-Pb zircon analyses are performed on a laser-ablation system with an Agilent 7500a ICP-MS instrument equipped with a 193 nm ArF excimer laser at Northwest University, China. The laser beam of 35μm in diameter and repetition rate of 7 Hz is adopted throughout the whole study. Nist610 glass is used as the trace elements external standard. Standard zircon 91500 is used as an external standard for isotope fractionation. Every five analyses are followed by one analysis of standard zircon 91500, and every 10 analyses are followed by measurements of GJ-1 and Nist 610.

Data processing: $^{207}Pb/^{206}Pb$, $^{206}Pb/^{238}U$, $^{207}Pb/^{235}U$, and $^{208}Pb/^{232}Th$ ratios are calculated using GLITTER 4.0 (Macquarie University, Sydney, Australia). Concordia diagrams and weighted mean U-Pb ages are processed by using ISOPLOT 3 (Ludwig, 2003). Ages and Concordia plots are reported at the 2σ error, while the uncertainties for weighted mean ages are at 95% confidence level.

4.3.3 Geochronological results

According to external morphology, internal zoning, Th/U ratio and REE pattern, the analyzed zircons can be classified into magmatic and metamorphic groups. However, some people argue that a more thorough interpretation is relating the differences and changes to growth or recrystallization mechanisms: only zircon grown by solid state (metamorphic) reactions may be called metamorphic, whereas zircon crystallized from melt is magmatic, and zircon crystallized from fluids is hydrothermal. Besides the difference in growth mechanism, an existing zircon could be altered by other processes (i.e., metamictisation, annealing, recrystallization, dissolution-reprecipitation) and thus the above criteria could be affected by these processes. For example, Th/U ratios of metamorphic zircons are not necessarily less than 0.1, and igneous zircons do not necessarily develop oscillatory zoning (Corfu et al., 2003). Undoubtedly, there is no one standard rule to distinguish among different types of zircons, and the above criteria are used together to make the most reasonable interpretation. In the following classifications, the U-Pb results are grouped into magmatic ages and metamorphic ages. The magmatic ages group generally displays well-developed zoning, and Th/U ratios of them are greater than 0.1 and show a typical REE pattern of unaltered igneous rocks. The other ages are all grouped into metamorphic ages, so the metamorphic age group is not a strict metamorphic age, and it may include ages that reflect other alteration processes or mixed processes.

The ^{206}Pb/^{238}U, ^{207}Pb/^{235}U, and the ^{207}Pb/^{206}Pb ages can be calculated from lead and uranium isotopes. In addition, the ^{208}Pb/^{232}Th age can be calculated through the thorium series decay but rarely used in zircon geochronology. ^{235}U is not directly measured from the mass spectrometer and is calculated from the fixed ^{238}U/^{235}U ratio (Hiess et al., 2012), and the ^{207}Pb/^{235}U is mainly used to calculate the discordance of analysis (e.g., Spencer et al., 2016). Therefore, two isotopic ages (i.e., ^{206}Pb/^{238}U and the ^{207}Pb/^{206}Pb) are used for further analyses (e.g., weighted mean average calculation, age spectra plot). It is generally accepted that the ^{207}Pb/^{206}Pb age is used for zircons older ages and the ^{206}Pb/^{238}U age is used for younger ones. However, ~1.0 Ga, ~1.2 Ga or ~1.5 Ga cutoffs are proposed in the literature (e.g., Gehrels et al., 2008; Voice et al., 2011; Roberts and Spencer, 2014). According to the clusters of the dating results, for the following analyses, ~1.5Ga is used as the cutoff in this study.

Zircon Rare-earth element (REE) abundances for the samples are normalized to chondrite values (Sun and McDonough, 1989) and plotted on logarithm coordinates to establish the REE patterns. The REE is grouped into light REE (LREE, La-Pr), middle REE (MREE, Nd-Gd) and heavy REE (HREE, Tb-Lu). According to Hoskin and Schaltegger (2003), the REE pattern for unaltered igneous zircon is characterized by a steeply-rising slope from the LREE to the HREE with a positive Ce-anomaly and negative Eu-anomaly, and metamorphic zircons can show patterns similar to the igneous zircon pattern or different from it.

The quality of the analytical data from the Yuanlong, Shetang and Xinyang areas is low. Namely, a large amount of analyzed spots show discordant ages and most of the zircons are xenocrystic zircons. Therefore, the detailed descriptions and results of each sample are in Appendix E. Only the results of XY1605 (Fig.4.13c) is discussed here, as it contains the youngest zircon age, and the dyke shows a clear relationship with the deformation in the Xingyang-Yuanlong shear zone.

56 spots are analyzed from XY1605 (Fig.E12), and 35 analyses of the 56 spots show concordant ages (disc.% ≤ ±5%). According to the structures of zircons in CL images, Th/U ratios and the REE patterns, magmatic ages from the 35 zircons are identified. The concordant magmatic ages can be divided into the following groups: 1769.8±39.99Ma (1 analysis, Spot No.24); 1501.9Ma (1 analysis, Spot No.05); 1089.8~1002 (3 analyses, Spot No.01, 07, 14); 999.5~882.6Ma (3 analyses, Spot No.04, 29, 49); 844.9~604.1 (3 analyses, Spot No.16, 25, 26); 490.3±7.03Ma (1 analysis, Spot No.47); 467.1~462.8 (2 analyses, Spot No.55, 56); 451~447.6Ma (analyses, Spot No.13, 21, 22); 441.6±4.02Ma (1 analysis, Spot No.23);

423.3±4.89Ma (1 analysis, Spot No.33); 408.1~405.5 (2 analyses, Spot No.31, 37); 374.6±4.7Ma (1 analysis, Spot No.03); 357.9±4.53Ma (1 analysis, Spot No.37); 234.5±2.98Ma (1 analysis, Spot No.15); 212.5±2.12Ma (1 analysis, Spot No.11); 201.8±2Ma (1 analysis, Spot No.10).

As the youngest magmatic events in this area is the early Mesozoic event (Fig.4.16), the youngest age (i.e., 201.8±2Ma) in XY1605 is likely to indicate the crystallization age of this dyke instead of inherited from country rocks.

4.4 Interpretations and summary

4.4.1 Xenocrystic ages from the samples

The ages from the geochronological dating results expand in a long range, as most of the ages are xenocrystic ages. Although they may not be able to indicate the deformation time of the Xinyang-Yuanlong shear zone, they contain information about the tectonic evolution of this area. Therefore, we compare the age spectra from our samples with the previous geochronology studies throughout this area and try to find out the tectonic evolution information in the geochronology data. The above "metamorphic" age group is not critically the metamorphic ages, as to study the metamorphic zircons and relate the metamorphic ages to the metamorphism and further the tectonism, more petrology and geochemical studies are needed, which is not the key problem that we try to solve in this work. Therefore, we mainly compare the whole ages and magmatic ages with previous studies.

In principle, dykes can capture xenocrystic zircons from anywhere they have passed by. However, as the samples are all in the Xinyang-Yuanlong shear zone that is composed of the Qinling Complex and the Huluhe Group, the geochronology studies in these two units are reviewed and compared with the above results.

4.4.1.1 The Archean and Proterozoic age group (2623.6~646.3Ma, 213/377 analyses)

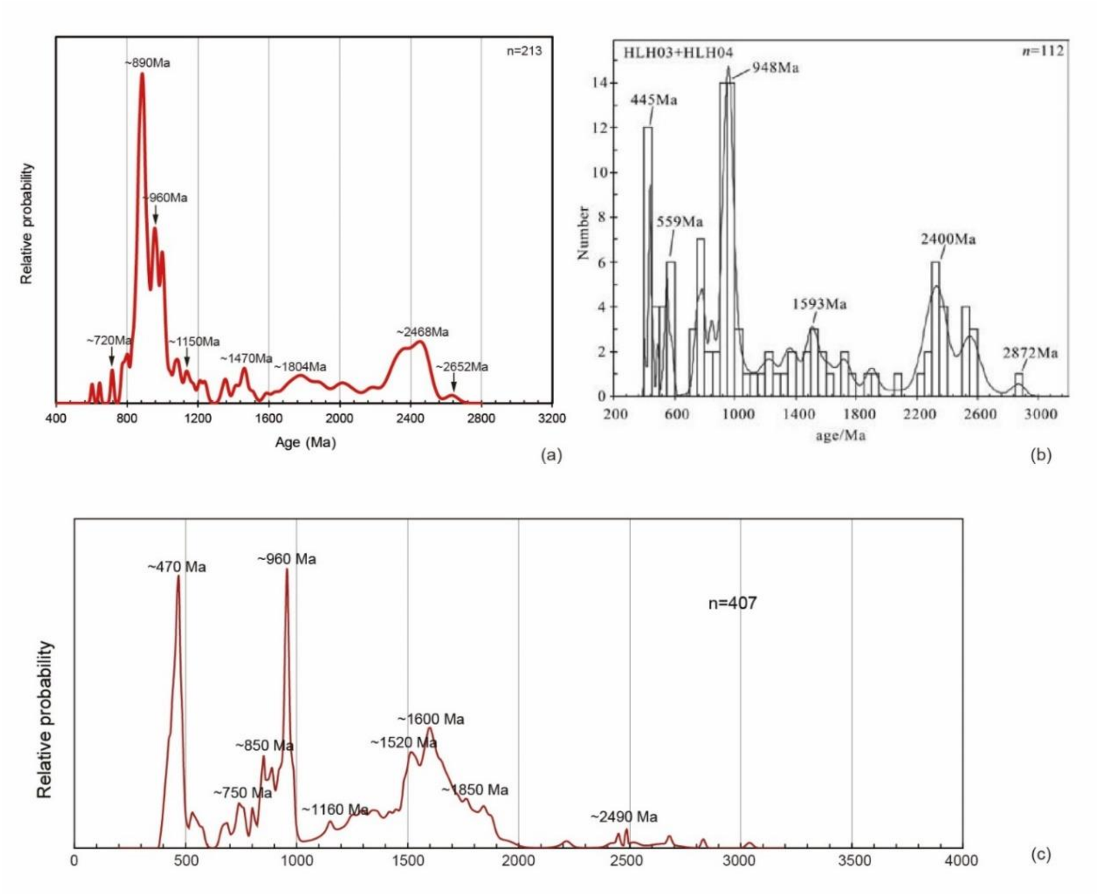

Figure 4.14 Age spectra from this study and previous studies. (a) Archean and Proterozoic age spectrum from this work. (b) Detrital zircon ages from the Huluhe Group (Pei et al., 2012). (c) Detrital zircon ages from the sedimentary units in the Qinling Complex (Wu and Zheng, 2013).

The age spectrum of Precambrian ages is in Fig.4.14a. The spectrum is comparable with the detrital zircon ages from the Huluhe Group (Fig.4.14b; Pei et al., 2012) and sedimentary rocks of the Qinling Complex (Fig.4.14c; Wu and Zheng, 2013 and reference therein). The age populations in Fig.4.14a are all subsets of the age spectra from the detrital zircons of the Huluhe Group and the Qinling complex

The xenocrystic ages show age peaks at ca.0.90-1.0Ga. Neoproterozoic granitoids showing emplacement ages from ca.890 to 980Ma have been reported in the Qinling Complex (e.g., Pei et al., 2003; Wang et al., 2003; Chen et al., 2006; Shi et al. 2009) and in the Qilian orogen (e.g., Guo and Zhao, 1999; Wan et al., 2003; Yong et al., 2008). Similar metamorphic ages (ca.859~978Ma) from the Qinling Complex by the Rb-Sr, Ar/Ar and Sm-Nd methods (e.g., Zhang et al., 1994; Wang et al., 2003; Dong et al.,2011c) have been obtained. All these ages are related to the Grenvillian orogeny (Dong et al., 2011a) and may be a response to the assembly of the supercontinent Rodinia in the early Neoproterozoic. According to Dong and Santosh (2016), the Neoproterozoic granitoids in the Qinling Complex indicate the southward subduction of the Kuanping Ocean and later collisional and post-collisional tectonic settings between the NCB and the NQB. The ages that are younger than 800Ma indicate an extensional setting after the collision between the NCB and NQB (Wang et al., 2013).

During 1.45~1.1Ga, the Qinling terrain was separated from the NCB by the Kuanping Ocean (Dong and Santosh, 2016), so the xenocrystic ages that are older than 1.1Ga represent the basement rocks (2.5~2.8Ga), Mesoproterozoic volcanic rocks and

Paleoproterozoic and Mesoproterozoic sedimentary rocks of NCB (Wu and Zheng, 2013).

4.4.1.2 The Paleozoic age group (524.3~343.6Ma, 159/377 analyses)

Figs.4.15a,b show the U-Pb results in the Paleozoic including the total results (Fig.4.15a) and the magmatic ages (Fig.4.15b). The ages that are younger than 445Ma do not overlap the detrital age spectra compared with the detrital ages in Figs.4.14b,c, and thus the magmatic zircons with age younger than 445Ma indicate the crystallization age of the dykes.

Fig.4.15c shows the early Paleozoic granitoids in the north Qinling belt from Zhang et al. (2013). Previous studies suggest that the early Paleozoic granitoids are arc magmatism and associated with the northward subduction of the Shangdan Ocean (e.g., Zhang et al., 2001; Ratschbacher et al., 2003; Dong et al., 2001b), while, recently, Zhang et al. (2013) grouped the early Paleozoic granites ages into three stages according to the age population. Based on the minerals in the plutons and geochemical features, Zhang et al. (2013) suggested that the first-stage (ca.500Ma) plutons are mainly from partial melting of crustal rocks during the crustal collision between the SQB and S-NCB; the second-stage (ca.450Ma) granitoids were generated from a mixed source of mantle and crust materials indicating a post-collisional setting; the third-stage (ca.420-400Ma) granitoids were formed from high differentiation of crust-derived magma in an extensional setting. The above interpretations of the early Paleozoic granitoids can be correlated to the HP-UHP metamorphism at ca.500Ma and two stages of retrograde metamorphisms at ca.470-450Ma and ca.420-400Ma (Liu et al., 2016).

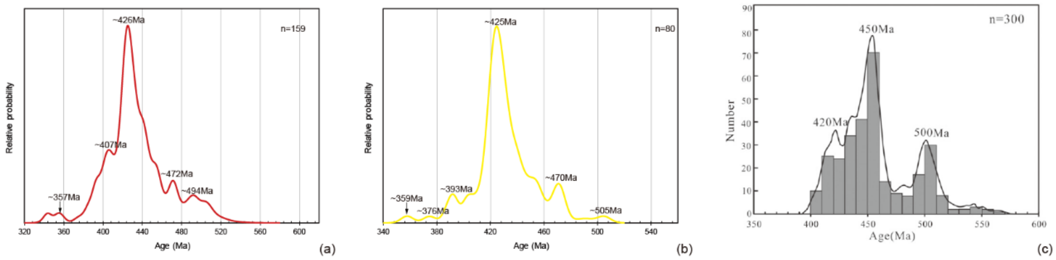

Figure 4.15 Paleozoic age spectra from this study and Paleozoic granitoids in the north Qinling belt. (a) the Paleozoic age spectrum from this work, (b) the magmatic Paleozoic age spectrum from this work, (c) Early Paleozoic granitoids in the north Qinling belt (from Zhang et al., 2013).

4.4.1.3 The Mesozoic age group (234.5~121.7Ma, 5/377 analyses)

There are only 5 U-Pb ages in this group: 3 magmatic ages (234.5-201.8Ma) and 2 ‘metamorphic’ ages (228.8 and 121.7Ma). Early Mesozoic magmatism between 252 and 185Ma is widespread in Western Qinling (Fig.4.16; Wang et al., 2013). The tectonic setting of the early Mesozoic magmatism is still in dispute. Zhang et al. (2001) proposed that Triassic granitoid magmatism resulted from northward subduction of Paleo-Tethyan oceanic crust, and some people argued that Triassic granitoids were developed during post-collisional delamination of thickened orogenic crust (e.g., Wang et al., 2005, 2007, 2011; Zhang et al., 2005; Qin et al., 2009, 2010). Wang et al. (2013) and Dong and Santosh (2016) suggested that early stage (250-240Ma) granitoids were related to northward subduction of the Mianlue Ocean to the SQB, and late stage (225-185Ma) granitoids indicate syn- or post-collision between the SQB and the SCB.

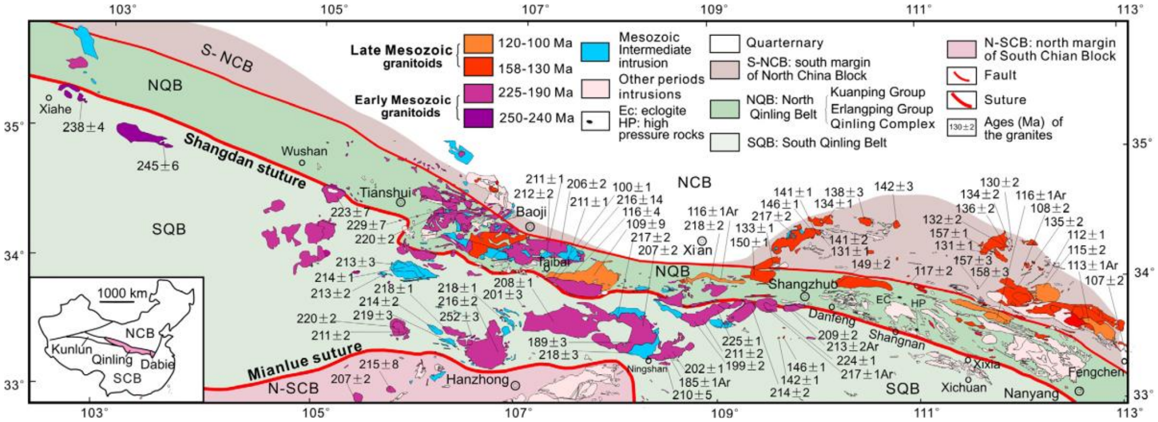

Figure 4.16 Distribution of granitoids with emphasis on Mesozoic granitoids in the Qinling orogenic belt (Fig.9 in Wang et al., 2013).

4.4.2 Deformation time and kinematic interpretations of the Xinyang-Yuanlong shear zone

According to the observations and geochronological studies in this study, and previous studies in this region, the Xinyang-Yuanlong shear zone may have experienced two deformation events. The work areas are summarized and interpreted as follows.

4.4.2.1 Deformation time in the Yuanlong area

Ding et al. (2009) have obtained a biotite ^{40}Ar/^{39}Ar age from the felsic gneiss in the Yuanlong area (351.70±1.72Ma). As the deformation fabrics in the Yuanlong area are clearly ductile deformation (Figs.4.2) and must have been formed under the temperature that is higher than ~300°C (the closure temperature of biotite), the ductile fabrics in the mylonites where the biotite ^{40}Ar/^{39}Ar age obtained in the Yuanlong area was mainly formed during a deformation event that is order than ca.352Ma. The 'metamorphic' age (384.7±3.3Ma, Spot No.16) in TS1408-2 may reflect that the zircon was reworked during the deformation.

4.4.2.2 Deformation time in the Xinyang area

Deformation in Xinyang can be divided into three districts according to the work locations: District 1, the Xiweizi valley (Figs.4.1c,4.4a); District 2, the Moshi valley (Figs.4.1c,4.4a); District 3, northeast of the Xiweizi and Moshi valleys (Figs.4.1c,4.9).

(1) District 1, the Xiweizi valley

The deformed rocks in the Xiweizi valley are granitic mylonites (Figs.4.4b,c), and Ding et al. (2009) have obtained a biotite $^{40}Ar/^{39}Ar$ age from the deformed rocks in the Xiweizi valley (347.95±2.17Ma). The age indicates that the fabrics in the Xiweizi valley should be formed in a deformation event before ca.348Ma. Compare with the deformation time in Yuanlong, the ductile fabrics in the Xiweizi valley was probably formed in the deformation event between ca.385Ma and 352Ma.

(2) District 2, the Moshi valley

In the Moshi valley, the syn-deformation syenite dyke (XY1605, Fig.4.13c) indicates the deformation time. The crystallization age of this dyke is 201.8±2Ma, and thus the dominant deformation in this valley should occur around 202Ma. However, the Xiweizi valley is south to the Moshi valley and should contain older deformation fabrics (ca.385-352Ma). It is highly likely that the deformed rocks in the Moshi valley (or in the whole area) had experienced at least two deformation events (ca.385-352Ma, ca.202Ma). Therefore, there are three types of fabrics in the Moshi valley: one type is the newly developed fabrics from the ca.202Ma deformation event; the second type contains the fabrics that were originally developed from the ca.385-352Ma deformation event but reworked during the ca.202Ma deformation event; the last type includes the fabrics that were developed from the ca.385-352Ma deformation but not reworked during the ca.202Ma deformation. In addition, the detailed mappings (Figs.4.5-4.8) in the Moshi valley show that each domain contains comparatively uniform fabrics, which suggests that the heterogeneous composition of the deformed rocks plays a key role to produce heterogenous fabrics (Fig.4.4d) in the Moshi valley.

(3) District 3, northeast of the Xiweizi and Moshi valleys

Unlike the fabrics in Districts 1&2, the Huluhe Group in District 3 were deformed into S-tectonites and does not develop mineral lineations. Furthermore, the fold axes of the intra-folia folds spread out along the average transposition foliation (Fig.4.9e). Therefore, fabrics in this area reflect a shortening deformation. This deformation probably occurred during the collision between the NQB and the Qilian orogen.

4.4.2.3 Deformation in the Shetang area

The steeply dipping transposition foliations in the Shetang area are constrained in the dashed-line region in Fig.4.3a, but the geochronological samples of granitic pegmatites are all from southern part of the Shetang area (Fig.4.3a). In the Qinling Complex, some foliations are extremely shallow (blue great circles in Fig.4.3f) with oblique lineations. These fabrics may be developed during Precambrian and correlated with the formation of the metamorphic basement rocks. Some foliations are moderately steep and strike WNW to ESE with oblique lineations, and this set of fabrics is related to the ca.390-352Ma deformation. The steeply dipping foliations that are striking NW to SE (grey great circles in Fig.4.3f and dashed-line region in Fig.4.3a) are correlated to the ca.202Ma deformation. The deformation in the Huluhe group corresponds to the collision between the NQB and the Qilian orogen like the District 3 in the Xinyang area.

Li (2008) obtained a biotite ^{40}Ar/^{39}Ar age (355.2±2.6Ma) from the deformed Huluhe Group in the Qingshui county that is northeast of our Shetang work area. This age indicates that the deformation of the Huluhe Group in District 3 in the Xinyang area and the deformation of the Huluhe Group in the Shetang area occurred before ca.355Ma. Combining with the age in Yuanlong, this deformation occurred between ca.385-355Ma corresponding with the collision among the NQB, the NCB and the Qilian orogen.

4.4.2.4 Deformation in the Wushan area

Li (2008) has obtained a muscovite ^{40}Ar/^{39}Ar age (226.76±2.21Ma) from the granitic mylonites in Wushan. The deformed rocks in the Wushan area are greenschists, granitic mylonites and felsic mylonites. The muscovite ^{40}Ar/^{39}Ar age (226.76±2.21Ma) from granitic mylonites may indicate that the deformation in this area occurred around 227Ma. This deformation may be correlated with the ca.202Ma deformation in the Moshi valley. The youngest strike-slip dominant dextral shear deformation occurred between ca.227Ma and 202Ma.

One exception is a recent work in the Wushan area (Liang et al., 2017). They dated an undeformed granitic intrusion in granitic mylonites, and the U/Pb zircon age of this intrusion is 403Ma. Combined with previous tectonic evolution models of

Qinling orogenic belt, they concluded that the Wushan ductile shearing occurred between ca.420 and 403Ma. From the picture of the undeformed intrusion (Fig.3d in Liang et al., 2017), the intrusion could act as a rigid body or be a product of boudinage during the deformation.

4.4.2.5 The kinematics of the Xinyang-Yuanlong shear zone

Overall, the dominant fabrics that are currently observed throughout the Xinyang-Yuanlong shear zone were produced by the deformation between ca.227Ma and 202Ma. The heterogeneity of the fabric data throughout the Xinyang-Yuanlong shear zone mainly resulted from the heterogeneity of the deformed rocks and can be explained by the multi-order power-law approach (MOPLA) that has been introduced in Chapter 1.

Fig.4.17c shows the overall fabrics across the Xinyang-Yuanlong shear zone. The fabrics in the Yuanlong, Shetang, Xiweizi, Wushan areas are relatively uniform, but the overall lineations spread out on the average foliation with the concentration close to the strike of the foliation. As the deformed rocks are extremely heterogeneous in the Moshi Valley, the overall lineations in the Moshi Valley spread along the average foliation, and the fabric in each mapping unit is relatively uniform (Figs.4.4-4.8). According to MOPLA, the Xinyang-Yuanlong shear zone can be considered as a Representative Volume Element (RVE) in MOPLA, and the RVE is made up by many Rheologically Distinct Phases (RDPs) (Fig.4.17a). The deformed rock units in the Yuanlong, Shetang, Xiweizi Valley, Moshi Valley and Wushan areas can be regarded as different RDPs. Except for the fabrics in the Moshi Valley, the fabrics in each RDP show a roughly uniform distribution. The deformed rocks in the Moshi Valley can be regarded as an RDP that consists of many 2nd-order RDPs (Fig.4.17b), and in each 2nd-order RDP, the fabrics are relatively uniform.

Jiang (2014) has systematically simulated the fabric patterns that are produced by the different boundary conditions based on MOPLA. The velocity gradient tensor in Jiang (2014) is written in the following format $\mathbf{L}=\begin{pmatrix} 0 & \cos\alpha & 0 \\ 0 & -\sin\alpha\sin\beta & 0 \\ 0 & -\sin\alpha\cos\beta & \sin\alpha\sin\beta \end{pmatrix}$, where α is the convergence angle and β is the dip of the deformation zone and set to 70° in Jiang (2014) (Fig.4.18). Here, the simulation results (Fig.4.19) in Jiang (2014) are compared with the measured data in this work.

The overall stretching lineations throughout the Xinyan-Yuanlong shear zone are mostly like the first and second rows of the simulation results (i.e., $\alpha = 0°, 5°$) indicating a strike-slip shear dominant deformation. This interpretation is consistent with the fact that all the shear-sense indicators are observed on the horizontal or sub-horizontal sections.

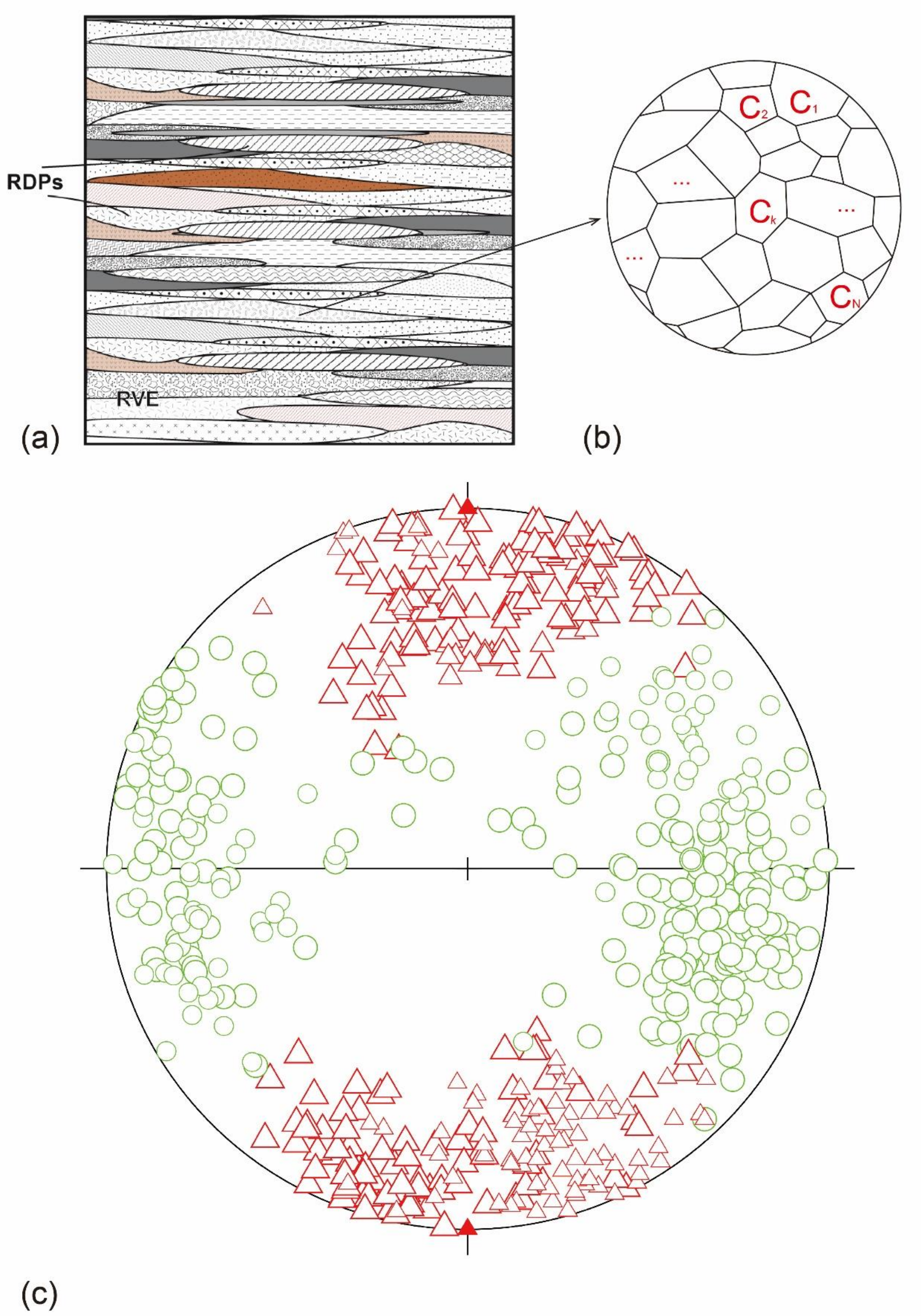
RDPs
RVE
(a)
C_2
C_1
...
C_k
...
...
C_N
(b)
(c)

Figure 4.17 A conceptual diagram to show the interpretation of the fabric data from the Xinyang-Yuanlong shear zone. (a) A conceptual diagram showing that the Xinyang-Yuanlong shear zone can be regarded as a Representative Volume Element (RVE) that is composed of many Rheologically Distinct Phases (RDPs). One can refer to Chapter 1 for the detailed concepts of RVE and RDPs. (b) One RDP can consist of a 2nd-order RDPs, which is the case of the deformed rocks in the Moshi Valley. (c) The equal-area lower-hemisphere projection of the overall transposition foliations and stretching lineations throughout the Xinyang-Yuanlong shear zone with respect to the model coordinate system in Fig.4.18. The black great circle is the average of the transposition foliations.

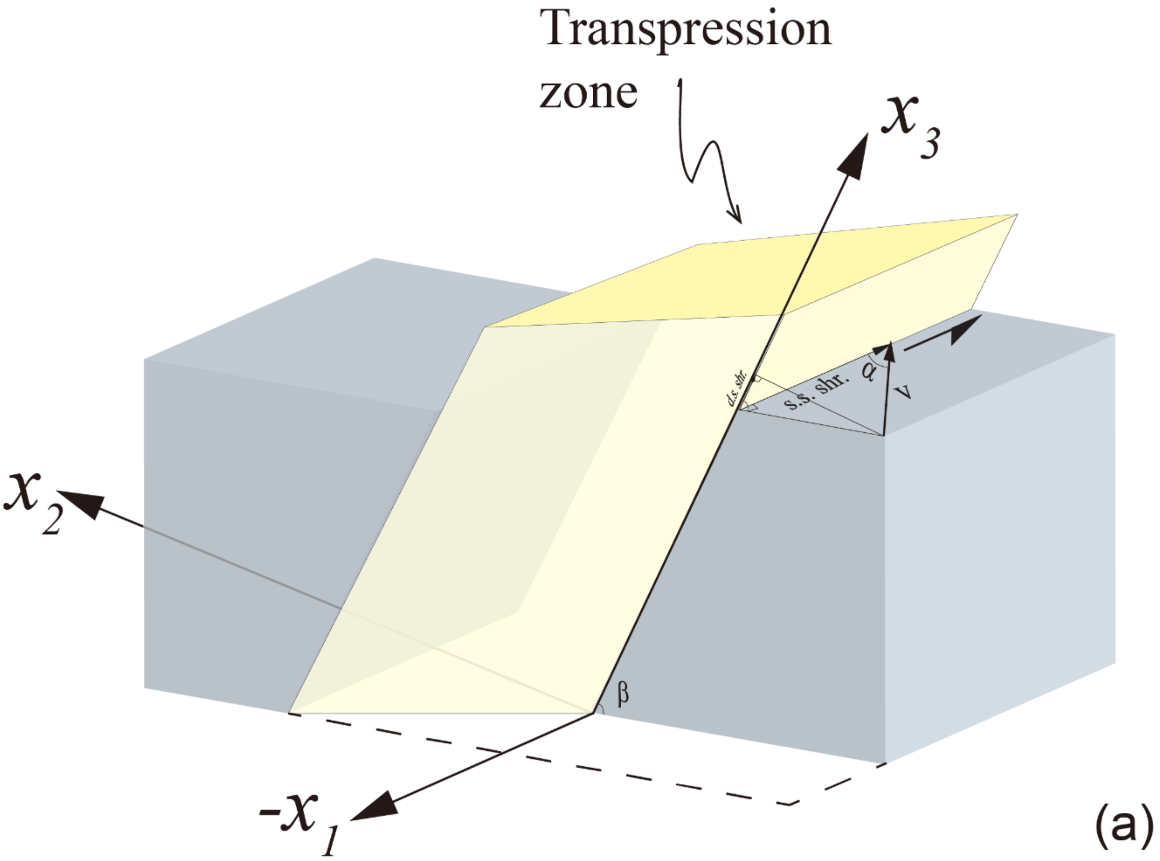

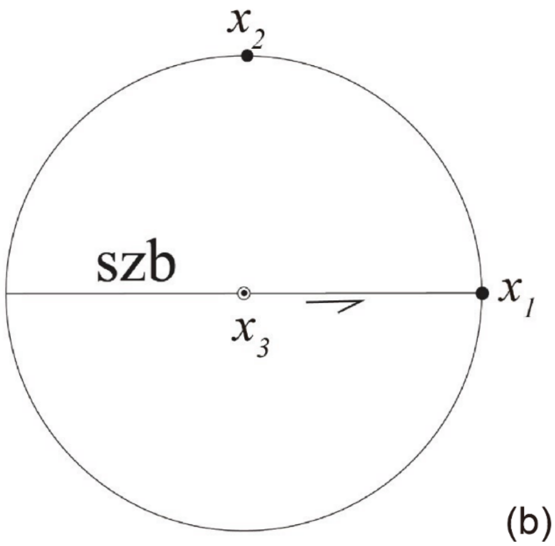

Figure 4.18 Transpression model in Jiang (2014). (a) Inclined transpression model in Jiang (2014). s.s.shr.: strike-slip shear; d.s.shr.: dip-slip shear. (b) The coordinate system that is used to make the equal-area projection in Fig.4.34 (Fig.6 in Jiang, 2014).

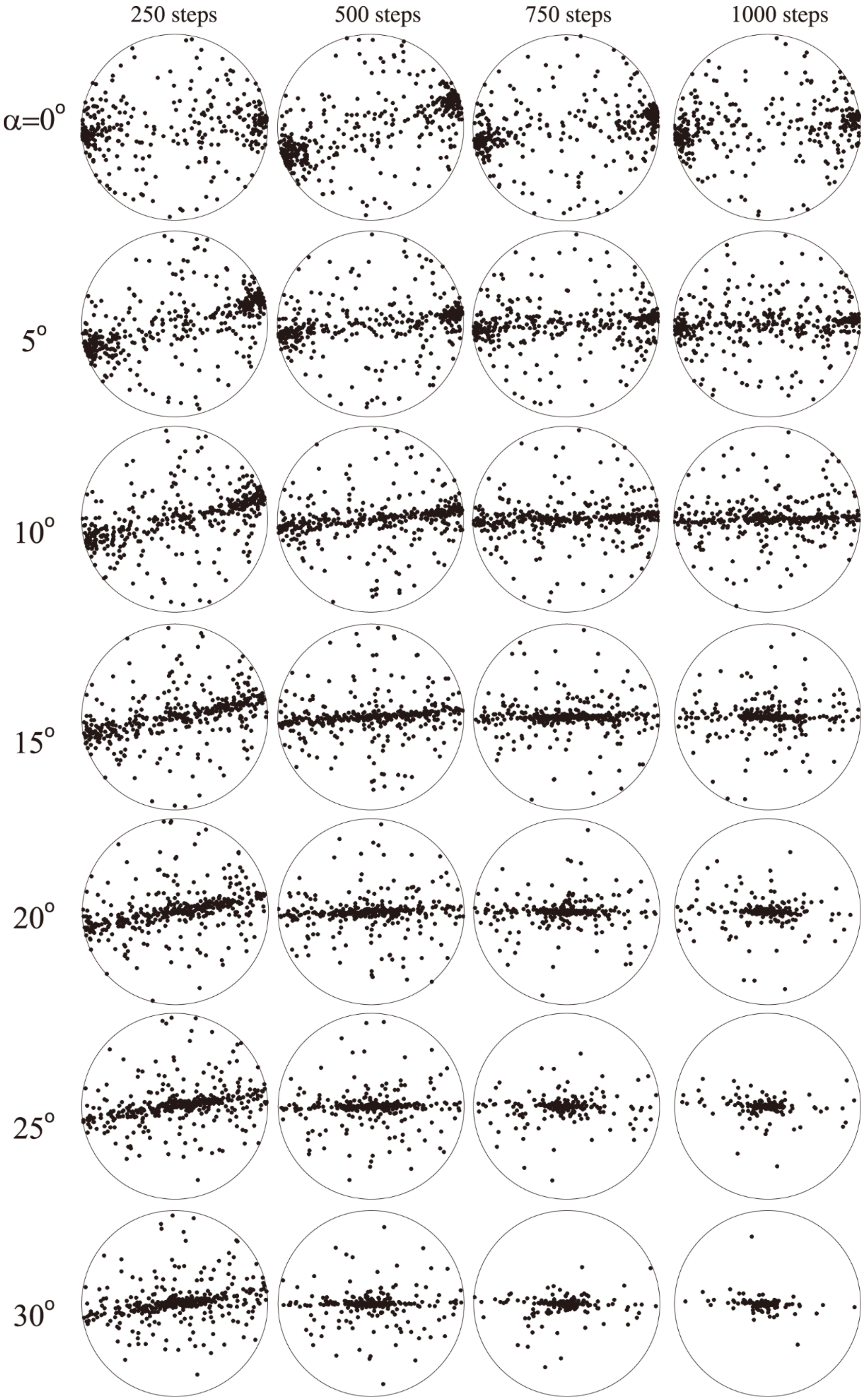

250 steps
500 steps
750 steps
1000 steps
α=0°
5°
10°
15°
20°
25°
30°

Figure 4.19 Model predicted 'stretching lineations' patterns produced by different boundary conditions in Jiang (2014). The 'stretching lineations' are defined by the maximum principal finite strain axes in RDPs throughout the deformation zone (Fig.10 in Jiang, 2014).

4.5 The deformation along the SDTZ in western Qinling

There are at least two deformation events in the Xinyang-Yuanlong shear zone in western Qinling. D_1 deformation occurred between ca.385Ma and 355Ma. D_1 deformation has been preserved in the Huluhe Group that is north of the Xinyang-Yuanlong shear zone and shows a NE-SW shortening deformation. D_2 deformation occurred between ca.227-202Ma and produced the dominant fabrics that are currently observed in the Xinyang-Yuanlong shear zone. D_2 deformation is a strike-slip dominant deformation with a dextral sense of shear.

The Shangdan suture was defined by the Danfeng Complex (purple areas in Fig.4.1c). In western Qinling, the mafic and ultramafic rocks in the Wushan and Guanzizhen areas are interpreted to be part of the Danfeng Complex (Fig.4.1). Lu (2008) has conducted extensive field work in the Wushan, Guanzizhen and Tangzang areas and, similarly, observed the dextral shear strike-slip dominant deformation in these areas and concluded that it occurred between the late Paleozoic and the early Mesozoic. In addition, the locations of Wushan, Guanzizhen, Xinyang, Shetang, Yuanlong and Tangzang from west to east are close to each other and show spatial correlations. As the mafic and ultramafic rocks in Wushan and Guanzizhen belong to the Danfeng Complex, the deformation documented in the Wushan, Guanzizhen, Shetang, Xinyang, Yuanlong and Tangzang areas represents the deformation of the

SDTZ in western Qinling. Therefore, we think that the deformation along the SDTZ in western Qinling is a dextral strike-slip dominant deformation and occurred between ca.227-202Ma. The Xinyang-Yuanlong shear zone is a branch of the SDTZ in western Qinling.

4.6 Tectonic implications

4.6.1 The importance of the strike-slip deformation in the QOB

The current tectonic models of the QOB (e.g., Zhang et al., 2001; Dong et al., 2011a; Dong and Santosh, 2016) mainly use the concept of the Wilson cycle (Wilson, 1966) as a unifying conceptual framework and consider the orthogonal subductions and collisions among different tectonic plates. In this study, the predominant strike-slip deformation along the SDTZ is well established, which suggests that the non-coaxial deformation inside the QOB may have a demonstrably profound effect on the tectonic evolution and the current style (i.e., linear zonation) of the QOB.

As shown in van Staal et al.(1998), the forward modeling of the oblique collision between Australia and Asia will produce a linear orogen (Fig.4.20) due to the transpressional flattening and non-coaxial deformation during the ultimate collision. Fig.4.20a (Fig.5a in van Staal et al., 1998) is a simplified tectonic map of the west and southwest Pacific at present. Fig.4.20b (Fig.5b in van Staal et al., 1998) shows the configuration of this area after 45Ma produced by the collision of the Australian plate with the Asian plate along a broad zone of sinistral oblique convergence assuming a 55-million-year constancy of relative plate motions (van Staal et al., 1998). They (van Staal et al., 1998) use this model to test if ‘the superficial simple zonation and linearity’ of the Appalachian-Caledonide Orogen could be a result of terminal collisional processes. The forward modeling result shows that the complexity of tectonic elements and an earlier complicated geometry may be obscured, and the broad zone results in a simple linear geometry because of the oblique convergence. The major effects of the oblique convergence that one should consider when trying to extrapolate the tectonic evolution of a linear orogenic belt are: 1) the tectonic units are transpressionally flattened, sheared and rotated into linear orogenic zones; 2) the final position and orientation of the tectonic elements after the ultimate collision may be quite different from the original paleogeographic position and orientation; 3) the once continuous tectonic element may be scattered and transported far away from each other during the final collision.

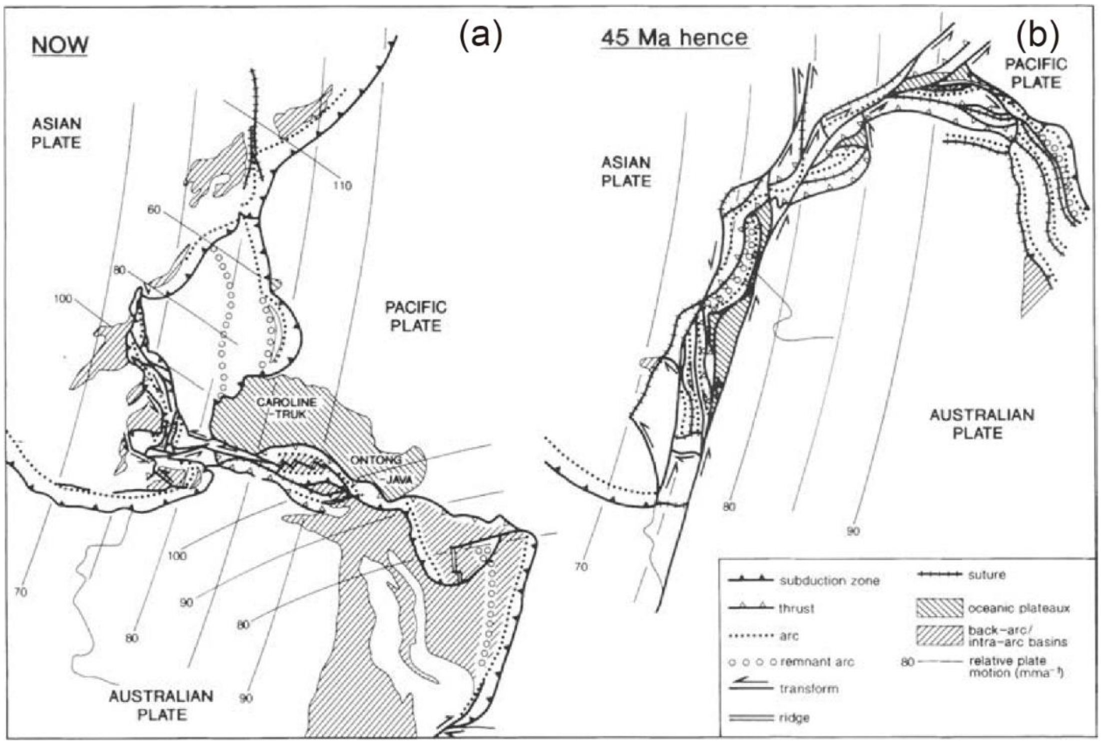

Figure 4.20 Forward modeling in van Staal et al. (1998). (a) The present-day tectonic configuration of the Australia-Asia area. (b) The interpretative plate configuration of the Australia-Asia collision 45Ma in the future (Fig.5 in van Staal et al., 1998).

Many ancient orogens, such as the Appalachian-Caledonide belt and the QOB, are strikingly linear or slightly arcuate over thousands of kilometers. The normal practice for the studies of these orogens is to draw zones and subzones that are featured by some tectonic elements in a linear manner along the great strike length. Namely, reseachers try to 'impose an along-strike correlative unity and continuity' of the tectonic elements (van Staal et al., 1998). However, this simple linearity and zonation of an orogenic belt are in contrast with the complexity of modern convergent systems such as the west and southwest Pacific region in Fig.4.20a. The above forward modeling (Fig.4.20) shows that the linear configuration of the ancient orogens may result from the terminal collisional processes and the tectonic elements will experience profound spatial and geometric changes during this time.

Van Staal et al. (1998) applied the above lessons to the northern Appalachian-Caledonian belt and proposed a refined tectonic model for the evolution of the belt during the Cambrian to the Silurian. The above lessons should be considerred in the tectonic evolution models of the QOB.

4.6.2 The tectonic configuration of the QOB before the Triassic

The fierce debate on the evolution of the QOB during the Paleozoic is focused on the precise location of the collisional zone. Some authors agree that the subduction and collision of the NCB and SCB were along the Shangdan suture zone with the Erlangping back-arc basin (e.g., Zhu, 2001; Xu et al., 2002; Dong et al., 2011a,b), while some authors argue that the major suture zone was marked by the Erlangping ophiolitic mélange (Xue et al., 1996; Ratschbacher et al., 2003, 2006; Wang et al., 2011). According to a recent review paper (Dong and Santosh, 2016), the Erlangping

Complex is composed of basaltic rocks, andesites and rhyolites with a few ultramafic and clastic rocks. The rhyolites may suggest that the Erlangping Ocean experienced a back-arc rift and formed arc-related volcanic and E-MORB rocks (Dong and Santosh, 2016). The Danfeng Complex is composed of N-MORB, E-MORB and arc-related volcanic rocks without rhyolite (Zhang et al., 2001; Dong et al., 2011a,b; Dong and Santosh, 2016). Considering the petrology, geochemistry, regional scale of the Shangdan suture, the Shangdan suture is regarded as the major boundary during the Paleozoic. Therefore, the idea that the Shangdan suture was the major suture with the Erlangping back-arc basin during the Paleozoic is adopted here.

Reflecting the idea that the Shangdan suture was the major suture with the Erlangping back-arc basin, there are two dominant models regarding the evolution of the NQB. One is summarized in Dong and Santosh (2016) (Fig.4.21 left), and the other is in Liu et al. (2016) (Fig.4.21 right). The two major differences between these two models are: 1) the question of when the Shangdan ocean closed; 2) if the close of the Shangdan ocean led to the collision of the SCB and the NCB or the amalgamation of the SQB with the NCB.

In Liu et al.(2016), the model is mainly based on the high-pressure and ultra-high pressure (HP-UHP) rocks in the Qinling Complex. Liu et al.(2016) interpreted that the HP-UHP metamorphic age at ca.500Ma and retrograde metamorphic ages of ca.470-450Ma and ca.420-400Ma from the HP-UHP rocks can be related to the magmatic ages in the Qinling Complex (~500Ma, ~450Ma and ~420Ma) indicating deep subduction/collision, slab-breakoff and crustal thinning during post-collisional extension, respectively. However, this model conflicts with the provenance studies of the fore-arc prism in the Heihe area (Dong et al., 2013a) and the Wuguan Complex in the Danfeng area (Yan et al., 2016). As the main proof of Liu et al.(2016)'s model was based on the metamorphic and magmatic ages and geochemical studies in the Qinling Complex, the data directly reflect the tectonic settings of the Qinling Complex but not the whole QOB. Especially, as the importance of the transcurrent movement among tectonic elements during an oblique convergence has been discussed in Section 6.3, the current connected tectonic elements may have been a great distance from each other before the terminal collision. Therefore, in our opinion, the model proposed by Liu et al. (2016) is not convincing.

Dong et al. (2013a) analyzed the detrital zircons from the fore-arc prism that is at the southern edge of the Shangdan Complex in Heihe. The detrital zircons show a uniform age spectrum of ca.455-600Ma that is only attributed to the NQB without any contribution from the SQB and the SCB, so the Shangdan ocean still existed at 455Ma (Dong et al., 2013a). Combined with the crystallization age of a diabase that is intruded into the fore-arc prism, the depositional age of the fore-arc prism is constrained to 455-435Ma. Yan et al. (2016) studied detrital zircons of the Wuguan Complex in the Danfeng area. The Wuguan Complex is to the southern side of the Shangdan Complex in the Danfeng area. The detrital zircons in the Wuguan Complex show an age spectrum with two major peaks at 453Ma and 800Ma and minor populations at 350-430Ma and 1000-2868Ma, and the weighted mean age of the youngest group is 358±3Ma (Yan et al., 2016). The age (358Ma) is related to the ages of 351Ma and 358Ma from andesites in the Shangdan and Fengxian areas (Chen, 2008; Chen et al., 2014). According to Yan et al. (2016), the geochemical characteristics of the Wuguan Complex indicate that the sedimentary rocks were originally deposited at an active continental margin corresponding to the northward subduction of the Shangdan ocean, so the northward subduction may have still been active at 358Ma.

The fore-arc prism in the Heihe area and the Wuguan Complex in the Danfeng area are now cropped as lenses along the SDTZ, and both have been interpreted as the sedimentary units along an active margin corresponding to the northward subduction of the Shangdan ocean (Dong et al., 2013a; Yan et al., 2016). They are likely to be one sedimentary unit but transposed to current locations and shapes by later deformation.

The Liuling Group is south of the Wuguan Complex and the Shangdan Complex. The detrital zircons of the Liuling Group (Dong et al., 2013a; Liao et al., 2017) yield an age spectrum with major groups of 500-400Ma, 850-700Ma and 1000-900Ma and minor populations at 1750-1450Ma, 2000Ma and 2600-2400Ma, and the source rocks of the sediments are from both the NQB and the SQB. The depositional age of the Liuling Group is further constrained by a pegmatite intruded into the Liuling Group. The crystallization age of the pegmatite is 373.8Ma (Shi, 2016), so the depositional age of the Liuling Group is during 373.8-400Ma. As the source rocks of the Liuling Group are from both the NQB and the SQB, the Shangdan ocean was nearly closed during Devonian.

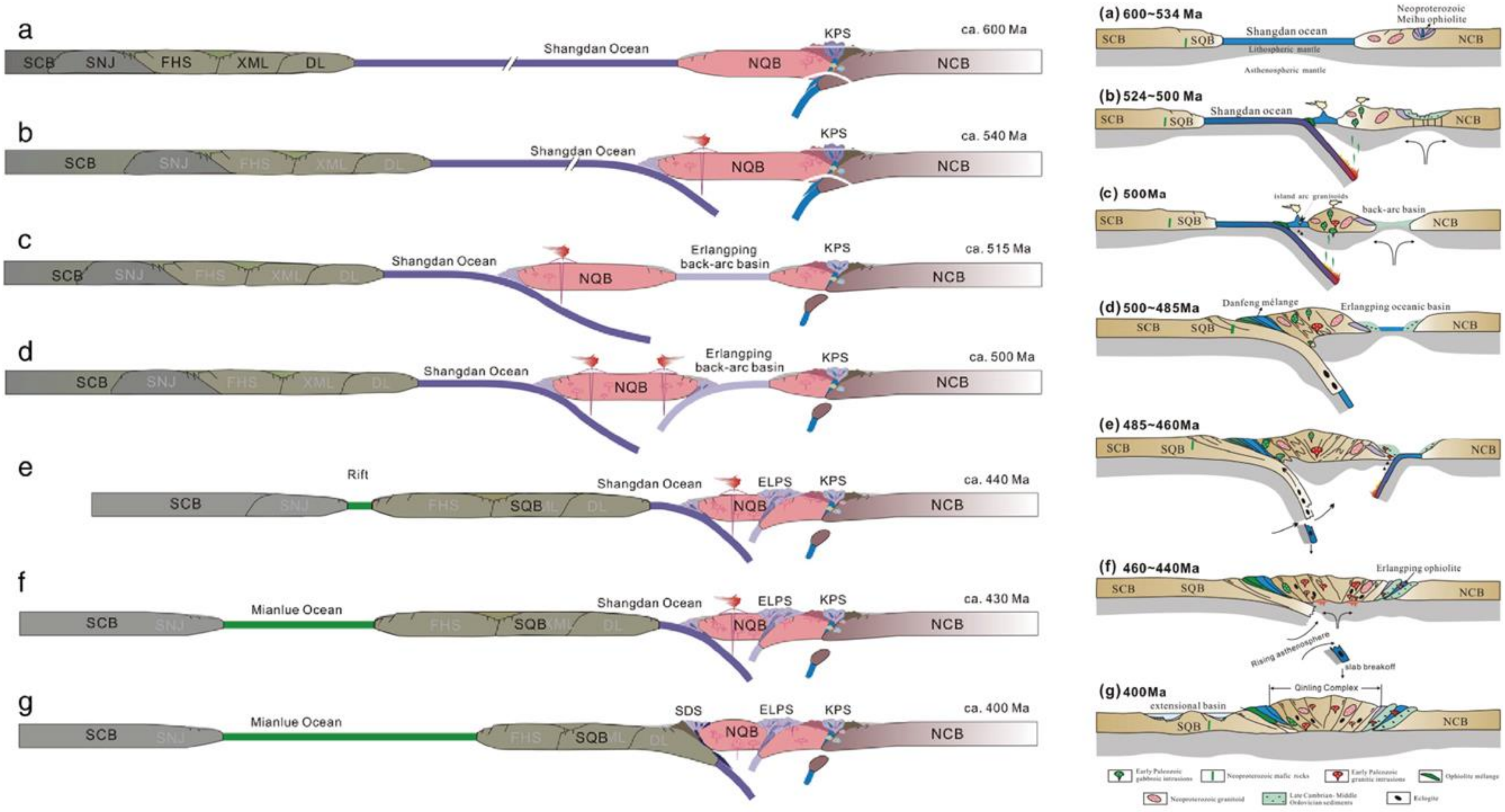

Figure 4.21 The comparison of the tectonic evolution models from Dong and Santosh (2016, left) and Liu et al. (2016, right) of the QOB during 600~400Ma.

As the youngest magmatic age in the NQB in the Paleozoic is ca.300Ma and it is I-type granitoid (Fig.13 in Wang et al., 2013), the subduction along the Shangdan suture may have ceased after 300Ma. However, there is a lack of the full collision between the NQB and the SQB (Dong and Santosh, 2016).

4.6.3 Tectonic model of the QOB during Triassic

The Mesozoic Mianlue suture is between the SCB and the SQB and marked by a serious of ophiolitic mélange, oceanic island and island-arc volcanic rocks (Zhang et al., 2001, 2015; Dong et al., 2011a; Dong and Santosh, 2016). The Triassic northward subduction and collision led to the final amalgamation of the NCB and the SCB and produced syn- and post-collisional granitoids in the SQB with ages of 245-200Ma (Dong et al., 2011a; Dong and Santosh, 2016).

In this thesis, the dominant strike-slip deformation along the SDTZ occurred at the late Triassic in the QOB is recognized. However, the late Triassic strike-slip deformation along the SDTZ show opposite kinematic senses in western Qinling (this chapter) and eastern Qinling (Chapter 3) that are separated by the narrowest segment in the SQB. In addition, the deformation along the Mianlue suture in western Qinling shows a sinistral sense of shear. The deformation age is constrained by a muscovite ^{40}Ar/^{39}Ar age (223Ma, Chen et al., 2010).

The tectonic evolution of the QOB during Triassic is proposed in Fig.4.22. Around 250Ma (Fig.4.22a), the Mianlue oceanic crust subducted under the SQB resulting in subduction-related volcanic rocks that are reported in the SQB (Wang et al., 2013). The subduction led to the gradual consumption of the oceanic crust

(Fig.4.22b), and the sediments of the Triassic Songpan-ganzi Complex came from both the SCB and the SQB (Enkelmann et al., 2007). According to the simulation results in Chapter 3, the convergence angle was in the range of $20° \sim 40°$. The Paleozoic Shangdan suture was acting as a weak inclusion in the QOB and accommodating strike-slip deformation in response to the oblique convergence. The voluminous granitoids ranging of ca.220-210Ma may reflect the collision between the SCB and the SQB. This model consists with the tectonic model proposed by Li et al. (2017) that is deduced from the syn-tectonic emplacement of the Baliping pluton in eastern Qinling during the Triassic. To the west (present coordinate) of the SQB, there might be some remnants of the Paleo-Tethys ocean so that the western Qinling and the Songpan-ganzi Complex had enough space to extrude to the west (Fig.4.22c). According to the results in this chapter and Chapter 3, the strike-slip deformation along the SDTZ may continue to ca.201Ma. The final collision between the SCB and the SQB led to the final amalgamation of the SCB and the NCB and produced the dramatic Dabashan thrust system and shortening structures in the SQB. According to Dong et al. (2013b), the Dabashan thrusting was active until the late Jurassic (ca.165Ma) in response to the convergence of the NCB and the SCB.

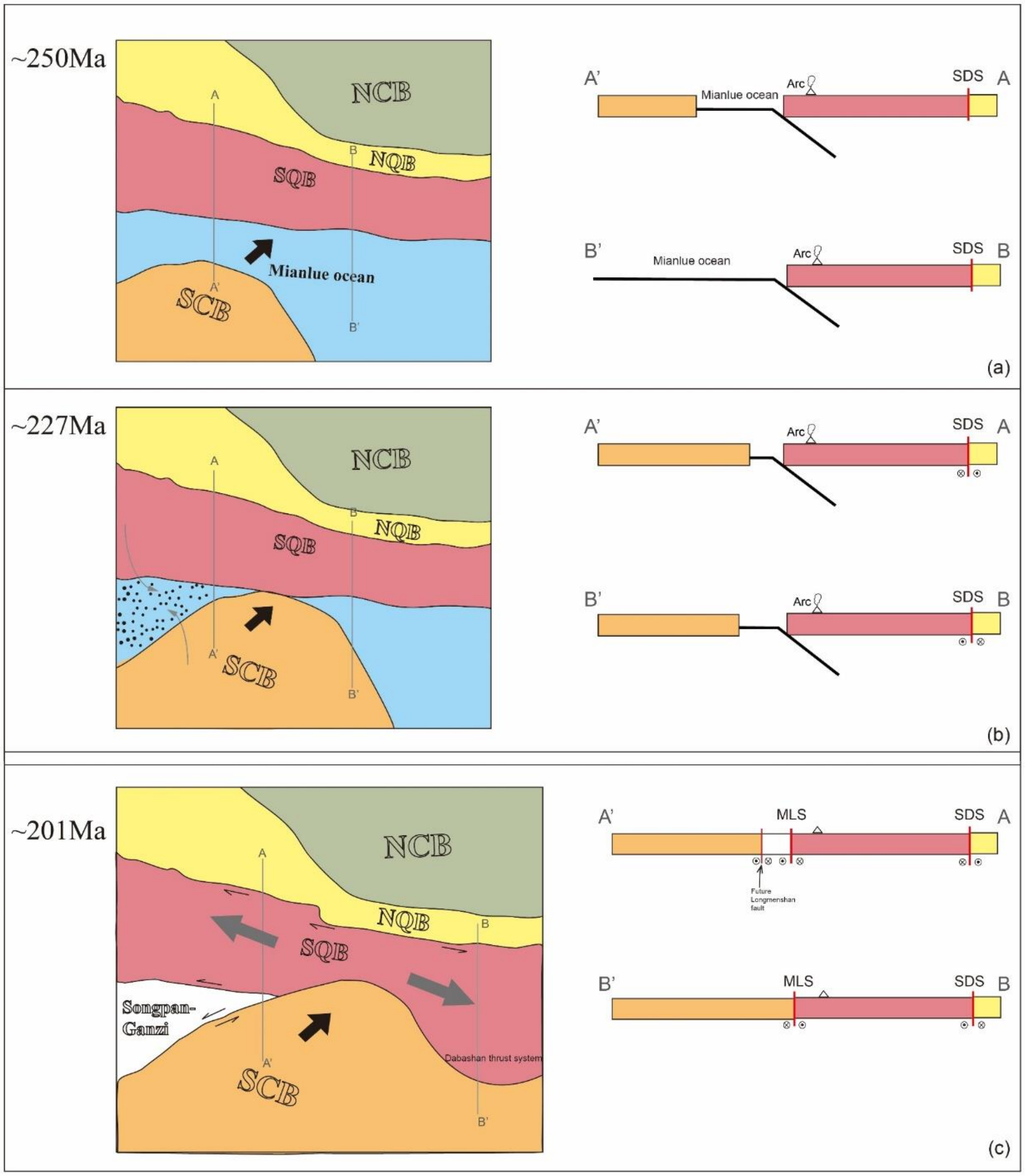

Figure 4.22 Schematic cartoons showing the tectonic evolution of the Qinling orogenic belt during the Triassic. NCB: North China Block, NQB: North Qinling Belt, SQB: South Qinling Belt, SCB: South China Block; SDS: Shangdan suture, MLS: Mianlue suture. Detailed explanation referred to the text.

4.6.4 The Cretaceous E-W extension recorded in the Liuling Group

The recumbent folds and the L-tectonites in the Liuling Group indicates an E-W extension and vertical thinning kinematic feature. The orogen-scale L-tectonites in the Tongbai orogenic belt can be correlated to this deformation in the Liuling Group according to the similar geometry and the locations (detailed discussion can be found in Section 3.4.2). As the L-tectonites in the Tongbai orogenic belt was developed between 140-135Ma (Liu et al., 2017), this deformation in the Liuling Group occurred during the same time, and they both reflect the early Cretaceous E-W extensional event in the Central China Orogenic Belt (CCOB).

However, this deformation is only observed in the Liuling Group in eastern Qinling but not found in western Qinling, which may indicate that the extension was not uniform throughout the whole orogen and it was more intense in the eastern part but weaker in the western part. This phenomenon is probably because, during the early Cretaceous, the Pacific Ocean was east (present coordinate) of the CCOB (Matthews et al., 2016) so that there was more space for the orogen to extrude to the east. This extension event may hold responsible for the formation of the Nanyang basin and the coeval magmatism in the eastern CCOB (Fig.4.23).

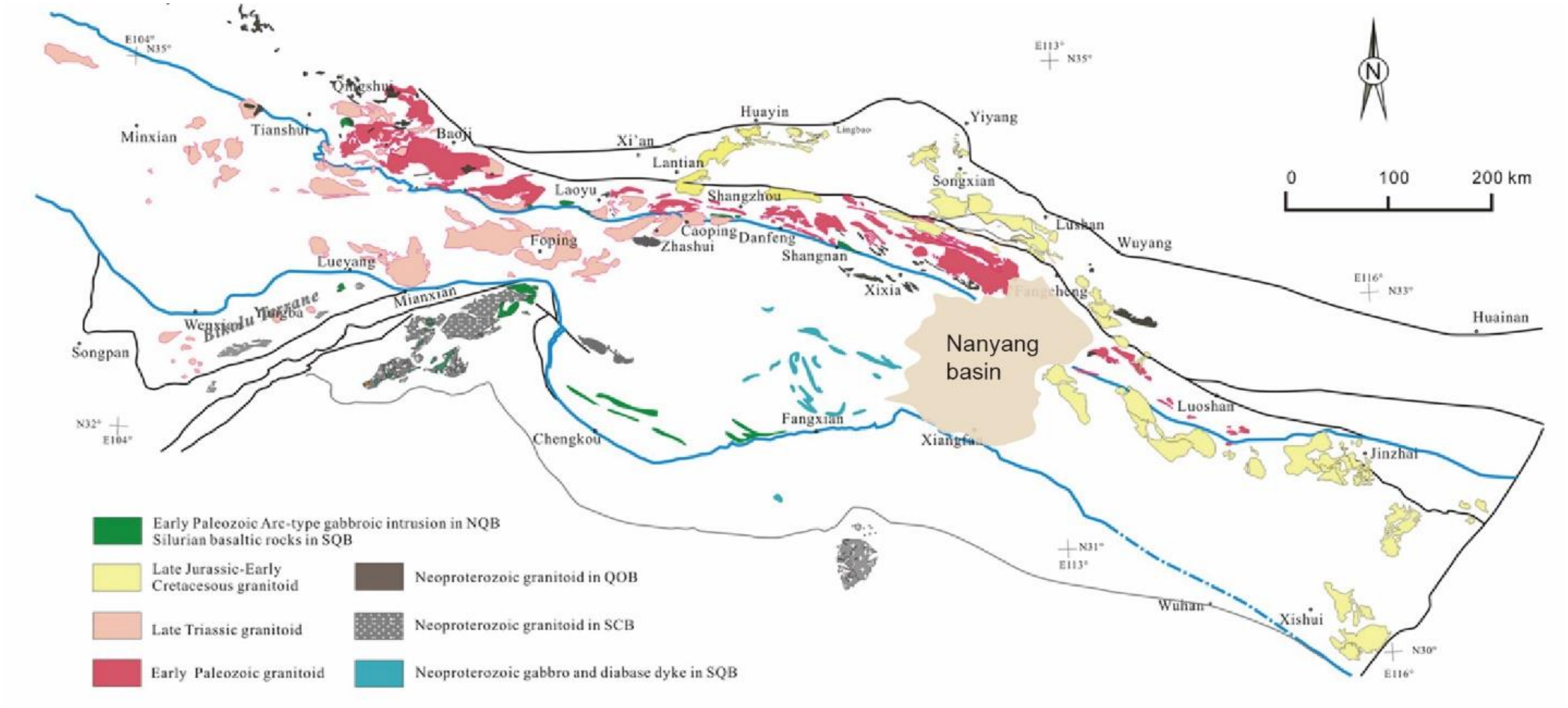

Figure 4.23 Geological map showing Neoproterozoic, Early Paleozoic, Late Triassic and Cretaceous magmatic intrusions in the Qinling orogenic belt (modified after Dong and Santosh, 2016).

4.7 References

Chen, D.L., Liu, L., Sun, Y., Zhang, A.D., Liu, X.M., Luo, J.H., 2004. Determination of the Neoproterozoic Shicaotou syn-collisional granite in the Eastern Qinling mountains and its geological implication. Acta Geol. Sin. (Engl. Ed.) 78, 73–82.

Chen, Z.H., Lu, S.N., Li, H.K., Li, H.M., Xiang, Z.Q., Zhou, H.Y., Song, B., 2006. Constraining the role of the Qinling orogen in the assembly and break-up of Rodinia: tectonic implications for Neoproterozoic granite occurrences. Journal of Asian Earth Sciences 28, 99–115.

Chen, J.L., 2008. Petrogenesis and Orogenic Processes of Early-Paleozoic Volcanic Rocks in the Western Segment of the North Qinling orogenic Belt, Central China Ph.D. Thesis, China University of Geoscience, Wuhan (192 pp.).

Chen, H., Hu, J. M., Wu, G. L., Gao, W., 2010. Study on the intracontinental deformation of the Mian-Lue suture belt, western Qinling. Acta Petrologica Sinica, 26, 1277–1288 (in Chinese with English abstract).

Chen, L., Liu, X., Qu, W., Hu, J., 2014. U-Pb zircon ages and geochemistry of the Wuguan complex in the Qinling orogen, central China: implications for the Late Paleozoic tectonic evolution between the Sino-Korean and Yangtze cratons. Lithos 192–195, 192–207.

Corfu, F., Hanchar, J.M., Hoskin, P.W. and Kinny, P., 2003. Atlas of zircon textures. Reviews in Mineralogy and Geochemistry, 53(1), pp.469-500.

Ding, S., Pei, X., Li, Y., Hu, B., Zhao, X., Guo, J., 2004. The dismemberment of the Liziyaun Group from Tianshui in Western Qinling and its tectonic setting analysis. Geological Bulletin of China, 23(12), pp.1209-1214 (in Chinese).

Ding, S., Pei, X., Li, Y., Li, B., Li, Z., Feng, J., Sun, Y., Zhang, Y., 2009. The biotite 40Ar-39Ar ages from the granitic mylonites in Xinyang-Yuanlong ductile shear zone in Western Qinling and its geological significance. Acta Geologica Sinica, 83(11), pp.1624-1632 (in Chinese).

Diwu, C.R., Sun, Y., Zhao, Y., Liu, B.X., Lai, S.C., 2014. Geochronological, geochemical, and Nd-Hf isotopic studies of the Qinling Complex, central China: implications for the evolutionary history of the North Qinling Orogenic Belt. Geosci. Front.5, 499–513.

Dong, Y. and Santosh, M., 2016. Tectonic architecture and multiple orogeny of the Qinling Orogenic Belt, Central China. Gondwana Research, 29(1), pp.1-40.

Dong, G., Yang, H.R., Yang, H.Y., Liu, D.Y., Zhang, J.X., Wan, Y.S., Zeng, J.Y., 2007a. SHRIMP U-Pb geochronology of Precambrian basement rocks in Qilian block and its tectonic significance. Chinese Science Bulletin, 52(13), pp.1572-1585 (in Chinese).

Dong, Y., Zhang, G., Yang, Z., Zhao, X., Ma, H., Yao., A., 2007b. Wushan E-MORB ophiolite and the geochemistry of related volcanic rocks in Western Qinling. Science in China (Series D)37(A01), pp.199-208 (in Chinese).

Dong, Y.P., Zhou, M.F., Zhang, G.W., Zhou, D.W., Liu, L., Zhang, Q., 2008. The Grenvillian Songshugou ophiolite in the Qinling Mountains, Central China: implications for the tectonic evolution of the Qinling orogenic belt. Journal of Asian Earth Sciences 32, 325–335.

Dong, Y., Zhang, G., Neubauer, F., Liu, X., Genser, J. and Hauzenberger, C., 2011a. Tectonic evolution of the Qinling orogen, China: review and synthesis. Journal of Asian Earth Sciences, 41(3), pp.213-237.

Dong, Y., Zhang, G., Hauzenberger, C., Neubauer, F., Yang, Z. and Liu, X., 2011b. Palaeozoic tectonics and evolutionary history of the Qinling orogen: evidence from geochemistry and geochronology of ophiolite and related volcanic rocks. Lithos, 122(1-2), pp.39-56.

Dong, Y., Genser, J., Neubauer, F., Zhang, G., Liu, X., Yang, Z. and Heberer, B., 2011c. U-Pb and 40Ar/39Ar geochronological constraints on the exhumation history of the North Qinling terrane, China. Gondwana Research, 19(4), pp.881-893.

Dong, Y., Liu, X., Neubauer, F., Zhang, G., Tao, N., Zhang, Y., Zhang, X. and Li, W., 2013a. Timing of Paleozoic amalgamation between the North China and South China Blocks: evidence from detrital zircon U–Pb ages. Tectonophysics, 586, pp.173-191.

Dong, S., Gao, R., Yin, A., Guo, T., Zhang, Y., Hu, J., Li, J., Shi, W. and Li, Q., 2013b. What drove continued continent-continent convergence after ocean closure? Insights from high-resolution seismic-reflection profiling across the Daba Shan in central China. Geology, 41(6), pp.671-674.

Enkelmann, E., Weislogel, A., Ratschbacher, L., Eide, E., Renno, A. and Wooden, J., 2007. How was the Triassic Songpan - Ganzi basin filled? A provenance study. Tectonics, 26(4).

Gehrels, G.E., Valencia, V.A. and Ruiz, J., 2008. Enhanced precision, accuracy, efficiency, and spatial resolution of U-Pb ages by laser ablation-multicollector-inductively coupled plasma-mass spectrometry. Geochemistry, Geophysics, Geosystems, 9(3).

Guo, J. and Zhao, F., 1999. Jinning collision-type granitoids in eastern of the middle Qilian block and its geological significance. Acta Geoscientica Sinica, 20(1), pp.10-15 (in Chinese).

Hiess, J., Condon, D.J., McLean, N. and Noble, S.R., 2012. 238U/235U systematics in terrestrial uranium-bearing minerals. Science, 335(6076), pp.1610-1614.

Hoskin, P.W. and Schaltegger, U., 2003. The composition of zircon and igneous and metamorphic petrogenesis. Reviews in Mineralogy and Geochemistry, 53(1), pp.27-62.

Jiang, D., 2014. Structural geology meets micromechanics: A self-consistent model for the multiscale deformation and fabric development in Earth's ductile lithosphere. Journal of Structural Geology, 68, pp.247-272.

Li, W.Y., 2008. Geochronology and geochemistry of the ophiolites and island-arc-type igneous rocks in the Western Qinling orogen and the Eastern Kunlun orogen: Implication for the evolution of the Tethyan Ocean. University of Science and Technology of China, Hefei, pp.1-154.

Li, Y., Liang, W., Zhang, G., Jiang, D. and Wang, J., 2017. Tectonic setting of the Late Triassic magmatism in the Qinling Orogen: New constraints from the interplay between granite emplacement and shear zone deformation in the Shagou area. Geological Journal, 52(S1), pp.250-271.

Liang, X., Sun, S., Dong, Y., Yang, Z., Liu, X. and He, D., 2017. Fabrics and geochronology of the Wushan ductile shear zone: Tectonic implications for the Shangdan suture zone in the Qinling orogen, Central China. Journal of Asian Earth Sciences, 139, pp.71-82.

Liao, X.Y., Wang, Y.W., Liu, L., Wang, C. and Santosh, M., 2017. Detrital zircon U-Pb and Hf isotopic data from the Liuling Group in the South Qinling belt: Provenance and tectonic implications. Journal of Asian Earth Sciences, 134, pp.244-261.

Liu, L., Liao, X., Wang, Y., Wang, C., Santosh, M., Yang, M., Zhang, C. and Chen, D., 2016. Early Paleozoic tectonic evolution of the North Qinling Orogenic Belt in Central China: Insights on continental deep subduction and multiphase exhumation. Earth-Science Reviews, 159, pp.58-81.

Liu, H., Lin, S., Song, C. and Wu, M., 2017. Structure and geochronology of the Tongbai complex and their implications for the evolution of the Tongbai orogenic belt, central China. International Geology Review, 59(4), pp.470-483.

Lu, S.N., Li, H.K., Chen, Z.H., Hao, G.J., Zhou, H.Y., Guo, J.J., Niu, G.H., Xiang, Z.Q., 2003. Meso-Neoproterozoic Geological Evolution of the Qinling and Its

Respondence to Rodinia Event. Geological Publishing House, Beijing, pp. 1–194 (in Chinese).

Lu, R., 2008. Tectonic framework and conjunction and transformation on the boundary belt of Qinling-Qilian in Indo-Chinese epoch. Ph.D. thesis (in Chinese with English abstract).

Lu, S.N., Yu, H.F., Li, H.K., Chen, Z.H., Wang, H.C., Zhang, C.L., 2009. Precambrian Geology of the West and Middle Central China Orogen. Geological Publishing House, pp. 76–98 (in Chinese).

Ludwig, K.R., 2003. User's manual for isoplot 3.00, a geochronological toolkit for Microsoft excel. Berkeley Geochronl. Cent. Spec. Publ., 4, pp.25-32.

Matthews, K.J., Maloney, K.T., Zahirovic, S., Williams, S.E., Seton, M. and Mueller, R.D., 2016. Global plate boundary evolution and kinematics since the late Paleozoic. Global and Planetary Change, 146, pp.226-250.

Meng, Q.R. and Zhang, G.W., 1999. Timing of collision of the North and South China blocks: controversy and reconciliation. Geology, 27(2), pp.123-126.

Pei, X.Z., Wang, T., Ding, S.P., Li, Y. and Hu, B., 2003. Geochemical characteristics and geological significance of Neoproterozoic adakitic granitoids on the north side of the Shangdan zone in the East Qinling. Chinese Geology, 30(4), pp.372-381(in Chinese with English abstract).

Pei, X., Ding, S., Li, Z., Liu, Z., Li, G., Li, R., Wang, F., Li, F., 2007a. The formation time of the Guanzizhen ophiolite in Western Qinling: evidences from LA-ICP-MS zircons ages of gabbro. Acta Geologica Sinica, 81(11), pp.1550-1561 (in Chinese).

Pei, X., Ding, S., Zhang, G., Liu, H., Li, Z., Li, W., Liu, Z., Meng, Y., 2007b. LA-ICP-MS zircon U-Pb ages from Neoproterozoic granitic gneiss in Western Qinling and their geological significance. Acta Geologica Sinica, 81(6), pp.772-786 (in Chinese).

Pei, X., Li, Z., Li, R., Pei, L., Liu, C., Gao, J., Wei, F., Wu, S., Wang, Y. and Chen, Y., 2012. LA-ICP-MS U-Pb ages of detrital zircons from the meta-detrital rocks of the Early Palaeozoic Huluhe Group in the eastern part of Qilian orogenic belt: Constraints of the material source and sedimentary age. Earth Sci. Front, 19(5), pp.205-224 (in Chinese with English abstract).

Qin, J.F., Lai, S.C., Grapes, R., Diwu, C., Ju, Y.J., Li, Y.F., 2009. Geochemical evidence for origin of magma mixing for the Triassic monzonitic granite and its enclaves at Mishuling in the Qinling orogen (central China). Lithos 112, 259–276.

Qin, J.F., Lai, S.C., Diwu, C.R., Ju, Y.J., Li, Y.F., 2010. Magma mixing origin for the post-collisional adakitic monzogranite of the Triassic Yangba pluton, northwestern margin of the South China Block: geochemistry, Sr–Nd isotopic, zircon U–Pb dating and Hf isotopic evidences. Contributions to Mineralogy and Petrology 159, 389–409.

Ratschbacher, L., Hacker, B.R., Calvert, A., Webb, L.E., Grimmer, J.C., McWilliams, M.O., Ireland, T., Dong, S. and Hu, J., 2003. Tectonics of the Qinling (Central China): tectonostratigraphy, geochronology, and deformation history. Tectonophysics, 366(1-2), pp.1-53.

Ratschbacher, L., Franz, L., Enkelmann, E., Jonckheere, R., Porschke, A., Hacker, B.R., Dong, S. and Zhang, Y., 2006. The Sino-Korean-Yangtze suture, the Huwan detachment, and the Paleozoic-Tertiary exhumation of (ultra) high-pressure rocks along the Tongbai-Xinxian-Dabie Mountains. Special Papers-Geological Society of America, 403, p.45.

Roberts, N.M. and Spencer, C.J., 2015. The zircon archive of continent formation through time. Geological Society, London, Special Publications, 389(1), pp.197-225.

Shi, Y., Yu, J.H., Xu, X.S., Q, J.S., Chen, L.H., 2009. Geochronology and geochemistry of the Qinling Group in the eastern Qinling Orogen. Acta Petrol. Sin. 25 (10), 2651–2670 (in Chinese with English abstract).

Spencer, C.J., Kirkland, C.L. and Taylor, R.J., 2016. Strategies towards statistically robust interpretations of in situ U–Pb zircon geochronology. Geoscience Frontiers, 7(4), pp.581-589.

Sun, S.S. and McDonough, W.S., 1989. Chemical and isotopic systematics of oceanic basalts: implications for mantle composition and processes. Geological Society, London, Special Publications, 42(1), pp.313-345.

van Staal, C.R., Dewey, J.F., Mac Niocaill, C. and McKerrow, W.S., 1998. The Cambrian-Silurian tectonic evolution of the northern Appalachians and British Caledonides: history of a complex, west and southwest Pacific-type segment of Iapetus. Geological Society, London, Special Publications, 143(1), pp.197-242.

Voice, P.J., Kowalewski, M. and Eriksson, K.A., 2011. Quantifying the timing and rate of crustal evolution: Global compilation of radiometrically dated detrital zircon grains. The Journal of Geology, 119(2), pp.109-126.

Wan, Y.S., Liu, D.Y., Dong, C.Y., Yin, X.Y., 2011. SHRIMP zircon dating of meta-sedimentary rock from the Qinling Group in the north of Xixia, North Qinling Orogenic Belt: constraints on complex histories of source region and timing of deposition and metamorphism. Acta Petrol. Sin. 27 (4), 1172–1178 (in Chinese with English abstract).

Wan, Y., Xu, Z., Yang, J. and Zhang, J., 2003. The Precambrian high-grade basement of the Qilian terrane and neighboring areas: its ages and compositions. Acta Geoscientia Sinica, 24(4; ISSU 77), pp.319-324(in Chinese with English abstract).

Wang, T., Wang, X.X., Zhang, G.W., Pei, X.Z., Zhang, C.L., 2003. Rernnants of a Neoproterozoic collisional orogenic belt in the core of the Phanerozoic Qinling orogenic belt (China). Gondwana Research 6, 699–710.

Wang, X.X., Wang, T., Happala, I., Lu, X.X., 2005. Genesis of mafic enclaves from rapakivi-textured granites in the Qinling and its petrological significance: evidence of elements and Nd, Sr isotopes. Acta Petrologica Sinica 20, 935–946 (in Chinese with English abstract).

Wang, X.X., Wang, T., Jahn, B.M., Hu, N.G., Chen, W., 2007. Tectonic significance of Late Triassic post-collisional lamprophyre dykes from the Qinling Mountains (China): 40Ar–39Ar dating, trace element and Sr–Nd, isotope characteristics. Geological Magazine 144 (4), 1–12.

Wang, T., Wang, X.X., Tian, W., Zhang, C.L., Li, W.P., Li, S., 2009. North Qinling Paleozoic granite associations and their variation in space and time: implications for orogenic processes in the orogens of central China. Sci. China Ser. D Earth Sci. 52, 1359–1384.

Wang, T.G., Ni, P., Sun, W.D., Zhao, K.D., Wang, X.D., 2011. Zircon U–Pb ages of granites at Changba and Huangzhuguan in western Qinling and implications for source nature. Chinese Science Bulletin 56, 659–669.

Wang, X.X., Wang, T., Zhang, C.L., 2013. Neoproterozoic, Paleozoic, and Mesozoic granitoid magmatism in the Qinling Orogen, China: constraints on orogenic process. J. Asian Earth Sci. 72, 129–151.

Wang, H.,Wu, Y.B., Gao, S., Liu, X.C., Gong, H.J., Li, Q.L., Li, X.H., Yuan, H.L., 2011. Eclogite origin and timings in the North Qinling terrane, and their bearing on the amalgamation of the South and North China Blocks. Journal of Metamorphic Geology 29, 1019–1031.

Wilson, J.T., 1966. Did the Atlantic Close and then Re-Open?. Nature, 211, pp.676-681.

Wu, Y.B. and Zheng, Y.F., 2013. Tectonic evolution of a composite collision orogen: an overview on the Qinling–Tongbai–Hong'an–Dabie–Sulu orogenic belt in central China. Gondwana Research, 23(4), pp.1402-1428.

Xu, J.F., Castillo, P.R., Li, X.H., Yu, X.Y., Zhang, B.R., Han, Y.W., 2002. MORB-type rocks from the Paleo-Tethyan Mian–Lueyang northern ophiolite in the Qinling

Mountains, central China: implications for the source of the low 206Pb/204Pb and high 143Nd/144Nd mantle component in the Indian Ocean. Earth and Planetary Science Letters 198, 323–337.

Xue, F., Lerch, M.F., Kroner, A., Reischmann, T., 1996. Tectonic evolution of the east Qinling Mountains, China, in the Palaeozoic: a review and new tectonic model. Tectonophysics 253, 271–284.

Yan, Z., Fu, C., Wang, Z., Yan, Q., Chen, L. and Chen, J., 2016. Late Paleozoic subduction–accretion along the southern margin of the North Qinling terrane, central China: evidence from zircon U-Pb dating and geochemistry of the Wuguan Complex. Gondwana Research, 30, pp.97-111.

Yang, Q.Y. and Santosh, M., 2015. Paleoproterozoic arc magmatism in the North China Craton: no Siderian global plate tectonic shutdown. Gondwana Research 28, 82–105.

Yang, J.S., Xu, Z.Q., Dobrzhinetskaya, L.F., Green, H.W., Pei, X.Z., Shi, R.D.,Wu, C.L.,Wooden, J.L., Zhang, J.X.,Wan, Y.S., 2003. Discovery of metamorphic diamonds in central China: an indication of a N4000 km long zone of deep subduction resulting from multiple continental collisions. Terra Nova 15, 370–379.

Yang, L., Chen, F.K., Yang, Y.Z., Li, S.Q., Zhu, X.Y., 2010. Zircon U-Pb ages of the Qinling group in Danfeng area: recording Mesoproterozoic and Neoproterozoic magmatism and Early Paleozoic metamorphism in the North Qinling terrain. Acta Petrol. Sin. 26 (5), 1589–1603 (in Chinese with English abstract).

Yong, Y., Xiao, W., Yuan, C., Li, J., Yan, Z., Mao, Q., 2008. LA-ICP-MS zircon U-Pb ages of granitoids in eastern part of the middle Qilian and their geological significance. Xinjiang Geology, 26(1), pp.62-62 (in Chinese).

You, Z.D., Suo, S.T., Han, Y.J., Zhong, Z.Q., Chen, N.S., 1991. The Metamorphic Progresses and Tectonic Analyses in the Core Complex of an Orogenic Belt: An

Example from the Eastern Qinling Mountains. China University of Geosciences, Wuhan, pp. 1–326 (in Chinese with English abstract).

Zhai, M.G., 2014. Multi-stage crustal growth and cratonization of the North China Craton. Geoscience Frontiers 5, 457–469.

Zhang, Z.Q. and Zhang, Q., 1995. Geochemistry of metamorphosed Late Proterozoic Kuanping ophiolite in the Northern Qinling, China. Acta Petrologica Sinica 11, 165-177 (in Chinese with English Abstract).

Zhang, Z.Q., Liu, D.Y., Fu, G.M., 1994. Isotopic Geochronology of Metamorphic Strata in North Qinling. Geological Publishing House, Beijing, pp. 1–191 (in Chinese with English abstract).

Zhang, G.W., Meng, Q.R., Lai, S.C., 1995. Structure and tectonics of the Qinling Orogenic belt. Science in China. Series B 25, 994–1003.

Zhang, H.F., Zhang, B.R., Ling, W.L., Luo, T.C., Xu, J.F., 1996. Paleo-oceanic crust recycling in north Qinling: evidence of Pb, Nd, Sr isotopes from island arc granitoids. Chinese Science Bulletin 41, 234–237.

Zhang, G.W., Zhang, B.R., Yuan, X.C., Xiao, Q.H., 2001. Qinling Orogenic Belt and Continental Dynamics. Science Press, Beijing, pp. 1–855 (in Chinese with English abstract).

Zhang, C.L., Liu, L., Zhang, G.W., Wang, T., Chen, D.L., Yuan, H.L., Liu, X.M., Yan, Y.X., 2004. Determination of Neoproterozoic post-collisional granites in the north Qinling Mountains and its tectonic significance. Earth Sci. Front. 11, 33–42 (in Chinese with English abstract).

Zhang, C.L., Zhang, G.W., Yan, Y.X., Wang, Y., 2005. Origin and dynamic significance of Guangtoushan granitic plutons to the north of Mianlue zone in southern Qinling. Acta Petrologica Sinica 21 (3), 711–720 (in Chinese with English abstract).

Zhang, C.L., Liu, L., Wang, T., Wang, X.X., Li, L., Gong, Q.F., Li, X.F., 2013. Granitic magmatism related to early Paleozoic continental collision in North Qinling. Chin. Sci. Bull. 35, 4405–4410.

Zhang, G.W., Dong, Y.P. and Li, S.Z., 2015. The Mianlue Tectonic Zone of the Qinling Orogen and China Continental Tectonics. Sci. Press, Beijing, pp.1-501 (in Chinese with English abstract).

Zhao, G.C. and Zhai, M.G., 2013. Lithotectonic elements of Precambrian basement in the North China Craton: review and tectonic implications. Gondwana Research 23, 1207–1240.

Zhu, B.Q., 2001. Geochemical Province and Geochemical Steep Zone. Science Press, Beijing, pp. 1–118 (in Chinese with English abstract).

Chapter 5: Conclusions and Future Work

In this thesis, the detailed field work is conducted along the Shangdan tectonic zone (SDTZ) in the Qinling orogenic belt (QOB), China. The multiscale structures along the SDTZ is documented and analyzed. With the help of the recently-developed multiscale approach and the geochronological studies, we try to understand the tectonic evolution and kinematics of the SDTZ and its implications for the Qinling tectonics.

5.1 Contribution of this work

The multiscale approach used in this thesis is called the multi-order power-law approach (MOPLA) (Jiang and Bentley, 2012; Jiang, 2014). MOPLA is developed to study the heterogenous deformation throughout Earth's lithosphere. The heterogenous deformation results from the rheological heterogeneities of the lithosphere (Lister and Williams, 1979, 1983), and MOPLA treats a heterogeneous material as a continuum of rheologically distinct elements. The rheological properties of the material and the mechanical fields of each constituent element are computed by solving the partitioning and homogenization equations self-consistently. The algorithm is based on the solution of an Eshelby viscous inclusion in a linear viscous medium and the extension of the solution to non-linear viscous materials (Jiang and Bentley, 2012; Jiang 2014, 2016). The bottleneck of the computation is to numerically evaluate Eshelby tensors for the constituent elements. In this thesis, we develop an optimal scheme for evaluating Eshelby tensors, using a combination of a product Gaussian quadrature and the Lebedev quadrature. We first establish, through numerical experiments, an empirical relationship between the inclusion shape and the computational time it takes to evaluate its Eshelby tensors. We then use the relationship to develop an optimal scheme for selecting the most efficient quadrature to obtain the Eshelby tensors. This optimal scheme is adopted into MOPLA. Currently, MOPLA is fully developed into MATLAB and Mathcad.

This work shows the importance of the structural geology studies to the tectonic evolution of an orogenic belt. The previous work in the QOB is mainly focused on the framework of the evolution of the QOB (e.g., Zhang et al., 2001; Ratschbacher et al., 2003, 2006; Bader et al., 2013a,b; Dong and Santosh, 2016), but the detailed kinematics of the orogen and the various structures in the orogen are not related to the tectonic evolution precisely, which is mainly because of the lack of detailed structural geology studies in the QOB.

In this thesis, three deformation events are identified in the SDTZ and its adjacent areas. They are labeled as D_1 deformation, D_2 deformation and D_3 deformation, respectively. D_1 deformation is a NE-SW (to the current coordinate system) shortening deformation and occurred between ca.385-355Ma. D_1 deformation is only observed to the north of the SDTZ in western Qinling. D_2 deformation is a strike-slip dominant deformation and occurred between ca.227-201Ma. In western Qinling, D_2 deformation is a dextral strike-slip along the SDTZ; In eastern Qinling, D_2 deformation is a sinistral strike-slip along the SDTZ and N-S (to the current coordinate system) shortening deformation in the Liuling Group that is south of the SDTZ. D_3

deformation is an along-orogen extension and occurred between ca.140-135Ma. D_3 deformation is only observed in the Liuling Group in eastern Qinling.

D_2 deformation, the opposite shearing along the SDTZ and the N-S (to the current coordinate system) shortening deformation in the Liuling Group, was a response to the oblique convergence between the South China Block and the North China Block. The convergence angle is constrained to 20°~40° using MOPLA.

In this thesis, predominant strike-slip along the SDTZ is clearly established, which suggests that the non-coaxial deformation inside the QOB have a demonstrably profound effect on the tectonic evolution and the current style (i.e., linear zonation) of the QOB (see discussions in Section 4.6.1 for detail). In previous Qinling models, the orthogonal subductions and collisions among different tectonic blocks are mainly considered. The geological units can be highly transposed during an oblique convergence, so the once continuous element may be scattered and far away from each other during the final convergence. This 'dynamic' idea should be adopted in the future studies of the QOB.

5.2 Future work

The strike-slip deformation time along the SDTZ in western Qinling is constrained by the age of a syn-deformation dyke (i.e., XY1605). However, there is only one analysis (Spot No.10 in XY1605, Fig.E12). More zircons from XY1605 will be analyzed for a better constrain of the crystallization age of this dyke.

In Fig.4.22, a tectonic model is proposed to explain the opposite shearing along the SDTZ. According to the model, the western Qinling was extruding to the west which resulted in the dextral strike-slip deformation along the SDTZ in western Qinling. In this case, there would be an along-strike extension component in the boundary condition of the SDTZ. However, in Jiang (2014), only the transpressional condition that does not include an along-strike stretching component has been considered. Therefore, to better constrain the boundary conditions of the fabrics in the SDTZ in western Qinling, more boundary conditions need to be tested.

According to the tectonic model in Fig.4.22, the neck area (i.e., the narrowest segment in the SQB) would show very interesting structures, and thus more field work will be conducted in this area.

5.3 References

Bader, T., Ratschbacher, L., Franz, L., Yang, Z., Hofmann, M., Linnemann, U. and Yuan, H., 2013a. The heart of China revisited, I. Proterozoic tectonics of the Qin mountains in the core of supercontinent Rodinia. Tectonics, 32(3), pp.661-687.

Bader, T., Franz, L., Ratschbacher, L., Capitani, C., Webb, A.A.G., Yang, Z., Pfänder, J.A., Hofmann, M. and Linnemann, U., 2013b. The Heart of China revisited: II Early Paleozoic (ultra) high-pressure and (ultra) high-temperature metamorphic Qinling orogenic collage. Tectonics, 32(4), pp.922-947.

Dong, Y. and Santosh, M., 2016. Tectonic architecture and multiple orogeny of the Qinling Orogenic Belt, Central China. Gondwana Research, 29(1), pp.1-40.

Jiang, D., 2014. Structural geology meets micromechanics: A self-consistent model for the multiscale deformation and fabric development in Earth's ductile lithosphere. Journal of Structural Geology, 68, pp.247-272.

Jiang, D. and Bentley, C., 2012. A micromechanical approach for simulating multiscale fabrics in large-scale high-strain zones: Theory and application. Journal of Geophysical Research: Solid Earth, 117(B12).

Lister, G.S. and Williams, P.F., 1979. Fabric development in shear zones: theoretical controls and observed phenomena. Journal of Structural Geology, 1(4), pp.283-297.

Lister, G.S. and Williams, P.F., 1983. The partitioning of deformation in flowing rock masses. Tectonophysics, 92(1-3), pp.1-33.

Ratschbacher, L., Hacker, B.R., Calvert, A., Webb, L.E., Grimmer, J.C., McWilliams, M.O., Ireland, T., Dong, S. and Hu, J., 2003. Tectonics of the Qinling (Central China): tectonostratigraphy, geochronology, and deformation history. Tectonophysics, 366(1-2), pp.1-53.

Ratschbacher, L., Franz, L., Enkelmann, E., Jonckheere, R., Porschke, A., Hacker, B.R., Dong, S. and Zhang, Y., 2006. The Sino-Korean-Yangtze suture, the Huwan detachment, and the Paleozoic-Tertiary exhumation of (ultra) high-pressure rocks along the Tongbai-Xinxian-Dabie Mountains. Special Papers-Geological Society of America, 403, p.45.

Zhang, G.W., Zhang, B.R., Yuan, X.C., Xiao, Q.H., 2001. Qinling Orogenic Belt and Continental Dynamics. Science Press, Beijing, pp. 1–855 (in Chinese with English abstract).

Appendices

Appendix A: Empirical functions for the domain boundaries in Fig.2.4

According to the computational time contours in Fig.3.3, we use MATLAB built-in function, *fit*, to empirically construct four curves: $R = f_1(\Phi)$ (computational time ~ 3s), $R = f_2(\Phi)$ (computational time ~ 15s), $R = f_3(\Phi)$ (computational time ~ 30s), $R = f_4(\Phi)$ (computational time ~ 40s).

The expressions of the four curves are as follows:

$$R_1 = -1.944\times10^{-8}\Phi^4 - 4.289\times10^{-6}\Phi^3 + 1.325\times10^{-3}\Phi^2 - 0.0958\Phi + 2.552 \tag{A1}$$

$$R_2 = 1.025\times10^{-8}\Phi^4 - 2.461\times10^{-6}\Phi^3 + 6.203\times10^{-4}\Phi^2 - 0.06954\Phi + 4.018 \tag{A2}$$

$$R_3 = 1.496\times10^{-7}\Phi^4 - 2.729\times10^{-5}\Phi^3 + 1.792\times10^{-3}\Phi^2 - 0.07242\Phi + 4.583 \tag{A3}$$

$$\begin{aligned} R_4 = 3.693 &+ 0.7857\cos(0.05009\Phi) + 0.4061\sin(0.05009\Phi) + \\ &0.1859\cos(2\times0.05009\Phi) - 0.09161\sin(2\times0.05009\Phi) + \\ &0.08343\cos(3\times0.05009\Phi) - 0.02982\sin(3\times0.05009\Phi) \end{aligned} \tag{A4}$$

Appendix B: The MATLAB package instruction in Chapter 2

The MATLAB package can be downloaded from the online version of this paper.

1. Before executing the four functions (i.e., *SGLRGD*, *SGLDEF*, *MLTRGD, MLTDEF*), one needs to add all folders and subfolders to the current path in MATLAB.
2. Input parameters for each function are as follows:

   1) SGLRGD

   L is the imposed velocity gradient tensor, a 3 by 3 matrix;

   a is the three semi-axes of the ellipsoid, a 3 by 1 matrix;

   ang is the three spherical angles (in degree), a 3 by 1 matrix;

   tincr is the time increment, the choice of *tincr* must ensure that each step of computation represents an infinitesimal rotation;

   steps is the total computational steps;

   mm is the number if computation steps between plotting sets;

   m is the anisotropy for the matrix.

   2) *SGLDEF*

   Besides the 7 parameters introduced in SGLRGD, the other 4 parameters are:

   Nm is the stress exponent of the matrix;

   Ne is the stress exponent of the ellipsoid;

   r is the initial ratio of the inclusion viscosity to the matrix η_n;

   REF is an initial effective viscosity of the ellipsoid.

   3) *MLTRGD*

L, *tincr*, *steps*, *m* are as same as those in *SGLRGD*, and

n is the number of ellipsoids;

a_1 the maximum semi-axis of ellipsoids;

4) *MLTDEF*

L, *tincr*, *steps*, *m*, *Nm*, *Ne* are as same as those in *MLTRGD* and *SGLDEF*, and

rmax and *rmin* define the range of viscosity ratio between the ellipsoids and the matrix at the initial state.

One may refer to the *"ReadMe.txt"* and comment lines in the package for more detailed descriptions.

Appendix C: Download link for the MATLAB package in Chapter 2.

The MATLAB package can be downloaded here: https://www.dropbox.com/sh/l8dbixpl0nq81ns/AAAtFKJykavgCY5lHy0HM411a?dl=0

Appendix D: The $R_f - \varphi$ data from the deformed conglomerate in Chapter 3.

Section 1 strike: 162° slope: 17°

Pebble type	long-axis (mm)	short-axis (mm)	R_f	ϕ (degree)
Granitoid	50	36	1.4	173
Granitoid	150	44	3.4	166
Granitoid	120	35	3.4	166
Granitoid	136	90	1.5	166
Granitoid	125	48	2.6	166
Granitoid	105	40	2.6	163
Granitoid	110	21	5.2	159
Granitoid	155	40	3.9	159
Granitoid	135	40	3.4	159
Granitoid	220	33	6.7	155
Granitoid	137	46	3.0	155
Granitoid	144	26	5.5	155
Granitoid	52	11	4.7	152
Granitoid	265	63	4.2	152
Granitoid	79	23	3.4	152
Granitoid	133	25	5.3	148
Granitoid	63	14	4.5	148
Granitoid	162	47	3.4	148
Granitoid	79	49	1.6	144
Granitoid	50	10	5.0	144
Granitoid	189	17	11.1	144
Granitoid	105	36	2.9	139
Granitoid	75	27	2.8	139
Granitoid	59	16	3.7	139
Granitoid	179	61	2.9	139
Granitoid	140	45	3.1	124
Granitoid	75	31	2.4	118
Granitoid	57	24	2.4	144
Marble	71	11	6.5	144
Marble	40	7	5.7	135
Marble	23	6	3.8	135
Marble	40	16	2.5	135
Marble	32	20	1.6	135
Marble	172	24	7.2	130
Marble	45	10	4.5	144
Marble	19	5	3.8	136
Marble	55	14	3.9	134
Marble	59	9	6.6	108
Marble	44	7	6.3	90
Quartzite	45	17	2.6	173
Quartzite	44	9	4.9	173
Quartzite	31	19	1.6	173
Quartzite	32	23	1.4	173
Quartzite	192	57	3.4	173
Quartzite	67	42	1.6	173
Quartzite	47	11	4.3	173
Quartzite	43	29	1.5	170
Quartzite	143	31	4.6	170
Quartzite	38	7	5.4	170
Quartzite	106	31	3.4	170
Quartzite	86	15	5.7	166
Quartzite	190	30	6.3	166
Quartzite	22	10	2.2	166
Quartzite	62	19	3.3	166
Quartzite	11	7	1.6	166
Quartzite	38	6	6.3	159
Quartzite	98	41	2.4	159
Quartzite	58	34	1.7	159
Quartzite	62	22	2.8	159
Quartzite	22	6	3.7	159
Quartzite	28	11	2.5	159
Quartzite	67	31	2.2	159
Quartzite	131	34	3.9	155
Quartzite	168	48	3.5	155
Quartzite	119	21	5.7	155
Quartzite	22	3	7.3	152
Quartzite	47	22	2.1	152
Quartzite	63	9	7.0	152
Quartzite	74	24	3.1	152
Quartzite	132	31	4.3	152
Quartzite	62	7	8.9	152
Quartzite	77	23	3.3	152
Quartzite	12	8	1.5	152
Quartzite	21	8	2.6	152
Quartzite	30	5	6.0	152
Quartzite	68	30	2.3	148
Quartzite	21	9	2.3	148
Quartzite	25	21	1.2	148
Quartzite	53	21	2.5	148
Quartzite	27	9	3.0	148
Quartzite	121	46	2.6	144
Quartzite	52	21	2.5	144
Quartzite	48	21	2.3	144
Quartzite	39	18	2.2	144
Quartzite	26	9	2.9	144
Quartzite	84	25	3.4	139
Quartzite	36	7	5.1	139
Quartzite	112	19	5.9	139
Quartzite	53	5	10.6	139
Quartzite	66	28	2.4	139
Quartzite	49	4	12.3	135
Quartzite	39	3	13.0	135
Quartzite	41	9	4.6	135
Quartzite	59	32	1.8	130
Quartzite	28	6	4.7	124
Quartzite	51	21	2.4	124
Quartzite	22	12	1.8	109

Section 2 strike: 169° slope: 21°

Pebble type	long-axis (mm)	short-axis (mm)	R_f	ϕ (degree)
Amphibolite	240	23	10.4	163
Amphibolite	107	22	4.9	157
Amphibolite	170	33	5.2	157
Amphibolite	128	20	6.4	151
Amphibolite	103	33	3.1	151
Amphibolite	98	31	3.2	148

Amphibolite	92	29	3.2	148
Amphibolite	125	35	3.6	148
Amphibolite	320	41	7.8	138
Amphibolite	54	23	2.3	134
Amphibolite	113	22	5.1	134
Amphibolite	58	60	1.0	130
Amphibolite	320	27	11.9	125
Amphibolite	116	39	3.0	107
Amphibolite	79	14	5.6	131
Amphibolite	200	54	3.7	131
Amphibolite	310	20	15.5	119
Amphibolite	145	55	2.6	110
Granitoid	150	64	2.3	169
Granitoid	117	34	3.4	163
Granitoid	154	62	2.5	163
Granitoid	183	69	2.7	154
Granitoid	90	57	1.6	148
Granitoid	138	54	2.6	148
Granitoid	129	57	2.3	145
Granitoid	193	73	2.6	145
Granitoid	102	66	1.5	145
Granitoid	59	9	6.6	145
Granitoid	94	37	2.5	141
Granitoid	160	31	5.2	138
Granitoid	66	21	3.1	138
Granitoid	136	52	2.6	134
Granitoid	82	20	4.1	134
Granitoid	75	50	1.5	130
Granitoid	124	44	2.8	130
Granitoid	65	28	2.3	130
Granitoid	56	21	2.7	130
Granitoid	64	30	2.1	125
Granitoid	110	42	2.6	125
Granitoid	122	47	2.6	125
Granitoid	97	46	2.1	120
Granitoid	136	65	2.1	120
Granitoid	105	62	1.7	120
Granitoid	121	62	2.0	120
Granitoid	108	40	2.7	115
Granitoid	132	63	2.1	115
Granitoid	57	32	1.8	107
Granitoid	127	47	2.7	107
Granitoid	161	40	4.0	107
Granitoid	149	42	3.5	107
Granitoid	74	28	2.6	107
Granitoid	122	59	2.1	107
Granitoid	122	21	5.8	107
Granitoid	68	30	2.3	90
Granitoid	129	59	2.2	131
Granitoid	48	12	4.0	131
Granitoid	142	60	2.4	131
Granitoid	58	24	2.4	126
Granitoid	120	74	1.6	126
Granitoid	124	54	2.3	122
Granitoid	173	42	4.1	122
Granitoid	80	34	2.4	119
Granitoid	122	35	3.5	119
Granitoid	90	70	1.3	110
Granitoid	116	51	2.3	104
Granitoid	112	50	2.2	104
Granitoid	79	47	1.7	95
Quartzite	39	13	3.0	169
Quartzite	54	18	3.0	163
Quartzite	160	43	3.7	160
Quartzite	43	15	2.9	157
Quartzite	49	22	2.2	157
Quartzite	64	29	2.2	154
Quartzite	114	24	4.8	151
Quartzite	112	23	4.9	151
Quartzite	36	23	1.6	145
Quartzite	123	65	1.9	145
Quartzite	32	13	2.5	138
Quartzite	37	11	3.4	138
Quartzite	115	43	2.7	138
Quartzite	48	15	3.2	138
Quartzite	31	15	2.1	138
Quartzite	45	19	2.4	138
Quartzite	34	16	2.1	134
Quartzite	40	16	2.5	134
Quartzite	85	29	2.9	130
Quartzite	45	27	1.7	130
Quartzite	103	28	3.7	130
Quartzite	83	24	3.5	130
Quartzite	99	34	2.9	130
Quartzite	91	18	5.1	125
Quartzite	51	18	2.8	125
Quartzite	32	16	2.0	120
Quartzite	56	19	2.9	120
Quartzite	36	18	2.0	120
Quartzite	99	18	5.5	120
Quartzite	109	38	2.9	120
Quartzite	41	16	2.6	120
Quartzite	34	12	2.8	120
Quartzite	113	42	2.7	115
Quartzite	143	19	7.5	107
Quartzite	65	23	2.8	107
Quartzite	39	17	2.3	107
Quartzite	84	33	2.5	107
Quartzite	35	11	3.2	90
Quartzite	112	43	2.6	131
Quartzite	75	33	2.3	131
Quartzite	82	41	2.0	131
Quartzite	121	52	2.3	131
Quartzite	119	41	2.9	126
Quartzite	116	46	2.5	126
Quartzite	62	20	3.1	126
Quartzite	94	36	2.6	126
Quartzite	93	35	2.7	119
Quartzite	33	11	3.0	119
Quartzite	62	24	2.6	90

Section 3 strike: 040° slope: 64°

Pebble type	long-axis (mm)	short-axis (mm)	R_f	ϕ (degree)
Amphibolite	218	42	5.2	18
Amphibolite	120	37	3.2	35
Amphibolite	111	37	3.0	45
Amphibolite	94	23	4.1	25
Amphibolite	117	30	3.9	35
Amphibolite	40	25	1.6	50
Amphibolite	65	45	1.4	30

Amphibolite	72	32	2.3	15
Amphibolite	80	21	3.8	150
Amphibolite	100	20	5.0	30
Granitoid	104	68	1.5	20
Granitoid	114	49	2.3	20
Granitoid	68	19	3.6	18
Granitoid	80	22	3.6	67
Granitoid	82	47	1.7	170
Granitoid	105	58	1.8	45
Granitoid	66	37	1.8	35
Granitoid	52	18	2.9	10
Granitoid	65	26	2.5	20
Granitoid	86	29	3.0	25
Granitoid	82	33	2.5	152
Granitoid	122	37	3.3	52
Granitoid	70	42	1.7	105
Granitoid	90	23	3.9	75
Granitoid	123	40	3.1	150
Granitoid	123	36	3.4	168
Granitoid	100	20	5.0	50
Granitoid	48	19	2.5	60
Granitoid	121	28	4.3	37
Granitoid	37	19	1.9	120
Granitoid	35	13	2.7	55
Granitoid	78	35	2.2	57
Granitoid	43	20	2.2	50
Quartzite	90	18	5.0	25
Quartzite	68	19	3.6	35
Quartzite	75	31	2.4	40
Quartzite	20	13	1.5	40
Quartzite	95	9	10.6	20
Quartzite	38	12	3.2	30
Quartzite	58	19	3.1	23
Quartzite	55	18	3.1	50
Quartzite	54	39	1.4	20
Quartzite	40	18	2.2	50

Section 4 strike: 072° slope: 47°

Pebble type	long-axis (mm)	short-axis (mm)	R_f	ϕ (degree)
Amphibolite	158	32	4.9	12
Amphibolite	175	18	9.7	9
Amphibolite	76	32	2.4	11
Amphibolite	108	25	4.3	14
Amphibolite	110	22	5.0	12
Amphibolite	96	23	4.2	13
Amphibolite	122	23	5.3	12
Amphibolite	41	11	3.7	10
Amphibolite	135	41	3.3	14
Amphibolite	203	30	6.8	21
Amphibolite	113	40	2.8	20
Amphibolite	120	28	4.3	13
Amphibolite	193	30	6.4	10
Amphibolite	130	40	3.3	10
Amphibolite	84	28	3.0	12
Amphibolite	90	31	2.9	20
Amphibolite	163	42	3.9	10
Amphibolite	257	90	2.9	12
Amphibolite	240	75	3.2	11
Amphibolite	42	12	3.5	10
Amphibolite	132	31	4.3	13
Amphibolite	184	60	3.1	15
Amphibolite	133	30	4.4	21
Amphibolite	90	21	4.3	14
Amphibolite	82	34	2.4	11
Amphibolite	126	21	6.0	12
Granitoid	216	50	4.3	15
Granitoid	177	50	3.5	12
Granitoid	112	12	9.3	25
Granitoid	135	21	6.4	10
Granitoid	115	33	3.5	14
Granitoid	165	48	3.4	13
Granitoid	160	30	5.3	8
Granitoid	144	53	2.7	12
Granitoid	309	52	5.9	15
Granitoid	120	21	5.7	15
Granitoid	230	38	6.1	10
Granitoid	190	55	3.5	15
Granitoid	141	45	3.1	15
Granitoid	155	35	4.4	15
Granitoid	156	26	6.0	3
Granitoid	230	46	5.0	2
Granitoid	220	55	4.0	10
Granitoid	176	64	2.8	15
Granitoid	114	25	4.6	8
Granitoid	180	55	3.3	8
Granitoid	211	45	4.7	5
Granitoid	134	30	4.5	13
Granitoid	245	50	4.9	16
Granitoid	140	40	3.5	9
Granitoid	120	37	3.2	7
Granitoid	125	50	2.5	7
Granitoid	190	48	4.0	9
Granitoid	125	43	2.9	14
Granitoid	220	22	10.0	13
Granitoid	141	35	4.0	12
Marble	106	9	11.8	12
Marble	55	3	18.3	10
Marble	69	15	4.6	11
Marble	96	13	7.4	12
Marble	30	4	7.5	3
Marble	87	20	4.4	10
Marble	63	20	3.2	8
Marble	26	9	2.9	10
Marble	43	3	14.3	10
Marble	20	2	10.0	10
Quartzite	120	26	4.6	12
Quartzite	165	7	23.6	7
Quartzite	95	6	15.8	11
Quartzite	55	12	4.6	6
Quartzite	77	12	6.4	6
Quartzite	165	75	2.2	12
Quartzite	105	33	3.2	9
Quartzite	23	9	2.6	10
Quartzite	18	4	4.5	12
Quartzite	27	7	3.9	135
Quartzite	222	19	11.7	13
Quartzite	31	6	5.2	10
Quartzite	137	11	12.5	11

Section 5 strike: 245° slope: 14°

Pebble type	long-axis (mm)	short-axis (mm)	R_f	ϕ (degree)
Granitoid	230	36	6.4	24
Granitoid	155	23	6.7	35
Granitoid	87	40	2.2	35
Granitoid	110	35	3.1	23
Granitoid	205	25	8.2	15
Granitoid	73	53	1.4	45
Granitoid	75	15	5.0	20
Granitoid	70	45	1.6	20
Granitoid	220	48	4.6	35
Granitoid	95	28	3.4	35
Granitoid	104	18	5.8	20
Granitoid	82	32	2.6	23
Granitoid	171	28	6.1	13
Granitoid	341	32	10.7	25
Granitoid	86	30	2.9	30
Granitoid	472	34	13.9	28
Granitoid	170	34	5.0	20
Granitoid	205	50	4.1	18
Granitoid	104	25	4.2	30
Granitoid	125	13	9.6	25
Granitoid	170	39	4.4	15
Granitoid	59	22	2.7	18
Granitoid	169	80	2.1	20
Granitoid	90	35	2.6	25
Granitoid	135	35	3.9	20
Granitoid	115	38	3.0	27
Granitoid	201	21	9.6	13
Granitoid	50	12	4.2	20
Granitoid	155	35	4.4	20
Granitoid	125	54	2.3	20
Granitoid	89	12	7.4	12
Granitoid	111	30	3.7	15
Granitoid	170	60	2.8	25
Granitoid	142	50	2.8	15
Granitoid	155	36	4.3	25
Granitoid	230	25	9.2	20
Granitoid	122	40	3.1	25
Granitoid	87	53	1.6	20
Granitoid	164	90	1.8	170
Granitoid	189	47	4.0	20
Granitoid	110	23	4.8	20
Granitoid	52	25	2.1	28
Granitoid	140	42	3.3	18
Granitoid	73	23	3.2	15
Granitoid	95	40	2.4	15
Granitoid	123	70	1.8	18
Granitoid	43	19	2.3	25
Granitoid	116	54	2.1	10
Granitoid	277	47	5.9	12
Granitoid	100	29	3.4	13
Quartzite	161	29	5.6	11
Quartzite	108	20	5.4	30
Quartzite	120	40	3.0	22
Quartzite	205	30	6.8	13
Quartzite	140	20	7.0	15
Quartzite	220	14	15.7	12
Quartzite	80	18	4.4	10
Quartzite	143	43	3.3	13
Quartzite	120	35	3.4	15
Quartzite	90	55	1.6	8

Section 6 strike: 145° slope: 10°

Pebble type	long-axis (mm)	short-axis (mm)	R_f	ϕ (degree)
Amphibolite	156	43	3.6	115
Amphibolite	90	27	3.3	110
Amphibolite	111	40	2.8	120
Amphibolite	138	45	3.1	115
Amphibolite	153	90	1.7	120
Amphibolite	155	35	4.4	120
Amphibolite	205	47	4.4	125
Amphibolite	264	90	2.9	100
Amphibolite	217	30	7.2	110
Amphibolite	242	46	5.3	106
Amphibolite	155	43	3.6	117
Amphibolite	172	30	5.7	125
Amphibolite	88	22	4.0	120
Amphibolite	168	32	5.3	115
Amphibolite	42	14	3.0	115
Amphibolite	163	50	3.3	105
Amphibolite	170	38	4.5	112
Amphibolite	133	47	2.8	110
Amphibolite	103	20	5.2	110
Amphibolite	105	27	3.9	120
Granitoid	80	12	6.7	115
Granitoid	180	75	2.4	105
Granitoid	80	37	2.2	115
Granitoid	90	24	3.8	114
Granitoid	180	100	1.8	122
Granitoid	188	42	4.5	120
Granitoid	125	50	2.5	124
Granitoid	190	64	3.0	115
Granitoid	90	20	4.5	102
Granitoid	120	39	3.1	117
Granitoid	60	25	2.4	102
Granitoid	90	24	3.8	130
Granitoid	82	21	3.9	130
Granitoid	55	21	2.6	125
Granitoid	75	23	3.3	122
Granitoid	120	38	3.2	123
Granitoid	170	50	3.4	115
Granitoid	60	35	1.7	130
Granitoid	90	27	3.3	115
Granitoid	73	25	2.9	110
Granitoid	105	43	2.4	107
Granitoid	125	50	2.5	103
Granitoid	100	50	2.0	102
Granitoid	55	25	2.2	100
Granitoid	92	32	2.9	129
Granitoid	173	60	2.9	115
Granitoid	75	50	1.5	110
Granitoid	95	20	4.8	115
Granitoid	75	25	3.0	113
Granitoid	100	35	2.9	114
Granitoid	140	40	3.5	107
Granitoid	82	30	2.7	115
Granitoid	42	35	1.2	85
Granitoid	82	27	3.0	107
Granitoid	90	34	2.6	106

Granitoid	105	50	2.1	100
Granitoid	50	22	2.3	102
Granitoid	100	45	2.2	100
Granitoid	72	27	2.7	123
Granitoid	108	30	3.6	107
Granitoid	93	47	2.0	100
Granitoid	73	28	2.6	105
Granitoid	217	30	7.2	110
Granitoid	102	35	2.9	108
Granitoid	54	18	3.0	130
Granitoid	97	28	3.5	108
Granitoid	120	18	6.7	120
Granitoid	164	53	3.1	98
Granitoid	140	39	3.6	117
Granitoid	120	20	6.0	109
Granitoid	54	17	3.2	110
Granitoid	85	20	4.3	120
Granitoid	460	53	8.7	108
Granitoid	105	50	2.1	106
Granitoid	80	17	4.7	110
Granitoid	100	45	2.2	120
Granitoid	50	15	3.3	105
Granitoid	95	30	3.2	110
Granitoid	45	15	3.0	120
Granitoid	105	30	3.5	115
Granitoid	75	30	2.5	113
Granitoid	155	44	3.5	113
Granitoid	93	49	1.9	120
Granitoid	65	50	1.3	112
Granitoid	50	40	1.3	110
Granitoid	55	35	1.6	130
Granitoid	73	42	1.7	95
Granitoid	75	40	1.9	102
Granitoid	143	43	3.3	110
Granitoid	102	40	2.6	115
Granitoid	155	49	3.2	120
Granitoid	155	47	3.3	115
Granitoid	220	65	3.4	115
Granitoid	100	40	2.5	130
Granitoid	93	30	3.1	103
Granitoid	95	34	2.8	100
Granitoid	100	45	2.2	105
Granitoid	135	33	4.1	135
Granitoid	105	25	4.2	103
Granitoid	54	15	3.6	120
Quartzite	104	41	2.5	130
Quartzite	170	41	4.1	120
Quartzite	90	20	4.5	135
Quartzite	140	19	7.4	125
Quartzite	136	20	6.8	123
Quartzite	56	30	1.9	105
Quartzite	50	23	2.2	125
Quartzite	117	20	5.9	115
Quartzite	126	39	3.2	120
Quartzite	72	27	2.7	125
Quartzite	81	13	6.2	120
Quartzite	122	46	2.7	105
Quartzite	45	27	1.7	132
Quartzite	94	28	3.4	125
Quartzite	105	30	3.5	118

Section 7 strike: 082° slope: 40°

Pebble type	long-axis (mm)	short-axis (mm)	R_f	ϕ (degree)
Amphibolite	43	14	3.1	16
Amphibolite	70	32	2.2	164
Amphibolite	66	15	4.4	164
Amphibolite	149	68	2.2	166
Amphibolite	28	9	3.1	162
Amphibolite	102	59	1.7	1
Amphibolite	183	49	3.7	169
Amphibolite	82	34	2.4	28
Amphibolite	51	19	2.7	167
Granitoid	138	56	2.5	26
Granitoid	72	25	2.9	14
Granitoid	51	24	2.1	165
Granitoid	32	16	2.0	152
Granitoid	161	36	4.5	174
Granitoid	294	79	3.7	168
Granitoid	161	42	3.8	162
Granitoid	57	16	3.6	169
Granitoid	58	21	2.8	179
Granitoid	42	12	3.5	11
Granitoid	58	22	2.6	9
Granitoid	126	27	4.7	12
Granitoid	95	39	2.4	24
Granitoid	166	59	2.8	168
Granitoid	149	41	3.6	2
Granitoid	118	26	4.5	21
Granitoid	92	20	4.6	23
Marble	69	20	3.5	9
Marble	80	30	2.7	171
Marble	47	16	2.9	6
Marble	105	50	2.1	177
Marble	86	11	7.8	6
Marble	30	4	7.5	18
Quartzite	29	6	4.8	1
Quartzite	24	4	6.0	178
Quartzite	34	12	2.8	176
Quartzite	34	14	2.4	12
Quartzite	70	11	6.4	6
Quartzite	91	29	3.1	17
Quartzite	39	18	2.2	172
Quartzite	20	7	2.9	162
Quartzite	64	7	9.1	176
Quartzite	61	19	3.2	172
Quartzite	158	24	6.6	12
Quartzite	44	17	2.6	166
Quartzite	52	29	1.8	8
Quartzite	59	9	6.6	16
Quartzite	58	8	7.3	169
Quartzite	44	17	2.6	11

Section 8 strike: 072° slope: 68°

Pebble type	long-axis (mm)	short-axis (mm)	R_f	ϕ (degree)
Amphibolite	162	59	2.7	174
Amphibolite	211	30	7.0	16
Amphibolite	113	24	4.7	171
Amphibolite	67	24	2.8	11
Amphibolite	168	31	5.4	19
Amphibolite	150	62	2.4	12

Amphibolite	181	82	2.2	19
Amphibolite	150	57	2.6	31
Amphibolite	162	40	4.1	13
Amphibolite	184	30	6.1	11
Amphibolite	87	23	3.8	175
Amphibolite	87	27	3.2	168
Granitoid	209	56	3.7	12
Granitoid	76	24	3.2	15
Granitoid	62	35	1.8	14
Granitoid	130	36	3.6	10
Granitoid	310	116	2.7	23
Granitoid	156	32	4.9	11
Granitoid	104	31	3.4	19
Granitoid	105	26	4.0	16
Granitoid	102	41	2.5	174
Granitoid	78	20	3.9	11
Granitoid	182	41	4.4	14
Granitoid	110	32	3.4	17
Granitoid	119	46	2.6	179
Granitoid	87	27	3.2	174
Granitoid	78	44	1.8	65
Granitoid	108	55	2.0	12
Granitoid	75	19	3.9	174
Granitoid	148	72	2.1	155
Marble	83	18	4.6	12
Marble	71	26	2.7	28
Marble	32	6	5.3	3
Marble	57	9	6.3	6
Marble	46	5	9.2	4
Marble	74	19	3.9	12
Marble	194	20	9.7	176
Marble	34	6	5.7	2
Marble	50	12	4.2	3
Quartzite	31	12	2.6	11
Quartzite	16	7	2.3	9
Quartzite	47	25	1.9	7
Quartzite	255	52	4.9	15
Quartzite	76	26	2.9	8
Quartzite	140	21	6.7	12
Quartzite	78	22	3.5	2
Quartzite	80	22	3.6	7
Quartzite	74	14	5.3	14
Quartzite	12	7	1.7	22
Quartzite	46	9	5.1	13
Quartzite	45	22	2.0	164
Quartzite	22	4	5.5	4
Quartzite	62	32	1.9	167
Quartzite	45	14	3.2	16
Quartzite	36	11	3.3	12
Quartzite	72	16	4.5	20
Quartzite	135	40	3.4	15
Quartzite	75	43	1.7	26
Quartzite	51	17	3.0	12

Section 9 strike: 067° slope: 28°

Pebble type	long-axis (mm)	short-axis (mm)	R_f	ϕ (degree)
Amphibolite	180	25	7.2	15
Amphibolite	60	22	2.7	175
Amphibolite	110	19	5.8	176
Amphibolite	80	26	3.1	167
Amphibolite	120	30	4.0	166
Amphibolite	70	12	5.8	13
Amphibolite	75	30	2.5	170
Amphibolite	55	12	4.6	172
Amphibolite	115	28	4.1	175
Amphibolite	95	21	4.5	15
Amphibolite	132	22	6.0	12
Amphibolite	12	6	2.0	5
Amphibolite	83	21	4.0	0
Amphibolite	80	10	8.0	10
Amphibolite	90	17	5.3	15
Amphibolite	190	31	6.1	170
Amphibolite	160	52	3.1	18
Amphibolite	72	13	5.5	12
Amphibolite	102	23	4.4	0
Granitoid	110	23	4.8	170
Granitoid	120	42	2.9	10
Granitoid	92	35	2.6	8
Granitoid	170	35	4.9	169
Granitoid	220	50	4.4	12
Granitoid	220	70	3.1	160
Granitoid	130	25	5.2	164
Granitoid	130	80	1.6	0
Granitoid	142	29	4.9	14
Granitoid	140	10	14.0	20
Granitoid	150	40	3.8	20
Granitoid	220	50	4.4	18
Granitoid	200	50	4.0	22
Granitoid	95	21	4.5	17
Granitoid	110	30	3.7	21
Granitoid	143	17	8.4	16
Granitoid	200	88	2.3	18
Granitoid	130	36	3.6	18
Granitoid	120	41	2.9	12
Granitoid	200	95	2.1	5
Granitoid	70	20	3.5	20
Granitoid	120	60	2.0	160
Granitoid	100	25	4.0	12
Granitoid	100	13	7.7	10
Granitoid	110	22	5.0	25
Granitoid	130	30	4.3	170
Marble	150	12	12.5	170
Marble	160	6	26.7	175
Marble	41	11	3.7	10
Marble	72	12	6.0	175
Marble	76	9	8.4	12
Marble	46	6	7.7	13
Marble	41	5	8.2	7
Marble	70	10	7.0	15
Marble	26	4	6.5	15
Marble	36	6	6.0	15
Marble	50	12	4.2	160
Marble	26	6	4.3	11
Marble	103	7	14.7	11
Marble	42	10	4.2	7
Marble	330	10	33.0	178
Marble	69	12	5.8	167
Marble	59	10	5.9	2
Marble	260	19	13.7	175
Marble	63	14	4.5	170

Marble	82	7	11.7	1
Marble	60	10	6.0	2
Quartzite	100	20	5.0	15
Quartzite	75	25	3.0	20
Quartzite	23	5	4.6	27
Quartzite	240	52	4.6	15
Quartzite	170	15	11.3	10
Quartzite	50	20	2.5	10
Quartzite	110	19	5.8	19
Quartzite	70	13	5.4	15
Quartzite	60	10	6.0	175
Quartzite	30	11	2.7	11
Quartzite	110	23	4.8	175
Quartzite	110	10	11.0	10
Quartzite	110	22	5.0	170
Quartzite	90	23	3.9	0
Quartzite	55	30	1.8	10
Quartzite	290	40	7.3	15
Quartzite	100	23	4.3	165
Quartzite	65	10	6.5	5
Quartzite	110	12	9.2	0
Quartzite	75	10	7.5	10
Quartzite	80	10	8.0	0

Section 10 strike: 154° slope: 48°

Pebble type	long-axis (mm)	short-axis (mm)	R_f	ϕ (degree)
Amphibolite	110	57	1.9	143
Amphibolite	74	36	2.1	132
Amphibolite	85	63	1.3	120
Amphibolite	66	35	1.9	126
Granitoid	120	32	3.8	120
Granitoid	86	23	3.7	150
Granitoid	53	16	3.3	145
Granitoid	90	63	1.4	90
Granitoid	50	31	1.6	138
Granitoid	62	29	2.1	147
Granitoid	62	11	5.6	133
Quartzite	42	30	1.4	125
Quartzite	39	23	1.7	110
Quartzite	29	13	2.2	105
Quartzite	62	31	2.0	60

Section 11 strike: 085° slope: 47°

Pebble type	long-axis (mm)	short-axis (mm)	R_f	ϕ (degree)
Amphibolite	50	16	3.1	168
Amphibolite	64	34	1.9	165
Amphibolite	32	22	1.5	167
Amphibolite	48	17	2.8	150
Amphibolite	150	22	6.8	160
Granitoid	100	83	1.2	170
Granitoid	56	21	2.7	179
Granitoid	105	31	3.4	11
Granitoid	95	22	4.3	175
Granitoid	75	13	5.8	165
Granitoid	55	22	2.5	155
Granitoid	110	20	5.5	178
Granitoid	80	36	2.2	150
Granitoid	62	16	3.9	170
Granitoid	51	22	2.3	165
Granitoid	60	9	6.7	170
Quartzite	49	30	1.6	2
Quartzite	19	8	2.4	5
Quartzite	21	13	1.6	3
Quartzite	40	18	2.2	0
Quartzite	110	30	3.7	175
Quartzite	36	10	3.6	170
Quartzite	165	33	5.0	14
Quartzite	43	18	2.4	15
Quartzite	56	19	2.9	170
Quartzite	95	12	7.9	2
Quartzite	103	7	14.7	175
Quartzite	33	7	4.7	178
Quartzite	42	20	2.1	170

Section 12 strike: 196° slope: 74°

Pebble type	long-axis (mm)	short-axis (mm)	R_f	ϕ (degree)
Amphibolite	56	52	1.1	155
Amphibolite	79	32	2.5	156
Amphibolite	38	16	2.4	166
Amphibolite	31	24	1.3	86
Amphibolite	45	27	1.7	102
Amphibolite	83	36	2.3	165
Granitoid	200	90	2.2	175
Granitoid	91	44	2.1	172
Granitoid	76	27	2.8	26
Granitoid	101	35	2.9	169
Granitoid	97	44	2.2	128
Granitoid	67	35	1.9	135
Granitoid	114	46	2.5	148
Granitoid	69	42	1.6	70
Granitoid	40	22	1.8	176
Granitoid	52	36	1.4	85
Granitoid	158	110	1.4	124
Granitoid	74	56	1.3	140
Granitoid	58	46	1.3	122
Granitoid	62	48	1.3	95
Granitoid	74	41	1.8	8
Granitoid	55	33	1.7	162
Granitoid	58	35	1.7	129
Granitoid	39	25	1.6	98
Granitoid	51	36	1.4	115
Granitoid	205	120	1.7	168
Granitoid	65	35	1.9	142
Granitoid	64	26	2.5	130
Granitoid	52	35	1.5	96
Granitoid	59	58	1.0	94
Quartzite	32	28	1.1	145
Quartzite	33	22	1.5	130
Quartzite	22	13	1.7	0
Quartzite	31	17	1.8	110
Quartzite	26	12	2.2	0
Quartzite	35	20	1.8	5
Quartzite	18	11	1.6	100
Quartzite	23	12	1.9	135
Quartzite	22	14	1.6	2
Quartzite	35	18	1.9	6

Section 13 strike: 162° slope: 17°

Pebble type	long-axis (mm)	short-axis (mm)	R_f	ϕ (degree)
Amphibolite	132	48	2.8	113

Amphibolite	48	12	4.0	107
Amphibolite	128	38	3.4	110
Amphibolite	86	27	3.2	105
Amphibolite	105	26	4.0	97
Amphibolite	58	16	3.6	107
Amphibolite	108	18	6.0	96
Amphibolite	174	53	3.3	100
Amphibolite	78	39	2.0	105
Amphibolite	123	37	3.3	102
Amphibolite	173	44	3.9	97
Amphibolite	168	17	9.9	94
Amphibolite	92	32	2.9	93
Amphibolite	117	34	3.4	97
Amphibolite	131	41	3.2	87
Amphibolite	61	22	2.8	92
Amphibolite	127	22	5.8	97
Granitoid	53	27	2.0	101
Granitoid	80	33	2.4	125
Granitoid	120	26	4.6	110
Granitoid	153	32	4.8	105
Granitoid	90	18	5.0	95
Granitoid	69	45	1.5	125
Granitoid	90	37	2.4	80
Granitoid	40	10	4.0	90
Granitoid	38	13	2.9	95
Granitoid	99	25	4.0	113
Granitoid	122	25	4.9	105
Granitoid	157	20	7.9	105
Granitoid	70	30	2.3	135
Granitoid	60	15	4.0	105
Granitoid	65	54	1.2	114
Granitoid	263	62	4.2	105
Granitoid	78	22	3.5	100
Granitoid	179	42	4.3	85
Granitoid	216	36	6.0	90
Granitoid	187	42	4.5	100
Granitoid	149	42	3.5	92
Granitoid	173	25	6.9	85
Granitoid	127	81	1.6	115
Granitoid	116	40	2.9	100
Granitoid	153	46	3.3	98
Granitoid	120	50	2.4	83
Granitoid	123	48	2.6	103
Granitoid	117	22	5.3	93
Granitoid	62	42	1.5	125
Granitoid	78	15	5.2	83
Granitoid	147	40	3.7	97

Section 14 strike: 162° slope: 13°

Pebble type	long-axis (mm)	short-axis (mm)	R_f	ϕ (degree)
Amphibolite	142	23	6.2	97
Amphibolite	59	11	5.4	96
Amphibolite	53	31	1.7	102
Amphibolite	64	22	2.9	102
Amphibolite	43	23	1.9	103
Amphibolite	43	26	1.7	93
Amphibolite	54	14	3.9	97
Amphibolite	72	17	4.2	88
Amphibolite	73	11	6.6	101
Amphibolite	54	16	3.4	97
Amphibolite	82	12	6.8	97
Amphibolite	73	18	4.1	96
Amphibolite	197	27	7.3	93
Amphibolite	136	37	3.7	107
Amphibolite	93	18	5.2	106
Amphibolite	72	12	6.0	103
Amphibolite	111	42	2.6	108
Amphibolite	43	19	2.3	104
Amphibolite	117	33	3.5	103
Amphibolite	100	36	2.8	101
Amphibolite	83	34	2.4	106
Amphibolite	92	23	4.0	102
Amphibolite	66	54	1.2	108
Amphibolite	85	26	3.3	109
Amphibolite	70	18	3.9	96
Amphibolite	69	30	2.3	97
Amphibolite	41	21	2.0	110
Amphibolite	81	29	2.8	95
Amphibolite	47	21	2.2	97
Amphibolite	62	27	2.3	97
Amphibolite	93	37	2.5	103
Amphibolite	64	31	2.1	100
Amphibolite	32	18	1.8	96
Amphibolite	39	13	3.0	102
Granitoid	218	80	2.7	80
Granitoid	82	20	4.1	107
Granitoid	119	28	4.3	99
Granitoid	75	20	3.8	90
Granitoid	187	42	4.5	110
Granitoid	150	90	1.7	107
Granitoid	52	25	2.1	125
Granitoid	120	77	1.6	135
Granitoid	63	26	2.4	100
Granitoid	138	56	2.5	90
Granitoid	130	49	2.7	117
Granitoid	114	65	1.8	98
Granitoid	145	33	4.4	115
Granitoid	90	22	4.1	110
Granitoid	110	80	1.4	85
Granitoid	200	62	3.2	83
Granitoid	92	20	4.6	98
Granitoid	49	42	1.2	70
Granitoid	60	43	1.4	158
Granitoid	32	15	2.1	115
Granitoid	118	47	2.5	98
Granitoid	111	20	5.6	93
Granitoid	100	25	4.0	113
Granitoid	62	15	4.1	113
Granitoid	55	15	3.7	105
Granitoid	86	29	3.0	78
Granitoid	35	10	3.5	100
Granitoid	45	34	1.3	108
Granitoid	81	27	3.0	98
Granitoid	56	40	1.4	170
Granitoid	64	14	4.6	100
Granitoid	105	18	5.8	115
Granitoid	64	30	2.1	113
Granitoid	72	19	3.8	117
Granitoid	79	20	4.0	110
Granitoid	64	14	4.6	107

Granitoid	34	10	3.4	105
Granitoid	46	20	2.3	125
Granitoid	72	41	1.8	140
Granitoid	173	71	2.4	115
Granitoid	72	20	3.6	120
Granitoid	76	32	2.4	107
Granitoid	85	13	6.5	105
Granitoid	78	16	4.9	105
Granitoid	46	27	1.7	143
Granitoid	36	18	2.0	110
Granitoid	67	25	2.7	107
Granitoid	115	37	3.1	82
Granitoid	47	20	2.4	140
Granitoid	68	20	3.4	95
Granitoid	44	13	3.4	100
Granitoid	42	27	1.6	65
Granitoid	72	27	2.7	100
Granitoid	65	43	1.5	145
Granitoid	43	15	2.9	115
Granitoid	46	22	2.1	98
Granitoid	44	24	1.8	140
Granitoid	13	8	1.6	110
Granitoid	43	16	2.7	90
Granitoid	40	20	2.0	105
Granitoid	70	39	1.8	125
Granitoid	75	37	2.0	120
Granitoid	45	14	3.2	120
Granitoid	97	20	4.9	115
Granitoid	125	50	2.5	80
Granitoid	38	21	1.8	120
Granitoid	82	50	1.6	150
Granitoid	76	27	2.8	135
Granitoid	187	48	3.9	88
Granitoid	67	24	2.8	120
Granitoid	62	15	4.1	75
Granitoid	64	38	1.7	95
Granitoid	105	42	2.5	100
Granitoid	246	72	3.4	98
Granitoid	47	16	2.9	105
Granitoid	100	70	1.4	100
Granitoid	38	18	2.1	100
Granitoid	204	60	3.4	106
Granitoid	83	63	1.3	110
Granitoid	65	24	2.7	100
Granitoid	53	20	2.7	95

Section 15 strike: 071° slope: 44°

Pebble type	long-axis (mm)	short-axis (mm)	R_f	ϕ (degree)
Amphibolite	108	25	4.3	18
Amphibolite	170	65	2.6	15
Amphibolite	240	23	10.4	10
Amphibolite	146	90	1.6	170
Amphibolite	150	25	6.0	15
Granitoid	60	20	3.0	163
Granitoid	115	53	2.2	30
Granitoid	100	44	2.3	25
Granitoid	75	35	2.1	10
Granitoid	113	37	3.1	10
Granitoid	68	30	2.3	20
Granitoid	62	35	1.8	25
Granitoid	47	37	1.3	15
Granitoid	153	53	2.9	15
Granitoid	60	40	1.5	8
Granitoid	225	30	7.5	10
Granitoid	110	13	8.5	10
Granitoid	68	20	3.4	170
Granitoid	263	55	4.8	10
Granitoid	195	20	9.8	8
Granitoid	68	41	1.7	15
Granitoid	180	65	2.8	45

Appendix E: The geochronological results in Chapter 4.

The analytical data from the Yuanlong, Shetang and Xinyang areas are in Table E1, Table E2 and Table E3, respectively. Rare-earth element (REE) contents are in Table E4, Table E5 and Table E6, respectively.

1. Results from the Yuanlong area

(1) TS1406

The size of zircons from TS1406 is in the range of 80μm~150μm (Fig.E1a). They are subhedral to euhedral prismatic with length-to-width ratios ranging from 1.5 to 4. Some of the zircons (Spot No.03, 10, 11, 13, 14, 16, 20-23, 26, 32) show no zoning, and others exhibit well-developed or relatively weak oscillatory zoning that is a dominant feature of igneous rocks. Spot No.02, 04, 05, 08, 09, 11, 12, 15, 17, 18, 21, 24, 25, 27, 29-31, 33, 34 are xenocrystic cores.

Spot No.01, 02, 09, 19 have Th/U ratios > 0.5, which probably indicates a magmatic origin. Spot No.13, 16, 22 and 26 have Th/U ratios < 0.1 indicating completely recrystallized zircon (Hoskin and Schaltegger, 2003).

Most zircons show REE patterns with a positive Ce-anomaly and negative Eu-anomaly with a steeply-rising slope from the LREE to the HREE and have less LREE abundances (Fig.E1b), except for Spot No.03, 05, 06, 13, 16, 17, 18 and 22 (Fig.E1c). Spot No.03, 05, 06, 13 and 17 have high LREE and MREE abundances, so the slope from LREE to HREE is shallow, and they do not show clearly negative Eu-anomaly. Spot No. 18 shows a positive La-anomaly instead of a Ce-anomaly, and Spot No.22

exhibits a positive Ce-anomaly as well as a positive Pr-anomaly. Spot No.16 has no positive Ce-anomaly, and all LREE are depleted. As Spot No.03, 05, 06, 13, 16, 17, 18 and 22 show REE patterns that differ from the typical REE pattern of unaltered igneous zircon, they were affected by later processes or completely recrystallized.

Table E1 LA-ICP-MS U-Pb zircon dating results of the samples from the Yuanlong area.

				Isotope ratios								Ages(Ma)								
Spot No.	Th(ppm)	U(ppm)	Th/U	Pb^{207}/Pb^{206}	1σ	Pb^{207}/U^{235}	1σ	Pb^{206}/U^{238}	1σ	Pb^{208}/Th^{232}	1σ	Pb^{207}/Pb^{206}	1σ	Pb^{207}/U^{235}	1σ	Pb^{206}/U^{238}	1σ	Pb^{208}/Th^{232}	1σ	Disc.%
TS1406																				
TS1406-01	3944.59	7163.29	0.55	0.05836	0.0012	0.51778	0.00559	0.06436	0.0006	0.02097	0.0002	543.4	45.28	423.7	3.74	402.1	3.53	419.5	3.47	5.1
TS1406-02	799.09	1473.97	0.54	0.05961	0.0013	0.55756	0.00718	0.06785	0.0006	0.01759	0.0002	589.3	47.45	449.9	4.68	423.2	3.79	352.5	3.4	5.93
TS1406-03	935.47	3829.67	0.24	0.12758	0.0027	1.11605	0.01151	0.06345	0.0006	0.06519	0.0006	2064.9	36.23	761.1	5.53	396.6	3.51	1276.5	10.6	47.89
TS1406-04	248.11	936.9	0.26	0.05574	0.0014	0.52164	0.00874	0.06788	0.0007	0.02352	0.0003	441.8	53.89	426.2	5.83	423.4	3.96	469.8	6.31	0.66
TS1406-05	684.74	1724.68	0.4	0.08285	0.0018	0.77193	0.00859	0.06758	0.0006	0.03081	0.0003	1265.8	40.82	580.9	4.92	421.5	3.73	613.3	5.35	27.44
TS1406-06	354.49	1497.3	0.24	0.1077	0.0024	0.96443	0.01251	0.06495	0.0006	0.0511	0.0006	1760.9	40.3	685.6	6.47	405.6	3.75	1007.4	10.6	40.84
TS1406-07	2190.83	9298.33	0.24	0.06006	0.0013	0.56843	0.00589	0.06865	0.0006	0.02543	0.0002	605.6	44.46	457	3.82	428	3.73	507.5	4.37	6.35
TS1406-08	406.39	1153.11	0.35	0.06119	0.0014	0.5919	0.00855	0.07015	0.0007	0.02546	0.0003	646	49.15	472.1	5.45	437.1	3.98	508.1	5.52	7.41
TS1406-09	792.97	1427.73	0.56	0.08341	0.0019	0.75875	0.0096	0.06597	0.0006	0.01694	0.0002	1278.7	42.7	573.3	5.54	411.8	3.72	339.5	3.42	28.17
TS1406-10	436.39	1294.27	0.34	0.06388	0.0015	0.70004	0.01094	0.07948	0.0008	0.02802	0.0003	737.5	50.06	538.8	6.53	493	4.56	558.5	6.72	8.5
TS1406-11	91.22	592.88	0.15	0.07098	0.0016	1.30344	0.01689	0.13316	0.0013	0.0463	0.0006	957	44.94	847.2	7.44	805.9	7.11	914.7	12.2	4.87
TS1406-12	339.05	921.86	0.37	0.06155	0.0014	0.58763	0.00862	0.06923	0.0007	0.02543	0.0003	658.5	49.41	469.4	5.51	431.5	3.94	507.6	5.49	8.07
TS1406-13	294.5	3717.22	0.08	0.13959	0.0029	1.03762	0.01062	0.0539	0.0005	0.14992	0.0013	2222.1	35.73	722.7	5.29	338.4	2.99	2823.5	23.6	53.18
TS1406-14	3181.54	11783.7	0.27	0.06648	0.0014	0.57052	0.00598	0.06222	0.0006	0.02547	0.0002	821.6	43.21	458.4	3.86	389.1	3.39	508.4	4.31	15.12
TS1406-15	99.9	692.96	0.14	0.07029	0.0016	1.54277	0.02119	0.15913	0.0015	0.05385	0.0008	937	46.08	947.6	8.46	952	8.41	1060.1	15.7	-0.46
TS1406-16	20.65	1891.13	0.01	0.06506	0.0014	0.66367	0.00781	0.07397	0.0007	0.21085	0.0036	776.1	44.98	516.9	4.77	460	4.04	3867.1	59.6	11.01
TS1406-17	1300.09	2815.01	0.46	0.10935	0.0023	1.00261	0.01104	0.06648	0.0006	0.03105	0.0003	1788.5	38.36	705.1	5.6	414.9	3.67	618.1	5.33	41.16
TS1406-18	389.99	1466.86	0.27	0.07053	0.0016	0.70046	0.00866	0.07201	0.0007	0.02924	0.0003	943.8	44.27	539.1	5.17	448.2	3.98	582.4	5.87	16.86
TS1406-19	2829.43	5499.06	0.51	0.06365	0.0014	0.59094	0.00635	0.06731	0.0006	0.02288	0.0002	729.9	44.23	471.5	4.05	420	3.65	457.2	3.72	10.92
TS1406-20	1907.88	6000.04	0.32	0.05546	0.0012	0.54444	0.00561	0.07117	0.0006	0.02114	0.0002	430.6	45.55	441.3	3.69	443.2	3.82	422.8	3.49	-0.43
TS1406-21	775.22	1657.72	0.47	0.06155	0.0014	0.59778	0.00859	0.07041	0.0007	0.02392	0.0002	658.6	49.21	475.8	5.46	438.6	3.97	477.8	4.82	7.82
TS1406-22	39.42	2406.57	0.02	0.06133	0.0013	0.58074	0.007	0.06865	0.0006	0.07309	0.0013	650.7	46.35	464.9	4.49	428	3.76	1425.8	25.3	7.94
TS1406-23	914.92	2796.24	0.33	0.06127	0.0014	0.59847	0.00749	0.07081	0.0007	0.02431	0.0002	648.7	46.94	476.3	4.76	441	3.89	485.4	4.71	7.41
TS1406-24	484.75	3049.82	0.16	0.06309	0.0014	0.53707	0.00702	0.06171	0.0006	0.02244	0.0003	711.3	47.16	436.5	4.63	386	3.44	448.6	5.48	11.57
TS1406-25	390.45	1199.75	0.33	0.06233	0.0015	0.59876	0.0087	0.06964	0.0007	0.02429	0.0003	685.3	49.3	476.4	5.52	434	3.92	485.1	5.39	8.9
TS1406-26	363.6	4758.42	0.08	0.05638	0.0013	0.55132	0.0075	0.07089	0.0007	0.02724	0.0004	466.5	50.34	445.9	4.91	441.5	3.93	543.2	8.59	0.99
TS1406-27	663.31	1457.66	0.46	0.05931	0.0015	0.54934	0.00967	0.06714	0.0007	0.02138	0.0003	578.4	54.61	444.6	6.34	418.9	3.93	427.6	5.14	5.78
TS1406-28	506.5	1687.14	0.3	0.05959	0.0015	0.50947	0.00872	0.06197	0.0006	0.01987	0.0003	588.8	53.82	418.1	5.87	387.6	3.62	397.7	5.34	7.29
TS1406-29	234.28	892.61	0.26	0.05647	0.0013	0.58996	0.00854	0.07572	0.0007	0.02567	0.0003	470.3	51.61	470.8	5.46	470.5	4.22	512.2	5.92	0.06
TS1406-30	509.02	1235.27	0.41	0.06143	0.0014	0.59751	0.00808	0.0705	0.0007	0.0249	0.0003	654.4	48.29	475.7	5.13	439.2	3.91	497	4.84	7.67
TS1406-31	294.73	961.66	0.31	0.05764	0.0014	0.56182	0.00944	0.07064	0.0007	0.02331	0.0003	515.9	54.32	452.7	6.14	440	4.06	465.8	5.96	2.81
TS1406-32	2538.15	7635.59	0.33	0.0563	0.0012	0.52853	0.00572	0.06804	0.0006	0.02121	0.0002	463.5	46.96	430.8	3.8	424.3	3.66	424.2	3.57	1.51
TS1406-33	362.76	1487.31	0.24	0.05836	0.0014	0.54745	0.00802	0.06799	0.0006	0.02267	0.0003	543.2	50.76	443.3	5.26	424	3.81	453.1	5.46	4.35
TS1406-34	839.19	2473.33	0.34	0.05698	0.0013	0.55322	0.00664	0.07037	0.0006	0.02202	0.0002	490	47.78	447.1	4.34	438.4	3.82	440.3	4.05	1.95
TS1406-35	827.45	3568.74	0.23	0.05867	0.0013	0.61537	0.00672	0.07602	0.0007	0.02629	0.0002	554.9	46.01	486.9	4.22	472.3	4.06	524.6	4.64	3
TS1406-36	360.38	1355.05	0.27	0.0569	0.0013	0.59415	0.00786	0.07568	0.0007	0.02481	0.0003	486.9	49.44	473.5	5.01	470.3	4.14	495.4	5.23	0.68
TS1408-1																				
TS1408-1-01	103.45	265.18	0.39	0.07177	0.0018	1.44553	0.02381	0.146	0.0015	0.04345	0.0006	979.4	49.36	908	9.89	878.5	8.17	859.8	11.7	3.25

TS1408-1-02	1135.59	2422.04	0.47	0.05574	0.0013	0.48376	0.00668	0.06292	0.0006	0.01987	0.0002	441.6	49.88	400.6	4.57	393.3	3.52	397.8	3.99	1.82
TS1408-1-03	111.82	273.11	0.41	0.06805	0.0017	1.28822	0.02138	0.13723	0.0014	0.04175	0.0006	870	50.37	840.5	9.49	829	7.69	826.8	10.8	1.37
TS1408-1-04	60.45	209.05	0.29	0.06975	0.0018	1.4486	0.02549	0.15055	0.0015	0.0473	0.0008	921	51.33	909.3	10.6	904.1	8.54	934	14.8	0.57
TS1408-1-05	63.68	205.04	0.31	0.07265	0.0021	1.5197	0.03302	0.15164	0.0017	0.05272	0.001	1004.2	56.73	938.4	13.3	910.2	9.39	1038.5	19.4	3.01
TS1408-1-06	684.01	2780.65	0.25	0.05661	0.0012	0.5713	0.00628	0.07316	0.0007	0.02547	0.0002	475.7	46.88	458.9	4.06	455.2	3.94	508.3	4.69	0.81
TS1408-1-07	109.12	254.38	0.43	0.06898	0.0022	1.37042	0.03473	0.14404	0.0017	0.04046	0.0008	898	63.42	876.3	14.9	867.5	9.5	801.7	16	1
TS1408-1-08	325.92	284.09	1.15	0.08822	0.002	2.84696	0.03984	0.23397	0.0023	0.07147	0.0007	1387.3	43.28	1368	10.5	1355.3	12	1395.4	13	0.93
TS1408-1-09	427.69	1220.76	0.35	0.07598	0.0017	0.65515	0.00904	0.06251	0.0006	0.02381	0.0003	1094.6	45.24	511.6	5.54	390.9	3.54	475.7	5.24	23.59
TS1408-1-10	151.57	364.15	0.42	0.07018	0.0017	1.44079	0.02135	0.14885	0.0014	0.02894	0.0004	933.6	47.48	906	8.88	894.5	8.02	576.5	7.74	1.27
TS1408-1-11	108.27	222.34	0.49	0.07182	0.0021	1.4566	0.03186	0.14706	0.0016	0.04276	0.0007	980.7	57.15	912.6	13.2	884.5	9.11	846.3	13.9	3.08
TS1408-1-12	788.63	2049.58	0.38	0.05713	0.0013	0.4944	0.00669	0.06274	0.0006	0.01959	0.0002	496.1	49.89	407.9	4.55	392.3	3.49	392	4.04	3.82
TS1408-1-13	267.46	497.5	0.54	0.07859	0.0018	2.03117	0.02823	0.18742	0.0018	0.0504	0.0006	1161.8	44.7	1126	9.46	1107.4	9.75	993.9	10.9	1.65
TS1408-1-14	1005.39	4848.27	0.21	0.05601	0.0012	0.53664	0.00541	0.06947	0.0006	0.02254	0.0002	452.6	45.27	436.2	3.57	433	3.7	450.5	3.89	0.73
TS1408-1-15	104.6	878.65	0.12	0.07215	0.0015	1.53845	0.01734	0.15463	0.0014	0.04635	0.0006	990.2	42.88	945.9	6.94	926.9	7.81	915.8	11.6	2.01
TS1408-1-16	116.71	351.76	0.33	0.09663	0.0021	3.214	0.03815	0.24119	0.0023	0.07272	0.0008	1560.1	40.09	1460.5	9.19	1392.9	11.7	1418.9	15.5	4.63
TS1408-1-17	830.62	3308.7	0.25	0.0579	0.0012	0.56922	0.00601	0.0713	0.0006	0.02074	0.0002	525.7	45.72	457.5	3.89	444	3.8	415	3.74	2.95
TS1408-1-18	199.53	764.62	0.26	0.05643	0.0014	0.52999	0.00829	0.06812	0.0006	0.02297	0.0003	468.4	52.98	431.8	5.5	424.8	3.85	459.1	5.87	1.62
TS1408-1-19	143.09	220.09	0.65	0.05544	0.0018	0.53053	0.01384	0.0694	0.0008	0.02168	0.0003	429.7	69.77	432.2	9.18	432.5	4.53	433.5	6.38	-0.07
TS1408-1-20	86.11	165.6	0.52	0.09549	0.0022	3.37139	0.04844	0.25605	0.0026	0.07431	0.0009	1537.8	42.82	1497.8	11.3	1469.6	13.1	1448.7	17.2	1.88
TS1408-1-21	90.45	359.27	0.25	0.09291	0.002	2.7247	0.03332	0.21269	0.002	0.07279	0.0009	1485.9	41	1335.2	9.08	1243.2	10.6	1420.3	16.7	6.89
TS1408-1-22	122.52	194.35	0.63	0.07057	0.0018	1.47303	0.02659	0.1514	0.0015	0.04575	0.0006	944.9	51.71	919.4	10.9	908.8	8.61	904.2	11.1	1.15
TS1408-1-23	79.65	338.69	0.24	0.07156	0.0017	1.56085	0.02247	0.15819	0.0015	0.05281	0.0007	973.5	46.59	954.8	8.91	946.7	8.37	1040.2	14	0.85
TS1408-1-24	84.94	422.97	0.2	0.06984	0.0016	1.47173	0.02014	0.15284	0.0014	0.04605	0.0007	923.7	46.06	918.8	8.28	916.8	8	909.9	12.5	0.22
TS1408-1-25	94.46	420.26	0.22	0.05588	0.0016	0.62778	0.01318	0.08148	0.0008	0.0247	0.0005	447.4	60.84	494.7	8.22	505	4.9	493.2	9.29	-2.08
TS1408-1-26	495.65	1400.03	0.35	0.05576	0.0012	0.55318	0.00694	0.07196	0.0007	0.02193	0.0002	442.4	48.09	447.1	4.54	448	3.89	438.4	4.26	-0.2
TS1408-1-27	2584.27	3780.71	0.68	0.06257	0.0013	0.60046	0.00686	0.06962	0.0006	0.01999	0.0002	693.5	45.08	477.5	4.35	433.8	3.73	400.1	3.34	9.15
TS1408-1-28	45.69	240.93	0.19	0.0685	0.0018	1.53913	0.02952	0.16298	0.0017	0.05239	0.0011	883.7	53.77	946.2	11.8	973.3	9.36	1032.1	20.8	-2.86
TS1408-1-29	44.95	343.66	0.13	0.07247	0.0017	1.63288	0.02294	0.16344	0.0015	0.0561	0.0009	999.2	45.93	983	8.85	975.9	8.54	1103.3	18	0.72
TS1408-1-30	97.05	248.34	0.39	0.07977	0.002	1.978	0.03252	0.17988	0.0018	0.06347	0.0009	1191.2	47.6	1108	11.1	1066.3	9.86	1243.8	16.4	3.76
TS1408-1-31	90.32	315.01	0.29	0.07243	0.0017	1.60313	0.02322	0.16056	0.0015	0.05098	0.0007	998.1	46.47	971.4	9.06	959.9	8.47	1004.9	12.9	1.18
TS1408-1-32	167.74	359.63	0.47	0.09906	0.0023	2.90643	0.03988	0.21284	0.0021	0.06533	0.0008	1606.5	41.74	1383.6	10.4	1243.9	11	1279.1	14.8	10.1
TS1408-1-33	46.46	231.1	0.2	0.06853	0.0017	1.57567	0.02558	0.16679	0.0016	0.04912	0.0009	884.7	49.55	960.7	10.1	994.4	9	969.1	16.3	-3.51
TS1408-1-34	75.82	393.88	0.19	0.07368	0.0017	1.68065	0.02225	0.16547	0.0015	0.05472	0.0007	1032.8	44.7	1001.2	8.43	987.1	8.5	1076.9	14.2	1.41
TS1408-1-35	88.35	180.85	0.49	0.08126	0.0021	2.14994	0.03794	0.19194	0.002	0.05868	0.0008	1227.7	48.68	1165	12.2	1131.9	10.8	1152.5	15.8	2.84
TS1408-1-36	644.89	1556.26	0.41	0.05956	0.0013	0.55984	0.00678	0.06819	0.0006	0.01402	0.0001	587.6	46.64	451.4	4.41	425.3	3.67	281.5	2.8	5.78
TS1408-2																				
TS1408-2-01	282.9	1135.56	0.25	0.05911	0.0015	0.55279	0.00888	0.06785	0.0006	0.02245	0.0003	571.1	52.76	446.8	5.81	423.2	3.8	448.7	6.03	5.28
TS1408-2-02	45.05	407.87	0.11	0.07277	0.0017	1.49963	0.02056	0.14949	0.0014	0.05083	0.0009	1007.6	45.76	930.2	8.35	898.1	7.74	1002.1	16.8	3.45
TS1408-2-03	632.92	1594.39	0.4	0.10012	0.0023	0.95507	0.01196	0.0692	0.0006	0.03393	0.0003	1626.4	41.14	680.7	6.21	431.3	3.8	674.4	6.5	36.64
TS1408-2-04	1240.83	2521.87	0.49	0.06737	0.0016	0.59667	0.00836	0.06425	0.0006	0.02183	0.0002	849.1	47.69	475.1	5.32	401.4	3.54	436.6	4.35	15.51
TS1408-2-05	547.3	1233.36	0.44	0.06013	0.0014	0.59004	0.00786	0.07118	0.0006	0.0246	0.0002	608.2	48.6	470.9	5.02	443.3	3.85	491.2	4.69	5.86
TS1408-2-06	2679.23	4920.38	0.54	0.05784	0.0013	0.5517	0.00615	0.06919	0.0006	0.02203	0.0002	523.5	46.83	446.1	4.02	431.2	3.65	440.5	3.62	3.34
TS1408-2-07	98.19	224.43	0.44	0.08843	0.0021	2.57825	0.03739	0.21147	0.0021	0.07404	0.0009	1391.8	44.16	1294.5	10.6	1236.6	10.9	1443.8	16.8	4.47
TS1408-2-08	71.94	254.02	0.28	0.07057	0.0018	1.48926	0.02618	0.15305	0.0015	0.04861	0.0008	945	51.36	926	10.7	918	8.53	959.3	15	0.86
TS1408-2-09	33.12	222.66	0.15	0.07081	0.0018	1.58369	0.02605	0.1622	0.0016	0.05166	0.001	952	49.71	963.8	10.2	969	8.81	1018	19.5	-0.54
TS1408-2-10	67.26	341.16	0.2	0.0717	0.0018	1.59726	0.02747	0.16156	0.0016	0.05535	0.001	977.4	50.51	969.1	10.7	965.4	8.94	1088.9	19	0.38

TS1408-2-11	192.4	376.92	0.51	0.06959	0.0017	1.46519	0.02187	0.15269	0.0015	0.04564	0.0005	916.3	47.93	916.1	9.01	916	8.11	902	9.94	0.01
TS1408-2-12	363.06	1411.03	0.26	0.06314	0.0015	0.60377	0.00838	0.06934	0.0006	0.02684	0.0003	712.9	48.22	479.6	5.3	432.2	3.82	535.2	6.02	9.88
TS1408-2-13	143.57	917.42	0.16	0.0554	0.0013	0.53191	0.00767	0.06962	0.0006	0.02249	0.0003	428.3	50.71	433.1	5.09	433.8	3.85	449.5	6.34	-0.16
TS1408-2-14	112.57	221.62	0.51	0.07112	0.0018	1.53718	0.02529	0.15672	0.0015	0.04571	0.0006	960.9	49.42	945.4	10.1	938.5	8.6	903.5	11.1	0.73
TS1408-2-15	140.03	308.6	0.45	0.07505	0.0018	1.54453	0.02356	0.14923	0.0014	0.03714	0.0005	1069.8	47.05	948.3	9.4	896.6	8.09	737.1	9.28	5.45
TS1408-2-16	1149.91	5006.71	0.23	0.05665	0.0012	0.4804	0.00525	0.06149	0.0005	0.02028	0.0002	477.1	46.66	398.3	3.6	384.7	3.3	405.8	3.73	3.41
TS1408-2-17	593.39	2038.7	0.29	0.05609	0.0013	0.56488	0.00761	0.07302	0.0007	0.02405	0.0003	455.6	49.39	454.7	4.94	454.3	4	480.3	5.15	0.09
TS1408-2-18	241.62	426.62	0.57	0.08673	0.0019	2.47946	0.03216	0.20728	0.002	0.06227	0.0007	1354.5	42.32	1266.1	9.39	1214.3	10.5	1221	12.3	4.09
TS1408-2-19	36.47	513.06	0.07	0.05507	0.0015	0.55549	0.01101	0.07313	0.0007	0.03133	0.0008	415.2	58.6	448.6	7.19	455	4.36	623.5	16.1	-1.43
TS1408-2-20	327.28	1215.45	0.27	0.05571	0.0013	0.54158	0.00752	0.07049	0.0007	0.02246	0.0003	440.3	49.7	439.5	4.95	439.1	3.9	449	5.11	0.09
TS1408-2-21	53.85	253.6	0.21	0.06954	0.0018	1.49297	0.02765	0.15566	0.0016	0.05135	0.001	914.8	52.44	927.5	11.3	932.6	8.93	1012.2	18.7	-0.55
TS1408-2-22	188.7	928.01	0.2	0.05613	0.0014	0.57037	0.00934	0.07367	0.0007	0.02429	0.0004	457.2	53.34	458.3	6.04	458.3	4.2	485.2	7.15	0
TS1408-2-23	61.26	345.62	0.18	0.06939	0.0016	1.52892	0.02176	0.15976	0.0015	0.05242	0.0008	910.3	46.57	942.1	8.74	955.4	8.45	1032.7	15.2	-1.41
TS1408-2-24	310.4	2117.41	0.15	0.06293	0.0014	0.59403	0.00702	0.06844	0.0006	0.03096	0.0003	706	45.16	473.4	4.47	426.7	3.73	616.3	6.6	9.86
TS1408-2-25	327.62	418.79	0.78	0.10446	0.0022	4.41365	0.04946	0.30634	0.0029	0.08815	0.0008	1704.8	38.23	1714.9	9.28	1722.7	14.1	1707.5	15	-0.45
TS1408-2-26	84.94	182.74	0.46	0.06951	0.0018	1.52496	0.02798	0.15906	0.0016	0.05015	0.0007	914.1	51.95	940.5	11.3	951.5	9.14	989.1	13.6	-1.17
TS1408-2-27	236.39	1084.87	0.22	0.0581	0.0014	0.61182	0.00948	0.07635	0.0007	0.02738	0.0004	533	51.62	484.7	5.97	474.3	4.34	546	7.32	2.15
TS1408-2-28	69.43	260.08	0.27	0.07577	0.0018	1.92562	0.02888	0.18426	0.0018	0.05864	0.0009	1089.1	45.99	1090	10	1090.2	9.86	1151.8	16.2	-0.02
TS1408-2-29	1297.14	2681.28	0.48	0.0696	0.0015	0.66377	0.00868	0.06915	0.0006	0.02596	0.0003	916.7	44.9	516.9	5.3	431	3.87	518.1	4.99	16.62
TS1408-2-30	198.97	314.33	0.63	0.0823	0.0019	2.27205	0.03172	0.20017	0.002	0.06804	0.0007	1252.8	43.47	1203.7	9.84	1176.2	10.5	1330.5	13.6	2.28
TS1408-2-31	139.04	2196.79	0.06	0.05811	0.0012	0.5946	0.00673	0.0742	0.0007	0.04048	0.0005	533.3	45.92	473.8	4.29	461.4	4.04	802	9.62	2.62
TS1408-2-32	464.03	1429.38	0.32	0.05463	0.0012	0.54829	0.00693	0.07278	0.0007	0.02266	0.0002	397	47.79	443.9	4.54	452.9	4.02	452.8	4.56	-2.03
TS1408-2-33	652.61	1756.46	0.37	0.06483	0.0014	0.61717	0.00798	0.06903	0.0006	0.01775	0.0002	768.9	45.58	488.1	5.01	430.3	3.86	355.6	3.85	11.84
TS1408-2-34	33.98	2169.67	0.02	0.06052	0.0013	0.58834	0.00772	0.0705	0.0007	0.10189	0.0021	622.1	46.89	469.8	4.94	439.2	3.94	1961.1	38	6.51
TS1408-2-35	29.09	2176.26	0.01	0.05471	0.0012	0.54138	0.00626	0.07176	0.0007	0.03175	0.0008	400.1	46.63	439.3	4.12	446.7	3.93	631.7	15.5	-1.68
TS1408-2-36	1086.11	2298.68	0.47	0.05974	0.0013	0.60096	0.00675	0.07295	0.0007	0.02375	0.0002	594.1	44.74	477.8	4.28	453.9	3.99	474.5	4.16	5

Table E2 LA-ICP-MS U-Pb zircon dating results of the samples from the Shetang area.

				Isotope ratios								Ages(Ma)								
Spot No.	Th(ppm)	U(ppm)	Th/U	Pb^{207}/Pb^{206}	1σ	Pb^{207}/U^{235}	1σ	Pb^{206}/U^{238}	1σ	Pb^{208}/Th^{232}	1σ	Pb^{207}/Pb^{206}	1σ	Pb^{207}/U^{235}	1σ	Pb^{206}/U^{238}	1σ	Pb^{208}/Th^{232}	1σ	Disc.%
ST1502																				
ST1502-01	49.36	52.39	0.94	0.15903	0.0041	9.34564	0.18489	0.4263	0.00608	0.12011	0.002	2445.4	42.99	2372.5	18.15	2289	27.46	2292.6	36.05	6.83
ST1502-02	137.75	138.76	0.99	0.16569	0.00353	10.62124	0.13668	0.46501	0.00532	0.12919	0.00134	2514.6	35.39	2490.6	11.94	2461.7	23.43	2455.8	23.99	-2.15
ST1502-03	11.43	380.9	0.03	0.10849	0.00252	4.53713	0.07164	0.30338	0.00361	0.18374	0.00687	1774.1	41.91	1737.8	13.14	1708	17.84	3409.3	117.31	-3.87
ST1502-04	89.98	261.39	0.34	0.15546	0.0034	9.3409	0.1293	0.43586	0.00513	0.15232	0.00216	2406.8	36.72	2372	12.7	2332.1	23.03	2865.7	37.93	-3.2
ST1502-05	422.22	347.25	1.22	0.15434	0.0034	7.94726	0.11147	0.3735	0.0044	0.10717	0.00115	2394.6	37.02	2225.1	12.65	2045.9	20.63	2057.8	20.97	-17.04
ST1502-06	98.55	154.93	0.64	0.15421	0.00353	7.92229	0.12209	0.37264	0.00458	0.08587	0.00126	2393.1	38.45	2222.2	13.89	2041.8	21.49	1665.1	23.51	-17.21
ST1502-07	547.64	484.72	1.13	0.15701	0.00328	8.52457	0.10321	0.3938	0.00439	0.10786	0.00102	2423.7	35.05	2288.5	11	2140.4	20.29	2070.4	18.61	-13.24
ST1502-08	24.81	124.45	0.2	0.12175	0.00276	6.07479	0.09114	0.36189	0.0043	0.1129	0.0021	1982	39.79	1986.6	13.08	1991.1	20.37	2162	38.19	0.46
ST1502-09	205.12	188.04	1.09	0.16051	0.00336	10.44609	0.12793	0.47202	0.0053	0.13237	0.00127	2461.1	34.99	2475.1	11.35	2492.4	23.23	2512.6	22.75	1.26
ST1502-10	50.55	91.89	0.55	0.15172	0.00334	9.23579	0.12974	0.4415	0.00524	0.12074	0.00158	2365.4	37.04	2361.7	12.87	2357.3	23.41	2304	28.42	0.34
ST1502-11	24.25	264.95	0.09	0.11565	0.00244	5.54988	0.06913	0.34804	0.00388	0.12739	0.00198	1890.1	37.53	1908.4	10.72	1925.2	18.56	2423.5	35.53	1.82
ST1502-12	799.87	758.46	1.05	0.16091	0.00329	10.31849	0.11694	0.46508	0.00508	0.12446	0.0011	2465.2	34.18	2463.8	10.49	2462	22.35	2370.9	19.85	-0.13
ST1502-13	557.34	444.25	1.25	0.16185	0.00334	10.04715	0.11706	0.45018	0.00498	0.1252	0.00113	2475	34.4	2439.1	10.76	2396	22.12	2384.2	20.34	-3.3
ST1502-14	80.39	243.02	0.33	0.14734	0.00309	8.88147	0.10953	0.43713	0.00492	0.16557	0.00185	2315.2	35.59	2325.9	11.26	2337.8	22.09	3096.8	32.06	0.97
ST1502-15	125.03	272.62	0.46	0.14292	0.00315	7.52261	0.10585	0.38167	0.0045	0.11489	0.00151	2262.9	37.5	2175.7	12.61	2084.1	21.01	2198.2	27.45	-8.58
ST1502-16	34.42	206.12	0.17	0.12334	0.00264	6.05574	0.07916	0.35602	0.00405	0.11295	0.00169	2005.1	37.58	1983.9	11.39	1963.3	19.27	2163	30.66	-2.13
ST1502-17	73.52	90.24	0.81	0.1564	0.00343	9.50981	0.13342	0.44089	0.00526	0.12583	0.00147	2417.1	36.77	2388.5	12.89	2354.6	23.51	2395.7	26.43	-2.65
ST1502-18	120.34	188.89	0.64	0.15676	0.00339	9.21215	0.12407	0.42612	0.00499	0.1109	0.00132	2421	36.22	2359.3	12.34	2288.2	22.55	2125.7	23.97	5.8
ST1502-19	63.78	135.09	0.47	0.14908	0.00327	9.20224	0.12931	0.44756	0.00533	0.12547	0.00168	2335.4	37.11	2358.3	12.87	2384.4	23.74	2389.2	30.22	2.06
ST1502-20	226.04	348	0.65	0.1631	0.00338	10.4906	0.12476	0.46635	0.00521	0.13483	0.00131	2488	34.51	2479.1	11.02	2467.5	22.93	2556.5	23.33	-0.83
ST1502-21	35.07	124.34	0.28	0.14222	0.00326	7.58002	0.11787	0.38643	0.00477	0.1163	0.0021	2254.4	39.05	2182.5	13.95	2106.2	22.18	2223.7	38.08	-7.04
ST1502-22	21.27	264.1	0.08	0.13572	0.00296	6.80993	0.09373	0.36379	0.00425	0.12844	0.00286	2173.2	37.53	2087	12.19	2000.1	20.1	2442.3	51.24	-8.65
ST1502-23	235.97	248.79	0.95	0.16239	0.00343	11.54145	0.14634	0.51526	0.00593	0.14406	0.00146	2480.7	35.18	2567.9	11.85	2679.1	25.23	2720.2	25.86	7.41
ST1502-24	46.34	56.89	0.81	0.1575	0.00378	9.91064	0.17165	0.45616	0.00607	0.12849	0.00193	2429	40.08	2426.5	15.97	2422.6	26.86	2443.2	34.55	-0.26
ST1502-25	73.55	168.07	0.44	0.14692	0.00319	9.07483	0.12446	0.44773	0.00529	0.14106	0.0018	2310.4	36.83	2345.6	12.54	2385.2	23.56	2667.1	31.94	3.14
ST1502-26	44.68	86.86	0.51	0.15535	0.00353	9.77361	0.15093	0.45604	0.00572	0.14676	0.00215	2405.6	38.15	2413.7	14.23	2422.1	25.31	2767.9	37.94	0.68
ST1502-27	45.82	47.15	0.97	0.16185	0.00383	10.23526	0.17301	0.45839	0.00604	0.1275	0.00177	2475.1	39.4	2456.3	15.64	2432.4	26.72	2425.5	31.74	-1.76
ST1502-28	5.05	600.09	0.01	0.10469	0.0023	4.10201	0.05708	0.28401	0.00328	0.12832	0.00679	1708.8	39.83	1654.7	11.36	1611.5	16.49	2440.2	121.65	-6.04
ST1502-29	336.62	315.35	1.07	0.16332	0.0034	10.6373	0.12979	0.47207	0.00536	0.13742	0.00131	2490.4	34.69	2492	11.32	2492.6	23.47	2602.5	23.28	0.09
ST1502-30	332.69	289.8	1.15	0.1613	0.00337	10.3933	0.12831	0.46702	0.00533	0.12983	0.00125	2469.3	34.89	2470.5	11.44	2470.5	23.41	2467.3	22.31	0.05
ST1502-31	176.12	257.7	0.68	0.16317	0.00345	9.99347	0.12718	0.44389	0.00513	0.12739	0.00135	2488.7	35.16	2434.2	11.75	2368	22.89	2423.5	24.2	-5.1
ST1502-32	134.19	195.5	0.69	0.14665	0.00309	9.12403	0.11559	0.4509	0.00518	0.12288	0.00128	2307.2	35.76	2350.5	11.59	2399.3	23.03	2342.6	23.08	3.84
ST1502-33	14.88	399.94	0.04	0.11445	0.00248	5.50885	0.07458	0.34882	0.00405	0.16431	0.00412	1871.2	38.54	1902	11.63	1929	19.34	3074.9	71.55	3
ST1502-34	101.32	133.22	0.76	0.15949	0.00342	10.17621	0.13519	0.46238	0.00544	0.13803	0.00151	2450.3	35.79	2450.9	12.28	2450.1	23.98	2613.3	26.85	-0.01
ST1502-35	88.19	305.16	0.29	0.14642	0.00317	7.95798	0.10818	0.39386	0.00464	0.15118	0.00203	2304.5	36.69	2226.3	12.26	2140.7	21.47	2845.7	35.6	-7.65
ST1510-1																				
ST1510-1-01	121.73	180.41	0.67	0.14816	0.00309	9.11498	0.11726	0.44602	0.00518	0.1349	0.00149	2324.8	35.37	2349.6	11.77	2377.5	23.08	2557.8	26.46	2.22
ST1510-1-02	59.66	346.29	0.17	0.1025	0.00227	4.15418	0.06133	0.29382	0.00346	0.09876	0.00175	1669.9	40.46	1665	12.08	1660.6	17.25	1903.7	32.16	-0.56

ST1510-1-03	98.64	755.91	0.13	0.10508	0.00221	3.84447	0.04961	0.26523	0.00301	0.09094	0.00137	1715.8	38.15	1602.1	10.4	1516.5	15.32	1759.3	25.31	13.14
ST1510-1-04	85.63	534.95	0.16	0.10403	0.00226	4.0117	0.05652	0.27957	0.00324	0.09542	0.00159	1697.2	39.58	1636.6	11.45	1589.2	16.35	1842.1	29.42	-6.8
ST1510-1-05	81.32	170.73	0.48	0.15503	0.00341	9.73147	0.14348	0.45507	0.00561	0.13628	0.00201	2402.2	36.97	2409.7	13.58	2417.8	24.85	2582.3	35.76	0.65
ST1510-1-06	45.46	280.97	0.16	0.10936	0.00229	4.92361	0.0629	0.3264	0.0037	0.10298	0.00147	1788.7	37.71	1806.3	10.78	1820.9	17.99	1981	27.03	1.77
ST1510-1-07	105.11	170.34	0.62	0.13591	0.0029	7.52844	0.10126	0.40159	0.00469	0.12541	0.00145	2175.7	36.68	2176.4	12.06	2176.4	21.57	2388	26.1	0.03
ST1510-1-08	117.34	219.61	0.53	0.14903	0.00321	8.92021	0.12357	0.43395	0.00517	0.13394	0.00171	2334.8	36.45	2329.9	12.65	2323.5	23.23	2540.6	30.53	-0.49
ST1510-1-09	67.62	656.42	0.1	0.11133	0.00227	5.07906	0.05965	0.33074	0.00367	0.12431	0.00155	1821.3	36.55	1832.6	9.96	1842	17.76	2368.3	27.91	1.12
ST1510-1-10	143.36	700.35	0.2	0.10887	0.00225	4.98382	0.06094	0.33188	0.00371	0.10857	0.0013	1780.6	37.28	1816.6	10.34	1847.5	17.97	2083.3	23.74	3.62
ST1510-1-11	104.49	171.31	0.61	0.14716	0.00321	8.88408	0.12669	0.43767	0.00527	0.13018	0.00168	2313.2	37	2326.2	13.01	2340.2	23.61	2473.5	29.96	1.15
ST1510-1-12	87.44	444.04	0.2	0.1252	0.00256	6.51426	0.07716	0.37723	0.0042	0.11491	0.00134	2031.6	35.79	2047.8	10.43	2063.4	19.65	2198.6	24.29	1.54
ST1510-1-13	83.43	200.06	0.42	0.15054	0.00317	9.24356	0.11915	0.44517	0.00513	0.13152	0.00162	2352.1	35.57	2362.4	11.81	2373.7	22.89	2497.4	28.87	0.91
ST1510-1-14	75.19	99.87	0.75	0.15011	0.00324	9.06264	0.12487	0.43772	0.00518	0.13204	0.00154	2347.2	36.47	2344.3	12.6	2340.4	23.22	2506.8	27.53	-0.29
ST1510-1-15	40.12	114.74	0.35	0.12983	0.00294	6.58372	0.10083	0.36766	0.00447	0.11371	0.00183	2095.7	39.24	2057.2	13.5	2018.4	21.05	2176.8	33.22	-3.83
ST1510-1-16	92.95	410.23	0.23	0.11494	0.00238	5.2966	0.06398	0.33411	0.00371	0.10183	0.00118	1879	36.83	1868.3	10.32	1858.2	17.94	1960.1	21.65	-1.12
ST1510-1-17	101.85	140.25	0.73	0.1373	0.00325	7.55379	0.1277	0.3989	0.00511	0.11609	0.0017	2193.4	40.56	2179.4	15.16	2164	23.56	2220	30.84	-1.36
ST1510-1-18	89.15	185.3	0.48	0.12243	0.00266	5.82728	0.08055	0.3451	0.004	0.11266	0.00138	1991.9	38.17	1950.5	11.98	1911.2	19.18	2157.7	25.05	-4.22
ST1510-1-19	17.8	53.34	0.33	0.15371	0.00376	9.43956	0.17144	0.44528	0.00605	0.12835	0.00291	2387.6	41.05	2381.7	16.67	2374.2	27.01	2440.7	52.05	-0.56
ST1510-1-20	53.89	144.29	0.37	0.15595	0.0033	9.80215	0.12595	0.45573	0.00524	0.13619	0.00172	2412.3	35.44	2416.4	11.84	2420.7	23.19	2580.6	30.57	0.35
ST1510-1-21	222.32	345.87	0.64	0.17859	0.00366	11.97902	0.14032	0.48637	0.00541	0.14431	0.00142	2639.8	33.67	2602.8	10.98	2554.9	23.45	2724.6	25.01	-3.32
ST1510-1-22	147.61	614.8	0.24	0.11038	0.00227	4.96571	0.05817	0.32619	0.00358	0.10049	0.00105	1805.7	36.93	1813.5	9.9	1819.9	17.4	1935.4	19.37	0.78
ST1510-1-23	72.58	182.07	0.4	0.15766	0.00335	9.7287	0.12622	0.44745	0.00515	0.13282	0.00168	2430.7	35.55	2409.4	11.95	2383.9	22.95	2520.7	29.94	-1.96
ST1510-1-24	30.44	93.69	0.32	0.11137	0.00258	5.03961	0.07981	0.32812	0.00394	0.10727	0.00173	1821.9	41.39	1826	13.42	1829.3	19.13	2059.6	31.49	0.4
ST1510-1-25	87.02	98.91	0.88	0.15146	0.00371	8.85154	0.15985	0.42382	0.00569	0.12654	0.00191	2362.4	41.25	2322.8	16.48	2277.8	25.77	2408.3	34.3	-3.71
ST1510-1-26	72.87	401.44	0.18	0.12908	0.00275	6.04815	0.07819	0.33978	0.00384	0.11267	0.00163	2085.5	37.05	1982.8	11.26	1885.6	18.47	2158	29.66	10.6
ST1510-1-27	156.9	316.63	0.5	0.12751	0.00272	6.43671	0.08306	0.36607	0.00413	0.12557	0.00139	2064	37.12	2037.3	11.34	2010.9	19.51	2391	24.93	-2.64
ST1510-1-28	115.86	201.67	0.57	0.14096	0.00309	5.90621	0.08185	0.30386	0.00352	0.10459	0.00124	2239.1	37.45	1962.1	12.03	1710.4	17.39	2010.6	22.72	-30.91
ST1510-1-29	63.4	169.36	0.37	0.15161	0.00329	9.13175	0.12431	0.43683	0.0051	0.14627	0.00198	2364.1	36.58	2351.3	12.46	2336.4	22.87	2759.2	34.83	-1.19
ST1510-1-30	75.31	364.15	0.21	0.11568	0.00244	5.40976	0.06698	0.33915	0.00376	0.1033	0.00129	1890.6	37.43	1886.4	10.61	1882.6	18.1	1987	23.56	-0.42
ST1510-1-31	82.46	250.54	0.33	0.15624	0.00328	9.74755	0.11942	0.45251	0.00506	0.13381	0.00157	2415.3	35.17	2411.2	11.28	2406.4	22.45	2538.3	27.94	-0.37
ST1510-1-32	99.44	752.65	0.13	0.10724	0.00233	4.29501	0.05765	0.2905	0.00327	0.09007	0.0015	1753	39.21	1692.4	11.06	1644	16.34	1743.2	27.77	-6.63
ST1510-1-33	41.56	228.84	0.18	0.11681	0.0027	5.40802	0.08431	0.33582	0.00401	0.1054	0.00212	1907.9	40.89	1886.1	13.36	1866.5	19.36	2025.5	38.78	-2.22
ST1510-1-34	99.88	158.2	0.63	0.17685	0.00378	12.07093	0.15703	0.49507	0.00571	0.14867	0.00172	2623.6	35.13	2609.9	12.2	2592.6	24.63	2801.6	30.19	-1.2
ST1510-1-35	67.82	307.66	0.22	0.12433	0.00262	5.92505	0.07319	0.34567	0.00382	0.10506	0.0013	2019.3	36.99	1964.9	10.73	1913.9	18.32	2019.1	23.72	-5.51
ST1510-2																				
ST1510-2-01	79.02	118.72	0.67	0.12656	0.00302	4.99268	0.08295	0.28604	0.00349	0.11388	0.00151	2050.7	41.52	1818.1	14.06	1621.7	17.52	2179.9	27.47	-26.45
ST1510-2-02	83.3	412.96	0.2	0.07374	0.00185	1.46885	0.02659	0.14442	0.00168	0.04811	0.0009	1034.5	49.82	917.7	10.94	869.6	9.48	949.8	17.32	5.24
ST1510-2-03	75.49	351.18	0.21	0.08059	0.0018	1.90679	0.02716	0.17155	0.00191	0.05682	0.00079	1211.5	43.31	1083.5	9.49	1020.6	10.51	1117	15.11	5.81
ST1510-2-04	121.84	371.91	0.33	0.06984	0.00171	1.38932	0.024	0.14423	0.00166	0.04376	0.00065	923.7	49.4	884.4	10.2	868.5	9.33	865.7	12.64	1.8
ST1510-2-05	48.22	302.49	0.16	0.07202	0.0018	1.42338	0.02578	0.14331	0.00167	0.05037	0.00101	986.4	50.14	898.8	10.8	863.3	9.4	993.2	19.34	3.95
ST1510-2-06	67.11	437.52	0.15	0.06983	0.00162	1.38922	0.02151	0.14425	0.00162	0.04925	0.00081	923.4	46.84	884.4	9.14	868.6	9.12	971.7	15.59	1.79
ST1510-2-07	39.43	252.73	0.16	0.08407	0.0019	1.96402	0.02885	0.1694	0.0019	0.06563	0.00103	1294	43.33	1103.3	9.88	1008.8	10.49	1284.8	19.6	8.57
ST1510-2-08	59.49	389.44	0.15	0.07095	0.00169	1.45833	0.02408	0.14904	0.0017	0.04964	0.00091	956	47.98	913.3	9.95	895.6	9.54	979.1	17.47	1.94
ST1510-2-09	62.76	250.82	0.25	0.07048	0.00189	1.53766	0.03162	0.15819	0.00191	0.0488	0.00098	942.4	54.08	945.6	12.65	946.7	10.65	963	18.86	-0.12

ST1510-2-10	91.78	360.46	0.25	0.077	0.00184	1.50414	0.02497	0.14164	0.00163	0.04992	0.00077	1121.3	46.93	932.1	10.13	853.9	9.18	984.7	14.75	8.39
ST1510-2-11	108.21	227.26	0.48	0.07226	0.00209	1.48838	0.03431	0.14934	0.00188	0.04824	0.00084	993.4	57.61	925.7	14	897.3	10.54	952.3	16.13	3.07
ST1510-2-12	111.08	373.08	0.3	0.07276	0.00174	1.46656	0.02448	0.14616	0.00168	0.04798	0.0007	1007.2	47.51	916.7	10.08	879.4	9.42	947.2	13.57	4.07
ST1510-2-13	59.27	250.72	0.24	0.07199	0.00189	1.44053	0.02869	0.14511	0.00174	0.04575	0.0009	985.5	52.67	905.9	11.93	873.5	9.8	904.2	17.41	3.58
ST1510-2-14	94.93	281.44	0.34	0.07254	0.0025	1.47558	0.04368	0.1475	0.00207	0.0452	0.00118	1001.1	68.43	920.4	17.92	887	11.6	893.5	22.91	3.63
ST1510-2-15	44.3	354.53	0.12	0.0698	0.00205	1.42995	0.03388	0.14855	0.00188	0.04828	0.00151	922.5	59.17	901.5	14.16	892.8	10.57	953.1	29.05	0.97
ST1510-2-16	71.32	313.71	0.23	0.07352	0.0019	1.49223	0.02886	0.14718	0.00176	0.04906	0.00094	1028.4	51.42	927.2	11.76	885.1	9.88	968.1	18.1	4.54
ST1510-2-17	221.58	363.79	0.61	0.07336	0.00168	1.51014	0.02309	0.14927	0.00169	0.03429	0.00041	1024	45.61	934.5	9.34	896.9	9.45	681.5	7.94	4.02
ST1510-2-18	82.16	294.25	0.28	0.07261	0.00198	1.45424	0.03077	0.14524	0.00178	0.04533	0.00089	1003	54.09	911.6	12.73	874.2	10.02	896	17.31	4.1
ST1510-2-19	137.46	302.08	0.46	0.14372	0.00298	8.21763	0.09926	0.41465	0.00462	0.1119	0.0012	2272.4	35.24	2255.3	10.93	2236.2	21.03	2143.9	21.87	-1.62
ST1510-2-20	177.92	335.8	0.53	0.07023	0.00163	1.43305	0.02278	0.14797	0.00168	0.04208	0.00051	935.1	47	902.8	9.51	889.6	9.45	833.2	9.81	1.46
ST1510-2-21	91.38	572.55	0.16	0.07947	0.00168	1.8318	0.02333	0.16717	0.00184	0.05908	0.00073	1183.8	41.24	1056.9	8.36	996.5	10.15	1160.2	13.87	5.71
ST1510-2-22	45.91	209.2	0.22	0.07134	0.00197	1.44414	0.03125	0.1468	0.00181	0.04609	0.00102	967.3	55.36	907.4	12.98	883	10.18	910.7	19.8	2.69
ST1510-2-23	68.41	194.28	0.35	0.06812	0.00213	1.39965	0.03636	0.149	0.00195	0.04725	0.00102	872.3	63.35	888.8	15.39	895.4	10.96	933.1	19.71	-0.74
ST1510-2-24	176.84	452.29	0.39	0.069	0.00156	1.39912	0.02105	0.14705	0.00166	0.0418	0.00051	898.7	46	888.6	8.91	884.4	9.3	827.6	9.92	0.47
ST1510-2-25	289.58	440.12	0.66	0.07545	0.00162	1.77664	0.02372	0.17077	0.00189	0.05065	0.0005	1080.6	42.48	1037	8.67	1016.3	10.43	998.6	9.71	2
ST1510-2-26	53.5	284.45	0.19	0.06934	0.0016	1.41297	0.02224	0.14779	0.00168	0.04784	0.00075	908.9	46.8	894.4	9.36	888.6	9.44	944.6	14.51	0.65
ST1510-2-27	94.68	412.86	0.23	0.06767	0.00162	1.28485	0.02177	0.13771	0.00159	0.04666	0.00073	858.5	48.91	839	9.67	831.7	8.99	921.7	14.08	0.87
ST1510-2-28	97.65	351.55	0.28	0.06884	0.00162	1.41115	0.02311	0.14869	0.00171	0.03282	0.00053	893.8	47.78	893.6	9.73	893.6	9.57	652.8	10.34	0
ST1510-2-29	71.81	283.32	0.25	0.07269	0.00162	1.69681	0.02499	0.16932	0.00191	0.05876	0.00077	1005.2	44.67	1007.3	9.41	1008.4	10.54	1154.1	14.67	-0.11
ST1510-2-30	35.22	370.66	0.1	0.06934	0.00159	1.41875	0.02199	0.1484	0.00169	0.05447	0.00105	909	46.4	896.8	9.23	892	9.46	1072.1	20.14	0.54
ST1510-2-31	294.64	541.87	0.54	0.07483	0.0016	1.74606	0.02336	0.16925	0.00188	0.05266	0.00054	1063.9	42.5	1025.7	8.64	1008	10.38	1037.3	10.29	1.73
ST1510-2-32	66.93	260.09	0.26	0.06814	0.00174	1.40052	0.02674	0.14909	0.00177	0.04735	0.00083	872.8	51.91	889.2	11.31	895.9	9.95	935	16.05	-0.75
ST1510-2-33	57.42	377.09	0.15	0.06832	0.00157	1.38663	0.02183	0.14722	0.00168	0.04469	0.00077	878.2	46.9	883.3	9.29	885.4	9.43	883.7	14.88	-0.24
ST1510-2-34	61.76	277.59	0.22	0.07704	0.00188	1.79192	0.03179	0.16871	0.002	0.04824	0.0009	1122.3	47.97	1042.5	11.56	1005	11.03	952.3	17.36	3.6
ST1510-2-35	71.13	471.12	0.15	0.06962	0.00151	1.40102	0.01929	0.14597	0.00163	0.04463	0.00063	917.2	43.9	889.4	8.16	878.3	9.15	882.6	12.19	1.25
ST1511																				
ST1511-01	129.18	679.38	0.19	0.07152	0.00196	0.62541	0.01306	0.06339	0.00074	0.03405	0.00062	972.3	54.87	493.2	8.16	396.2	4.51	676.8	12.03	19.67
ST1511-02	88.36	314.51	0.28	0.07816	0.00186	1.74484	0.02842	0.16182	0.00183	0.05742	0.00084	1151	46.54	1025.3	10.51	966.9	10.18	1128.5	16.11	5.7
ST1511-03	62.51	103.43	0.6	0.05578	0.00267	0.53603	0.02349	0.06967	0.00106	0.02367	0.00058	443.1	103.26	435.8	15.53	434.2	6.37	472.9	11.4	0.37
ST1511-04	223.07	289.69	0.77	0.05911	0.00215	0.56095	0.01767	0.0688	0.00091	0.02451	0.00041	571.1	77.29	452.1	11.5	428.9	5.46	489.4	8.02	5.13
ST1511-05	156.74	687.38	0.23	0.0566	0.00173	0.52768	0.01311	0.06758	0.00082	0.02164	0.00048	475.4	66.23	430.3	8.72	421.6	4.93	432.8	9.48	2.02
ST1511-06	192.88	282.83	0.68	0.05728	0.00211	0.5486	0.01752	0.06943	0.00092	0.02419	0.00042	501.8	79.45	444.1	11.49	432.7	5.52	483.2	8.34	2.57
ST1511-07	356	372.56	0.96	0.08393	0.00285	1.4123	0.04053	0.12199	0.0017	0.04538	0.00074	1290.8	64.69	894.1	17.06	742	9.77	897	14.29	17.01
ST1511-08	175.82	682.09	0.26	0.0801	0.00181	1.53066	0.02235	0.13854	0.00154	0.05694	0.00073	1199.5	43.97	942.8	8.97	836.4	8.71	1119.2	13.87	11.29
ST1511-09	264.76	378.88	0.7	0.05954	0.00199	0.56466	0.01588	0.06876	0.00087	0.02284	0.00037	586.9	70.82	454.6	10.3	428.7	5.26	456.5	7.25	5.7
ST1511-10	161.94	433.99	0.37	0.07946	0.00181	1.9268	0.02881	0.1758	0.00197	0.06169	0.00076	1183.7	44.46	1090.4	10	1044	10.81	1210	14.52	4.26
ST1511-11	121.13	312.08	0.39	0.0659	0.00182	1.07175	0.02291	0.1179	0.00141	0.03841	0.00064	803.3	56.82	739.6	11.23	718.5	8.15	761.8	12.37	2.85
ST1511-12	196.44	345.51	0.57	0.10582	0.00229	3.91917	0.05155	0.26853	0.00298	0.08412	0.00091	1728.5	39.08	1617.6	10.64	1533.3	15.17	1632.5	16.91	12.73
ST1511-13	281.2	577.5	0.49	0.15895	0.0033	8.23338	0.09748	0.37557	0.00413	0.12823	0.0013	2444.5	34.77	2257	10.72	2055.6	19.34	2438.6	23.33	18.92
ST1511-14	390.05	516.51	0.76	0.06287	0.00225	0.59653	0.01835	0.06879	0.00092	0.02284	0.00039	704	74.27	475	11.67	428.9	5.52	456.5	7.74	9.71
ST1511-15	94.39	171.71	0.55	0.07125	0.0029	0.69675	0.02514	0.0709	0.00104	0.02405	0.00056	964.6	80.89	536.8	15.04	441.6	6.26	480.4	11.15	17.73
ST1511-16	23.51	102.39	0.23	0.07273	0.00287	0.94129	0.03284	0.09384	0.00138	0.04271	0.00133	1006.4	78.11	673.6	17.18	578.2	8.14	845.4	25.78	14.16

ST1511-17	60.05	560.21	0.11	0.11531	0.00259	2.33711	0.03371	0.14696	0.00167	0.20117	0.00285	1884.7	39.92	1223.6	10.26	883.9	9.39	3704.9	47.91	27.76
ST1511-18	226.27	198.42	1.14	0.07066	0.00184	1.53329	0.02979	0.15735	0.00187	0.04805	0.00056	947.5	52.36	943.8	11.94	942	10.44	948.5	10.77	0.19
ST1511-19	190.27	250.29	0.76	0.05884	0.00227	0.55323	0.01881	0.06818	0.00093	0.02356	0.00042	561	82	447.1	12.3	425.2	5.64	470.7	8.28	4.9
ST1511-20	327.56	421.91	0.78	0.07166	0.00222	0.58716	0.01485	0.05941	0.00075	0.01837	0.00028	976.4	61.88	469.1	9.5	372.1	4.56	368	5.6	20.68
ST1511-21	258.26	502.32	0.51	0.07926	0.00218	1.78509	0.03798	0.16331	0.00204	0.05605	0.00089	1178.7	53.35	1040	13.85	975.2	11.28	1102.3	16.97	6.23
ST1511-22	80.17	266.86	0.3	0.07288	0.00185	1.65067	0.03063	0.16424	0.00195	0.05155	0.00086	1010.6	50.51	989.8	11.73	980.3	10.78	1015.9	16.46	0.96
ST1511-23	179.28	720.53	0.25	0.07986	0.00205	0.58666	0.01104	0.05327	0.00062	0.03119	0.00046	1193.6	49.85	468.7	7.07	334.6	3.82	620.8	8.98	28.61
ST1511-24	464.92	524.98	0.89	0.05603	0.00146	0.52075	0.01016	0.0674	0.00078	0.02195	0.00025	453.3	56.89	425.7	6.78	420.5	4.7	438.8	4.91	1.22
ST1511-25	319.97	1131.63	0.28	0.06776	0.00145	1.33435	0.01736	0.14281	0.00158	0.04464	0.00049	861.3	43.89	860.8	7.55	860.5	8.89	882.7	9.39	0.03
ST1511-26	57.88	487.28	0.12	0.09675	0.00207	3.14568	0.04102	0.23579	0.00264	0.07351	0.00112	1562.4	39.68	1443.9	10.05	1364.8	13.76	1433.8	21.03	5.48
ST1511-27	617.26	483.99	1.28	0.09131	0.00252	0.82211	0.01741	0.0653	0.00081	0.02139	0.00026	1452.9	51.65	609.2	9.7	407.8	4.89	427.8	5.19	33.06
ST1511-28	312.34	366.92	0.85	0.07497	0.00169	1.82059	0.02667	0.17613	0.002	0.05181	0.00054	1067.6	44.54	1052.9	9.6	1045.8	10.94	1020.9	10.36	0.67
ST1511-29	51.6	81.15	0.64	0.07692	0.00278	1.4624	0.04589	0.13789	0.002	0.04738	0.00096	1119.1	70.38	915	18.92	832.7	11.34	935.6	18.62	8.99
ST1511-30	67.82	106.68	0.64	0.05519	0.00271	0.52385	0.02372	0.06885	0.00107	0.02227	0.00055	419.6	105.94	427.7	15.8	429.2	6.46	445.2	10.82	-0.35
ST1511-31	247.06	361.7	0.68	0.09867	0.00283	0.9614	0.02166	0.07067	0.00091	0.03172	0.00046	1599.1	52.57	684	11.21	440.2	5.45	631.2	9	35.64
ST1511-32	336.2	439.71	0.76	0.05938	0.00163	0.56003	0.01192	0.06841	0.00082	0.02201	0.00028	581.1	58.56	451.5	7.76	426.5	4.92	440.1	5.5	5.54
ST1511-33	350.29	617.63	0.57	0.05864	0.00151	0.5472	0.01048	0.06769	0.00079	0.02259	0.00028	553.7	55.27	443.2	6.88	422.2	4.77	451.5	5.57	4.74
ST1511-34	75.9	230.9	0.33	0.10166	0.0023	3.69213	0.05545	0.26342	0.00309	0.08202	0.00116	1654.7	41.37	1569.7	12	1507.3	15.75	1593.3	21.66	9.78
ST1511-35	210.38	283.09	0.74	0.05582	0.0019	0.52158	0.01513	0.06777	0.00088	0.02172	0.00034	445	73.97	426.2	10.1	422.7	5.29	434.3	6.8	0.82
ST1515																				
ST1515-01	58.59	989.93	0.06	0.06195	0.00142	0.60993	0.00933	0.07139	0.0008	0.03894	0.00071	672.5	48.23	483.5	5.89	444.5	4.81	772.2	13.75	8.07
ST1515-02	109.12	1375.5	0.08	0.05405	0.00119	0.47407	0.00665	0.0636	0.0007	0.01901	0.00031	372.8	48.8	394	4.58	397.5	4.25	380.6	6.16	-0.89
ST1515-03	164.58	1766.62	0.09	0.13558	0.00281	1.18672	0.01418	0.06347	0.0007	0.16121	0.0016	2171.5	35.7	794.4	6.58	396.7	4.22	3021	27.91	50.06
ST1515-04	136.27	1616.11	0.08	0.06207	0.00136	0.5555	0.00774	0.0649	0.00072	0.03327	0.00047	676.4	46.3	448.6	5.06	405.4	4.34	661.6	9.15	9.63
ST1515-05	102.85	1373.03	0.07	0.05562	0.00124	0.4863	0.00704	0.0634	0.0007	0.02014	0.00035	437	48.61	402.4	4.81	396.3	4.26	403	6.97	1.52
ST1515-06	87.96	1218.51	0.07	0.05363	0.00121	0.46343	0.00682	0.06266	0.00069	0.01961	0.00035	355.5	50.09	386.6	4.73	391.8	4.21	392.5	6.99	-1.35
ST1515-07	137.62	1536.13	0.09	0.05643	0.00129	0.50938	0.00782	0.06546	0.00073	0.02264	0.0004	468.4	50.52	418	5.26	408.7	4.42	452.5	7.81	2.22
ST1515-08	114.48	1356.4	0.08	0.05504	0.0013	0.46244	0.00755	0.06092	0.00068	0.0183	0.00037	413.9	51.28	386	5.24	381.2	4.16	366.6	7.42	1.24
ST1515-09	126.39	1625.86	0.08	0.05411	0.0012	0.4892	0.00701	0.06556	0.00072	0.02054	0.00034	375.4	49.26	404.4	4.78	409.3	4.38	410.9	6.82	-1.21
ST1515-10	94.03	1156.48	0.08	0.05466	0.00121	0.48489	0.00691	0.06433	0.00071	0.02006	0.00033	398.3	48.64	401.4	4.72	401.9	4.3	401.4	6.58	-0.12
ST1515-11	78.6	491.86	0.16	0.06788	0.00158	1.18878	0.01882	0.127	0.00144	0.04588	0.00073	864.8	47.53	795.4	8.73	770.7	8.25	906.7	14.15	3.11
ST1515-12	59.35	1090.13	0.05	0.07613	0.00166	0.74877	0.01015	0.07132	0.00079	0.0905	0.00119	1098.6	42.94	567.5	5.89	444.1	4.75	1751	22.06	21.74
ST1515-13	126.61	562.83	0.22	0.07149	0.00163	1.41206	0.02143	0.14323	0.00162	0.04315	0.00062	971.5	45.86	894	9.02	862.9	9.14	853.9	12.07	3.48
ST1515-14	67.75	571.59	0.12	0.06893	0.0015	1.37372	0.01872	0.14452	0.0016	0.04396	0.00066	896.5	44.32	877.8	8.01	870.2	9.03	869.6	12.69	0.87
ST1515-15	107.85	1319.43	0.08	0.05499	0.0012	0.50114	0.00691	0.06608	0.00073	0.02011	0.00031	411.8	47.52	412.5	4.67	412.5	4.4	402.4	6.22	0
ST1515-16	140.68	361.85	0.39	0.06985	0.00162	1.35245	0.02119	0.14039	0.0016	0.03973	0.00051	924	46.88	868.6	9.15	846.9	9.02	787.4	9.91	2.5
ST1515-17	98.92	1286.69	0.08	0.05434	0.0012	0.48797	0.00689	0.06511	0.00072	0.01969	0.00033	385.3	48.76	403.5	4.7	406.6	4.34	394.1	6.49	-0.77
ST1515-18	180.16	1918.65	0.09	0.06999	0.00151	0.58361	0.00772	0.06046	0.00066	0.04199	0.00051	928.1	43.68	466.8	4.95	378.4	4.04	831.3	9.8	18.94
ST1515-19	114.2	1084.19	0.11	0.05439	0.00122	0.48846	0.00707	0.06513	0.00072	0.01811	0.00029	387	49.25	403.9	4.82	406.7	4.36	362.9	5.73	-0.69
ST1515-20	255.97	1607.8	0.16	0.06321	0.00137	0.54993	0.0074	0.06309	0.00069	0.01776	0.00023	715.2	45.48	444.9	4.85	394.4	4.21	355.9	4.57	11.35
ST1515-21	51.73	1440.18	0.04	0.0638	0.0015	0.50933	0.00822	0.05789	0.00065	0.05462	0.00109	734.9	49.11	418	5.53	362.8	3.97	1074.9	20.87	13.21
ST1515-22	72.33	1673.66	0.04	0.05703	0.00134	0.43056	0.00687	0.05474	0.00061	0.02679	0.00058	492.1	51.44	363.6	4.88	343.6	3.75	534.3	11.49	5.5
ST1515-23	100.22	1393.84	0.07	0.05678	0.00129	0.55656	0.00839	0.07108	0.00079	0.02115	0.00041	482.2	49.79	449.3	5.47	442.7	4.76	423.1	8.16	1.47

ST1515-24	74.61	1489.92	0.05	0.06119	0.00134	0.53086	0.00735	0.06291	0.00069	0.03771	0.00059	646.1	46.53	432.4	4.87	393.3	4.2	748.2	11.47	9.04
ST1515-25	180.2	1763.59	0.1	0.0566	0.00129	0.48842	0.00729	0.06258	0.00069	0.02148	0.00034	475.2	49.9	403.8	4.97	391.3	4.21	429.5	6.75	3.1
ST1515-26	122.41	1513.67	0.08	0.05673	0.00124	0.49673	0.00683	0.06349	0.0007	0.02206	0.00033	480.4	48.05	409.5	4.63	396.8	4.23	440.9	6.58	3.1
ST1515-27	117.56	1404.52	0.08	0.05465	0.00121	0.48289	0.00674	0.06408	0.0007	0.01952	0.00031	397.8	48.38	400.1	4.62	400.4	4.27	390.7	6.1	-0.07
ST1515-28	94.75	1250.48	0.08	0.05499	0.00122	0.50152	0.00712	0.06613	0.00073	0.02054	0.00035	411.8	48.2	412.7	4.81	412.8	4.41	411	6.86	-0.02
ST1515-29	170.6	386.23	0.44	0.07052	0.00162	1.39447	0.02125	0.1434	0.00162	0.04288	0.00051	943.4	46.23	886.6	9.01	863.8	9.13	848.6	9.94	2.57
ST1515-30	128.37	1518.64	0.08	0.05493	0.0012	0.48592	0.00667	0.06415	0.0007	0.0201	0.0003	409.2	47.98	402.1	4.56	400.8	4.27	402.2	6.03	0.32
ST1515-31	105.87	536.42	0.2	0.07065	0.00168	1.38332	0.02281	0.14198	0.00163	0.04507	0.00074	947.4	47.97	881.9	9.72	855.8	9.19	891	14.31	2.96
ST1515-32	79.33	1380.49	0.06	0.05852	0.00134	0.52503	0.00797	0.06506	0.00072	0.03035	0.00056	549.1	49.26	428.5	5.31	406.4	4.38	604.3	11.04	5.16
ST1515-33	84.25	294.86	0.29	0.06963	0.00163	1.38946	0.02206	0.1447	0.00164	0.04025	0.00057	917.5	47.32	884.5	9.37	871.2	9.26	797.5	11.16	1.5
ST1515-34	222.28	2318.8	0.1	0.05599	0.0012	0.50156	0.00646	0.06496	0.00071	0.02121	0.00027	451.6	46.61	412.8	4.37	405.7	4.29	424.3	5.36	1.72
ST1515-35	124.16	765.81	0.16	0.07151	0.00155	1.25994	0.01681	0.12776	0.00141	0.04087	0.00053	972.1	43.6	827.9	7.55	775.1	8.06	809.6	10.22	6.38
ST1512																				
ST1512-01	304.6	474.29	0.64	0.05878	0.00168	0.55754	0.01256	0.06877	0.00083	0.02161	0.0003	559	61.04	449.9	8.19	428.7	4.99	432.1	5.93	4.71
ST1512-02	114.37	174.38	0.66	0.06117	0.00284	0.57906	0.02447	0.06864	0.00106	0.02272	0.00054	645.1	96.59	463.9	15.73	428	6.4	454.1	10.65	7.74
ST1512-03	210.3	397.48	0.53	0.24895	0.00624	3.75388	0.06624	0.10933	0.00145	0.12312	0.00168	3178.1	39.12	1582.9	14.15	668.9	8.45	2346.8	30.15	57.74
ST1512-04	283.76	319.47	0.89	0.0577	0.00181	0.53915	0.01393	0.06775	0.00084	0.0203	0.00029	518.3	67.54	437.9	9.19	422.6	5.09	406.3	5.65	3.49
ST1512-05	497.53	1340.73	0.37	0.05622	0.00126	0.52382	0.00763	0.06755	0.00075	0.01983	0.00022	460.4	49.49	427.7	5.08	421.4	4.54	396.8	4.39	1.47
ST1512-06	297.66	2266.19	0.13	0.06544	0.00151	0.61755	0.00949	0.06842	0.00077	0.03314	0.00047	788.5	47.66	488.3	5.96	426.6	4.65	659	9.29	12.64
ST1512-07	238.58	767.58	0.31	0.05765	0.00152	0.52999	0.01056	0.06666	0.00078	0.02162	0.00033	516.2	57.27	431.8	7	416	4.71	432.3	6.63	3.66
ST1512-08	98.4	163.43	0.6	0.06566	0.00269	0.6127	0.02239	0.06766	0.00098	0.02289	0.0005	795.5	83.7	485.3	14.1	422.1	5.92	457.4	9.82	13.02
ST1512-09	89.12	124.84	0.71	0.0635	0.0027	0.6005	0.0229	0.06857	0.00101	0.02221	0.00047	724.9	87.55	477.6	14.53	427.5	6.09	444	9.32	10.49
ST1512-10	449.47	962.07	0.47	0.06439	0.00196	0.52534	0.01304	0.05916	0.00074	0.02063	0.00034	754.4	63.06	428.7	8.68	370.5	4.49	412.6	6.83	13.58
ST1512-11	192.9	275.79	0.7	0.06194	0.00232	0.5861	0.01918	0.0686	0.00094	0.02201	0.00041	672.2	78.12	468.4	12.28	427.7	5.68	440.1	8.11	8.69
ST1512-12	249.27	634.93	0.39	0.05775	0.00181	0.54438	0.01413	0.06835	0.00085	0.02142	0.0004	520.1	67.68	441.3	9.29	426.2	5.16	428.4	7.89	3.42
ST1512-13	92.33	160.98	0.57	0.05729	0.00314	0.51727	0.02642	0.06547	0.0011	0.02051	0.00061	502.1	116.67	423.3	17.68	408.8	6.67	410.4	12.06	3.43
ST1512-14	249.46	776.94	0.32	0.05581	0.00133	0.52221	0.00868	0.06785	0.00077	0.02097	0.00027	444.3	52.01	426.6	5.79	423.2	4.64	419.5	5.36	0.8
ST1512-15	127.52	166.24	0.77	0.08273	0.00228	2.24335	0.04826	0.19663	0.00251	0.05681	0.00085	1262.7	52.76	1194.7	15.11	1157.2	13.53	1116.7	16.19	3.14
ST1512-16	136.3	192.99	0.71	0.05651	0.00245	0.52508	0.02058	0.06737	0.00098	0.0212	0.00045	471.8	93.93	428.5	13.7	420.3	5.94	423.9	8.88	1.91
ST1512-17	232.57	262.61	0.89	0.06527	0.00232	0.61114	0.01876	0.06789	0.00092	0.02125	0.00035	783	73.1	484.3	11.83	423.4	5.54	425	6.99	12.57
ST1512-18	51.6	156.5	0.33	0.06875	0.00262	1.50545	0.05068	0.15877	0.00237	0.04601	0.00138	891.2	76.67	932.6	20.54	950	13.18	909.1	26.67	-1.87
ST1512-19	251.1	681.22	0.37	0.0553	0.00142	0.51443	0.00983	0.06745	0.00078	0.02115	0.0003	424.2	55.86	421.4	6.59	420.8	4.72	423.1	5.89	0.14
ST1512-20	342.84	848.3	0.4	0.05682	0.00135	0.52922	0.00873	0.06754	0.00077	0.02108	0.00026	483.8	51.75	431.3	5.8	421.3	4.62	421.7	5.06	2.32
ST1512-21	155.17	318.64	0.49	0.16419	0.00448	1.9275	0.03976	0.08512	0.00114	0.06919	0.00105	2499.3	45.2	1090.7	13.79	526.6	6.79	1352.3	19.78	51.72
ST1512-22	79.61	274.35	0.29	0.05626	0.00248	0.53201	0.02128	0.06857	0.00102	0.02127	0.00069	461.8	95.7	433.1	14.11	427.5	6.12	425.5	13.61	1.29
ST1512-23	149.81	492.93	0.3	0.05537	0.00142	0.52196	0.00995	0.06835	0.00079	0.01993	0.00031	426.8	55.82	426.5	6.64	426.2	4.78	398.9	6.05	0.07
ST1512-24	86.6	91.07	0.95	0.05669	0.0028	0.52969	0.02416	0.06775	0.00106	0.01998	0.00043	478.7	106.36	431.6	16.04	422.6	6.42	399.8	8.62	2.09
ST1512-25	99.82	117.06	0.85	0.05789	0.00334	0.56474	0.03056	0.07073	0.00125	0.02292	0.0006	525.4	121.99	454.6	19.83	440.6	7.53	458.1	11.81	3.08
ST1512-26	274.75	526.4	0.52	0.05514	0.00154	0.52105	0.01147	0.06852	0.00082	0.02205	0.00031	417.7	60.77	425.9	7.66	427.2	4.94	440.8	6.16	-0.31
ST1512-27	144.47	189.7	0.76	0.08809	0.00286	0.85613	0.02313	0.07047	0.00095	0.02793	0.00045	1384.4	60.94	628	12.65	439	5.74	556.8	8.9	30.1
ST1512-28	239.89	433.8	0.55	0.06168	0.00163	0.58112	0.0117	0.06832	0.00081	0.02182	0.00029	663	55.77	465.2	7.51	426	4.87	436.3	5.78	8.43
ST1512-29	152.75	530.37	0.29	0.0609	0.00158	0.57442	0.01119	0.06839	0.0008	0.02287	0.00036	635.8	54.95	460.9	7.22	426.4	4.84	457.1	7.12	7.49
ST1512-30	126.02	667.84	0.19	0.05478	0.00132	0.51981	0.00883	0.06881	0.00078	0.02114	0.00033	403.3	52.64	425	5.9	429	4.73	422.9	6.52	-0.94

ST1512-31	300.2	930.89	0.32	0.05485	0.00134	0.5094	0.00887	0.06734	0.00077	0.02089	0.00028	406.1	52.91	418	5.97	420.1	4.65	417.9	5.56	-0.5
ST1512-32	101.71	461.78	0.22	0.05594	0.00156	0.5288	0.01158	0.06854	0.00082	0.02082	0.00041	449.7	60.73	431	7.69	427.4	4.94	416.4	8.11	0.84
ST1512-33	128.37	364.49	0.35	0.05742	0.0018	0.54477	0.01412	0.06879	0.00086	0.02156	0.00042	507.4	67.74	441.6	9.28	428.9	5.2	431.1	8.24	2.88
ST1512-34	139.71	533.26	0.26	0.05472	0.00168	0.51772	0.01308	0.0686	0.00085	0.02062	0.00044	401	66.55	423.6	8.75	427.7	5.13	412.5	8.67	-0.97
ST1512-35	109.6	288.66	0.38	0.06817	0.00153	1.50345	0.02208	0.15993	0.00181	0.04711	0.00056	873.7	45.67	931.8	8.96	956.4	10.08	930.4	10.84	-2.64
ST1513																				
ST1513-01	67.98	74.78	0.91	0.16284	0.00428	9.74011	0.20133	0.43359	0.0064	0.11977	0.00214	2485.3	43.61	2410.5	19.03	2321.9	28.79	2286.5	38.55	-7.04
ST1513-02	169.83	524.27	0.32	0.15624	0.00324	6.73517	0.07998	0.31249	0.00342	0.09581	0.00108	2415.4	34.75	2077.2	10.5	1752.9	16.8	1849.3	19.93	-37.8
ST1513-03	55.18	37.39	1.48	0.07829	0.00355	1.72958	0.07182	0.16015	0.00274	0.05321	0.001	1154.2	87.5	1019.6	26.72	957.6	15.21	1047.8	19.22	6.08
ST1513-04	33.18	330.1	0.1	0.05618	0.00175	0.51624	0.01327	0.06662	0.00081	0.02173	0.00072	458.6	68.16	422.6	8.89	415.8	4.91	434.5	14.32	1.61
ST1513-05	199.45	753.52	0.26	0.08332	0.00193	1.62536	0.02538	0.14143	0.0016	0.04627	0.00068	1276.5	44.69	980.1	9.82	852.7	9.03	914.2	13.11	13
ST1513-06	12.45	44.85	0.28	0.0707	0.00265	1.5843	0.05237	0.16246	0.00236	0.05074	0.00162	948.8	74.95	964.1	20.58	970.4	13.1	1000.5	31.2	-0.65
ST1513-07	303.36	493.88	0.61	0.09544	0.00263	0.76629	0.01618	0.05821	0.00071	0.01791	0.00028	1536.7	51	577.6	9.3	364.8	4.34	358.7	5.57	36.84
ST1513-08	243.15	419.25	0.58	0.06128	0.00199	0.57685	0.01564	0.06825	0.00086	0.02087	0.00036	649.2	68.18	462.4	10.07	425.6	5.19	417.5	7.1	7.96
ST1513-09	432.17	533.26	0.81	0.07709	0.00198	1.66927	0.03177	0.15701	0.00187	0.04797	0.00061	1123.5	50.38	996.9	12.08	940.1	10.4	947	11.7	5.7
ST1513-10	104.61	186.53	0.56	0.07426	0.00243	1.38531	0.03809	0.13526	0.00182	0.04157	0.00081	1048.7	64.54	882.7	16.22	817.8	10.33	823.2	15.66	7.35
ST1513-11	704.53	1121.35	0.63	0.06437	0.00143	0.93608	0.01322	0.10545	0.00116	0.03109	0.00032	753.8	46.21	670.8	6.93	646.3	6.74	618.9	6.24	3.65
ST1513-12	25.32	379.03	0.07	0.05744	0.00157	0.53075	0.01122	0.067	0.00078	0.02103	0.00072	508.1	59.6	432.3	7.44	418.1	4.72	420.7	14.2	3.28
ST1513-13	910.08	1024.5	0.89	0.077	0.00176	1.4884	0.02242	0.14017	0.00157	0.04069	0.00043	1121.3	44.93	925.7	9.15	845.6	8.89	806.2	8.26	8.65
ST1513-14	466.35	725.46	0.64	0.08996	0.00235	1.11913	0.02174	0.09022	0.00108	0.02992	0.00041	1424.6	49.13	762.6	10.41	556.8	6.4	595.9	8.07	26.99
ST1513-15	320.22	421.76	0.76	0.16065	0.00335	8.62316	0.10337	0.38927	0.0043	0.1233	0.0012	2462.6	34.8	2299	10.91	2119.4	19.97	2350	21.62	-16.19
ST1513-16	145.16	196.46	0.74	0.16279	0.00343	10.14697	0.12597	0.45207	0.00508	0.12158	0.00127	2484.8	35.08	2448.3	11.47	2404.4	22.57	2319.1	22.82	-3.34
ST1513-17	90.19	135.94	0.66	0.12888	0.00299	6.24218	0.09895	0.35128	0.00427	0.10422	0.00139	2082.7	40.31	2010.4	13.87	1940.7	20.37	2003.9	25.5	-7.32
ST1513-18	266.05	318.32	0.84	0.05819	0.00199	0.52062	0.01513	0.06489	0.00083	0.02018	0.00031	536.4	73.64	425.6	10.1	405.3	5.03	403.8	6.15	4.77
ST1513-19	90.33	740.91	0.12	0.10587	0.00227	3.37931	0.04351	0.23152	0.00257	0.01806	0.00043	1729.4	38.77	1499.6	10.09	1342.5	13.44	361.7	8.6	10.48
ST1513-20	51.38	2362.54	0.02	0.06693	0.00172	0.54815	0.01031	0.0594	0.00069	0.0793	0.0022	835.7	52.6	443.8	6.76	372	4.17	1542.5	41.14	16.18
ST1513-21	61.87	93.14	0.66	0.05886	0.00269	0.5509	0.02288	0.06789	0.00101	0.02103	0.00048	561.9	96.46	445.6	14.98	423.4	6.1	420.7	9.59	4.98
ST1513-22	60.01	91.19	0.66	0.05775	0.00268	0.52806	0.0224	0.06633	0.00099	0.0207	0.00048	519.9	99.08	430.5	14.88	414	6.01	414.2	9.56	3.83
ST1513-23	20.46	463.27	0.04	0.05912	0.0016	0.55603	0.01146	0.06822	0.0008	0.02155	0.00085	571.4	57.78	448.9	7.48	425.4	4.81	430.9	16.83	5.24
ST1513-24	163.36	241.43	0.68	0.05521	0.00182	0.511	0.01419	0.06714	0.00084	0.0204	0.00032	420.5	71.65	419.1	9.53	418.9	5.09	408.1	6.4	0.05
ST1513-25	667.73	660.06	1.01	0.05788	0.00145	0.51517	0.0093	0.06457	0.00074	0.01874	0.0002	524.9	54.38	421.9	6.23	403.3	4.46	375.2	3.96	4.41
ST1513-26	59.78	102.81	0.58	0.06314	0.00343	0.61931	0.03133	0.07115	0.00122	0.02392	0.0007	712.8	111.53	489.4	19.64	443.1	7.34	477.7	13.82	9.46
ST1513-27	98.09	106.64	0.92	0.09569	0.00287	1.7578	0.04242	0.13326	0.00177	0.06662	0.0009	1541.7	55.33	1030	15.62	806.4	10.06	1303.5	17.08	21.71
ST1513-28	427.54	701.24	0.61	0.07522	0.00217	0.62191	0.01414	0.05997	0.00074	0.01736	0.00027	1074.5	56.96	491	8.85	375.5	4.48	347.9	5.33	23.52
ST1513-29	369.38	707.06	0.52	0.06636	0.0018	0.53111	0.01096	0.05806	0.00069	0.02013	0.00027	817.9	55.72	432.5	7.27	363.8	4.18	402.9	5.42	15.88
ST1513-30	192.84	353.95	0.54	0.1123	0.0026	2.70679	0.04166	0.17485	0.00204	0.03751	0.00051	1837	41.4	1330.3	11.41	1038.8	11.18	744.3	9.93	21.91
ST1513-31	120.02	498.41	0.24	0.16479	0.00357	8.22895	0.10927	0.36226	0.00418	0.10463	0.00153	2505.4	36.04	2256.5	12.02	1992.9	19.78	2011.3	28.02	-25.72
ST1513-32	254.51	306.92	0.83	0.06204	0.00206	0.56328	0.01572	0.06586	0.00084	0.01987	0.0003	675.5	69.49	453.7	10.21	411.2	5.11	397.7	6	9.37
ST1513-33	124.79	484.23	0.26	0.07922	0.00224	0.70343	0.01546	0.06442	0.00079	0.02908	0.00053	1177.5	54.97	540.8	9.22	402.4	4.79	579.4	10.32	25.59
ST1513-34	52.88	287.41	0.18	0.0838	0.00224	1.0435	0.02087	0.09034	0.00109	0.02387	0.00057	1287.8	51.16	725.7	10.37	557.5	6.45	476.9	11.16	23.18
ST1513-35	213.79	555.54	0.38	0.10666	0.00226	4.40374	0.054	0.29951	0.00331	0.08189	0.00083	1743.2	38.21	1713	10.15	1688.9	16.43	1590.8	15.48	-3.22

Table E3 LA-ICP-MS U-Pb zircon dating results of the samples from the Xinyang area.

				Isotope ratios								Ages(Ma)								
Spot No.	Th(ppm)	U(ppm)	Th/U	Pb^{207}/Pb^{206}	1σ	Pb^{207}/U^{235}	1σ	Pb^{206}/U^{238}	1σ	Pb^{208}/Th^{232}	1σ	Pb^{207}/Pb^{206}	1σ	Pb^{207}/U^{235}	1σ	Pb^{206}/U^{238}	1σ	Pb^{208}/Th^{232}	1σ	Disc.%
XY1605																				
XY1605-01	218.73	287.85	0.76	0.07651	0.0019	1.77501	0.0307	0.16817	0.0017	0.05205	0.0006	1108.4	49.88	1036.4	11.2	1002	9.43	1025.6	11.69	3.32
XY1605-02	233.86	508.95	0.46	0.14765	0.0034	3.90996	0.0533	0.19195	0.0019	0.07922	0.001	2318.9	38.91	1615.7	11	1132	10.5	1541	18.33	29.94
XY1605-03	144.75	314.84	0.46	0.06126	0.0025	0.50564	0.0183	0.05983	0.0008	0.01928	0.0005	648.4	86.02	415.5	12.3	374.6	4.7	386	9.09	9.84
XY1605-04	108.01	305.46	0.35	0.07163	0.0019	1.65732	0.0324	0.16771	0.0018	0.05148	0.0009	975.6	53.97	992.4	12.4	999.5	9.78	1014.6	16.57	-0.72
XY1605-05	110.53	229.16	0.48	0.09369	0.0023	3.1011	0.0509	0.23993	0.0025	0.07506	0.0011	1501.9	45.79	1433	12.6	1386.3	13.1	1462.9	19.71	3.26
XY1605-06	280.37	967.45	0.29	0.12245	0.0026	4.414	0.0452	0.26131	0.0024	0.08665	0.0008	1992.2	36.85	1715	8.48	1496.5	12.1	1679.6	15.58	12.74
XY1605-07	116.23	481.57	0.24	0.07824	0.0018	1.95295	0.0272	0.18093	0.0017	0.02735	0.0005	1153.1	44.97	1099.5	9.35	1072.1	9.46	545.4	9.35	2.49
XY1605-08	352.29	727.08	0.48	0.06924	0.002	0.57513	0.0122	0.06022	0.0006	0.02004	0.0003	905.9	57.25	461.3	7.87	376.9	3.81	401	5.84	18.30
XY1605-09	228.55	465.14	0.49	0.13961	0.0034	2.08338	0.0323	0.10818	0.0011	0.05451	0.0007	2222.4	41.22	1143.3	10.7	662.2	6.53	1072.7	13.12	42.08
XY1605-10	559.79	1657.6	0.34	0.0519	0.0015	0.22762	0.0051	0.03179	0.0003	0.01041	0.0002	281.1	65.17	208.2	4.2	201.8	2	209.3	3.26	3.07
XY1605-11	433.18	903.67	0.48	0.05039	0.0015	0.23298	0.0054	0.03352	0.0003	0.01046	0.0002	213.1	67.37	212.7	4.43	212.5	2.12	210.3	2.98	0.09
XY1605-12	220.11	261.46	0.84	0.07329	0.0027	1.01785	0.0316	0.10069	0.0013	0.03114	0.0006	1021.9	72	712.8	15.9	618.4	7.59	619.8	10.76	13.24
XY1605-13	90.99	145.66	0.62	0.05701	0.0029	0.56979	0.027	0.07246	0.0011	0.02195	0.0006	491.4	110.1	457.9	17.5	451	6.64	439	11.51	1.51
XY1605-14	123.06	302.03	0.41	0.0739	0.0019	1.87725	0.0359	0.18419	0.002	0.05478	0.0009	1038.6	52.17	1073.1	12.7	1089.8	10.7	1077.9	16.66	-1.56
XY1605-15	399.13	533.64	0.75	0.05537	0.0024	0.28291	0.011	0.03705	0.0005	0.01133	0.0002	426.9	94.12	253	8.68	234.5	2.98	227.8	4.45	7.31
XY1605-16	108.72	256.25	0.42	0.07487	0.0018	1.44604	0.0216	0.14004	0.0014	0.03173	0.0004	1065.1	46.26	908.2	8.95	844.9	7.68	631.3	8.13	6.97
XY1605-17	106.29	345.31	0.31	0.06928	0.0016	1.44065	0.0192	0.15077	0.0014	0.04302	0.0005	907.2	45.32	906	8.01	905.3	7.94	851.3	9.85	0.08
XY1605-18	59.21	583.78	0.10	0.13728	0.0028	4.68081	0.0458	0.24723	0.0022	0.1325	0.0014	2193.2	34.87	1763.8	8.19	1424.2	11.6	2515	25.64	19.25
XY1605-19	143.45	26.72	5.37	0.11976	0.0034	5.73187	0.1312	0.34706	0.0048	0.09516	0.0009	1952.7	50.07	1936.2	19.8	1920.5	23	1837.2	17.08	-1.68
XY1605-20	85.99	131.03	0.66	0.06772	0.0027	0.71563	0.0255	0.07663	0.001	0.02336	0.0005	860.1	81.76	548.1	15.1	476	6.2	466.7	9.9	13.15
XY1605-21	178.01	290.89	0.61	0.05772	0.0016	0.57232	0.0124	0.0719	0.0007	0.02162	0.0003	519	60.98	459.5	8	447.6	4.46	432.3	5.64	2.59
XY1605-22	165.28	275.87	0.60	0.06001	0.0021	0.59581	0.0172	0.072	0.0008	0.02175	0.0004	603.9	72.43	474.6	10.9	448.2	5.06	434.9	7.49	5.56
XY1605-23	250.56	2007.1	0.12	0.05626	0.0013	0.55008	0.0082	0.07091	0.0007	0.0207	0.0004	461.9	51.13	445.1	5.4	441.6	4.02	414.1	6.89	0.79
XY1605-24	69.32	111.08	0.62	0.10823	0.0024	4.93555	0.0676	0.33074	0.0034	0.09216	0.0011	1769.8	39.99	1808.4	11.6	1842	16.3	1781.8	19.81	3.92
XY1605-25	96.59	140.12	0.69	0.06328	0.0023	0.85702	0.0266	0.09824	0.0012	0.03001	0.0005	717.6	74.65	628.5	14.5	604.1	7.21	597.6	10.58	3.88
XY1605-26	108.15	254.57	0.42	0.06214	0.0018	1.11331	0.0264	0.12997	0.0015	0.03799	0.0007	678.8	62.13	759.8	12.7	787.7	8.3	753.6	13.06	-3.67
XY1605-27	136.77	357.45	0.38	0.05311	0.0022	0.41802	0.0158	0.05709	0.0007	0.01756	0.0005	333.6	92.8	354.6	11.3	357.9	4.53	351.9	8.95	-0.93
XY1605-28	97.82	438.01	0.22	0.07011	0.0017	0.9779	0.0156	0.10119	0.001	0.03557	0.0005	931.6	47.96	692.5	8.02	621.4	5.81	706.5	10.35	10.27
XY1605-29	52.5	290.77	0.18	0.06897	0.0016	1.58829	0.0248	0.16706	0.0017	0.0472	0.0008	898	47.48	965.6	9.73	995.9	9.13	932.2	15.98	-3.14
XY1605-30	110.41	272.47	0.41	0.06962	0.0016	1.60522	0.0223	0.16727	0.0016	0.04728	0.0005	917.2	45.06	972.2	8.7	997.1	8.87	933.6	10.37	-2.56
XY1605-31	200.77	250.39	0.80	0.05657	0.0024	0.51002	0.0195	0.06536	0.001	0.02133	0.0004	474	91.91	418.5	13.1	408.1	5.78	426.6	8.35	2.49
XY1605-32	13.87	183.04	0.08	0.05684	0.002	0.61954	0.0184	0.07902	0.001	0.02463	0.0012	484.6	74.97	489.6	11.5	490.3	6.21	491.9	24.52	-0.14
XY1605-33	184.94	725.05	0.26	0.06082	0.0016	0.56929	0.0111	0.06786	0.0008	0.02085	0.0004	632.8	54.82	457.6	7.2	423.3	4.89	417.1	7.15	7.50
XY1605-34	409.01	1177.6	0.35	0.07494	0.0017	0.60403	0.0096	0.05843	0.0007	0.02027	0.0003	1067	45.86	479.8	6.06	366.1	4.14	405.7	5.15	23.70
XY1605-35	60.11	219.2	0.27	0.06809	0.0018	1.38829	0.0281	0.14783	0.0018	0.04732	0.0009	871.2	53.65	884	11.9	888.8	10.2	934.5	16.9	-0.54
XY1605-36	182.09	162.94	1.12	0.06514	0.0038	0.34655	0.0188	0.03857	0.0007	0.01286	0.0003	778.8	117.5	302.1	14.2	244	4.25	258.3	6.13	19.23
XY1605-37	127.76	397.17	0.32	0.0572	0.0019	0.51225	0.0141	0.06493	0.0008	0.02039	0.0004	498.9	70.78	420	9.48	405.5	5.08	407.9	8.79	3.45
XY1605-38	134.61	369.53	0.36	0.05456	0.0017	0.55045	0.0145	0.07315	0.0009	0.02324	0.0005	394.3	68.54	445.3	9.52	455.1	5.59	464.3	8.88	-2.20
XY1605-39	116.4	178.39	0.65	0.05755	0.0024	0.61979	0.023	0.07809	0.0011	0.02507	0.0005	512.3	88.45	489.7	14.4	484.7	6.78	500.5	10.47	1.02
XY1605-40	129.35	321.05	0.40	0.05551	0.0017	0.60186	0.0152	0.07862	0.001	0.02379	0.0004	432.5	66.55	478.4	9.65	487.9	5.94	475.3	8.58	-1.99
XY1605-41	87.89	573.01	0.15	0.09125	0.0021	2.45358	0.0378	0.19498	0.0023	0.06803	0.0012	1451.7	42.81	1258.5	11.1	1148.3	12.5	1330.3	22.79	8.76
XY1605-42	5.16	188.33	0.03	0.05709	0.002	0.6339	0.0191	0.08052	0.0011	0.03373	0.0027	494.3	75.47	498.5	11.8	499.2	6.43	670.4	53.22	-0.14
XY1605-43	164.36	224.05	0.73	0.08476	0.0024	0.9582	0.022	0.08198	0.0011	0.03475	0.0005	1310	54.83	682.4	11.4	508	6.31	690.4	9.65	25.56

XY1605-44	346.29	375.06	0.92	0.13665	0.0029	7.18369	0.0949	0.38127	0.0045	0.10198	0.0011	2185.1	36.45	2134.5	11.8	2082.2	20.9	1962.8	19.82	-4.94
XY1605-45	188.78	651.02	0.29	0.06849	0.0015	1.44069	0.0202	0.15255	0.0018	0.04748	0.0006	883.4	44.48	906	8.41	915.3	9.83	937.6	10.9	-1.03
XY1605-46	0.171	0.904	0.19	0.14522	0.0375	4.75459	1.2147	0.23746	0.0212	0.44885	0.0977	2290.3	387.6	1776.9	214	1373.5	110	7494	1363	22.70
XY1605-47	57.35	98.09	0.58	0.05994	0.0026	0.65302	0.0256	0.07902	0.0012	0.0247	0.0006	601.4	90.76	510.3	15.7	490.3	7.03	493.2	11.59	3.92
XY1605-48	51.14	172.43	0.30	0.05703	0.0021	0.64039	0.0207	0.08144	0.0011	0.02476	0.0007	492.2	79.74	502.5	12.8	504.7	6.65	494.3	13.02	-0.44
XY1605-49	156.2	357.98	0.44	0.06822	0.0016	1.38002	0.0221	0.14673	0.0017	0.04481	0.0006	875.2	47.28	880.4	9.42	882.6	9.72	886	10.87	-0.25
XY1605-50	1147.86	1695.6	0.68	0.10274	0.0024	0.83465	0.0132	0.05893	0.0007	0.01374	0.0002	1674.2	42.23	616.2	7.31	369.1	4.26	275.8	3.5	40.10
XY1605-51	7.87	145.48	0.05	0.06093	0.0025	0.69125	0.0251	0.08229	0.0012	0.04035	0.0025	636.8	84.9	533.5	15.1	509.8	7.19	799.5	47.96	4.44
XY1605-52	9.41	180.39	0.05	0.05724	0.0021	0.64689	0.0203	0.08198	0.0011	0.02795	0.0017	500.1	77.77	506.6	12.5	508	6.65	557.1	33.26	-0.28
XY1605-53	56.71	185.8	0.31	0.05713	0.0023	0.55542	0.0198	0.07052	0.001	0.02333	0.0007	496.1	86.19	448.5	12.9	439.3	6.05	466.1	12.93	2.05
XY1605-54	29.27	128.91	0.23	0.07282	0.0032	0.81678	0.0319	0.08137	0.0013	0.05292	0.0016	1008.9	85.26	606.3	17.8	504.3	7.67	1042.2	30.61	16.82
XY1605-55	193.53	327.97	0.59	0.05809	0.0018	0.59603	0.0154	0.07444	0.001	0.02318	0.0004	532.5	67.19	474.7	9.81	462.8	5.75	463.2	7.48	2.51
XY1605-56	715.42	765.54	0.93	0.06106	0.0015	0.63255	0.0114	0.07515	0.0009	0.02341	0.0003	641.4	52.25	497.7	7.09	467.1	5.37	467.7	5.21	6.15
XY1601A																				
XY1601A-01	24.28	869.13	0.03	0.08292	0.0018	1.65036	0.0218	0.14445	0.0016	0.05467	0.0014	1267.2	40.49	989.7	8.34	869.8	9.24	1075.9	26.13	12.11
XY1601A-03	279.29	739.06	0.38	0.07343	0.0016	1.45368	0.0221	0.14367	0.0017	0.04335	0.0006	1025.8	44.66	911.4	9.13	865.4	9.39	857.8	10.65	5.05
XY1601A-04	0.146	1.436	0.10	0.15961	0.0675	2.07298	0.8545	0.09425	0.011	0.19625	0.0949	2451.5	580	1139.9	282	580.6	64.7	3621.8	1604	49.07
XY1601A-05	373.57	365.79	1.02	0.05623	0.0015	0.61641	0.0122	0.07955	0.001	0.02499	0.0003	460.6	56.78	487.6	7.64	493.5	5.65	499	5.59	-1.21
XY1601A-06	99.01	156.6	0.63	0.06118	0.0027	0.70855	0.0286	0.08405	0.0013	0.02789	0.0007	645.4	92.47	543.9	17	520.2	7.74	556.1	13.08	4.36
XY1601A-07	173.55	170.07	1.02	0.06848	0.0029	0.5108	0.0192	0.05412	0.0008	0.01953	0.0004	883.1	84.24	419	12.9	339.8	4.95	390.9	7.01	18.90
XY1601A-08	71.71	565.5	0.13	0.08756	0.0019	1.55574	0.0226	0.12893	0.0015	0.03739	0.0007	1372.8	41.63	952.8	8.99	781.7	8.52	742	13.2	17.96
XY1601A-09	106.9	176.66	0.61	0.0615	0.0024	0.58869	0.0204	0.06945	0.001	0.02237	0.0005	656.9	81.28	470	13	432.8	5.96	447.3	9.3	7.91
XY1601A-10	17.22	1258.9	0.01	0.05691	0.0012	0.57213	0.0082	0.07294	0.0008	0.03778	0.0012	487.3	47.45	459.4	5.27	453.9	4.97	749.5	23.3	1.20
XY1601A-11	287.81	326.89	0.88	0.06228	0.0019	0.64994	0.0158	0.07571	0.001	0.02519	0.0004	683.9	62.11	508.4	9.73	470.5	5.73	502.8	6.81	7.45
XY1601A-12	550.45	321.64	1.71	0.05354	0.0019	0.26664	0.008	0.03613	0.0005	0.01105	0.0001	351.9	76.16	240	6.4	228.8	2.9	222.1	2.76	4.67
XY1601A-13	197.96	317.26	0.62	0.08667	0.0026	0.91988	0.022	0.07699	0.001	0.0324	0.0005	1353.2	55.75	662.3	11.7	478.2	6.04	644.6	9.93	27.80
XY1601A-15	335.73	508.19	0.66	0.08939	0.0019	2.84309	0.0404	0.23071	0.0027	0.07813	0.0009	1412.5	40.86	1367	10.7	1338.2	14.1	1520.6	15.96	2.11
XY1601A-16	75.95	94.82	0.80	0.10002	0.0029	3.96523	0.0958	0.28757	0.0042	0.09016	0.0016	1624.4	53.25	1627.1	19.6	1629.4	20.8	1744.9	29.63	-0.14
XY1601A-17	246.23	821.11	0.30	0.10139	0.0022	1.44796	0.0202	0.10359	0.0012	0.03013	0.0004	1649.7	39.52	909	8.39	635.4	6.98	600.1	7.78	30.10
XY1601A-18	606.96	907.55	0.67	0.05636	0.0013	0.58867	0.009	0.07576	0.0009	0.02484	0.0003	465.7	49.35	470	5.72	470.8	5.2	496	5.12	-0.17
XY1601A-19	571.74	856.16	0.67	0.05751	0.0013	0.60127	0.0093	0.07583	0.0009	0.0252	0.0003	510.8	49.29	478	5.9	471.2	5.22	503	5.25	1.42
XY1601A-20	2.72	25.14	0.11	0.06412	0.0073	0.74909	0.0829	0.08473	0.0026	0.17095	0.0128	745.6	223.8	567.7	48.1	524.3	15.4	3189.9	220.9	7.64
XY1601A-21	211.17	380.97	0.55	0.05655	0.0015	0.59022	0.0116	0.07569	0.0009	0.02375	0.0003	473.3	56.22	471	7.38	470.4	5.4	474.4	6.12	0.13
XY1601A-22	131.19	272.38	0.48	0.09596	0.0021	3.68997	0.0542	0.27886	0.0033	0.09611	0.0012	1547.1	40.72	1569.2	11.7	1585.6	16.6	1854.8	21.69	-1.05
XY1601A-23	124.83	584.35	0.21	0.08323	0.0019	1.79847	0.027	0.1567	0.0018	0.06674	0.0009	1274.5	42.9	1044.9	9.78	938.4	10.2	1305.9	17.7	10.19
XY1601A-24	226.32	297.16	0.76	0.05993	0.0016	0.67111	0.0142	0.08121	0.001	0.02654	0.0003	601	57.26	521.4	8.61	503.3	5.89	529.4	6.68	3.47
XY1601A-25	82.34	106.8	0.77	0.05601	0.0032	0.42373	0.0228	0.05486	0.0009	0.01843	0.0005	452.3	122.9	358.7	16.3	344.3	5.77	369.1	9.62	4.01
XY1601A-26	0.929	6.17	0.15	0.18431	0.0243	2.75535	0.3464	0.10839	0.0059	0.36952	0.0387	2692	202.8	1343.5	93.7	663.4	34.3	6356	571.7	50.62
XY1601A-27	444.65	543.16	0.82	0.05991	0.0015	0.64203	0.0123	0.0777	0.0009	0.02505	0.0003	600.4	53.95	503.6	7.6	482.4	5.54	500	5.83	4.21
XY1601A-28	43.68	691.88	0.06	0.10126	0.0022	1.95057	0.0272	0.13966	0.0016	0.06316	0.0013	1647.4	39.43	1098.6	9.37	842.7	9.16	1237.9	23.74	23.29
XY1601A-29	204.78	317.82	0.64	0.06689	0.002	0.69563	0.0173	0.0754	0.001	0.02715	0.0004	834.3	61.66	536.2	10.4	468.6	5.82	541.4	8.22	12.61
XY1601A-30	251.09	411.32	0.61	0.05845	0.0017	0.62194	0.0143	0.07714	0.001	0.02504	0.0004	546.7	60.96	491.1	8.94	479	5.72	499.9	7.13	2.46
XY1601A-31	32.09	630.88	0.05	0.07093	0.0017	0.73407	0.0126	0.07503	0.0009	0.08547	0.0016	955.4	47.95	558.9	7.36	466.4	5.31	1657.6	30.46	16.55
XY1601A-32	341.15	525.69	0.65	0.05731	0.0016	0.57739	0.0134	0.07303	0.0009	0.02416	0.0003	503.2	62.17	462.8	8.59	454.4	5.44	482.6	6.75	1.82
XY1601B																				
XY1601B02	44.98	122.01	0.37	0.06887	0.002	1.52297	0.0352	0.16035	0.0021	0.05274	0.001	894.8	57.81	939.7	14.2	958.7	11.5	1038.9	19.24	-2.02
XY1601B03	55.63	87.71	0.63	0.069	0.0031	1.35641	0.0552	0.14254	0.0024	0.04563	0.0012	898.8	88.98	870.3	23.8	859	13.4	901.8	23.19	1.30
XY1601B04	43.83	544.17	0.08	0.06492	0.0016	1.052	0.0195	0.1175	0.0014	0.05352	0.0013	771.7	51.71	729.9	9.67	716.2	8.15	1053.8	24.39	1.88

XY1601B05	77.29	97.54	0.79	0.0842	0.0025	1.57032	0.0381	0.13523	0.0018	0.0471	0.0007	1297.1	56.7	958.6	15.1	817.6	10.3	930.3	14.23	14.71
XY1601B06	0.274	2.54	0.11	0.21138	0.0348	3.27024	0.5111	0.11217	0.0076	0.35611	0.0648	2916.2	244	1474	122	685.4	44	6157.1	966.1	53.50
XY1601B07	1.156	1.79	0.65	0.36388	0.0476	9.07251	1.1172	0.18078	0.0142	0.24106	0.0242	3766.1	185.5	2345.3	113	1071.2	77.7	4365.1	394.1	54.33
XY1601B08	45.6	123.54	0.37	0.0693	0.002	1.54656	0.0365	0.1618	0.0021	0.049	0.001	907.8	58.74	949.1	14.6	966.8	11.7	967	18.85	-1.86
XY1601B09	178.69	229.24	0.78	0.06289	0.0019	0.57858	0.014	0.06671	0.0008	0.02226	0.0003	704.5	61.99	463.6	9.01	416.3	5.06	445.1	6.16	10.20
XY1601B10	106.45	165.53	0.64	0.06937	0.0018	1.40593	0.0281	0.14695	0.0018	0.04728	0.0006	909.8	52.95	891.4	11.9	883.8	10.2	933.7	12.39	0.85
XY1601B11	36.72	145.71	0.25	0.07674	0.0022	1.82549	0.042	0.17249	0.0023	0.06648	0.0014	1114.3	56.02	1054.7	15.1	1025.8	12.4	1300.9	27.35	2.74
XY1601B12	112.2	678.24	0.17	0.07214	0.0016	1.31659	0.0189	0.13233	0.0015	0.06808	0.0009	989.8	44.28	853	8.29	801.2	8.65	1331.3	16.4	6.07
XY1601B13	81.19	138.48	0.59	0.0707	0.0023	1.50082	0.0416	0.15393	0.0021	0.04928	0.0009	948.6	65.57	930.7	16.9	922.9	11.8	972.3	17.95	0.84
XY1601B14	83.34	150.45	0.55	0.07658	0.0025	1.6114	0.0443	0.15258	0.0021	0.04828	0.001	1110.2	63.68	974.7	17.2	915.4	11.9	953	18.43	6.08
XY1601B15	143.99	415.1	0.35	0.06948	0.0018	1.40036	0.0264	0.14615	0.0018	0.0462	0.0007	912.9	51.5	889.1	11.2	879.3	9.94	912.9	13.88	1.10
XY1601B16	3.14	9.67	0.32	0.33054	0.0252	7.95444	0.5634	0.17449	0.0083	0.42782	0.0299	3619.6	112.1	2225.9	63.9	1036.8	45.3	7198.6	423.2	53.42
XY1601B18	238.4	781.38	0.31	0.05069	0.0018	0.13325	0.004	0.01906	0.0002	0.00826	0.0002	226.7	78.62	127	3.57	121.7	1.54	166.3	3.21	4.17
XY1602																				
XY1602-01	168.88	341.44	0.49	0.07102	0.005	0.11246	0.0074	0.01148	0.0002	0.00514	0.0002	958	136.4	108.2	6.77	73.6	1.49	103.7	3.89	31.98
XY1602-02	149.45	250.25	0.60	0.07978	0.003	0.95893	0.0316	0.08716	0.0013	0.03696	0.0008	1191.6	72.13	682.7	16.4	538.7	7.81	733.6	15.09	21.09
XY1602-03	158.59	523.69	0.30	0.09441	0.002	2.77883	0.0393	0.21343	0.0026	0.09054	0.0011	1516.4	40.22	1349.9	10.6	1247.1	13.7	1751.8	20.29	7.62
XY1602-04	4212.22	4443.2	0.95	0.08977	0.0019	0.67472	0.0091	0.0545	0.0006	0.00567	6E-05	1420.5	40.03	523.6	5.53	342.1	3.94	114.3	1.29	34.66
XY1602-05	65.55	534.83	0.12	0.07163	0.0017	1.29159	0.0218	0.13074	0.0016	0.06226	0.0011	975.5	47.4	842	9.68	792.1	9.12	1220.8	20.98	5.93
XY1602-06	156.6	417.75	0.37	0.13744	0.0031	4.72029	0.0739	0.24903	0.0031	0.08595	0.0013	2195.2	38.85	1770.8	13.1	1433.5	16.2	1666.6	24.08	19.05
XY1602-07	55.99	2001	0.03	0.07326	0.0017	0.79403	0.0126	0.07858	0.0009	0.13929	0.0026	1021.3	45.68	593.5	7.12	487.7	5.64	2635.7	46.41	17.83
XY1602-08	830.86	1006.2	0.83	0.08898	0.0019	2.51862	0.0354	0.20525	0.0025	0.06567	0.0007	1403.6	40.76	1277.4	10.2	1203.5	13.1	1285.5	13.02	5.79
XY1602-09	30.22	793.19	0.04	0.10122	0.0022	3.4098	0.0488	0.24425	0.0029	0.06992	0.0021	1646.6	39.84	1506.7	11.2	1408.8	15.3	1366.1	38.81	6.50
XY1602-10	142.75	323.41	0.44	0.08912	0.0019	3.10888	0.0445	0.25293	0.003	0.07809	0.0009	1406.7	41.07	1434.9	11	1453.6	15.6	1519.8	17.33	-1.30
XY1602-11	165.66	519.83	0.32	0.09122	0.0021	2.06718	0.0324	0.1643	0.002	0.07657	0.001	1451.2	42.87	1138	10.7	980.6	11.1	1491.3	18.71	13.83
XY1602-12	51.2	485.4	0.11	0.15495	0.0033	9.47174	0.1241	0.44322	0.0053	0.11857	0.0022	2401.3	35.19	2384.8	12	2365	23.8	2264.8	38.87	0.83
XY1602-13	525.51	647.66	0.81	0.09415	0.002	3.29644	0.0437	0.25386	0.003	0.07647	0.0008	1511.1	39.45	1480.2	10.3	1458.4	15.3	1489.4	14.56	1.47
XY1602-14	221.97	345.43	0.64	0.09014	0.0021	2.38646	0.0374	0.19195	0.0023	0.06502	0.0008	1428.5	42.94	1238.5	11.2	1131.9	12.6	1273.2	14.51	8.61
XY1602-15	74.11	155.8	0.48	0.10333	0.003	3.63004	0.086	0.25472	0.0037	0.08117	0.0017	1684.8	52.51	1556.1	18.9	1462.8	18.8	1577.5	31.9	6.00
XY1602-16	397.55	798.2	0.50	0.08007	0.0017	1.6948	0.0231	0.15346	0.0018	0.06001	0.0006	1198.8	41.77	1006.6	8.72	920.3	10	1178	11.92	8.57
XY1602-17	71.6	422.5	0.17	0.08243	0.0019	1.90952	0.0308	0.16796	0.002	0.07715	0.0012	1255.8	44.61	1084.4	10.8	1000.9	11.2	1502.2	23.03	7.70
XY1602-18	205.05	454.86	0.45	0.08598	0.002	2.1679	0.0357	0.18281	0.0022	0.06433	0.0008	1337.7	44.65	1170.8	11.4	1082.3	12.1	1260.1	16.01	7.56
XY1602-19	27.66	1399.9	0.02	0.05779	0.0013	0.6315	0.0098	0.07923	0.0009	0.0322	0.001	521.6	49.43	497	6.09	491.5	5.54	640.6	19.8	1.11
XY1602-20	101.23	238.55	0.42	0.10667	0.0025	3.62507	0.0591	0.2464	0.0031	0.07958	0.0012	1743.4	42.04	1555.1	13	1419.9	15.8	1547.6	21.5	8.69
XY1602-21	164.14	231.32	0.71	0.06135	0.0021	0.6087	0.0181	0.07195	0.001	0.02189	0.0004	651.4	72.56	482.7	11.5	447.9	5.86	437.7	7.6	7.21
XY1602-22	165	639.23	0.26	0.08551	0.002	1.83098	0.0307	0.15526	0.0019	0.07561	0.0011	1327	45.33	1056.6	11	930.4	10.5	1473.2	20.53	11.94
XY1602-23	46.75	1020.8	0.05	0.07475	0.0019	0.96619	0.0175	0.09373	0.0011	0.033	0.0011	1061.7	49.01	686.5	9.01	577.5	6.7	656.1	21.29	15.88
XY1602-24	348.3	6204.7	0.06	0.05885	0.0013	0.45861	0.0069	0.05651	0.0007	0.01218	0.0003	561.5	48.2	383.3	4.77	354.3	4	244.6	5.6	7.57

Table E4. REE contents (ppm) of the samples from the Yuanlong area.

Spot No.	La	Ce	Pr	Nd	Sm	Eu	Gd	Tb	Dy	Ho	Er	Tm	Yb	Lu
TS1406														
TS1406-01	7.86	79.56	8	51.64	43	12.97	129.77	39.98	391.05	121.01	469.37	88.57	780.91	126.5
TS1406-02	1.51	22.43	0.95	7.8	10.87	2.18	54.77	18.41	199.68	65.7	258.52	49.11	428.32	71.82
TS1406-03	38.38	255.86	38.96	231.02	154.78	61.46	337.26	92.75	806.24	208.77	741	132.78	1148.27	180.77
TS1406-04	0.071	4.94	0.123	1.48	3.27	0.61	19.96	7.78	90.82	33.73	148.72	30.74	306.35	56.02
TS1406-05	11.74	87.34	13.16	79.46	53.44	21.12	120.85	32.71	288.44	79.06	285.04	52.7	467.38	78.17
TS1406-06	12.48	67.67	11.88	72.29	43.93	15.45	88.13	24.26	210.63	55.14	198.58	38.11	347.66	55.1
TS1406-07	7.68	52.35	6.02	35.78	29.05	8.9	104.06	37.79	408.26	137.2	562.48	110.39	1001.82	162.1
TS1406-08	1.71	14.23	1.35	11.17	9.79	2.69	38.33	11.72	122.81	42.15	174.37	35.15	331.35	58.29
TS1406-09	5.07	28.49	3.6	21.9	15.2	4.34	46.13	14.18	144.92	46.36	191.59	38.69	376.84	65.74
TS1406-10	1.54	16.71	1.66	11.99	10.53	2.93	36.43	11.8	119.94	39.7	162.57	32.72	314.42	53.66
TS1406-11	0.326	4.13	0.436	4.42	8.93	0.68	37.74	11.05	97.36	27.7	104.86	20.58	195.12	33.04
TS1406-12	1.23	18.65	1.41	9.74	9.48	3	31.17	9.89	98.75	32.44	130.76	26.29	247.24	43.13
TS1406-13	34.62	241.64	36.87	214.26	129.01	54.37	250.33	62.48	511.1	120.89	387.13	67.32	581.03	80.36
TS1406-14	17.31	137.29	15.99	82.63	54.8	18.41	149.67	49.74	539.91	174.04	691.04	133.6	1179.98	180.23
TS1406-15	0.49	5.07	0.451	3.41	5.34	0.36	24.68	9.52	103.5	37.09	158.42	32.99	317.84	55.03
TS1406-16	0.395	1.94	0.333	1.72	1.36	0.322	6.23	3.9	55.35	18.17	68.35	12.39	101.24	13.8
TS1406-17	23.56	144.59	20.01	119.65	76.05	26.66	154.1	45.21	403.11	112.84	418.85	80.28	730.65	115.45
TS1406-18	21.73	46.72	4.39	20.83	12.25	2.72	38.03	12.35	134.19	46.22	194.59	39.49	373.39	64.76
TS1406-19	6.52	59.95	6	34.97	29.92	9.68	86.2	26.83	266.48	81.81	308.54	57.87	512.1	78.81
TS1406-20	7.62	65.36	8.22	51.53	34.66	11.72	100.82	30.59	312	101.86	412.84	81.07	731.74	122.46
TS1406-21	6.14	31.81	2.81	16.61	14.57	3.47	52.84	16.96	172.33	56.91	232.21	45.35	418.08	72.01
TS1406-22	1.48	8.75	1.5	9.32	6.81	2.02	18.66	8.02	91.68	27.82	106.32	20.5	179.07	26.1
TS1406-23	2.47	23.8	2.06	13.14	13.24	5.08	47.17	16.95	184.18	63.01	263.8	52.71	487.36	83.66
TS1406-24	3.82	24.65	3.64	20.46	16.04	4.68	54.76	19.66	219.86	70.88	287.77	57.82	528.69	85.03
TS1406-25	1.29	9.65	0.98	6.12	6.13	1.3	27.53	9.47	101.53	35.94	150.47	31.12	296.22	52.84
TS1406-26	0.2	2.24	0.26	1.8	4.5	0.21	37.06	19.78	246.63	82.11	317.86	60.77	530.86	77.71
TS1406-27	4.62	32.27	3.03	23.79	25.26	2.98	90.86	27.82	267.56	79.67	293.12	54.21	482.73	79.36
TS1406-28	0.125	7.22	0.21	2.54	5.88	0.84	30.4	11.08	126.6	45.55	193.63	40.24	378.97	67.45
TS1406-29	0.173	5.13	0.191	1.46	3.35	0.618	17.11	6.25	73.54	27.22	118.51	25.29	244.76	44.8
TS1406-30	1.97	16.83	1.35	10.6	11.93	2.05	43.16	13.63	134.65	43.98	175.75	34.26	312.69	54.3
TS1406-31	0.59	7.76	0.587	4.75	6.33	0.91	24.67	8.39	94.97	31.76	130.12	26.84	253.62	45.05

TS1406-32	2.43	31.65	1.83	12.19	15.28	2.46	75.99	28.34	315.7	111.17	462.19	92.52	832.03	134.99
TS1406-33	0.61	10.86	0.562	3.95	5.04	1.51	29.32	11.09	126.09	45.35	189.28	38.48	353.98	60.56
TS1406-34	0.32	10.63	0.421	3.98	7.78	1.33	44.92	17.41	201.72	74.23	320.34	65.16	617.1	107.6
TS1406-35	3.54	21.97	2.82	16.81	13.06	3.16	53.54	19.98	227.46	82.19	346.94	71.02	658.37	111.07
TS1406-36	0.137	6.45	0.176	1.87	3.41	0.51	20.54	7.49	88.64	33.04	146.64	30.97	297.73	53.95
TS1408-1														
TS1408-1-01	<0.068	2.69	0.093	1.52	3.84	0.107	23.64	8.23	87.51	30.17	122.31	23.88	220.81	40.01
TS1408-1-02	<0.091	12.53	0.267	2.75	5.3	0.84	29.6	10.75	114.91	39.44	162.71	31.88	297.16	53.44
TS1408-1-03	<0.085	1.7	0.191	3.8	10.19	0.199	46.98	12.53	98.16	26.73	92.41	16.37	141.4	24.32
TS1408-1-04	<0.105	1.14	0.071	1.26	4.32	<0.115	31.02	11.5	128.87	43.16	168.6	31.15	272.96	47.68
TS1408-1-05	0.08	5.82	0.104	1.43	3.56	0.154	26.31	9.8	108.8	38.02	153.12	29.41	267.5	47.36
TS1408-1-06	1.5	19.79	1.91	10.89	11.15	1.81	37.98	13.8	159.59	57.86	250.82	50.42	467.07	82.91
TS1408-1-07	<0.069	1.98	0.204	4.82	12.64	0.183	53.65	12.26	84.31	17.89	51.73	7.69	58.91	9.51
TS1408-1-08	0.288	38.12	0.191	2.6	4.19	1.5	19.17	6.34	73.98	29.9	145.57	33.52	364.75	77
TS1408-1-09	4.54	41.29	5.49	34.61	23.79	8.41	54.52	15.98	160.07	53.31	211.89	40.91	383.36	68.02
TS1408-1-10	0.195	2.15	0.328	3	5.89	0.207	30.88	10.14	102.58	32.44	126.89	24.35	217.78	38.13
TS1408-1-11	0.042	1.92	0.221	3.96	8.56	0.322	48.64	15.94	157.69	53.27	209.39	39.33	355.62	62.83
TS1408-1-12	0.56	13.9	0.674	5.39	7.27	1.32	34.51	11.6	131.12	47.03	197.22	39.18	369.65	67.3
TS1408-1-13	106.06	245.47	25.31	96.24	19.72	0.9	31.52	9.96	117.64	46	222.31	49.88	520.6	100.16
TS1408-1-14	1.44	18.88	1.43	9.47	12.08	1.68	64.52	27.66	340.25	127.56	554.2	109.37	993.58	169.43
TS1408-1-15	<0.064	1.37	0.097	1.07	3.44	0.22	26.44	10.59	117.81	39.74	161.96	32.7	304.61	53.6
TS1408-1-16	0.403	5.85	0.166	1.75	3.3	0.293	19.18	6.76	73.85	25.16	105.57	21.15	200.38	34.99
TS1408-1-17	2.82	27.69	3.45	19.86	14.77	4.04	44.94	16.42	185.18	65.07	280.92	56.38	520.6	90.47
TS1408-1-18	0.107	4.79	0.13	1.61	3.68	0.505	19.77	7.68	89.24	33.47	147.03	30.09	289.17	54.02
TS1408-1-19	2.13	68.32	0.525	2.59	1.47	0.606	6.47	2.3	27.36	11	55.48	13	143.72	31.3
TS1408-1-20	<0.074	7.71	0.054	0.84	2.03	0.124	9.85	3.1	31.46	10.97	48.39	10.34	104.53	19.36
TS1408-1-21	0.176	3.48	0.102	1.79	4.14	0.426	19.65	6.84	74.09	25.59	107.84	21.78	208.99	38.9
TS1408-1-22	<0.078	2.12	0.179	3.09	6.03	0.211	37.86	15.53	190.28	72.84	304.44	59.05	527.67	89.39
TS1408-1-23	1.53	7.91	0.557	5.28	7.58	0.93	32.04	9.75	93.51	30.07	123.91	25.94	258.51	47.58
TS1408-1-24	0.035	1.09	0.348	1.69	6.9	0.102	41.48	14.23	134.44	36.6	120.47	19.94	158.4	23.63
TS1408-1-25	<0.085	3.31	<0.078	0.84	1.99	0.376	11.24	4.5	50.16	17.7	76	15.33	144.05	26.7
TS1408-1-26	0.591	9.42	0.743	5.53	5.28	0.94	21.07	6.93	77.31	27.2	114.62	23.43	220.23	39.31
TS1408-1-27	8.54	63.61	10.14	59.01	39.17	15.41	91.4	26.45	253.65	78.89	303.53	58.07	514.18	83.18
TS1408-1-28	3.29	8.86	1.04	6	4.06	0.263	19	5.85	52.43	14.48	50.37	9.42	84.37	13.9
TS1408-1-29	0.067	1.23	0.063	0.91	3.71	0.116	23.43	9.06	89.72	25.85	90.92	16	134.71	22
TS1408-1-30	5.85	23.83	1.65	8.37	4.7	0.417	19.57	6.76	74.9	27.13	121.79	27.52	281.12	52.1
TS1408-1-31	13.19	36.52	4.2	19.64	7.87	0.377	28.77	9.64	96.79	31.26	129.77	29.29	327.43	68.52
TS1408-1-32	62.63	147.75	16.81	73.23	20.22	2.01	40.01	11.24	113.67	38.21	160.29	33.12	319.5	56.68

TS1408-1-33	<0.102	0.76	0.051	1.08	3.66	<0.097	22.1	7.39	68.57	19.19	63.33	11.1	91.03	14.82
TS1408-1-34	0.065	2.39	0.069	1.24	3.4	0.137	21.09	7.46	73.57	23.01	92.01	18.71	179.84	32.19
TS1408-1-35	<0.043	9.89	0.079	1.14	2.63	0.63	13.33	4.57	54.3	20.64	96.68	21.46	228.66	46.25
TS1408-1-36	1.6	16.49	2.2	14.5	11.22	2.2	34.23	12.1	136.25	48.94	213	44.26	416.31	73.65
TS1408-2														
TS1408-2-01	0.278	5.57	0.277	2.42	3.97	0.64	22.59	8.02	91.03	33.65	144.96	30.13	289.34	52.91
TS1408-2-02	0.211	1.24	0.183	1.28	2.97	0.151	17.02	6.21	66.22	20.36	81.07	15.84	148.84	25.8
TS1408-2-03	11.86	76.15	11.71	76.14	50.51	13.39	113.85	28.15	232.27	68.2	250.94	46.15	408.66	70.39
TS1408-2-04	1.19	16.91	0.97	8.72	9.22	1.59	33.96	10.8	112.63	38.08	150.82	29.66	269.55	45.43
TS1408-2-05	0.465	14.91	0.48	4.9	8.37	1.88	35.15	11.57	120.12	40.97	170.68	33.5	313.06	56.41
TS1408-2-06	1.77	32.41	1.8	15.9	16.69	3.02	71.57	23.18	242.05	82.9	326.75	62.43	557.88	93.38
TS1408-2-07	<0.119	6.82	0.188	2.93	5.82	1.02	31.55	10.93	125.26	47.3	205.46	41.89	392.87	72.19
TS1408-2-08	0.1	1.6	0.129	3.1	8.27	0.136	37.49	9.16	72.83	18.37	57.84	9.64	80.86	13.11
TS1408-2-09	0.017	0.602	<0.050	0.65	3.21	<0.071	18.45	6.56	64.83	19.42	68.03	12.37	104.09	17.55
TS1408-2-10	0.75	6.6	0.388	3.45	4.69	0.33	22.2	6.31	56.48	17.21	71.08	15.09	159.08	29.23
TS1408-2-11	0.043	3.12	0.32	5.37	9.87	0.189	49.81	16.93	182.98	64.79	262.24	50.57	456.42	78.49
TS1408-2-12	0.93	9.6	0.97	7.4	7.77	1.41	27.16	8.45	93.74	33.86	145.36	30.46	290.04	50.88
TS1408-2-13	<0.060	3.42	0.066	1.11	2.34	0.479	12.53	4.63	56.77	21.26	93.63	19.11	181.66	33.47
TS1408-2-14	0.11	2.66	0.166	2.57	5.67	0.165	33.24	11.4	126.93	44.2	182.13	35.41	327.92	57.83
TS1408-2-15	2	12.04	2.03	14.47	12.93	1.11	52.78	18.34	210.25	76.19	326.27	65.75	615.04	107.33
TS1408-2-16	1.03	18.65	1.02	7.66	10.12	1.77	51.85	19.45	226.71	82.43	355.84	73.78	692.18	118.23
TS1408-2-17	0.359	10.42	0.561	3.71	7.01	0.97	32.05	11.29	131.18	48.03	211.42	43.84	420.15	75.3
TS1408-2-18	8.09	35.64	2.6	13.84	5.32	0.64	15.7	5.01	57.94	21.85	104.61	24.83	266.66	54.39
TS1408-2-19	<0.044	5.97	0.025	<0.37	0.34	0.076	4.24	3.03	54.71	27.23	166.18	46.37	562.9	108.27
TS1408-2-20	<0.058	6.07	0.051	1.22	3.26	0.392	20.85	7.9	99.27	37.63	166.91	34.57	331.33	59.68
TS1408-2-21	0.065	2.05	0.076	1.45	4.18	0.11	25.89	8.7	77.42	20.17	64.98	11.29	97.06	15.64
TS1408-2-22	<0.068	3.75	0.079	0.7	2.16	0.31	14.24	5.2	63.41	24.08	107.44	23.13	230.78	42.87
TS1408-2-23	<0.078	0.88	0.098	2.01	6.04	<0.122	37.95	12.41	108.22	28.59	92.66	15.61	131.45	21.24
TS1408-2-24	2.79	26.74	3.32	19.09	10.03	1.58	32.21	12.59	155.42	59.14	263.59	54.95	531.98	89.45
TS1408-2-25	0.23	19.52	0.76	9.52	10.7	1.34	33.81	9.55	100.1	34.72	142.73	28.1	255.58	45.05
TS1408-2-26	<0.042	1.72	0.224	3.88	8.7	0.261	41.02	12.61	123.13	38.91	151.49	28.95	264.95	46.52
TS1408-2-27	0.14	3.63	0.146	1.27	2.66	0.296	13.85	5.83	68.97	25.24	110.46	23.17	221.69	39.24
TS1408-2-28	<0.079	0.62	0.084	1.51	5.31	0.101	29.01	8.43	69.85	17.47	57.45	9.93	85.15	13.79
TS1408-2-29	6.14	50.12	6.25	42.4	26.53	7.62	75.87	19.66	183.18	57.09	216.09	40.16	366.86	60.79
TS1408-2-30	0.153	15.73	0.298	4.09	8.79	0.66	44.37	14.87	153.2	51.09	210.5	42.7	401.59	70.81
TS1408-2-31	1.29	5.72	0.745	4.68	3.2	0.589	12.82	5.92	86.32	37.25	195.13	50.46	588.17	118.41
TS1408-2-32	0.48	8.07	0.388	3.62	4.64	0.79	20.58	6.64	75.1	26.22	110.94	22.17	209.57	37.6
TS1408-2-33	6.89	19.09	4.99	28.01	16.9	3.31	43.36	13.53	138.78	46.16	190.22	38.6	364.54	63.48

TS1408-2-34	1.65	3.57	0.98	6.18	2.76	0.75	7.99	3.8	57.42	24.19	119.88	29.55	301.71	52.14
TS1408-2-35	0.268	1.35	0.174	1.33	1.07	0.195	4.95	3.09	55.48	23.69	120.2	28.99	301.66	49.4
TS1408-2-36	2.68	17.93	2.36	15.4	12.78	2.42	47.08	14.73	153.59	52.75	213.92	42.77	395.15	69.5

Table E5. REE contents (ppm) of the samples from the Shetang area.

Spot No.	La	Ce	Pr	Nd	Sm	Eu	Gd	Tb	Dy	Ho	Er	Tm	Yb	Lu
ST1502														
ST1502-01	1.57	17.63	0.97	8.84	7.36	1.52	28.31	9.77	108.69	40.89	175.11	37.78	358.17	57.64
ST1502-02	0.15	20.88	0.405	5.77	8.86	0.662	39.49	13.88	164.87	61.57	266.87	56.44	535.54	86
ST1502-03	0.91	5.39	0.391	2.73	1.39	0.53	5.89	2.35	31.32	13.21	70.72	18.93	233.51	52.5
ST1502-04	0.173	13.19	0.099	1.78	2.42	0.074	14.01	5.12	69.87	28.62	141.33	33.46	359.09	62.98
ST1502-05	5.05	48.8	2.91	19.83	15.92	3.31	55.38	20.04	230.92	81.25	344.09	74.08	724.56	108.01
ST1502-06	2.94	22.9	1.72	13.28	8.89	1.22	27.95	8.87	105.15	39.22	174.09	38.19	374.72	62.87
ST1502-07	156.01	247.23	21.53	105.9	26.24	4.33	70.17	21.92	257.02	95.98	412.68	89.66	859.39	135.71
ST1502-08	1	9.61	0.361	2.22	2.57	0.557	12.41	4.39	51.7	20.53	95.68	21.75	221.67	39.14
ST1502-09	0.612	27.21	0.296	3.69	6.46	0.333	32.86	11.84	145.33	55.76	247.76	54.24	519.13	83.17
ST1502-10	3.12	20.73	1.5	10.94	8.58	3.16	30.69	10.67	123.08	45.35	196.66	42.95	411.48	66.46
ST1502-11	0.93	9.63	0.517	4.22	3.62	0.853	14.38	4.88	58.61	22.8	107.45	25.21	275.96	53.02
ST1502-12	2.17	64.25	1.492	11.48	10.99	1.49	41.9	16.02	204.69	81.18	377.94	88.03	873.99	139.18
ST1502-13	0.487	40.63	0.838	12.21	17.51	0.848	89.56	31.33	372.13	139.16	587.12	119.84	1080.87	168.97
ST1502-14	0.898	15.32	0.533	3.52	3.13	0.499	12.54	4.75	61.11	24.16	113.37	27.16	281.06	49.85
ST1502-15	0.34	18.27	0.311	2.85	3.81	0.164	17.87	7.03	89.97	35.49	165.48	39.24	401.55	68.79
ST1502-16	1.34	13.01	0.865	6.33	6.02	1.39	22.19	7.28	85.85	32.35	145.2	32.82	337.65	60.82
ST1502-17	1.5	18.68	0.849	6.35	6.52	0.645	28.26	9.8	116.13	44.49	193.5	41.48	396.29	63.41
ST1502-18	1.65	22.66	1.19	9.56	7.39	2.19	28.68	10.36	123.85	46.51	209.41	47.25	470.22	77
ST1502-19	8.55	35.09	4.37	29.02	16.44	3.8	36.02	9.26	96.72	35.36	165.03	41	482.31	96.73
ST1502-20	0.923	27.04	0.765	8.43	11.23	0.57	51.41	17.78	212.19	77.92	330.12	71.79	673.55	105.17
ST1502-21	2.19	17.25	1.08	6.6	3.87	1.16	15.57	5.28	62.87	23.98	109.55	25.32	266.58	46.61
ST1502-22	3.36	17.02	1.72	10.23	6.85	2.63	16.9	6.26	72.24	28.37	134.44	33.55	381.84	75.63
ST1502-23	2.1	34.44	0.991	9.98	11.38	0.88	51.05	17.93	218.36	82.43	356.67	76	709.48	110.48
ST1502-24	2.6	16.25	0.826	5.58	4.6	1.1	21.43	7.35	90.27	34.12	148.91	32.57	315.38	52.09
ST1502-25	1.05	14.46	0.645	5.65	5.54	0.62	22.03	7.49	89.65	33.13	146.64	32.11	315.44	54.27
ST1502-26	0.85	12.85	0.518	5.18	5.73	1.2	26.28	9.08	106.33	39.4	172.35	37.7	372.57	62.07
ST1502-27	24.38	54.1	5.32	24.6	9.53	1.69	29.51	9.66	110.38	40.43	174.37	37.76	367.78	58.38
ST1502-28	2.23	8.59	0.89	4.66	2.41	0.36	3.77	1.27	16.67	8.13	47.56	14.39	198.28	46.06
ST1502-29	5.28	45.35	2.57	20.4	18.1	0.99	76.19	25.76	301.58	112.47	479.65	99.86	919.09	139.29

ST1502-30	7.1	51.78	3.05	19.56	14.97	0.88	61.95	21.8	261.12	96.45	416.03	89.02	835.79	126.87
ST1502-31	1.53	30.64	0.613	5.51	5.94	0.71	26.87	10.03	121.62	47.47	214.14	48.42	480.25	77.94
ST1502-32	2.05	28.15	0.741	4.95	4.95	1.4	22.27	8.06	102.67	39.77	178.56	40.72	399.89	63.79
ST1502-33	1.68	7.42	1.02	5.66	3.48	0.83	8.54	2.64	30.51	12.37	63.35	17.82	224.45	51.44
ST1502-34	1.53	22.49	1.013	9.45	8.7	1.1	33.03	11.32	130.61	48.1	207.77	44.65	427.49	65.41
ST1502-35	4.44	35.41	2.58	15.85	7.19	1.71	17.78	5.82	69.96	27.73	129.47	31.72	349.46	64.13
ST1510-1														
ST1510-1-01	0.727	15.3	0.851	9.8	13.57	1.54	57.2	19.75	232.16	83.47	340.65	71	677.5	93.61
ST1510-1-02	2.4	13.05	0.583	4.76	4.84	0.84	20.96	9.11	126.33	55.21	270.15	69.89	792.06	127.23
ST1510-1-03	3.42	30.22	2.01	16.36	12.37	1.83	52.09	23.48	338.1	142.7	681.72	170.94	1853.49	258.56
ST1510-1-04	7.23	39.28	4.12	24.73	13.42	1.88	49.27	21.23	291.95	121.71	574.86	142.44	1547.68	219.72
ST1510-1-05	<0.037	2.05	<0.031	0.24	0.35	0.189	2.54	1.34	16.48	7.33	37.12	10.19	121.59	19.71
ST1510-1-06	<0.076	9.27	0.027	0.57	2.2	0.39	19.12	9.58	146.48	63.17	310	76.3	810.78	128.01
ST1510-1-07	7.63	41.73	6.58	49.85	25.77	2.29	58.33	16.78	181.66	63.49	267.15	57.49	565.97	85.75
ST1510-1-08	0.408	15.25	0.555	6.37	8.31	0.94	38.09	14.03	171.82	62.17	267.23	58.27	572.1	79.57
ST1510-1-09	9.6	19.02	2.6	19.53	7.4	1.81	25.44	8.63	112.9	47.32	231.29	55.88	603.89	100.69
ST1510-1-10	1.21	21.54	0.587	4.9	6.06	2.26	44.4	19.6	280.07	117.38	556.75	127.94	1286.98	206.47
ST1510-1-11	0.347	13.72	0.448	6.15	8.92	0.96	43.07	15.58	186.35	68.27	291.17	62.74	606.53	85.66
ST1510-1-12	1	14.88	0.565	5.11	4.47	0.89	20.7	8.38	112.76	45.78	213.89	50.68	528.31	80.97
ST1510-1-13	24.37	98.44	20.02	132.38	59.88	4.4	111.94	29.6	285.09	91.14	345.71	70.92	673.31	90.89
ST1510-1-14	0.212	7.67	0.771	12.74	20.85	4.25	89.68	28.8	316.59	108.06	422.65	86.21	796.24	114.14
ST1510-1-15	0.069	11.4	0.138	1.97	3.39	0.81	17.28	6.69	87.75	35.38	170.28	41.89	446.85	72.97
ST1510-1-16	0.807	22	0.738	5.95	6.74	1.33	31.33	13.65	186.35	77.87	364.72	87.57	905.75	136.5
ST1510-1-17	1.53	16.69	1.11	12.72	11	1.7	49.79	15.97	186.56	66.54	273.8	59.38	579.12	78.6
ST1510-1-18	0.402	11.67	0.377	5.08	8.13	1.53	40.56	14.66	175.86	66.31	290.95	66.18	695.14	100.69
ST1510-1-19	0.095	3.56	0.078	0.84	1.39	0.353	7.05	2.6	34.4	13.2	64.78	16.28	188.72	31.88
ST1510-1-20	0.011	11.12	<0.032	0.53	1.86	0.204	12.03	4.99	68.45	27.21	127.3	30.48	313.15	46.53
ST1510-1-21	0.99	39.76	0.205	1.82	2.42	0.657	9.92	2.99	30.47	11.23	51.36	12.98	150.13	25.81
ST1510-1-22	0.619	20.27	0.513	4.7	5.95	1.18	35.96	15.99	219.97	92.03	429.81	101.96	1058.82	163.37
ST1510-1-23	0.088	7.61	0.54	8.55	14.26	2.21	66.77	22.05	248.32	88.12	351.81	73.77	707.01	103.17
ST1510-1-24	<0.061	7.87	<0.029	0.42	1.65	0.338	10.25	4.49	62.44	26.61	127.75	31.48	349.11	59.03
ST1510-1-25	0.125	15.05	0.246	4.71	6.74	1.77	38.22	12.65	154.1	56.29	234.91	50.28	483.6	72.69
ST1510-1-26	6.46	36.15	3.91	26.34	15.04	2.4	44.26	13.63	164.77	62.97	286.04	69.43	716.2	112.5
ST1510-1-27	3.48	33.7	4.56	36.56	21.58	2.27	60.36	19.38	214.93	76.15	311.95	67.61	660.57	89.51
ST1510-1-28	0.722	20.98	2.21	28.33	28.73	8.95	53.18	12.92	112.88	36.03	148.44	32.6	333.09	53.07
ST1510-1-29	0.103	11.73	0.111	1.1	1.89	0.264	9.41	4.16	58.26	24.49	118.25	29.01	299.24	45.16
ST1510-1-30	0.098	9.85	0.062	0.94	2.25	0.451	15.65	7.45	106.77	46.51	222.57	52.46	548.23	90.54
ST1510-1-31	0.107	12.86	0.121	1.02	2.01	0.201	11.2	4.86	67.75	29.99	152.56	39.25	423.06	68.64

ST1510-1-32	0.8	19.41	0.56	4.5	6.43	1.13	44.83	22.34	342.58	155.56	772.67	183.97	1877.85	332.01
ST1510-1-33	0.423	10.53	0.372	3.36	3.65	0.65	18.87	7.81	108.45	45.59	218.23	54.27	586.27	95.35
ST1510-1-34	0.162	18.41	0.217	2.19	2.47	0.95	11.67	3.88	46.33	18.56	89.29	22.3	249.24	45.6
ST1510-1-35	0.674	13.93	0.314	2.65	2.34	0.407	16.23	7.63	113.83	50.83	256.92	64.72	692.68	114.26
ST1510-2														
ST1510-2-01	3.15	44.28	1.41	13.17	12.77	3.66	30.39	7.41	61.41	16.21	56.15	11.12	104.71	15.92
ST1510-2-02	10.59	24.21	2.84	14.15	10.06	0.198	47.37	14.52	128.65	32.6	103.73	19.67	175.26	24.78
ST1510-2-03	0.228	2.63	0.162	2.26	4.91	0.283	25.99	8.01	74.55	21.07	79.09	16.45	155	23.47
ST1510-2-04	0.094	1.64	0.209	3.24	9.56	0.179	58.42	21.15	232.11	73.73	281.17	55.55	490.16	71.66
ST1510-2-05	<0.0245	0.94	0.035	1.34	4.58	0.113	28.41	9.07	79.61	20.1	66.49	12.51	110.81	15.9
ST1510-2-06	<0.035	1.24	0.081	1.64	6.62	0.075	41.65	14.59	130.11	32.17	103.06	18.39	156.39	22.58
ST1510-2-07	0.211	1.7	0.093	1.16	3.14	0.105	19.43	6.98	68.4	19.13	64.59	11.91	102.81	14.32
ST1510-2-08	<0.045	1.12	0.083	1.71	6.2	0.154	35	12.59	119.59	31.99	107.48	20.41	175.92	25.09
ST1510-2-09	<0.037	1.08	0.057	1.22	4.71	0.075	31.98	12.78	148.77	50	194.15	39.61	360.52	53.82
ST1510-2-10	2.13	7.43	0.94	6.82	8.39	0.97	40.74	13.15	145.87	49.73	206.73	46.57	489.57	78.11
ST1510-2-11	0.04	1.59	0.219	3.79	9.87	0.189	52.57	16.2	149.46	41.73	141.03	26.52	227.3	31.85
ST1510-2-12	0.062	4.04	0.197	3.22	8.04	0.347	43.3	15.01	149.45	44.43	170.8	35.11	334.17	49.85
ST1510-2-13	0.122	1.31	0.143	2.33	6.84	0.153	34.64	8.97	70.11	16.84	53.47	9.85	84.06	11.59
ST1510-2-14	<0.044	1.39	0.202	3.81	10.69	0.18	54.9	17.94	162.11	45.1	152.49	28.26	236.99	32.28
ST1510-2-15	<0.00	0.76	0.066	1.01	3.55	0.094	24.98	9.77	90.83	23.07	76.56	14.18	119.53	16.75
ST1510-2-16	0.091	1.63	0.148	1.92	5.98	0.16	31.67	10.63	101.72	29.88	109.33	21.5	202.18	29.17
ST1510-2-17	200.08	490.26	61.15	266.2	54.15	1.31	59.39	12.14	100.16	27.55	100.44	21.04	203.66	30.98
ST1510-2-18	3.16	7.77	0.97	6.09	9.33	0.291	40.5	9.74	77.41	18.75	59.87	11.47	97.67	13.77
ST1510-2-19	0.067	7.54	0.227	4.86	7.38	1.58	36.27	11.22	120.29	41.53	169.34	35.05	326.46	51.9
ST1510-2-20	0.061	2.68	0.234	4.42	9.08	0.312	45.01	13.77	145.3	47.87	189.57	38.91	357.98	54.65
ST1510-2-21	0.104	5.73	0.151	2.06	5.45	0.342	27.94	9.28	95.61	31.6	141.92	34.71	372.45	60.67
ST1510-2-22	<0.046	0.8	0.067	1.28	4.35	0.076	27.44	8.85	79.12	20.49	64.4	11.62	95.51	12.53
ST1510-2-23	<0.052	1.3	0.096	1.83	4.72	0.152	29.9	11.52	139.45	50.24	214.18	46.81	453.65	68.18
ST1510-2-24	0.073	2.97	0.143	2.22	6.49	0.094	40.92	13.74	135.81	38.66	137.36	26.27	229.69	32.77
ST1510-2-25	7.36	25.67	2.31	13.63	12.26	0.564	49.24	14.62	135.38	39.64	151.8	31.61	294.36	45.76
ST1510-2-26	<0.047	1.32	0.05	1.04	3.57	0.231	23.59	8.83	99.8	33.1	131.75	27.07	252.98	37.32
ST1510-2-27	0.113	1.75	0.217	2.62	5.82	0.209	33.01	12.22	133.32	42.42	162.15	32.94	297.31	46.6
ST1510-2-28	0.409	5.29	0.768	6.61	8.2	0.8	35.27	13.59	171.38	62.83	276.27	62.02	616.66	98.04
ST1510-2-29	0.027	4.66	0.041	1.23	4.15	0.363	25.03	8.73	89.34	27.15	104.11	21.82	214.76	34.35
ST1510-2-30	<0.026	3.44	0.06	1.3	3.51	0.291	22.96	9.2	102.19	35.29	149.68	33.82	337.1	54.26
ST1510-2-31	1.99	27.76	0.538	3.68	4.98	0.62	25.51	8.31	81.83	27.27	115.48	27.59	296.31	50.74
ST1510-2-32	<0.049	1.22	0.084	2.14	6.87	0.184	38.82	12.35	108.88	27.55	85.88	14.84	123.95	16.31
ST1510-2-33	<0.031	0.958	0.097	1.96	5.36	0.092	32.73	13.43	142.72	45.16	170.76	33.05	293.1	43.3

ST1510-2-34	0.082	1.34	0.092	1.33	4.32	0.105	29.21	10.88	120.93	41.85	174.76	37.04	353.46	53.77
ST1510-2-35	0.02	1.206	0.039	0.83	3.25	0.194	22.65	8.11	85.31	24.58	83.73	15.91	134.91	18.69
ST1511														
ST1511-01	0.63	8.31	0.163	1.46	4.43	2.04	21.11	5.8	50.12	13.03	43.08	8.24	70.35	9.49
ST1511-02	0.602	10.6	1.31	10.94	10.64	0.8	36.67	9.95	86.89	24.38	91.53	18.71	185.54	27.83
ST1511-03	<0.036	6.89	0.175	2.46	3.58	1.64	12.25	3.06	22.96	4.97	13.22	2	13.46	1.6
ST1511-04	0.64	19.84	0.327	4.81	6.27	2.36	20.02	4.73	35.98	8.65	26.27	4.33	35.1	4.55
ST1511-05	0.115	9.58	0.315	3.6	6.99	3.13	34.71	9.65	82.66	21.57	68.79	13.15	112.77	15.38
ST1511-06	0.029	14.03	0.227	3.1	6.01	2.05	19.92	4.9	39.18	8.43	20.78	2.88	21.73	2.58
ST1511-07	0.77	21.5	0.83	7.43	10.65	0.35	33.58	11.14	132.15	44.57	183.04	41.17	408.32	60.63
ST1511-08	2.03	26.51	2.6	13.8	5.27	0.86	13.09	4.08	49.27	19.07	91.71	22.75	251.42	42.13
ST1511-09	<0.066	17.65	0.454	7.55	10.95	4.53	38.75	9.02	64.4	13.03	32.75	4.55	29.91	3.55
ST1511-10	1.26	18.25	2.02	12.83	6.15	1.35	21.46	6.9	79.73	29.46	128.37	29.45	302.96	50.77
ST1511-11	0.152	15.7	0.329	2.94	3.78	0.249	18.13	6.38	77.49	28.77	125.48	28	273.5	41.27
ST1511-12	0.096	7.32	0.404	6.4	11.05	1.8	47.16	14.47	143.01	44.05	161.41	31.76	283.04	41.59
ST1511-13	1.46	43.66	2.83	17.17	10.22	2	27.87	7.85	80.4	26.32	109.76	24.16	251.11	40.16
ST1511-14	0.121	32.89	0.285	3.27	4.23	1.43	20.19	6.96	79.26	29.73	135.25	33.58	369.52	60.57
ST1511-15	<0.042	11.12	0.14	1.79	2.55	1.36	11.04	2.93	28.36	8.56	32.96	6.8	68.36	9.96
ST1511-16	0.038	8.34	0.077	0.86	1.19	0.343	5.21	1.76	19.1	7.3	32.43	7.41	79.08	13.01
ST1511-17	2.51	9.13	1.26	7.57	3.12	0.307	12.95	6.12	82.14	32.04	153.57	38.04	412.47	70.91
ST1511-18	0.064	6.16	0.586	9.38	15.95	0.67	78.39	25.26	298.61	114.55	508.22	112.44	1096.69	170.03
ST1511-19	0.044	16.88	0.259	4.55	6.76	2.46	23.23	5.28	42.97	10.28	30.88	5.43	46.05	6.21
ST1511-20	1.49	39.99	3.83	24.26	14.96	4.88	34.81	8.69	70.13	15.57	43.78	6.99	56.06	6.71
ST1511-21	0.33	22.92	0.4	3.17	3.62	0.31	15.58	4.99	57.71	20.64	86.92	19.52	192.22	28.96
ST1511-22	<0.030	1.43	0.105	1.38	4.04	0.09	25.58	10.32	117.44	38.21	145.22	29.25	255.26	36.77
ST1511-23	10.67	133.06	22.83	137.23	53.91	8.34	71.03	16.81	161.13	54.93	225.06	49.58	499.2	79.85
ST1511-24	1.03	39.18	3.17	28.19	26.24	7.89	61.05	13.8	99.93	21.96	59.15	9.06	64.06	7.7
ST1511-25	0.448	6.64	1.04	6.73	4.09	0.532	9.22	2.83	30.19	10.35	41.17	8.93	82.17	12.25
ST1511-26	0.226	6.53	0.472	3.54	3.03	0.465	13.32	4.36	47.06	17.03	78.32	19.23	214.92	36.55
ST1511-27	6.12	90.98	11.07	59.65	16.51	2.73	28.76	8.75	106.98	42.46	201.94	49.75	533.21	92.08
ST1511-28	0.23	25.3	0.174	2.1	3.66	0.695	18.55	6.54	80.64	30.85	142.09	33.1	353.6	58.61
ST1511-29	0.032	9.54	0.047	0.85	1.94	0.58	7.3	2.67	31.43	12.62	60.4	15.98	191.13	35.97
ST1511-30	0.058	7.37	0.197	2.78	4.65	2.02	15.1	3.78	29.61	6.84	18.61	2.75	19.4	2.19
ST1511-31	0.436	24.44	0.485	6.1	8.76	3.13	27.53	7.13	56.39	14.11	42.94	7.9	66.9	9.94
ST1511-32	5.48	36.03	3	20.25	18.03	3.99	42.11	9.76	69.17	14.62	38.89	5.98	45.51	5.71
ST1511-33	0.26	23.43	0.846	6.11	4.56	1.83	19.97	7.19	94.47	38.92	199.07	51.52	621.71	119.29
ST1511-34	<0.039	5.84	0.045	1.5	3.14	0.82	15.8	5.84	73.16	28.71	129.03	29.5	300.39	49.45
ST1511-35	3.93	27.62	2.28	17.02	14.29	4.4	38.62	8.54	60.75	12.38	30.02	4.29	30.3	3.6

ST1515														
ST1515-01	1.69	4.41	0.478	2.43	1.84	0.093	13.49	6.87	96.2	38.95	181.67	40.41	396.72	72.89
ST1515-02	<0.032	1.52	<0.022	0.47	2.51	0.101	22.13	11.16	143.8	55.34	254.97	57.11	559.61	102.37
ST1515-03	11.14	70.09	12.82	77.06	41.65	4.34	81.74	27.22	283.57	96.08	416.82	89.24	866.35	152.82
ST1515-04	6.76	41.75	7.55	42.1	24.85	2.36	61.79	22.13	240.1	82.94	362.74	77.73	743.33	132.68
ST1515-05	0.077	1.53	0.099	1.13	3.17	0.146	26.1	14.02	180.55	69.97	321.78	71.92	700.16	127.42
ST1515-06	0.207	2.65	0.268	1.98	3.1	0.245	24.28	12.17	157.4	59.09	271.71	59.56	578.58	105.46
ST1515-07	0.75	7.2	0.99	5.38	5.91	0.426	29.43	14.46	178.8	67.89	311.57	68.26	670.76	122.56
ST1515-08	0.117	3.16	0.183	2.01	3.66	0.253	25.96	12.7	163.54	62.21	288.2	64.33	636.52	115.58
ST1515-09	0.086	2.13	0.159	1.47	3.51	0.165	29.02	15.05	188.84	71.89	324.31	70.87	686.25	123.7
ST1515-10	0.041	1.54	0.06	0.55	2.39	0.072	18.98	9.9	128.05	49.69	230.27	52.09	511.86	93.4
ST1515-11	0.045	1.2	0.066	1.01	3.03	0.083	22.6	10.99	144	57.74	264.76	56.89	539.34	96.94
ST1515-12	7.06	49	9.48	52.78	19.93	1.66	35.54	10.98	117.29	41.01	175.15	36.82	349.6	60.7
ST1515-13	13.33	30.72	3.33	15.43	7.47	0.342	29.39	12.07	148.19	57.45	265.34	58.16	572.95	102.91
ST1515-14	0.315	3.75	0.515	3.98	4.97	0.327	30.45	14.44	192.46	75.4	342.93	74.35	713.67	124.68
ST1515-15	0.095	2.34	0.19	1.22	2.58	0.18	20.16	9.9	125.37	47.81	217.69	48.44	478.23	83.89
ST1515-16	0.131	4.05	0.324	3.34	5.02	0.231	26.25	10.97	142.44	56.4	256	54.53	519.84	89.7
ST1515-17	<0.024	1.33	0.034	0.57	2.36	0.104	23.83	12.12	163.91	62.79	289.99	65.67	649.63	115.44
ST1515-18	31.04	202.63	31.42	158.5	80.93	10.35	143.36	40.32	360.82	108.31	434.49	93.19	898.88	149.05
ST1515-19	0.598	7.4	1.067	7.64	6.8	0.674	26.56	11.43	135.64	50.01	228	50.59	505.29	89.66
ST1515-20	11.51	91.1	12.9	74.18	48.57	6.09	97	30.46	272.2	78.66	309.11	64.53	616.5	100.98
ST1515-21	16.05	152.86	26.46	159.67	66.14	5.96	85.15	18.62	161.2	48.51	191.05	39.5	384.75	63.92
ST1515-22	3.3	25.1	3.93	22.29	12.53	1.19	28.5	10.56	119.47	41.75	181.41	40.06	395.85	65.01
ST1515-23	1.4	10.75	1.58	9.58	8.88	0.72	30.55	12.51	140.4	48.07	211.54	47.42	472.47	80.83
ST1515-24	3.89	28.43	4.13	25.06	17.51	2.06	48.61	17.75	191.44	65.81	280.85	60.9	579.54	98.31
ST1515-25	0.41	5.13	0.507	3.16	4.55	0.284	30.74	14.81	188.27	70.45	315.34	70.3	675.97	115.95
ST1515-26	0.368	4.9	0.57	3.86	4.97	0.328	31.35	15.88	202.98	77.33	354.33	78.43	773.19	135.27
ST1515-27	0.033	1.85	0.034	0.56	2.54	0.096	24.37	12.71	163.85	62.66	285.24	64.2	638.97	112.3
ST1515-28	0.019	1.53	<0.044	0.4	2.16	0.083	20.66	10.8	142.76	55.99	258.98	59.43	596.18	105.78
ST1515-29	1.97	18.28	2.66	16.56	9.84	0.94	31.09	10.16	120.29	45.24	197.9	41	389.6	66.23
ST1515-30	<0.062	1.96	0.101	1.16	3.88	0.165	31.5	16.05	209.25	80.02	366.64	82.1	805.03	140.09
ST1515-31	0.138	1.87	0.109	0.7	2.77	<0.048	20.19	9.76	134.03	52.22	233.75	51.51	490.15	84.07
ST1515-32	1.13	4.75	1.83	9.59	6.66	0.59	19.37	8.97	107.19	37.52	160.15	34.45	334.69	56.14
ST1515-33	0.076	1.78	0.125	1.21	2.6	<0.074	17.43	7.23	97.56	39	180.81	39.9	389.75	67.56
ST1515-34	0.981	10.9	1.211	6.62	7.9	0.604	41.21	18.97	233.21	85.12	372.29	81.52	784.69	132.48
ST1515-35	2.5	17.35	2.66	16.87	9.46	1.25	33.14	14.36	187.32	70.59	312.28	67.95	651.44	110.91
ST1512														
ST1512-01	0.387	18.19	0.379	5.17	7.55	1.56	30.91	9.57	97.42	31.19	119.95	23.53	212.84	34.26

ST1512-02	<0.026	10.13	0.208	3.47	5.4	1.33	21.1	6.32	62.63	19.1	74.95	14.37	130.17	20.86
ST1512-03	1.82	21.85	1.58	12.1	10.33	1.91	29.33	7.85	78.69	23.4	95.88	18.84	178.03	29.58
ST1512-04	0.517	20.85	0.577	7.43	11.19	2.63	40.72	12.15	118.16	35.84	132.71	25.32	220.55	34.5
ST1512-05	0.311	10.51	0.204	2.16	4.3	0.486	24.56	8.57	97.38	33.38	137.49	28.4	259.18	42.82
ST1512-06	2.41	24.98	2.62	13.21	10.14	2.53	30.46	11.48	142.45	52.49	230.2	49.53	473.19	75.49
ST1512-07	0.07	6.29	0.104	1.77	4.24	0.58	23.9	8.52	98.1	35.09	149.86	32.24	302.28	52.13
ST1512-08	20.41	59.23	6.34	34.33	12.11	2.45	25.73	6.83	64.41	20.45	79.73	15.85	145.08	24.13
ST1512-09	1.04	13.36	0.406	2.85	4.21	1.17	15.53	4.88	49.28	15.29	58.04	11.18	101.27	16.2
ST1512-10	0.128	13.05	0.25	4.73	7.92	0.98	34.23	11.28	122.92	41.72	170.45	35.03	321.39	53.63
ST1512-11	0.286	14.7	0.43	5	7.89	1.82	30.31	8.8	88.75	27.14	98.8	19.83	169.22	26.35
ST1512-12	<0.029	10.75	0.061	1.63	3.72	0.62	18.95	6.76	77.82	27.87	113.08	23.4	217.39	36.45
ST1512-13	1.68	18.41	0.77	5.48	5.14	1.48	18.56	5.47	57.13	19.47	77.13	15.53	147.66	25.06
ST1512-14	0.039	8.09	0.131	2.61	5.55	1.15	28.47	9.32	91.6	28.47	104	19.66	174.63	27.53
ST1512-15	<0.041	3.91	0.181	3.56	7.24	0.348	33.95	11.32	124.72	44.09	179.83	35.76	323.78	52.47
ST1512-16	0.71	13.18	0.337	4.85	6.22	1.39	23.28	7.19	70.98	21.78	85.26	16.13	147.35	23.65
ST1512-17	21.87	77.63	9.97	57.66	29.79	5.54	63.13	16.13	136.6	37.9	132.05	24.36	212.73	33.21
ST1512-18	<0.048	4.22	0.05	1.12	2.5	1.1	17.19	6.67	90.78	37.6	188.86	45.89	513.78	99.48
ST1512-19	0.027	10.43	0.137	1.8	4.1	0.58	17.68	5.77	64.24	22.45	93.5	19.61	186.6	31.62
ST1512-20	49.16	116.03	13.48	60.41	16.89	1.43	37.49	10.4	104.32	33.93	132.87	26.74	244.99	40.97
ST1512-21	0.203	9.71	0.179	1.95	4.05	0.79	17.66	5.44	56.38	18.24	73.61	14.8	131.73	22
ST1512-22	<0.050	4.55	0.048	0.88	1.54	0.217	7.93	2.77	31.74	10.8	45.69	9.74	98.14	16.2
ST1512-23	0.875	8.41	0.322	2.82	4.24	0.83	17.22	5.47	58.12	18.78	75.11	15.32	144.43	24.06
ST1512-24	0.05	15.73	0.331	5.04	6.59	2.51	22.78	6.71	61.43	18.41	65.55	12.28	106.61	16.28
ST1512-25	<0.043	13.12	0.238	4.49	5.59	1.79	21.1	5.91	59.33	18.4	67.7	13.31	114.35	18.6
ST1512-26	<0.051	14.15	0.198	2.39	5.14	2.14	26.85	9.32	101.36	33.42	130.19	25.08	231.67	36.85
ST1512-27	0.047	24.99	0.15	3.34	4.72	1.73	21.77	6.85	71.85	24.65	97.48	19.17	174.76	28.92
ST1512-28	0.059	13.47	0.268	3.91	7.05	2.45	28.69	8.75	83.44	26.05	96.71	18.58	166.16	27.05
ST1512-29	0.054	3.28	0.056	1.09	3.46	0.283	18.38	6.45	69.47	22.64	86.7	16.88	151.81	23.84
ST1512-30	0.021	2.18	0.056	1.33	4.3	0.395	26.12	8.8	87.48	25.68	90.43	16.03	135.16	20.58
ST1512-31	0.723	9.34	0.27	2.4	4.23	0.63	26.14	8.47	92.62	30.55	120.6	24.26	212.88	34.65
ST1512-32	<0.038	3.53	0.092	1.69	3.73	0.71	16.56	4.91	49.41	14.85	54.03	10.66	95.71	15.06
ST1512-33	<0.041	4.32	0.136	2.23	4.71	0.99	14.54	2.62	15.39	2.86	6.65	0.975	6.76	0.844
ST1512-34	0.095	4.01	0.105	1.74	5.11	1	26.46	8.49	80.4	25.09	96.58	19.49	184.23	30.41
ST1512-35	0.231	2.42	0.196	2.87	6.04	0.192	35.36	13.42	162.38	59.94	258.43	53.53	501.91	84.92
ST1513														
ST1513-01	<0.041	31.61	0.041	0.86	1.05	0.247	4.79	2	23.6	9.01	41.65	10.26	109.37	19.41
ST1513-02	30.57	73.2	7.77	34.44	11.3	2.28	22.68	6.64	67.36	22.47	96.6	22.07	228.26	41.47
ST1513-03	0.085	6.96	0.514	7.63	11.38	0.98	47.05	15.36	164.33	54.28	218.4	43	391.56	61.47

ST1513-04	<0.041	4.4	0.02	0.47	1.64	0.6	11.33	3.51	32.89	10.22	39.92	8.64	88.62	15.82
ST1513-05	1.29	17.04	1.35	10.14	10.33	2.26	25.64	9	84.49	26.34	116.83	28.69	318.71	55.36
ST1513-06	0.016	6.54	0.061	0.92	1.75	0.78	7.55	2.56	31.09	13.03	65.46	16.51	195.69	41.17
ST1513-07	1.79	16.53	2.63	15.87	17.87	3.91	45.06	12.23	84.99	17.68	51.59	9.67	83.09	13.82
ST1513-08	0.65	28.01	0.96	7.41	9.45	2.98	34.06	11.19	106.58	34.62	131.4	25.64	232.88	37.17
ST1513-09	0.254	18.53	0.92	11.91	21.25	4.24	94.8	28.47	295.12	96.02	388.33	79.27	734.62	123.34
ST1513-10	77.22	227.84	28.65	164.04	50.03	6.95	113.43	32.45	354.84	122.68	488.1	94.75	834.61	126.42
ST1513-11	1.38	30.75	1.87	12.16	13.2	3.15	40.33	13.77	139.9	46.06	195.43	42.79	425.81	70.64
ST1513-12	<0.030	4.54	<0.021	0.6	2.3	0.68	13.86	4.14	35.81	9.88	36.81	7.83	78.99	14.34
ST1513-13	1.45	22.06	1.42	12.37	15.26	1.66	47.85	12.61	113.57	34.32	125.92	24.38	217.69	33.3
ST1513-14	6.67	46.97	5.13	32.93	28.83	7.76	68.89	21.78	201.75	57.94	241.11	53.11	521.69	86.94
ST1513-15	16.53	51.62	3.9	16.93	6.19	0.64	14.7	5.09	57.16	20.83	91.56	20.74	204.17	34.35
ST1513-16	0.836	18.8	0.294	1.94	2.01	0.246	9.58	3.33	40.69	15.13	68.53	15.54	154.88	25.87
ST1513-17	0.239	10.19	0.139	1.8	3.15	0.399	14.08	4.87	56.56	20.89	92.58	20.84	207.73	36.45
ST1513-18	0.086	33.53	0.348	4.41	6.49	3.1	30.74	10.73	119.02	41.39	168.69	34.83	322.49	53.6
ST1513-19	0.74	3.61	0.479	3.07	2.79	0.72	10.57	4.79	66.23	23.8	107.43	25.48	270.83	46.14
ST1513-20	0.35	3.76	0.46	3.4	5.65	0.4	21.3	8.75	106.25	39.73	195.33	51.71	593.27	113.28
ST1513-21	<0.054	10.75	0.093	1.64	3.03	1.48	13.38	4.13	41.96	14.36	59.19	12.76	125.04	22.22
ST1513-22	<0.049	10.84	0.098	1.57	2.88	1.33	12.33	3.73	39.15	13.11	55.7	11.96	116.85	19.97
ST1513-23	<0.029	0.678	0.036	0.66	2.48	0.273	16.57	5.2	43.82	10.44	31.22	4.96	39.67	5.57
ST1513-24	1.54	23.08	0.64	5.61	6.53	2.91	24.3	7.97	87.39	31.45	134.51	28.44	275.75	46.83
ST1513-25	1.43	50.6	0.855	6.28	6.45	2.39	21.82	6.75	63.29	20.13	84.85	19.33	204.66	39.65
ST1513-26	0.09	9.53	0.281	2.34	3.4	1.34	13.1	3.71	38.14	13.09	52.9	11.39	114.45	19.8
ST1513-27	13.89	50.55	4.26	22.3	12.68	2.04	38.07	11.31	118.49	40.28	160.78	32.14	306	49.95
ST1513-28	2.28	39.12	2.57	17.04	13.86	3.96	40.62	12.92	126.32	37.59	141.78	28.3	267.1	40.08
ST1513-29	0.497	27.02	0.88	5.84	7.31	2.8	34.96	11.24	118.95	37.98	145.75	28.43	261.22	40.23
ST1513-30	2.5	25.44	3.55	22.46	16.81	3.82	34.74	10.06	89.99	26	106.73	22.96	229.54	37.77
ST1513-31	0.04	17.05	0.061	0.4	0.82	0.4	5.96	2.06	25.24	11.25	55.43	16.05	191.36	37.66
ST1513-32	0.276	30.6	0.354	4.94	6.71	2.98	32.74	10.52	116.67	40.13	159.8	32.56	303.28	50.09
ST1513-33	0.94	13.71	1	6.95	7.3	2.69	26.57	8.93	82.48	23.18	87.71	17.99	169.09	25.52
ST1513-34	0.034	6.79	0.086	1.35	2.3	0.81	10.47	3.27	37.46	12.33	52.47	12.03	130.59	23.58
ST1513-35	3.92	21.81	2.38	16.17	11.29	1.68	39.89	13.57	158.65	59.17	251.23	51.46	473.66	77.62

Table E6. REE contents (ppm) of the samples from the Xinyang area.

Spot No.	La	Ce	Pr	Nd	Sm	Eu	Gd	Tb	Dy	Ho	Er	Tm	Yb	Lu
XY1605														

XY1605-01	13.03	44.79	4.48	27.86	21.17	2.8	106.01	46.43	536.25	171.88	627.75	108.16	878.75	134.03
XY1605-02	19.81	407.75	28.2	139.33	59.46	18.04	90.32	24.72	232.42	67.52	264.72	53.14	491.19	82.37
XY1605-03	<0.062	6.58	0.028	0.61	2.33	0.154	14.73	5.79	73.9	29.22	133.33	28.19	269.56	47.78
XY1605-04	<0.049	1.88	<0.041	0.89	2.99	0.056	20.96	8.79	111.4	43.84	200.07	42.02	404.13	73.56
XY1605-05	<0.065	11.56	0.104	1.49	3.9	0.78	21.42	8.29	99.82	38.61	170.4	34.43	326.51	58.05
XY1605-06	1.77	37.24	0.87	5.83	5.14	2.82	17.42	5.7	63.74	23.53	115.86	28.78	331.71	70.51
XY1605-07	0.79	42.92	1.63	11.4	8.95	1.95	28.98	10.16	106.46	34.24	140.94	28.71	276.71	50.14
XY1605-08	3.04	404.89	5.99	37.44	28.38	9.01	61.56	19.3	194.64	63.26	263.86	55.51	533.66	91.74
XY1605-09	14.25	227.43	8.74	58.48	30.03	12.01	67.03	21.84	222.32	69.95	289.81	57.54	560.58	94.68
XY1605-10	4.13	48.03	1.7	11.9	10.91	3.88	39.47	11.86	121.49	43.09	189.95	42.43	436.65	85.71
XY1605-11	1.36	43.53	0.378	2.84	2.9	0.73	13.67	5.2	61.47	23.93	113.91	26.23	271.05	53.09
XY1605-12	0.72	17.78	0.72	8.84	14.91	5.41	71.4	25.32	244.59	85.1	359.94	72.2	681.37	116.37
XY1605-13	<0.056	12.39	0.048	1.09	2.03	0.54	8.11	3.05	35.92	13.94	68.83	15.4	169.25	33.74
XY1605-14	0.69	12.97	0.342	2.58	2.97	0.148	12.41	5.15	70.7	28.76	139.47	31.21	310.46	52.83
XY1605-15	0.42	19.2	0.5	6.76	8.94	2.3	39.05	13.43	149.48	54.78	240.61	51.75	505.76	89.37
XY1605-16	0.427	20.72	1.5	13.17	10.82	2.26	32.64	10.87	119.24	39.5	153.71	28.94	256.98	43.21
XY1605-17	0.226	16.78	0.592	4.56	5.33	0.97	21.39	8.53	101.19	37.56	164.66	33.91	323.24	56.49
XY1605-18	7.69	38.83	3.01	13.31	5.47	2.7	9.45	2.92	32.55	12.99	66.6	17.31	211.17	46.38
XY1605-19	0.018	23.65	0.095	1.34	2.38	0.363	8.03	2.03	17.87	5.51	21.8	4.53	42.7	7.68
XY1605-20	2.66	10.25	0.99	6.44	5.34	0.73	19.78	7.07	84.29	32.23	140.81	29.5	282.93	50.96
XY1605-21	<0.106	8.85	0.141	2.07	4.32	0.7	24.4	9.13	115.55	44.66	199.53	40.94	389.81	68.93
XY1605-22	0.156	11.75	0.236	2.67	4.76	1.01	23.22	7.97	92.59	33.81	152.55	32.28	315.08	56.46
XY1605-23	<0.064	4.3	<0.036	0.75	1.75	0.41	14.19	5.9	79.89	33.26	159.44	37.55	394.78	72.81
XY1605-24	<0.058	10.87	0.038	0.73	1.56	0.578	6.17	1.93	21.5	7.74	34.46	7.38	75.63	14.61
XY1605-25	0.435	22.56	0.382	5.07	6.89	0.78	24.33	7.69	78.01	25.45	101.81	19.14	183.02	29.65
XY1605-26	<0.031	19.43	0.034	1.15	4.45	0.55	36.21	15.58	214.79	93.85	454.31	101.4	1041.9	197.12
XY1605-27	<0.082	5.57	0.085	1.34	2.99	0.31	21.13	8.04	95.41	34.95	157.67	32.44	319.04	56.26
XY1605-28	0.074	7.41	0.083	1	1.64	0.438	11.36	4.78	60.35	23.29	107.83	24.02	236.32	41.15
XY1605-29	<0.038	4.96	0.071	0.92	2.25	0.254	11.37	4.24	43.62	13.74	53.18	10.54	101.22	16.89
XY1605-30	0.069	10.07	0.172	2.12	3.52	0.529	18.52	6.78	78.24	27.84	114.75	22.82	215.41	36.03
XY1605-31	<0.066	11.86	0.192	3.4	6.98	1.37	47.25	19.78	265.18	105.17	471.19	103.58	997.2	162.05
XY1605-32	<0.048	2.33	<0.023	0.74	1.62	0.97	4.82	1.089	7.53	1.63	4.96	0.814	6.68	0.899
XY1605-33	6.79	34.96	5.89	33.75	24.67	3.82	53	17.3	182.88	62.66	273.61	60.72	599.58	102.88
XY1605-34	30.75	169.61	29.88	167.95	119.7	16.81	193.41	53.28	453.99	119.34	450.45	93.7	886.98	136.95
XY1605-35	0.038	3.57	0.174	2.49	3.82	0.353	18.47	6.71	79.1	29.12	127.11	27.5	265.12	45.3
XY1605-36	0.043	31.47	0.153	2.59	5.03	2.52	21.66	7.16	79.45	27.03	114.14	25.86	257.41	40.26
XY1605-37	0.05	7.73	0.094	0.64	1.93	0.123	10.5	4.48	58.25	22.62	103.76	22.56	226	38.69
XY1605-38	0.041	1.18	0.068	<0.29	0.54	0.211	3.69	1.6	21.33	8.59	42.16	10.47	112.92	22.16
XY1605-39	0.225	9.67	0.232	2.51	2.16	0.76	7.5	2.57	32.59	12.84	65.35	17.07	201.67	43.22

XY1605-40	<0.031	0.606	0.0092	<0.25	0.32	0.255	2.66	0.947	11.78	4.16	17.1	3.47	31.4	4.6
XY1605-41	0.52	6.54	0.617	4.69	5.67	0.7	19.9	6.74	88.38	33.38	160.3	38.52	411.63	75.93
XY1605-42	<0.049	1.48	0.017	<0.35	0.82	0.492	2.42	0.699	5.2	1.31	4	0.701	6.6	0.836
XY1605-43	0.27	15.01	0.171	1.53	1.96	0.7	8.16	2.88	37.54	15.83	78.03	19.77	224.22	45.29
XY1605-44	0.167	33.95	0.811	11.49	14.4	4.65	43.56	12.62	127.1	42.44	179.95	38.96	386.47	65.78
XY1605-45	<0.035	10.37	0.049	1.01	2.9	0.091	18.4	7.7	103.12	41.78	196.3	44.37	428.84	70.53
XY1605-46	<0.049	0.068	<0.033	<0.28	<0.155	<0.063	<0.45	0.0021	<0.206	0.031	0.114	0.035	1.32	0.052
XY1605-47	<0.068	2.98	<0.040	0.4	0.8	0.48	4.86	1.84	24.08	10.5	53.54	14.17	172.65	37.73
XY1605-48	<0.047	1.76	0.106	0.85	0.58	4.04	2.38	1.06	13.39	5.51	27.34	6.76	73.71	14.46
XY1605-49	<0.051	11.29	0.065	1.15	3.06	0.092	20.21	7.81	100.63	38.88	170.82	36.76	349.38	57.18
XY1605-50	47.78	477.71	68.34	420.24	320.21	54.75	519.25	127.71	892.98	170.39	470.19	78.91	636.34	78.15
XY1605-51	0.05	1.79	0.055	0.59	0.82	0.45	3.43	1.53	18.68	8.74	50.3	14.5	167.88	33.89
XY1605-52	<0.061	2.3	<0.054	0.71	1.26	0.64	3.36	0.776	5.59	1.46	4.23	0.696	5.42	0.788
XY1605-53	<0.030	0.699	0.037	<0.25	0.31	0.156	1.91	0.832	11.44	4.79	24.64	6.24	72.88	14.62
XY1605-54	<0.038	0.94	0.038	<0.38	0.28	0.142	2.51	0.94	13.02	5.46	26.95	6.57	76.07	14.88
XY1605-55	<0.044	3.05	0.038	0.57	2.1	0.481	16.58	6.18	81.42	32.71	148.85	33.41	328.22	56.72
XY1605-56	0.411	13.61	0.475	3.49	8.93	1.86	50.57	18.55	217.91	79.34	335.24	68.55	634.8	104.26
XY1601A														
XY1601A-01	0.302	2.39	0.072	1.01	2.69	2.05	14.02	4.52	31.02	6.19	18.67	3.72	37.22	6.06
XY1601A-03	1.31	11.31	1.39	8.68	9.7	1.05	36.23	13.47	150.85	53.24	217.11	46.39	441.12	66.72
XY1601A-04	<0.049	<0.072	<0.074	<0.29	0.43	0.331	1.42	0.615	6.2	1.81	5.62	0.816	7.13	0.96
XY1601A-05	0.09	21.87	0.892	13.74	14.65	1.22	36.64	8.8	78.58	24.01	92.38	18.65	170.31	26.95
XY1601A-06	<0.046	9.96	0.144	1.73	2.39	0.257	8.03	2.38	22.95	7.43	32.82	6.71	68.14	11.56
XY1601A-07	0.81	22.42	0.9	7.05	3.98	1.5	19.15	6.68	80.89	31.17	138.74	30.88	306.46	52.18
XY1601A-08	55.86	117.32	13.61	59.5	14.26	2.49	21.55	6.08	60.4	17.76	69.03	16.16	166.74	26.78
XY1601A-09	0.22	20.63	0.109	2.44	4.43	1.65	23.95	9.45	129.26	54.07	264.28	64.81	708.21	129.29
XY1601A-10	1.6	7.51	1.93	11.69	7.46	4.05	17.55	4.79	40.8	11.74	43.97	9.76	104.05	17.1
XY1601A-11	0.11	22.55	0.368	4.31	5.17	0.57	15.18	3.89	38.97	12.66	51.07	10.93	108.42	17.73
XY1601A-12	1.42	107.31	1.144	13.82	19.34	5.02	70.55	19.55	191.21	59.47	226.15	45.48	414.17	62.68
XY1601A-13	0.062	17.94	0.121	1.56	2.87	0.342	9.18	2.64	26.67	9.91	41.26	9.29	95.77	16.93
XY1601A-15	0.158	34.26	0.164	2.33	4.4	0.57	23.39	9.07	118.32	46.28	214.68	50.37	511.21	87.32
XY1601A-16	0.058	12.81	0.049	0.72	1.83	0.35	11.98	4.64	59.38	23.19	106.12	24.84	251.51	44.6
XY1601A-17	83.15	246.86	31.15	151.42	52.17	6.59	59.43	13.54	111.82	30.22	113.63	25.34	258.58	39.51
XY1601A-18	0.205	32.34	0.245	2.83	4.51	0.539	14.98	4.22	42.86	14.48	60.95	13.48	134.97	21.91
XY1601A-19	0.077	28.8	0.178	2.75	3.98	0.521	13.62	3.88	39.15	13.27	56.6	12.28	122	19.93
XY1601A-20	0.099	0.58	0.102	0.98	0.89	0.49	3.9	1.27	12.87	4.14	14.26	2.18	17.62	1.67
XY1601A-21	0.032	17.88	0.085	1.32	1.76	0.214	7.06	2.11	22.28	7.7	33.16	7.57	77.54	13.09
XY1601A-22	1.02	36.42	0.315	3.09	5.05	0.81	24.22	8.88	104.75	38.54	168.4	37.66	370.73	57.89

XY1601A-23	1.92	28.17	2.08	13.07	9.46	1.92	25.52	9.09	107.24	40.84	187.83	44.51	483.08	82.88
XY1601A-24	<0.048	14.88	0.236	3.92	5.82	0.568	17.66	4.58	46.22	14.66	59.09	12.3	119.44	19.31
XY1601A-25	0.052	14.77	0.07	1.22	2.58	1.13	12.65	4.97	60.65	24.75	118.34	28.53	309.72	55.39
XY1601A-26	<0.064	0.391	<0.062	<0.60	<0.20	<0.118	<0.57	0.271	6.47	2.64	7.98	1.11	8.25	0.78
XY1601A-27	<0.050	27.33	0.203	3.27	4.65	0.65	18.92	5.23	53.77	17.96	74.79	15.96	156.95	25.64
XY1601A-28	0.057	1.61	0.086	1.01	2.11	0.419	11.75	4.74	55.07	19.37	82.25	19.46	200.43	32.08
XY1601A-29	<0.040	16.62	0.131	2.6	3.58	0.373	10.62	2.87	29.73	9.48	39.37	8.44	83.51	13.46
XY1601A-30	<0.028	16.43	0.103	1.53	2.39	0.308	7.67	2.29	24.2	8.22	34.9	7.76	78.01	12.84
XY1601A-31	0.073	2.27	0.318	4.03	7.44	2.05	27.78	7.9	77.24	24.63	87.39	17.05	160.86	22.71
XY1601A-32	<0.046	19.49	0.132	1.93	3.02	0.357	10.64	3.06	29.97	10.68	44.04	9.62	94.89	15.78
XY1601B														
XY1601B02	<0.054	4.03	0.077	1.57	2.85	0.324	14.82	5.31	65.71	24.57	108.34	23.85	232.97	38.07
XY1601B03	0.46	6.57	0.75	10.68	12	1.87	49.68	15.89	171.78	59.34	235.83	48.43	441.88	66.05
XY1601B04	<0.046	1.38	<0.022	<0.27	0.3	0.078	2.08	0.87	14.09	6.52	36.92	10.05	121.18	22.67
XY1601B05	0.314	5.33	0.669	11.63	17.91	2.73	77.48	24.41	264.39	91.15	367.15	73.14	661.84	106.71
XY1601B06	<0.050	<0.043	0.014	<0.29	<0.23	<0.183	2.65	1.92	27.51	8.74	33.74	6.45	56.48	8.09
XY1601B07	0.03	<0.052	<0.051	<0.25	<0.34	0.244	2.12	1.23	18.39	7.45	28.94	4.91	40.36	5.57
XY1601B08	<0.054	4.25	<0.033	0.63	1.6	0.101	9.1	3.51	44.23	17.45	79.35	17.69	172.58	28.01
XY1601B09	0.079	15.2	0.075	1.4	2.1	0.82	9.94	3.36	40.91	16.66	81.25	20.2	230.59	42.63
XY1601B10	0.051	5.79	0.19	3.32	6.13	0.317	29.47	10.24	115.26	42.01	177.83	36.42	345.16	53.26
XY1601B11	0.043	2.41	0.182	2.46	4.86	0.96	24.1	8.09	94.01	34.11	141.16	30.19	298.64	47.19
XY1601B12	<0.044	7.55	0.052	0.8	1.88	0.486	12.16	5.47	61.59	20.24	84.34	20.38	219.6	36.66
XY1601B13	0.032	5.67	0.285	4.87	8.31	1.03	43.14	14.61	164.51	58.04	233.85	48.74	450.69	68.52
XY1601B14	0.104	6.23	0.279	4.39	7.72	0.84	37.46	12.92	143.93	51.18	211.1	43.78	415.26	61.64
XY1601B15	0.011	11.03	0.034	0.98	2.95	<0.092	17.28	7.48	94.99	37.4	165.32	36.97	356.14	53.88
XY1601B16	3.09	22.63	5.73	44.4	22.15	11.79	32.04	7.66	53.5	11.2	31.9	5.21	41.36	5.3
XY1601B18	0.086	24.6	0.187	2.47	3.66	1.5	15.33	5.12	56.35	19.81	86.24	19.95	216.77	38.58
XY1602														
XY1602-01	1.28	14.97	0.479	3.95	4.7	0.147	25.06	9.01	105.19	38.88	163.3	33.67	320.65	49.7
XY1602-02	<0.041	13.96	0.075	0.94	1.72	0.63	8.32	2.58	34.67	13.57	66.14	16.1	183.94	37.58
XY1602-03	0.102	7.61	0.103	1.73	3.54	0.413	22.39	9.08	120.66	45.85	200.58	42.22	394.65	65.57
XY1602-04	78.16	424.45	63.65	356.55	179.46	58.11	261.43	66.75	555.55	138.35	478.46	97.63	911.47	132.81
XY1602-05	0.132	2.98	0.149	1.77	1.73	0.394	10.65	5.2	75.71	32.03	155.5	39.81	437.18	77.16
XY1602-06	33.06	95.93	8.57	39.58	11.26	3.14	17.27	5	56.43	19.15	85.41	19.84	211.31	34.89
XY1602-07	0.261	3.07	0.2	1.45	1.47	0.93	6.99	3.68	52.91	21.47	101.95	24.06	253.25	45.42
XY1602-08	0.429	113.96	0.63	7.92	13.07	4.18	67	24.21	297.27	110.59	492.74	107.99	1045.48	173.18
XY1602-09	0.048	2.1	0.047	0.61	0.23	0.207	2.98	1.65	26.27	11.9	65.29	18.67	232.94	53.02
XY1602-10	0.046	12.62	0.102	1.43	2.73	0.182	17.64	7.42	100.6	41.43	198.4	45.11	450.43	77.13

XY1602-11	0.557	11	0.394	5.55	9.35	1.89	37.11	11.9	135.61	47.08	195.58	41.55	401.1	66.46
XY1602-12	<0.050	4.66	0.091	0.75	0.89	0.53	5.23	2.15	29.56	11.83	59.98	15.6	181.93	34.48
XY1602-13	0.573	22.73	0.434	6.54	13.54	1.38	77.16	28.15	345.75	130.9	577.27	122.55	1177.57	204.42
XY1602-14	0.195	22.4	0.118	1.48	2.96	0.451	15.1	6.08	79.06	31.64	150.41	34.78	348.41	61.6
XY1602-15	0.4	7.35	0.455	4.94	6.52	1.6	29.68	9.78	111.15	40.17	168.1	34.15	325.67	52.02
XY1602-16	4.03	22.25	1.48	10.48	12.11	1.78	58.68	22.22	256.41	92.3	391.68	83.23	772.65	127.08
XY1602-17	3.9	13.48	0.882	4.37	2.8	0.56	11.66	4.65	57.43	22.21	104.51	25.51	283.4	50.22
XY1602-18	0.123	35.4	0.078	1.76	3.15	0.52	17.92	6.77	86.4	35.03	165.8	39.34	415.38	72.84
XY1602-19	0.171	3.63	0.23	2.03	2.78	1.13	9	2.1	16.07	3.91	13.25	2.25	19.38	2.31
XY1602-20	0.107	12.54	0.062	1.47	2.4	0.214	13.19	4.92	60.53	23.39	106.13	24.05	238.08	38.63
XY1602-21	4.17	21.62	1.72	10.48	4.34	1.53	10.18	3.29	39.89	16.82	87.68	23.11	277.72	58.26
XY1602-22	0.177	18.17	0.284	3.7	6.14	2.63	29.09	10.95	140.56	55.7	262.74	64.24	700.22	131.06
XY1602-23	1.86	13.49	2.32	12.07	5.67	7.68	15.75	6.38	78.6	26.37	116.64	28.54	329.53	57.24
XY1602-24	26.79	132.9	19.6	117.63	69.67	97.31	132.95	46.33	513.36	152.59	567.87	110.99	950.16	120.53

According to the CL images, Th/U ratios and REE patterns, the zircons that are suspiciously not from a magmatic origin or affected by later processes are Spot No.03, 05, 06, 10, 11, 13, 14, 16-18, 20-23, 26, 32. Among all these zircons, Spot No.10, 11, 20-23, 26, 32 display concordant ages (disc.% < ±10%).

The Th/U ratio of Spot No.22 is 0.02, and its REE pattern is not a typical unaltered igneous zircon, and most importantly, Spot No.22 is a dark zircon like Spot No.10, 20, 23 and 26, 32. In the case that the domains are homogeneously dark in CL, they are considered as no zoning, and the low luminescence may be caused by high trace-element contents or by metamictization or by high-pressure metamorphism (Corfu et al., 2003). These analyses are grouped into metamorphic ages. Spot No.11&21 are xenocrystic cores with dark overgrowth rims. As the zoning in Spot No.11&21 is blurred, the age U-Pb age is reset due to the recrystallization (Hoskin and Schaltegger, 2003). These analyses are considered to reflect metamorphism. The metamorphic ages fall into several groups: 805.9±7.11Ma (1 analysis, Spot No.11); 493±4.56Ma (1 analysis, Spot No.10); 443.2~438.6Ma (4 analyses, Spot No.20, 21, 23, 26); 424.2~428Ma (2 analyses, Spot No.22, 23).

Other concordant ages are interpreted as magmatic ages, and can be divided into several groups: 952±8.41Ma (1 analysis, Spot No.15); 472.4~470.3Ma (3 analyses, Spot No.29, 35, 36); 440~431.5Ma (6 analyses, Spot No.08, 12, 25, 30, 31, 34); 428~418.9Ma (6 analyses, Spot No.02, 04, 07, 19, 27, 33); 402.1±3.53Ma (1 analysis, Spot No.01); 387.6±3.62Ma (1 analysis, Spot No.28). The youngest age group (although only one analysis) may indicate the crystallization age of the dyke, and the age is 387.6±3.62Ma.

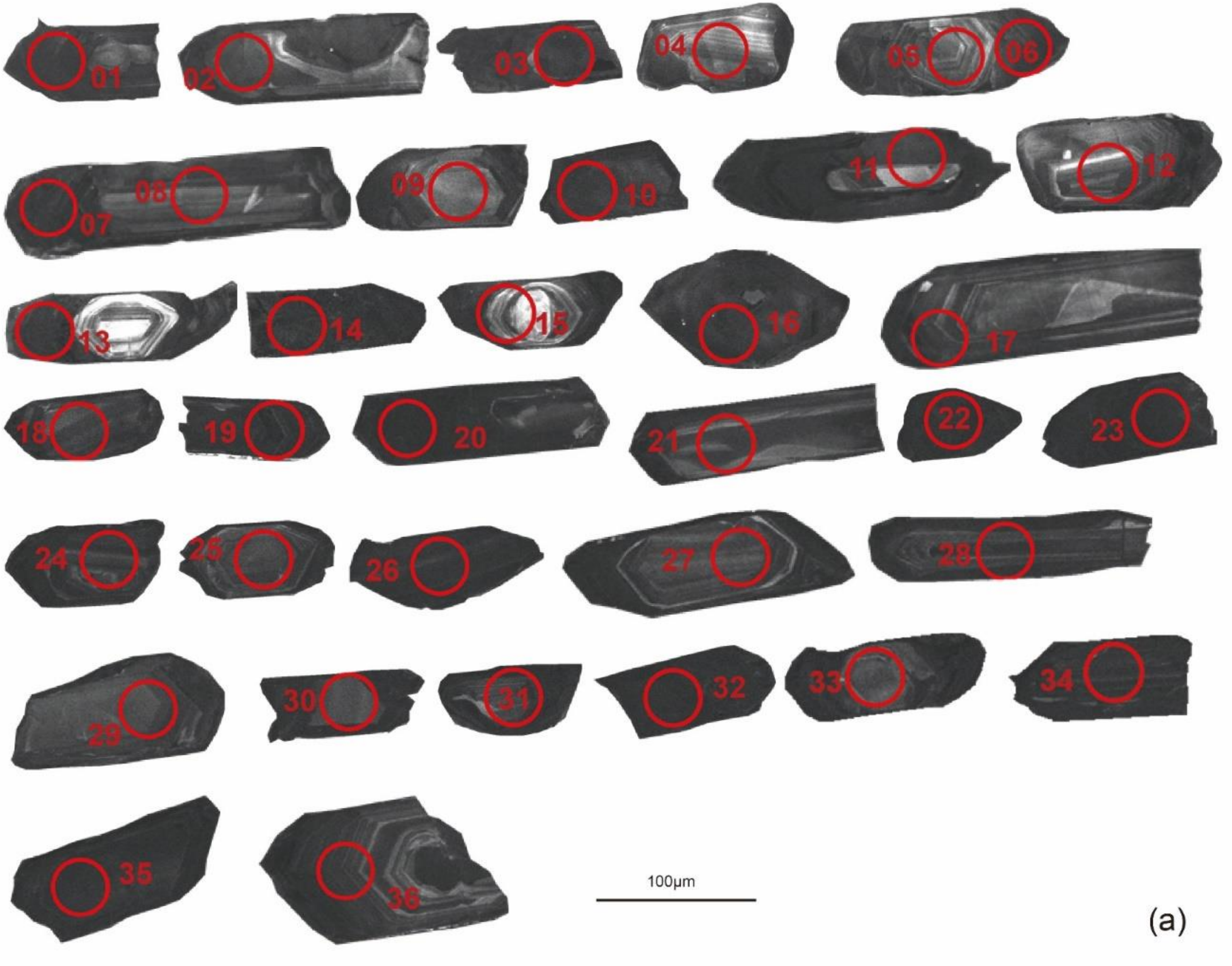
01
02
03
04
05
06
07
08
09
10
11
12
13
14
15
16
17
18
19
20
21
22
23
24
25
26
27
28
29
30
31
32
33
34
35
36
100μm
(a)

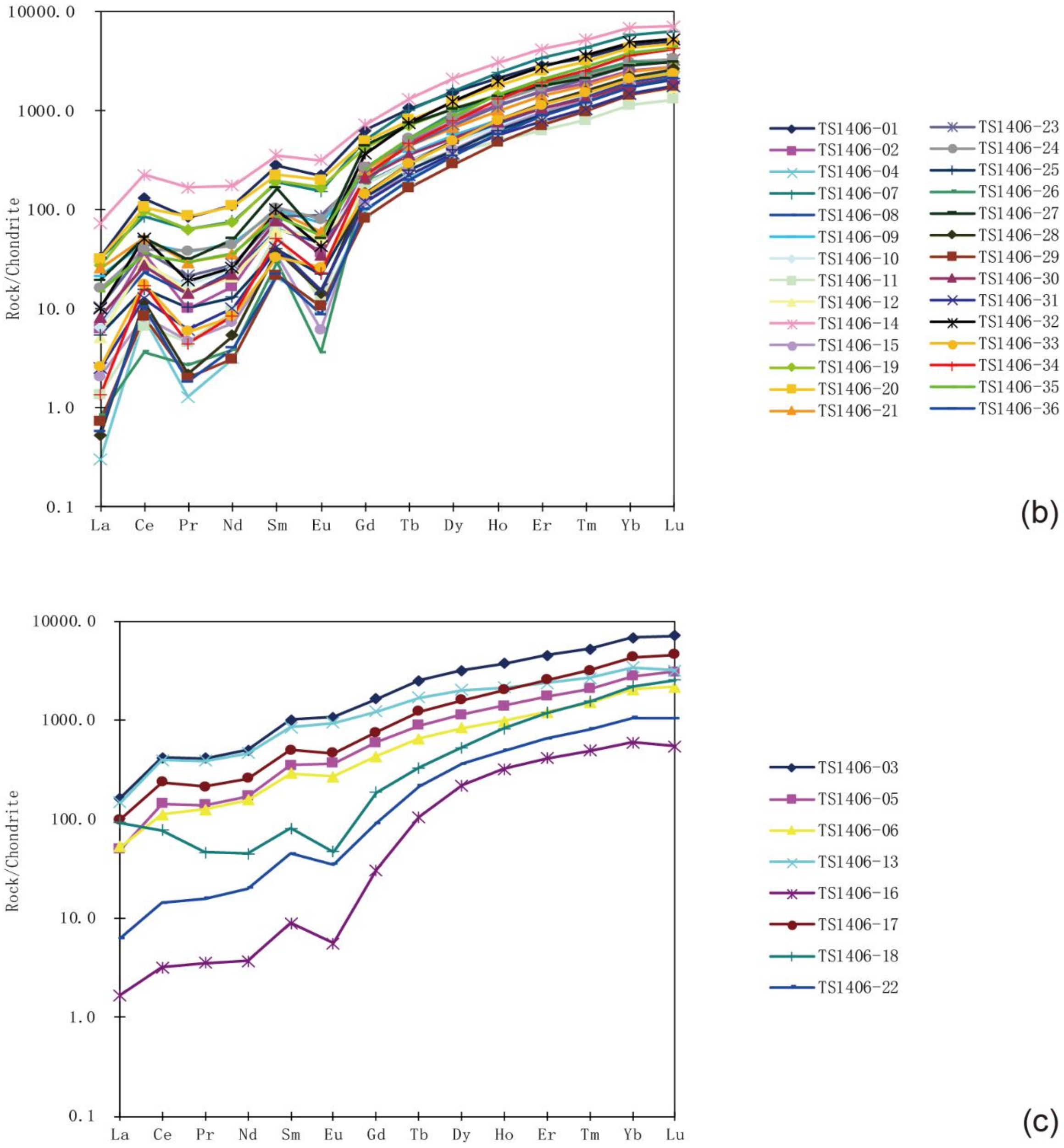

Figure E1 CL images and the REE pattern of TS1406.

(2) TS1408-1

Zircon grains range from 30μm to 150μm in TS1408-1. Some zircons are ellipsoidal or rounded shapes (Spot No.03, 07, 08, 16, 24, 28, 30, 31, 32 and 33), and others are subhedral to euhedral prismatic with length-to-width ratios ranging from 1.5 to 2.5. Most of the zircons show a medium-luminescent core with a low-luminescent rim (e.g., Spot No.05, 07, 08, Fig.E2a). Unfortunately, the rims are too thin to be measured. Most xenocrystic cores exhibit well-developed zoning, except for Spot No.03, 10, 16, 31. Spot No.06, 14, 17 and 36 are homogeneously dark with no zoning.

Th/U ratios are in the range of 0.13~1.14. Spot No.08, 13, 19, 20, 22, 27 have Th/U ratios > 0.5.

Most of the zircons have REE patterns showing a positive Ce-anomaly and negative Eu-anomaly and a steeply rising from LREE to HREE (Fig.E2b), while Spot No.09, 13, 24, 27, 31 and 32 show different patterns (Fig.E2c). Spot No.13, 31 and 32 are relatively abundant in LREE, and Spot No. 09 and 27 are abundant in Ce and Pr as well as no negative Eu-anomaly, and Spot No.24 does not show positive Ce-anomaly.

According to external morphology, internal texture, Th/U ratio and REE pattern, the analyzed spots that are suspected not to be magmatic origin are Spot No.03, 06, 09, 10, 13, 14, 16, 17, 24, 27, 31, 36. As Spot No.09&16 show discordant ages (disc.%=23.6%-12.0%), we do not discuss these two analyses further.

Spot No.03, 10, 13, 16, 24 and 31 are xenocrystic cores, and the primary igneous oscillatory zoning is blurred. The blurred primary zoning is an indication of the metamorphic disturbance (Hoskin and Schaltegger, 2003), so their ages are interpreted as metamorphic ages. Spot No.06, 14, 17, 27 and 36 are homogenous dark zircons, and some of them even contain darker domains. This characteristic may be related to metamorphism, so these ages are interpreted as metamorphic ages. The metamorphic ages fall into distinct groups: 1107.4±9.75Ma (1 analysis, Spot No.13); 959.9±8.47Ma (1 analysis, Spot No.31); 916.8~894.5Ma (2 analyses, Spot No.09, 24); 829±7.69Ma (1 analysis, Spot No.03); 444~425.3Ma (4 analyses, Spot No.14, 17, 27, 36).

Excluding the metamorphic ages and discordant ages, the magmatic ages can be grouped into several sets: 1469.6±13.1Ma (1 analysis, Spot No.20); 1355.3±11.98Ma (1 analysis, Spot No.08); 1131.9~1066.3Ma (2 analyses, Spot No.30, 35); 994.4~973.3Ma (4 analyses, Spot No.28, 29, 33, 34); 946.7~904.1Ma (5 analyses, Spot No.04, 05, 15, 22, 23); 884.5~867.5Ma (3 analyses, Spot No.01, 07, 11); 505±4.9Ma (1 analysis, Spot No.25); 455.2~424.8Ma (4 analyses, Spot No.06, 18, 19, 26); 393.3~392.3Ma (2 analyses, Spot No.02, 12). The weighted mean age of the youngest group is 392.8±4.9Ma (MSWD=0.041) and may indicate the crystallization age of this dyke.

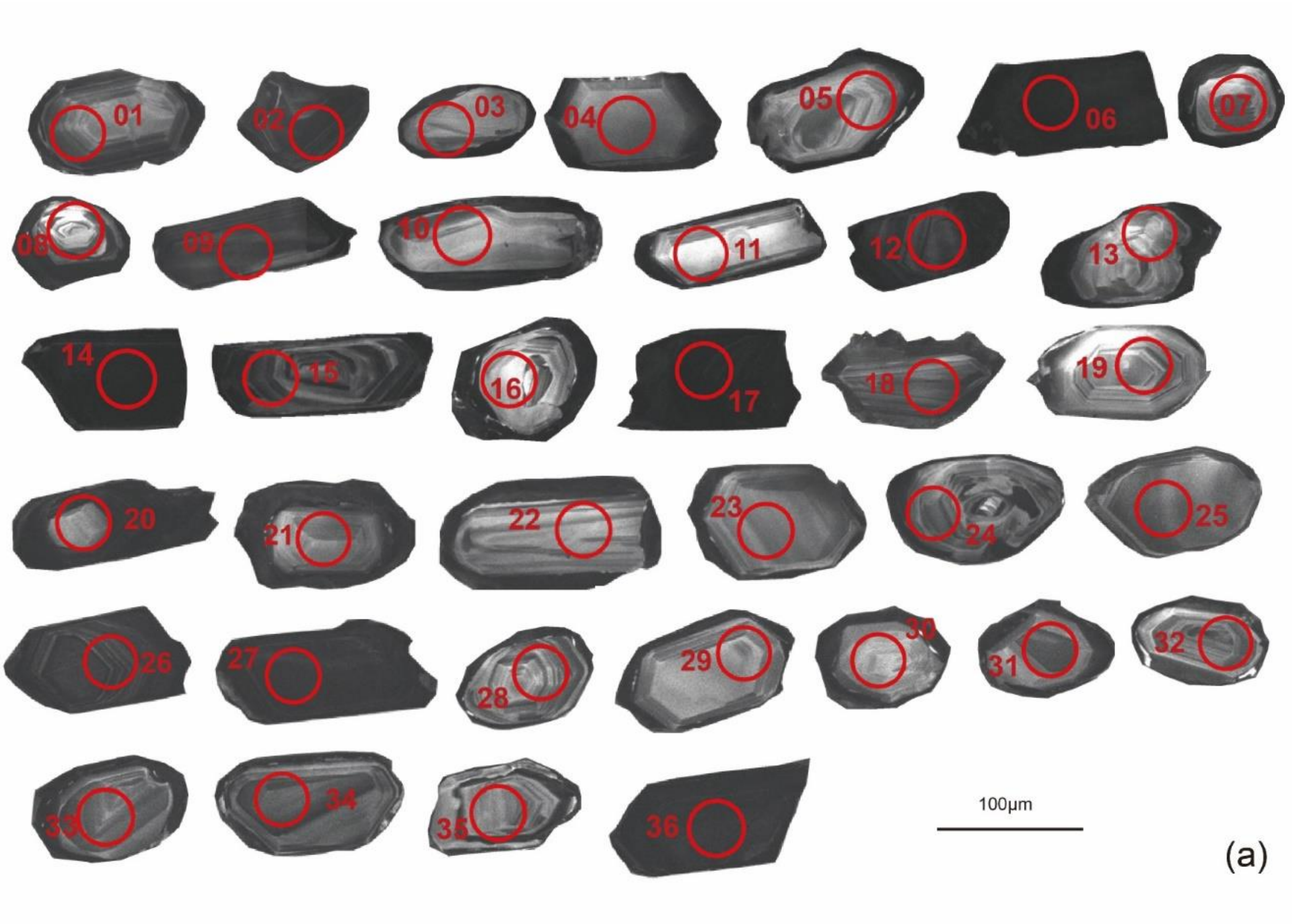
01
02
03
04
05
06
07
08
09
10
11
12
13
14
15
16
17
18
19
20
21
22
23
24
25
26
27
28
29
30
31
32
33
34
35
36
100μm
(a)

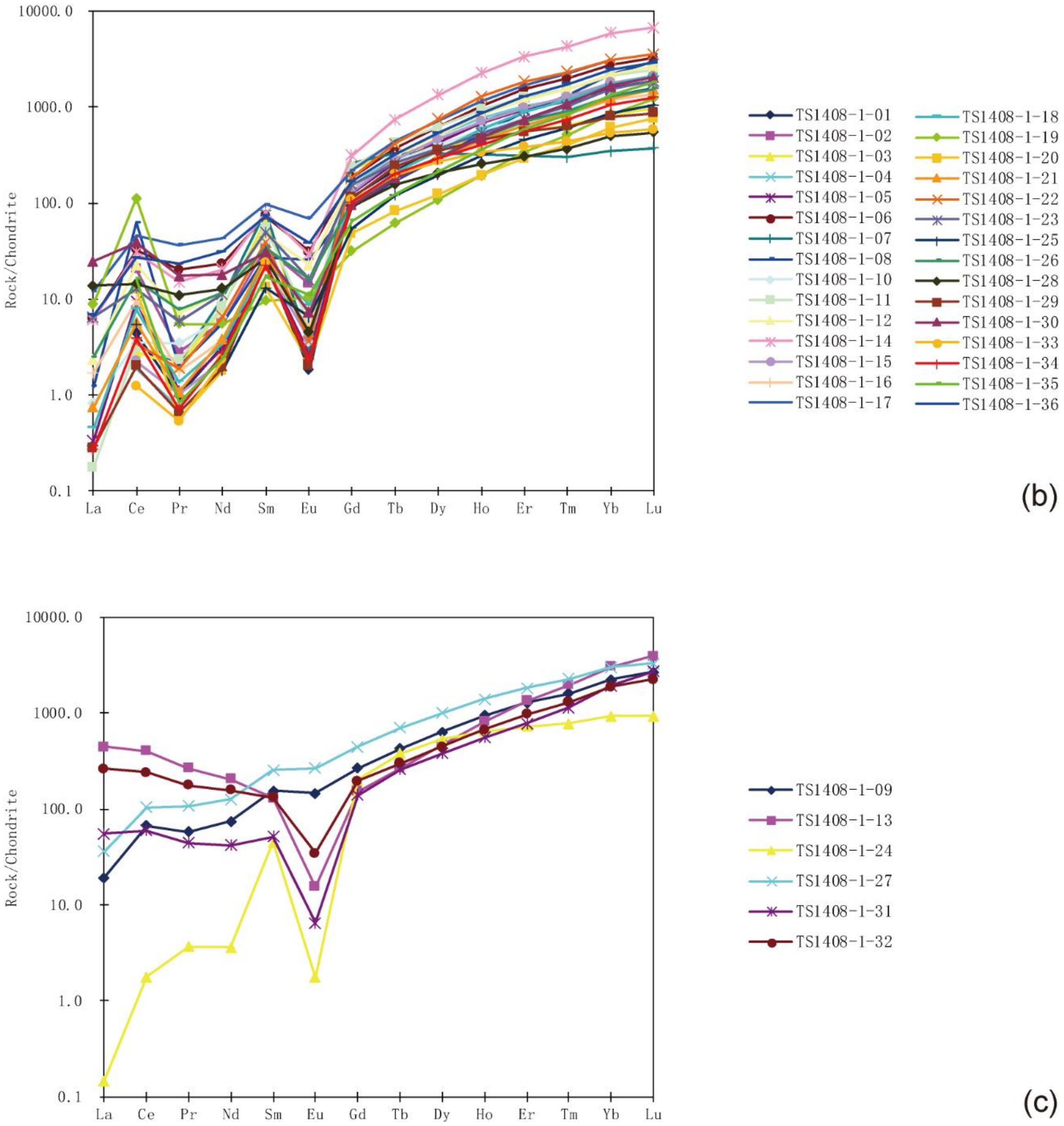

Figure E2 CL images and the REE pattern of TS1408-1.

(3) TS1408-2

The size of zircon grains is from 30μm to 100μm. Some zircons (e.g., Spot No.01, 02, 05) are subhedral to euhedral prismatic with length-to-width ratios ranging from 1.5 to 4, and some are rounded in shape (e.g., Spot No.21, 28, 30). Most of the zircons preserve xenocrystic magmatic cores with dark overgrowth rims (e.g., Spot No.02, 07, 08). The analyzed spots that exhibit magmatic oscillatory zoning are Spot No.01-10, 12-14, 17, 18, 20-24, 26-28, 30, 32 (Fig.E3a). Namely, according to the CL imaging, the analyzed spots that are not magmatic zircons are Spot No.11, 15, 16, 19, 25, 29, 31, 33-36.

Th/U ratios are between 0.01 and 0.64. Spot No.19, 31, 34 and 35 have Th/U ratios < 0.1 which may indicate a metamorphic origin.

Most analyses show a featured magmatic REE pattern with a steeply rising from LREE to HREE, a positive Ce-anomaly, and a negative Eu-anomaly, except Spot No.03, 15, 33, and 34 (Figs.E3b,c). Spot No.03, 15, 33 and 34 all show negative Eu-anomalies. Spot No. 03 and 33 are abundant in LREE, Spot No.15 is abundant in Ce and Pr, and Spot No.24 shows a negative Ce-anomaly.

Among all analyses, Spot No.03, 04, 29 and 33 show discordant ages, and will not be discussed further. According to CL imaging, Th/U ratio and REE pattern, analyzed spots that are considered as metamorphic ages are Spot No.11, 15, 16, 19, 25, 31, 34-36. These ages fall into several groups: 1704.8±38.32Ma (1 analysis, Spot No.25); 916~896.6Ma (2 analyses, Spot No.11, 15); 461.4~446.7Ma (4 analyses, Spot No.19, 31, 35, 36); 439.2±3.94Ma (1 analysis, Spot No.34); 384.7±3.3Ma (1 analysis, Spot No.16).

The magmatic ages can be divided into distinct groups:1236.6~1090.2Ma (4 analyses, Spot No.07, 18, 28, 30); 969~951.5Ma (4 analyses, Spot No.09, 10, 23, 26);

938.5~932.6Ma (2 analyses, Spot No.14, 21); 918~898.1Ma (2 analyses, Spot No.02, 08); 474.3±4.34Ma (1 analysis, Spot No.27); 458.3~443.3Ma (4 analyses, Spot No.05, 17, 22, 32); 439.1~423.3Ma (6 analyses, Spot No.01, 06, 12, 13, 20, 24). The weighted mean age of the youngest group is 430.9±5.8Ma (MSWD=2.1) and indicate the crystallization age of this dyke.

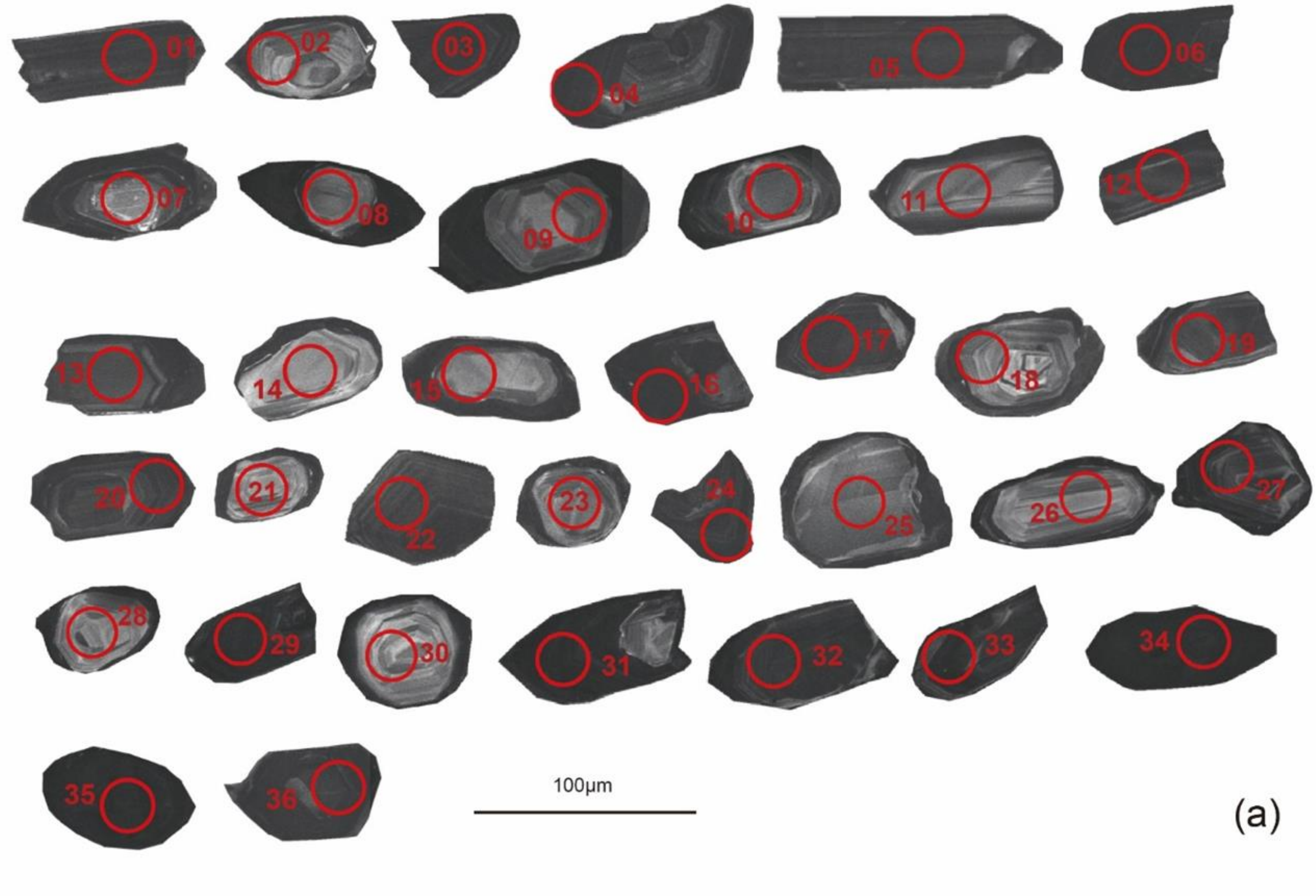
01
02
03
04
05
06
07
08
09
10
11
12
13
14
15
16
17
18
19
20
21
22
23
24
25
26
27
28
29
30
31
32
33
34
35
36
100μm
(a)

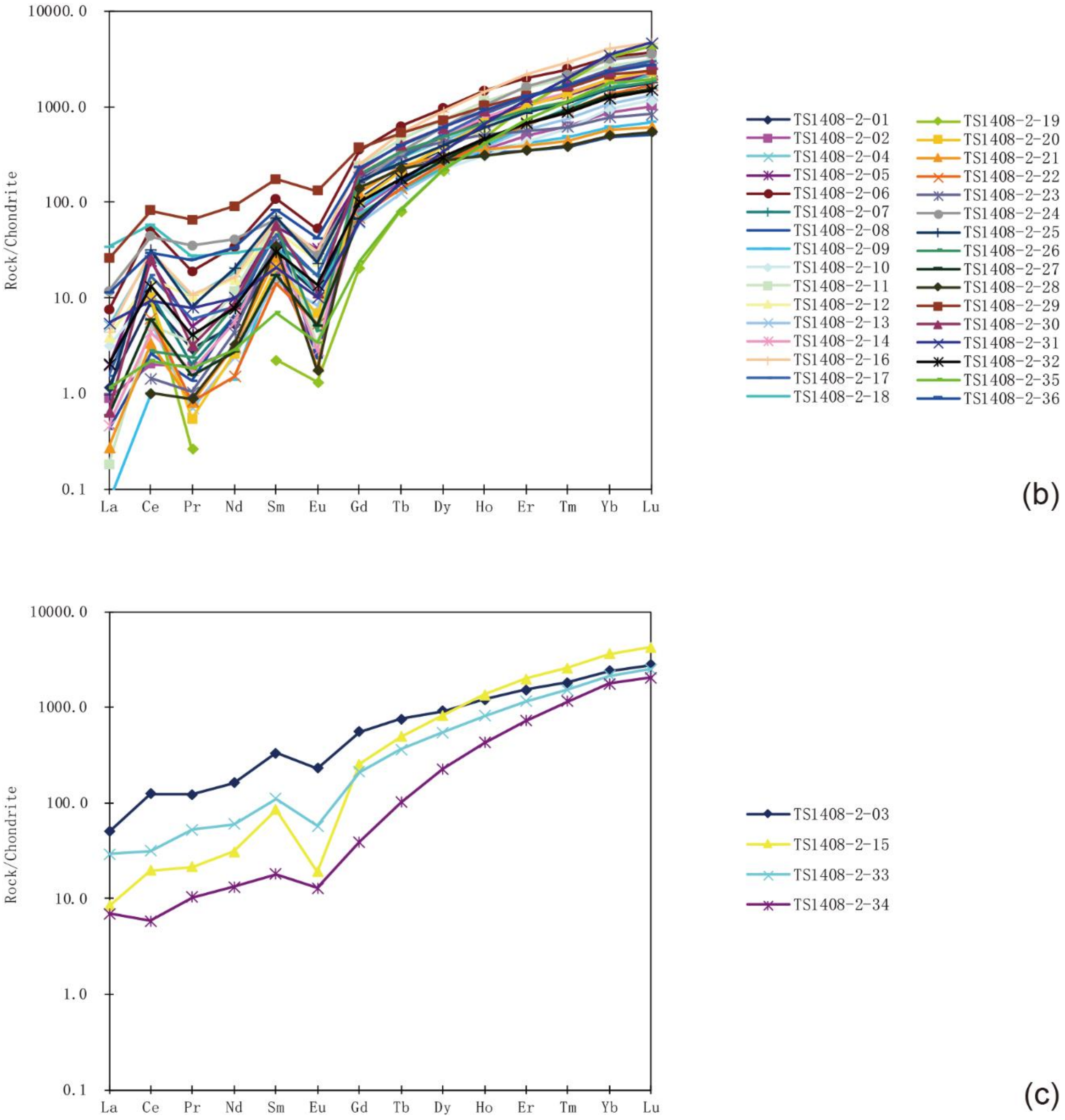

Figure E3 CL images and the REE pattern of TS1408-2.

2. Results from the Shetang area

(1) ST1502

CL images of analyzed zircons from ST1502 are in Fig.E4a. Most zircons are fragments of zircon grains. Even though they are fragments, the diameters of them are about 200 μm, so they are extremely large zircon grains. Most of the zircons show magmatic oscillatory zoning structures and medium to less luminescent. Spot No.04, 06, 16, 18, 20 and 27 show homogenous dark or grey domains that may result from metamorphism.

The Th/U ratios of these analyzed spots are in the range of 0.008~1.255. Spot No.03, 11, 22, 28 and 33 have Th/U ratios < 0.1.

Most of the analyzed spots show typical igneous REE pattern (Fig.E4b) with a positive Ce-anomaly, a negative Eu-anomaly and a steeply rising from LREE to HREE. Spot No.03, 07, 22 and 27 show different patterns. Spot No.03&07 do not show negative Eu-anomaly, and Spot No.07&27 are abundant in LREE (Fig.E4c).

Based on the features of CL image, Th/U ratio and REE pattern, the spots that are not magmatic origin are Spot No.03, 04, 06, 07, 11, 16, 18, 20, 22, 27, 28, 33. Among them, Spot No. 06&07 display discordant ages. Other metamorphic ages fall into distinct groups: 2488~2406.8Ma (4 analyses, Spot No.04, 18, 20, 27); 2173.2~2005.1Ma (2 analyses, Spot No.16, 22); 1890.1~1708.8Ma (4 analyses, Spot No.03, 11, 28, 33).

The magmatic zircons with concordant ages fall into several groups: 2514.6~2304.5Ma (20 analyses, Spot No.01, 02, 09, 10, 12-15, 17, 19, 23-26, 29-32, 34, 35); 2262.9~2254.4Ma (2 analyses, Spot No.15, 21); 1982±39.79Ma (1 analysis, Spot No.08). They are all xenocrystic ages.

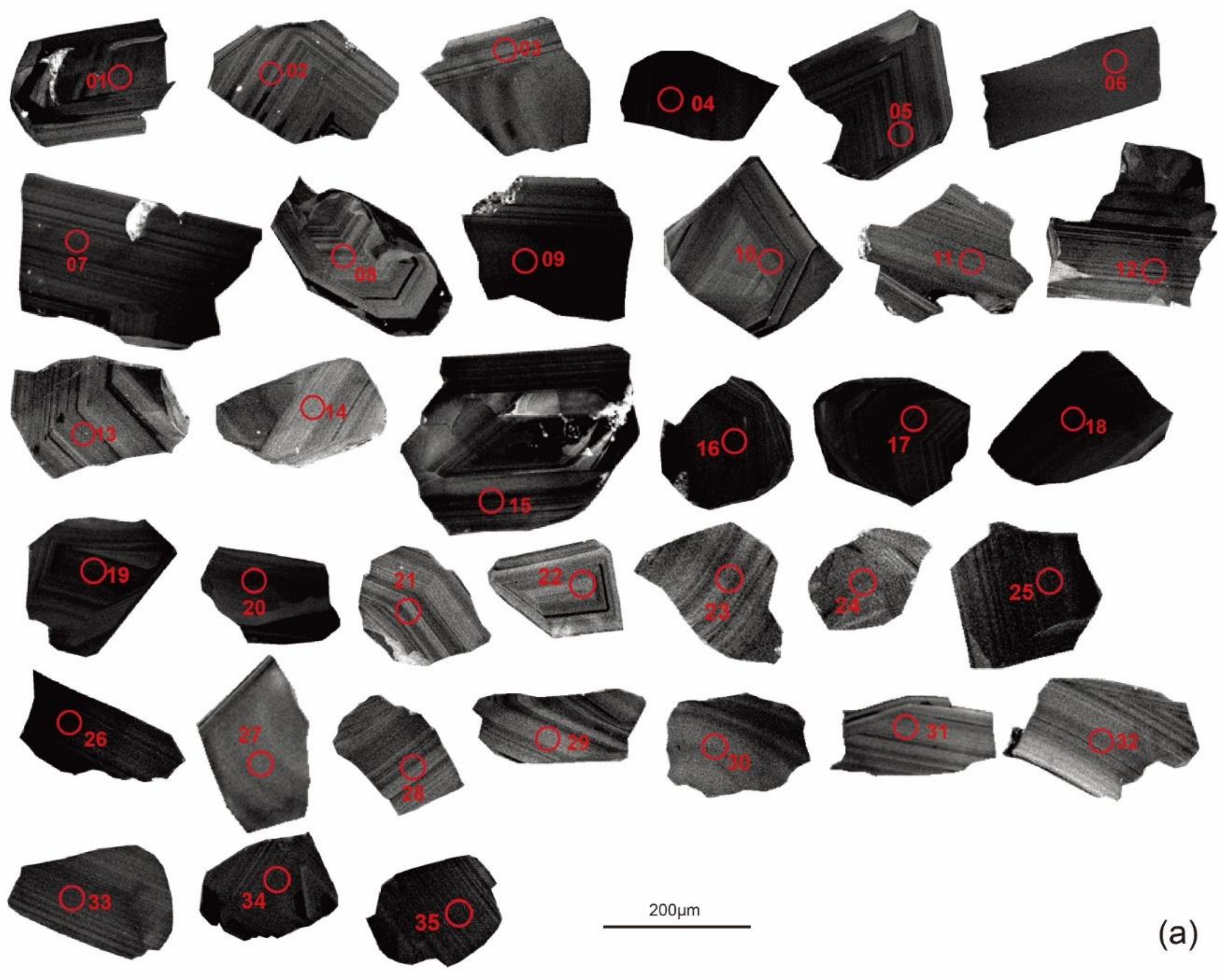
01
02
03
04
05
06
07
08
09
10
11
12
13
14
15
16
17
18
19
20
21
22
23
24
25
26
27
28
29
30
31
32
33
34
35
200μm
(a)

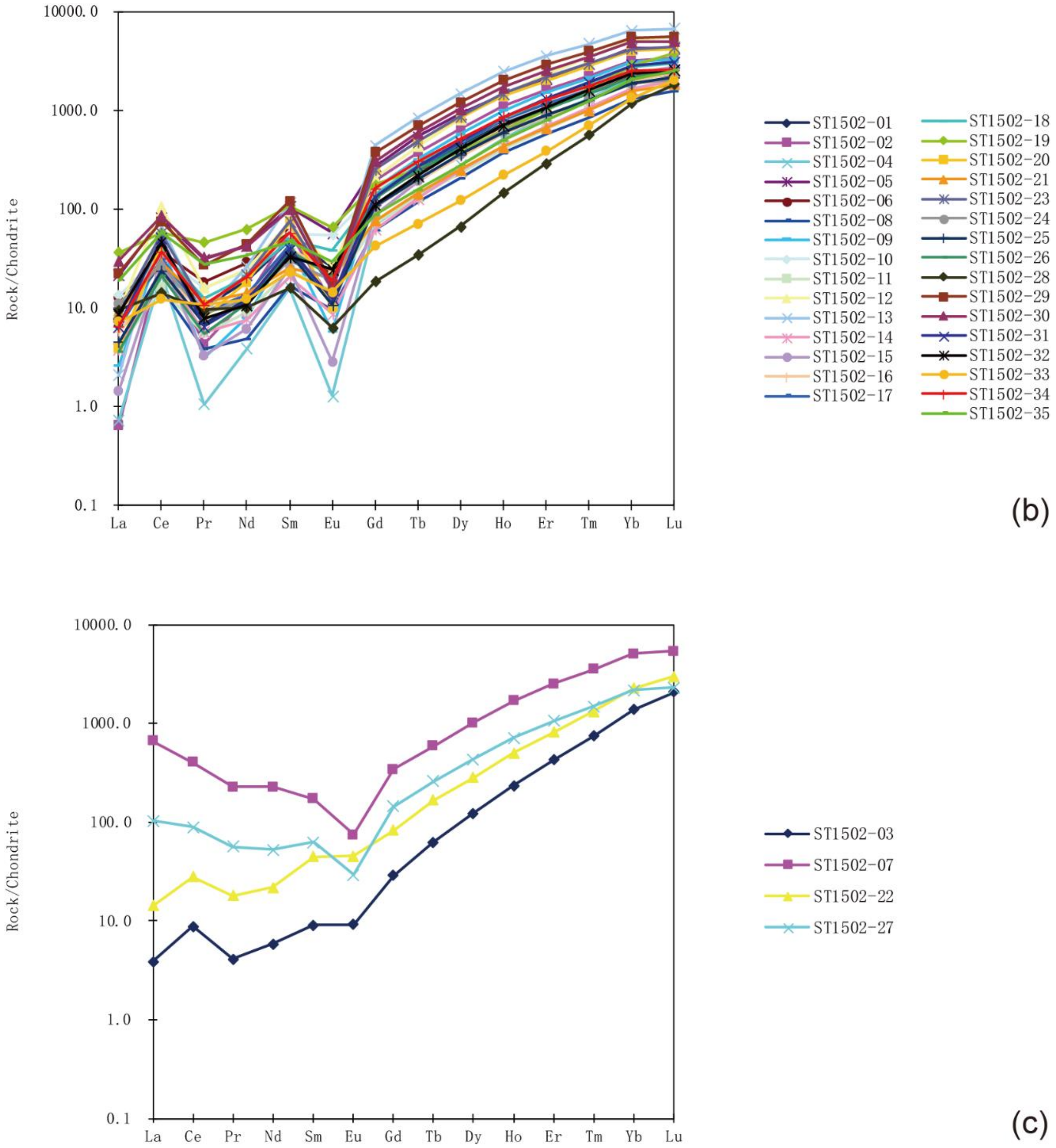

Figure E4 CL images and the REE pattern of ST1502.

(2) ST1510-1

Zircon grains from ST1510-1 are large, and the size is in the range of 150~250 μm (Fig.E5a). Most of them are subhedral to euhedral prismatic with length-to-width ratios ranging from 1.5 to 4. Most of the zircons show well-developed magmatic oscillatory zoning structures, and Spot No.01, 21 show typical magmatic sector zoning structures. Many of the grains show a magmatic core with a dark rim (Spot No.02, 05, 09, 10, 11, 12, 13&14, 15, 16, 27&28, 30, 31 and 33). Unfortunately, most of the rims are too thin to be measured. Only one dark rim is analyzed (Spot No.28), and its ^{207}Pb/^{206}Pb age is 2230.1±37.45Ma (disc.% = -30.9%). Instead of a dark rim, one grain shows a magmatic overgrowth (Spot No. 34&35) and one grain shows a weakly zoning rim with high luminescent (Spot No.26). Some zircons show no igneous oscillatory zoning (Spot No.04, 20, 24, 26, 31 and 32), and they may be metamorphic zircons.

The Th/U ratios range from 0.10 to 0.75.

Most REE patterns (Fig.E5b) show positive Ce-anomalies, negative Eu-anomalies and steeply-rising slopes from LERR to HERR, except for Spot No.05, 07, 09, 13, 34. Spot No.05&34 do not show negative Eu-anomaly, and Spot 07, 09, 13 are relatively abundant in LREE, especially, Spot No.13 (Fig.E5c).

In summary, the analyzed spots that may reflect metamorphic ages are Spot No.04, 05, 07, 09, 13, 20, 24, 26, 31-34. Spot No.26 is not concordant. The other metamorphic ages can be divided into the following groups: 2623.6±35.13Ma (1 analysis, Spot No.34); 2415.3~2352.1Ma (4 analyses, Spot No.05, 13, 20, 31); 2175.7±36.68Ma (1 analysis, Spot No.07); 1907.9~1821.9Ma (3 analysis, Spot No.09, 24, 33); 1753~1697.2Ma (2 analyses, Spot No.04, 32).

01
02
03
04
05
06
07
08
09
10
11
12
13
14
15
16
17
18
19
20
21
22
23
24
25
26
27
28
29
30
31
32
33
34
35
200μm
(a)

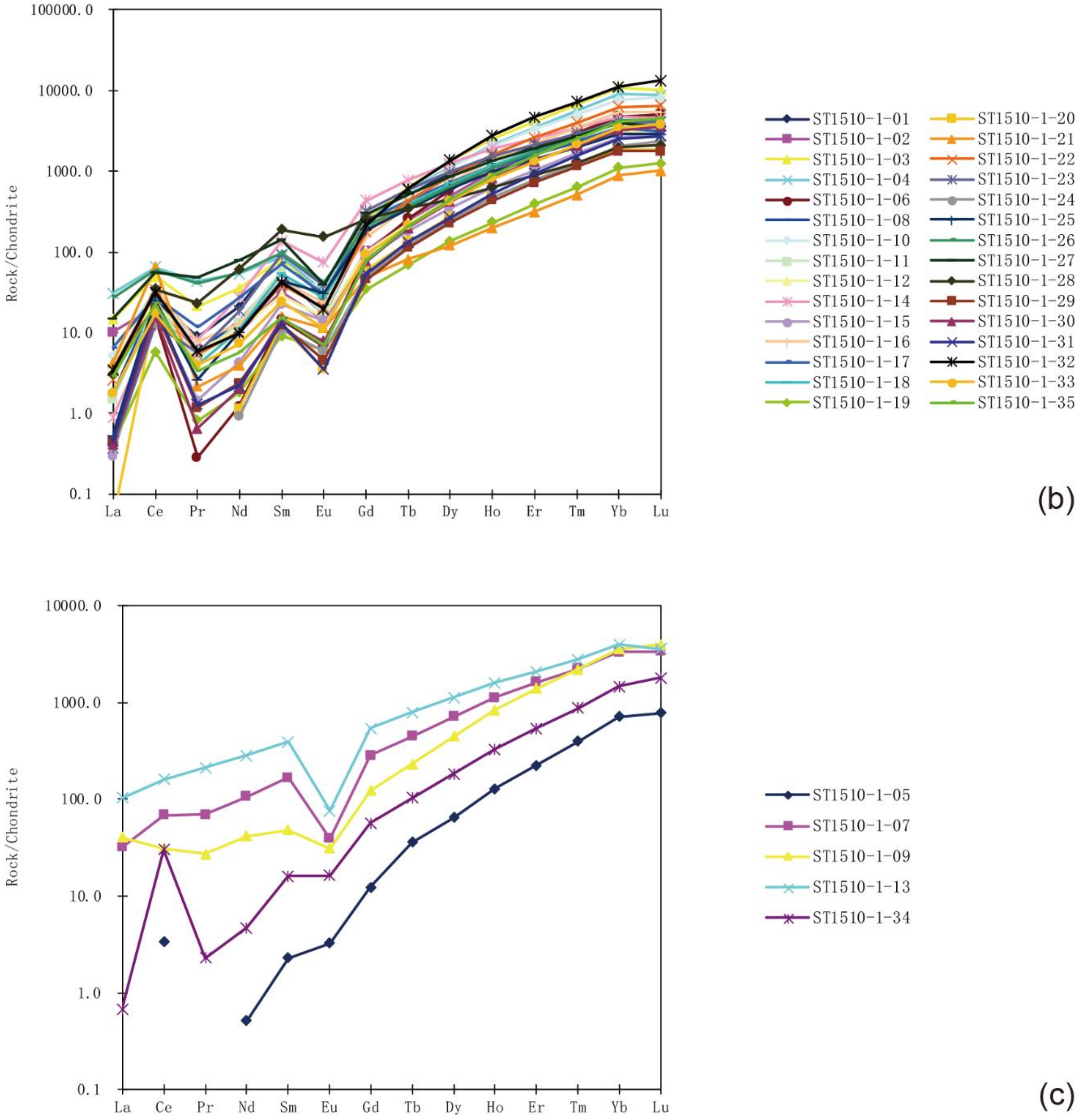

Figure E5 CL images and the REE pattern of ST1510-1.

The magmatic concordant ages can be grouped into distinct sets: 2639.8±33.67Ma (1 analysis, Spot No.21); 2430.7~2313.2Ma (8 analyses, Spot No.01, 08, 11, 14, 19, 23, 25, 29); 2193.4±40.56Ma (1 analysis, Spot No.17); 2095.7~2064Ma (2 analyses, Spot No.15, 17); 2031.6~1805.7Ma (6 analyses, Spot No.12, 16, 18, 22, 30, 35); 1788.7~1669.9Ma (3 analyses, Spot No.02, 06, 10). They are all xenocrystic ages.

(3) ST1510-2

Zircon grains (Fig.E6a) from ST1510-2 are 100~220 μm in size, and most of the grains are subhedral to euhedral prismatic with length-to-width ratios ranging from 1.5 to 4. Spot No.18, 27, 31 show rounded shapes. Most of them show a magmatic core with an extremely thin dark rim. The cores display well-developed igneous oscillatory zoning structures, and some of them show sector zoning structures. Spot No.05, 10, 12, 13, 18, 22, 26 and 34 show blurred primary zoning.

Th/U ratios are in the range of 0.10~0.66.

No.02, 17, 18 show REE patterns that differ from a typical igneous REE pattern. Spot No.02&18 are relatively abundant in LREE, and Spot No.17 is extremely abundant in LREE even close to HREE (Fig.E6c).

The spots that may reflect metamorphism are No.02, 05, 10, 12, 13, 17, 18, 22, 26 and 34. They fall into two groups: 1005~896.9Ma (2 analyses, Spot No.17, 34); 888.6~853.9Ma (8 analyses, Spot No.02, 05, 10, 12, 13, 18, 22, 26).

The concordant magmatic ages fall into several groups: 2272.4±35.24Ma (1 analysis, Spot No.19); 1020.6~1008Ma (5 analyses, Spot No.03, 07, 25, 29, 31); 996.5~868.5Ma (17 analyses, Spot No.04, 06, 08, 09, 11, 14-16, 20, 21, 23, 24, 28, 30, 32, 33, 35); 831.7±8.99Ma (1 analysis, Spot No.27). They are all xenocrystic ages.

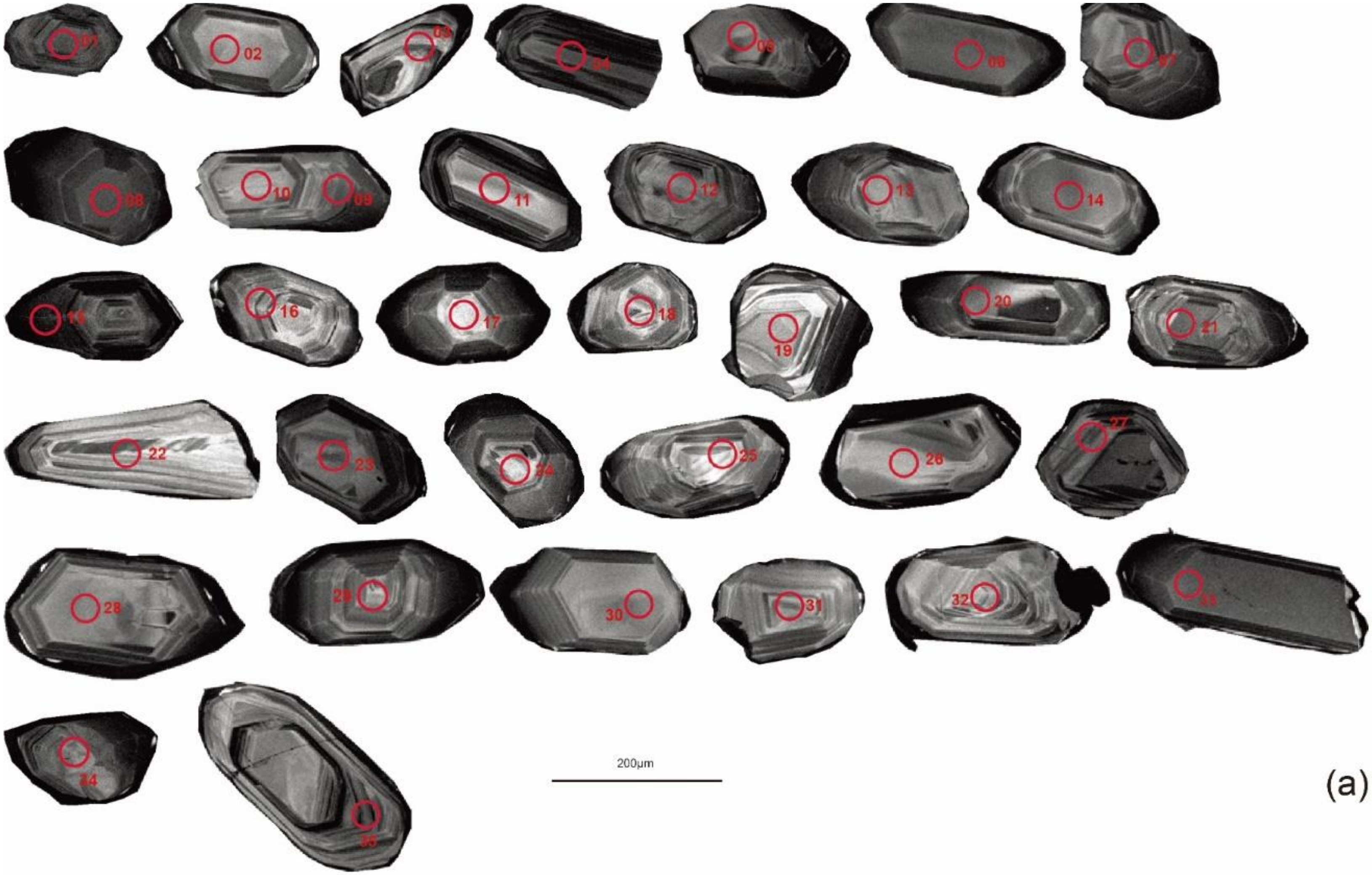
01
02
03
04
05
06
07
08
10
09
11
12
13
14
15
16
17
18
19
20
21
22
23
24
25
26
27
28
29
30
31
32
33
34
35
200μm
(a)

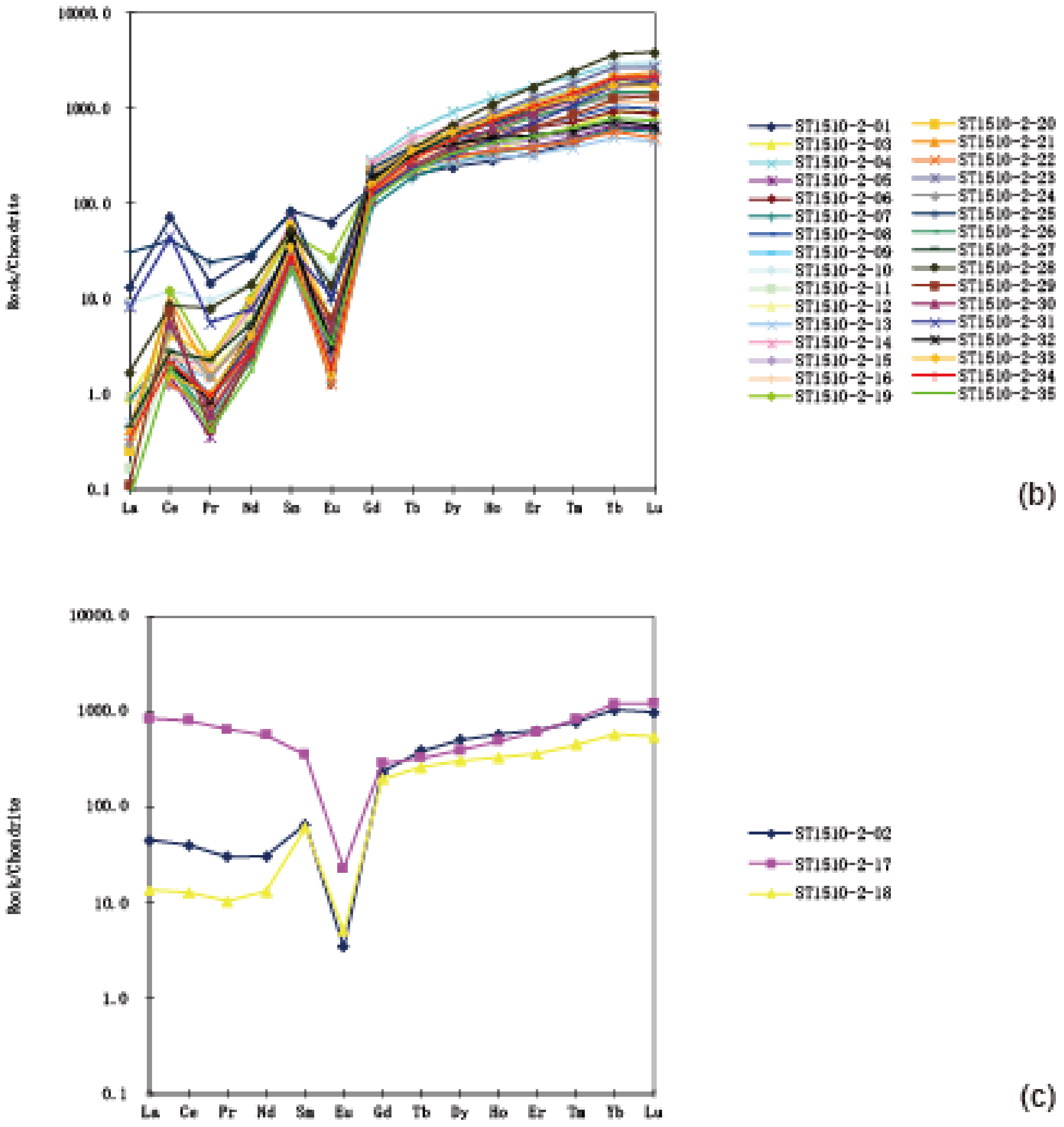

Figure E6 CL images and the REE pattern of ST1510-2.

(4) ST1511

The size of zircons in ST1511 is between 80μm and 200μm (Fig.E7a). Most of the grains are subhedral to euhedral prismatic with length-to-width ratios ranging from 1.5 to 3, and Spot No.17, 21, 22, 25-27 show rounded shapes. Most of the zircons show well-developed igneous oscillatory zoning and sector zoning structures. Some show blurred zoning or homogenous domain which may indicate metamorphic effect (Spot No.03, 12, 15, 16, 22, 24, 25, 31, 35).

Th/U ratios are in the range of 0.11~1.28. Spot No.18&27 have Th/U ratios > 1.

REE patterns of Spot No.02, 07, 08, 10-14, 17, 18, 21, 22, 26, 28, 29, 33 and 34 consist with the classical igneous REE pattern: a positive Ce-anomaly, a negative Eu-anomaly and a steeply rising slope from LREE to HREE (Fig.E7b). REE patterns of Spot No.01, 03-06, 09, 15, 16, 19, 24, 29, 30-32, 35 show the relative depletion of HREE resulting in shallower slopes. Spot No.25 shows abundance in Ce and Pr, and Spot No. 23&27 are relatively abundant in LREE (Fig.E7c).

The spots that may indicate metamorphic ages are Spot No.01, 03-06, 09, 12, 15, 16, 19, 23-25, 27, 29, 30-32, 35. Among them, the spots that yield concordant ages are Spot No.03-06, 09, 19, 25, 29, 30, 32, 35. They fall into several groups: 860±8.89Ma (1 analysis, Spot No.25); 832.7±11.34Ma (1 analysis, Spot No.29); 434.2~421.6Ma (9 analyses, Spot No.03-06, 09, 19, 25, 29, 30, 32, 35).

The concordant magmatic ages fall into following groups: 1507.3±15.75Ma (1 analysis, Spot No.34); 1364.8±13.76Ma (1 analysis, Spot No.26); 1045.8~1044Ma (2 analyses, Spot No.10, 28); 980.3~942Ma (4 analyses, Spot No.02, 18, 21, 22); 718.5±8.15Ma (1 analysis, Spot No.11); 428.9~420.5Ma (3 analyses, Spot No.14, 24, 33). The weighted mean age of the youngest group is 423.4±5.6Ma (MSWD=0.72) and may indicate the crystallization age of this dyke.


(a)
200μm
01
02
03
04
05
06
07
08
09
10
11
12
13
14
15
16
17
18
19
20
21
22
23
24
25
26
27
28
29
30
31
32
33
34
35

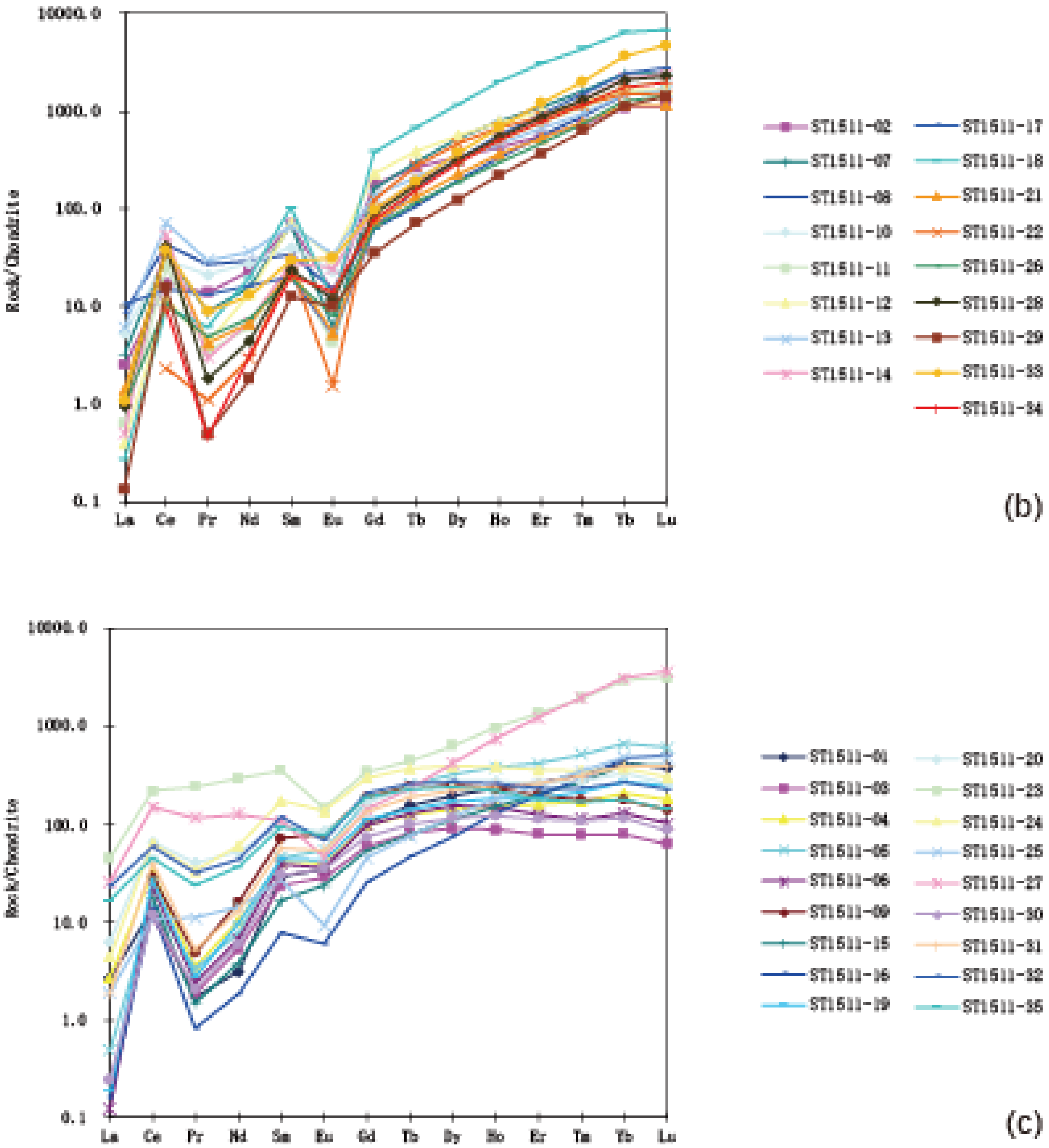

Figure E7 CL images and the REE pattern of ST1511.

(5) ST1515

The size of zircons in ST1515 ranges from 100 to 220 μm (Fig.E8a). Some of them show euhedral prismatic with length-to-width ratios ranging from 1.5 to 4 (e.g., Spot No.01, 12, 13, 21, 22), some are fragments (e.g., Spot No. 05, 09, 17), and some show rounded shapes (e.g., Spot No.04, 11, 15). Many of them show no or weak zoning structures, and several show oscillatory clearly zoning structures (Spot No.11, 12, 14, 21, 22, 25, 32-35). Namely, Spot No.01-10, 13, 15-20, 23, 24, 26-31 may reflect metamorphism.

Th/U ratios of all analyzed spots in ST1515 are in the range of 0.04~0.44. Spot No.01-10, 12, 15, 17, 18, 21-24, 26-28, 30, 32 and 34 have Th/U ratios < 0.1.

Spot No.02, 05-11, 14-17, 19, 25-28, 30, 31, 33, 34 show REE patterns that are characterized by positive Ce-anomalies, negative Eu-anomalies and steeply rising slopes from LREE to HREE (Fig.E8b). Spot No.01, 03, 04, 12, 13, 18, 20-24, 29, 32, 35 show different patterns. Spot No.03, 04, 12, 18, 20-24, 29 and 35 are abundant in both Ce and Pr, and Spot No. 01 and 13 are relatively abundant in La and Ce, and Spot No. 32 is abundant in Pr but not Ce (Fig.E8c).

There are many metamorphic ages in this sample. They are Spot No.01-10, 12, 13, 15-24, 26-32, 34, 35. Excluding the discordant ages, the remaining ages fall into the following groups: 863.8~846.9Ma (4 analyses, Spot No.13, 16, 29, 31); 775.1±8.96Ma (1 analysis, Spot No.35); 444.5~442.7Ma (2 analyses, Spot No.01, 23); 412.8~381.2Ma (18 analyses, Spot No.02, 04-10, 15, 17, 19, 24, 26-28, 30, 32, 34); 343.6±3.75Ma (1 analysis, Spot No.22).

There are only four magmatic ages, and they fall into three groups: 871.2~870.2Ma (2 analyses, Spot No.14, 33); 770.7±8.25Ma (1 analysis, Spot No.11); 391.3±4.21Ma (1 analysis, Spot No.33). The youngest age may indicate the crystallization age of this dyke (i.e., 391.3±4.21Ma).

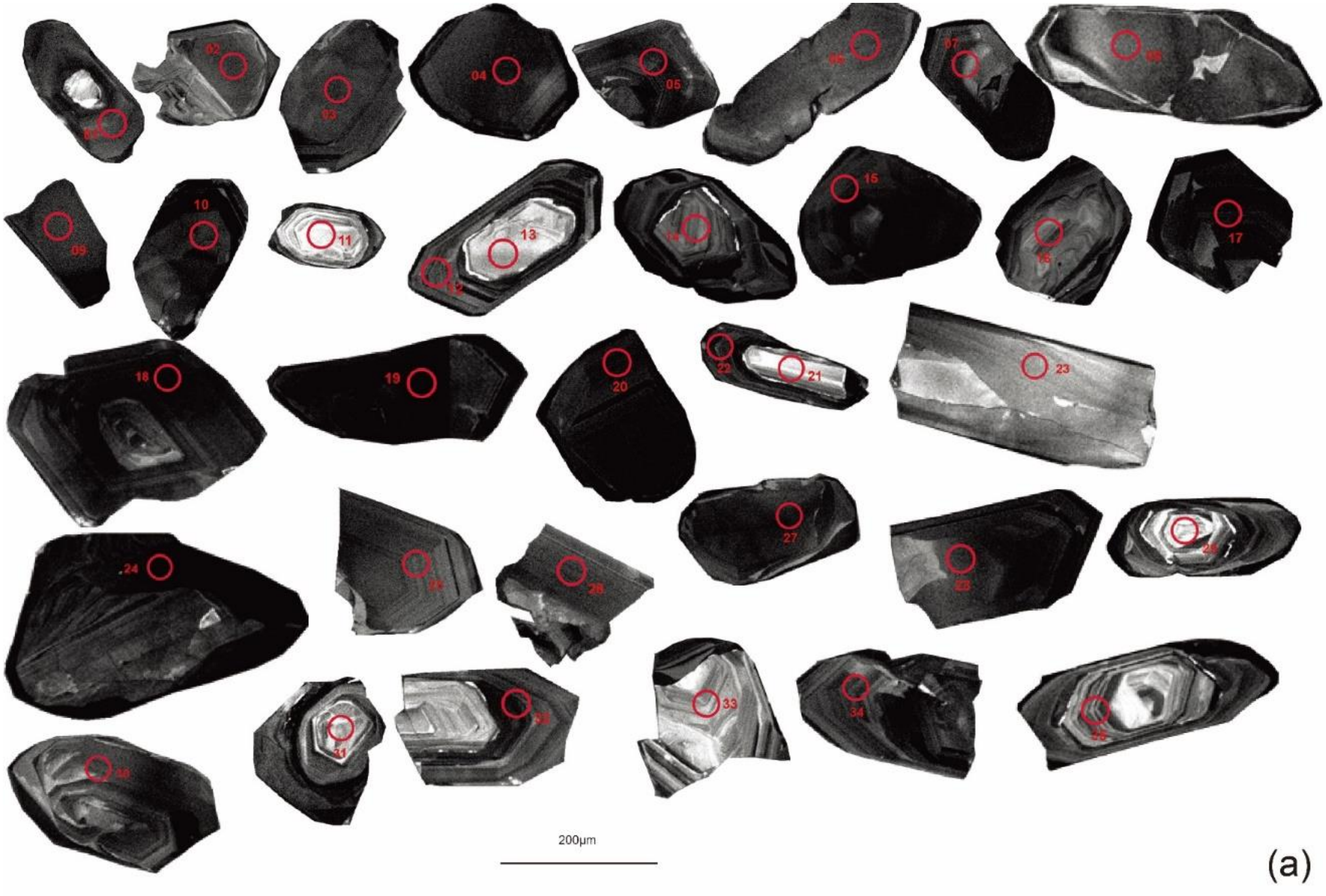
01
02
03
04
05
06
07
08
09
10
11
12
13
14
15
16
17
18
19
20
21
22
23
24
25
26
27
28
29
30
31
32
33
34
35
200μm
(a)

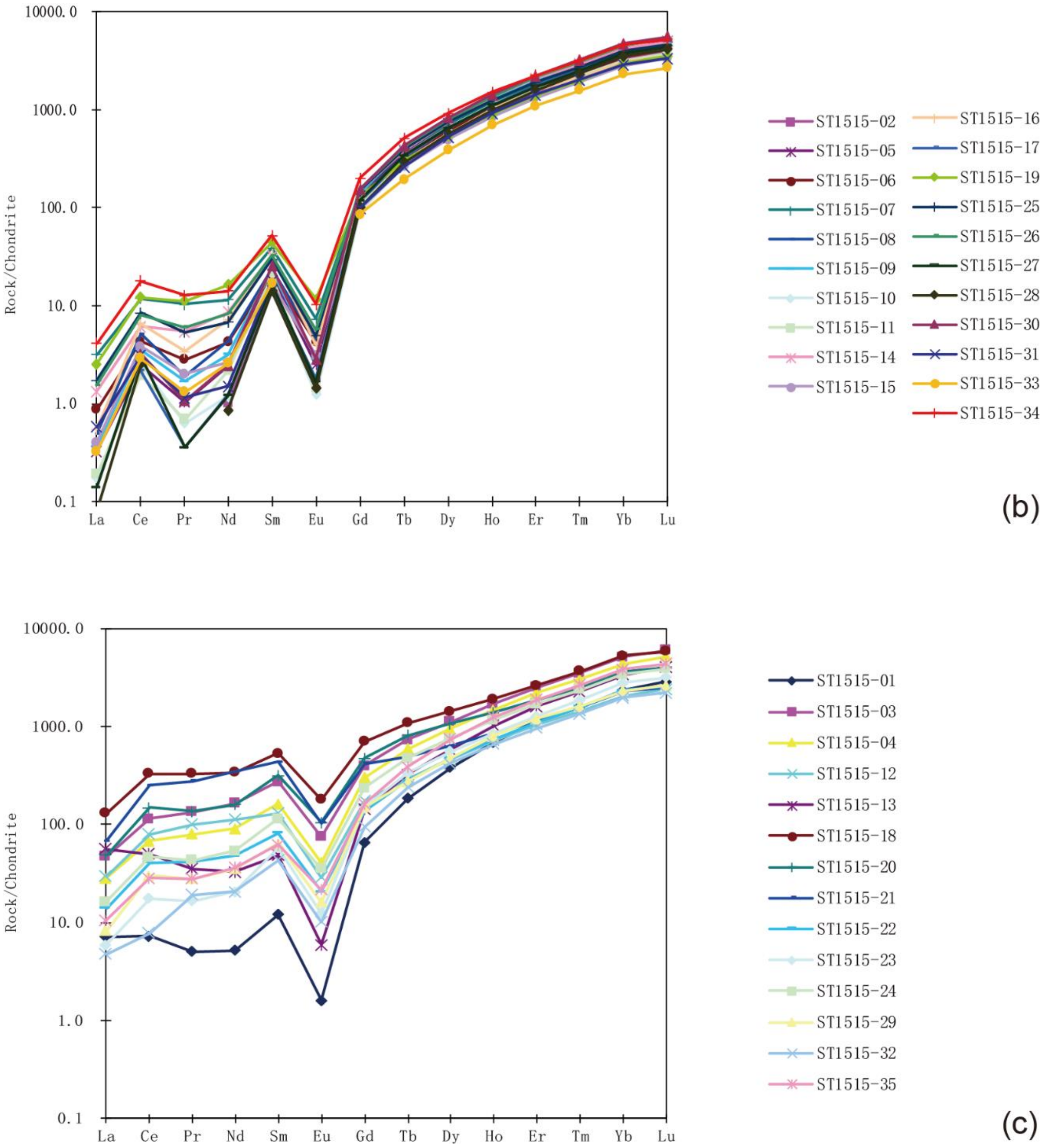

Figure E8 CL images and the REE pattern of ST1515.

(6) ST1512

The longest dimension of the zircon grains in ST1512 ranges from 50μm to 200μm (Fig.E9a). Some of them show subhedral to euhedral prismatic with length-to-width ratios ranging from 1.5 to 4 (e.g., Spot No.01, 04, 05, 10), and some are rounded in shape (e.g., Spot No.08, 24, 35). Some of them show well-developed igneous oscillatory zoning structures, and others show blurred zoning or homogenous domain (Spot No.04, 06, 08, 09, 13, 15, 17, 27, 35).

Th/U ratios are in the range of 0.13~0.95.

Most REE patterns are consistent with the typical igneous zircon showing a steeply rising from LREE to HREE, a positive Ce-anomaly and a negative Eu-anomaly (Fig.E9b). Spot No.33 shows a drop from MREE to HREE, and Spot No.08, 17, 20 are relatively abundant in LREE (Fig.E9c).

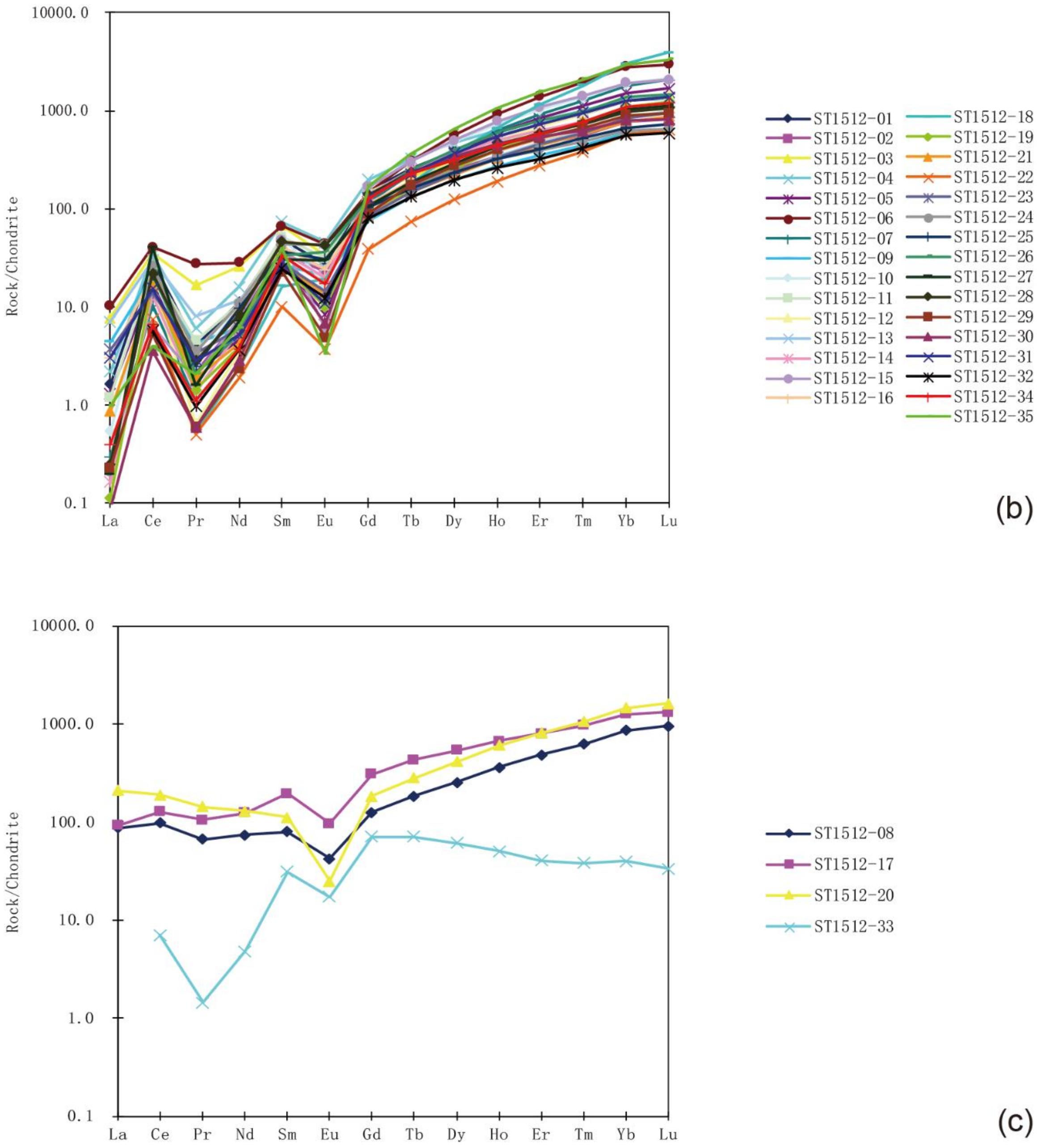

Figure E9 CL images and the REE pattern of ST1512.

The concordant metamorphic ages can be divided into the following groups: 1157±13.53Ma (1 analysis, Spot No.15); 956.4±10.08Ma (1 analysis, Spot No.35); 428.9~421.3Ma (2 analyses, Spot No.20, 33); 408.8±6.67Ma (1 analysis, Spot No.13).

The concordant magmatic ages fall into three groups: 950±13.18Ma (1 analysis, Spot No.18); 440±7.53Ma (1 analysis, Spot No.25); 429~416Ma (21 analyses, Spot No.01, 02, 04, 05, 07, 11, 12, 14, 16, 19, 22-24, 26, 28-32, 34).

(7) ST1513

Zircons from ST1513 vary in size. The longest dimension ranges from 30μm to 200μm (Fig.E10a). Most of them are subhedral to euhedral prismatic in shape, and the length-to-width ratio ranges from 1.5 to 4.5, and others are either fragments (e.g., Spot No.04, 12) or rounded in shape (e.g., Spot No.05, 13). About half of them show igneous oscillatory zoning structures, and others show no or weakly zoned characteristic (Spot No.03-05, 07, 10-13, 15, 17-20, 23, 30, 33, 35).

The Th/U ratio ranges from 0.02 to 1.48. Spot No.12, 20, 23 have Th/U ratios < 0.1.

Spot No.02, 10, 15, 23 show abnormal REE patterns. Spot No.02, 10, 15 are relatively abundant in LREE, and Spot No.23 is relatively depleted in HREE (Figs.E10b,c).

In summary, the analyzed spots that may reflect metamorphism are Spot No.02-05, 07, 10-13, 15, 17-20, 23, 30, 33 and 35. Excluding discordant ages, the metamorphic ages can be grouped into the following sets: 2082.7±40.31Ma (1 analysis, Spot No.17); 1743.2±38.21Ma (1 analysis, Spot No.35); 957.6±15.21Ma (1 analysis, Spot No.03); 845.6~817.8Ma (2 analyses, Spot No.10,13); 646.3±6.74Ma (1 analysis, Spot No.11); 434.5~420.7Ma (3 analyses, Spot No.04,12,23); 405.3±5.03Ma (1 analysis, Spot No.18).

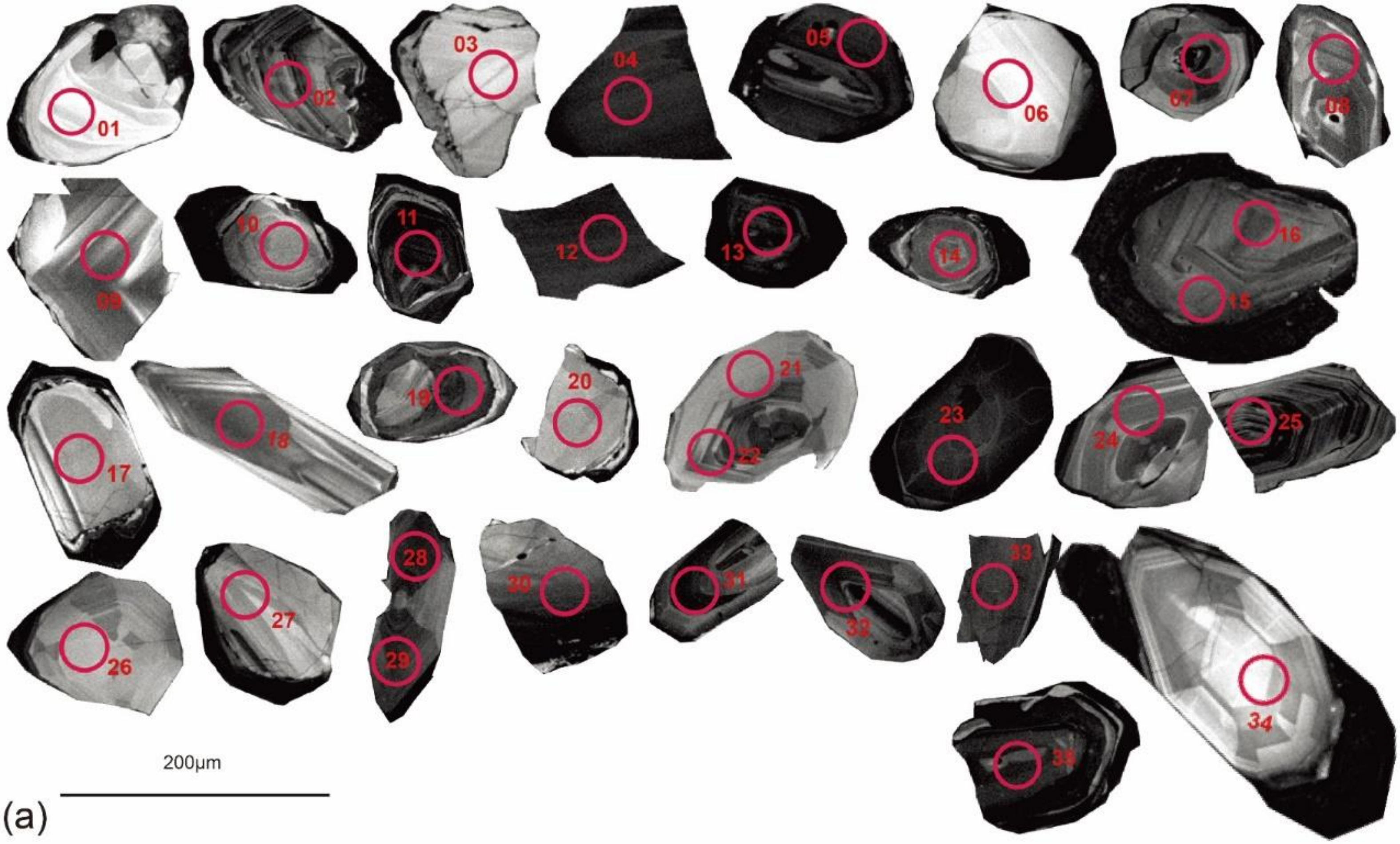
01
02
03
04
05
06
07
08
09
10
11
12
13
14
15
16
17
18
19
20
21
22
23
24
25
26
27
28
29
30
31
32
33
34
35
200µm
(a)

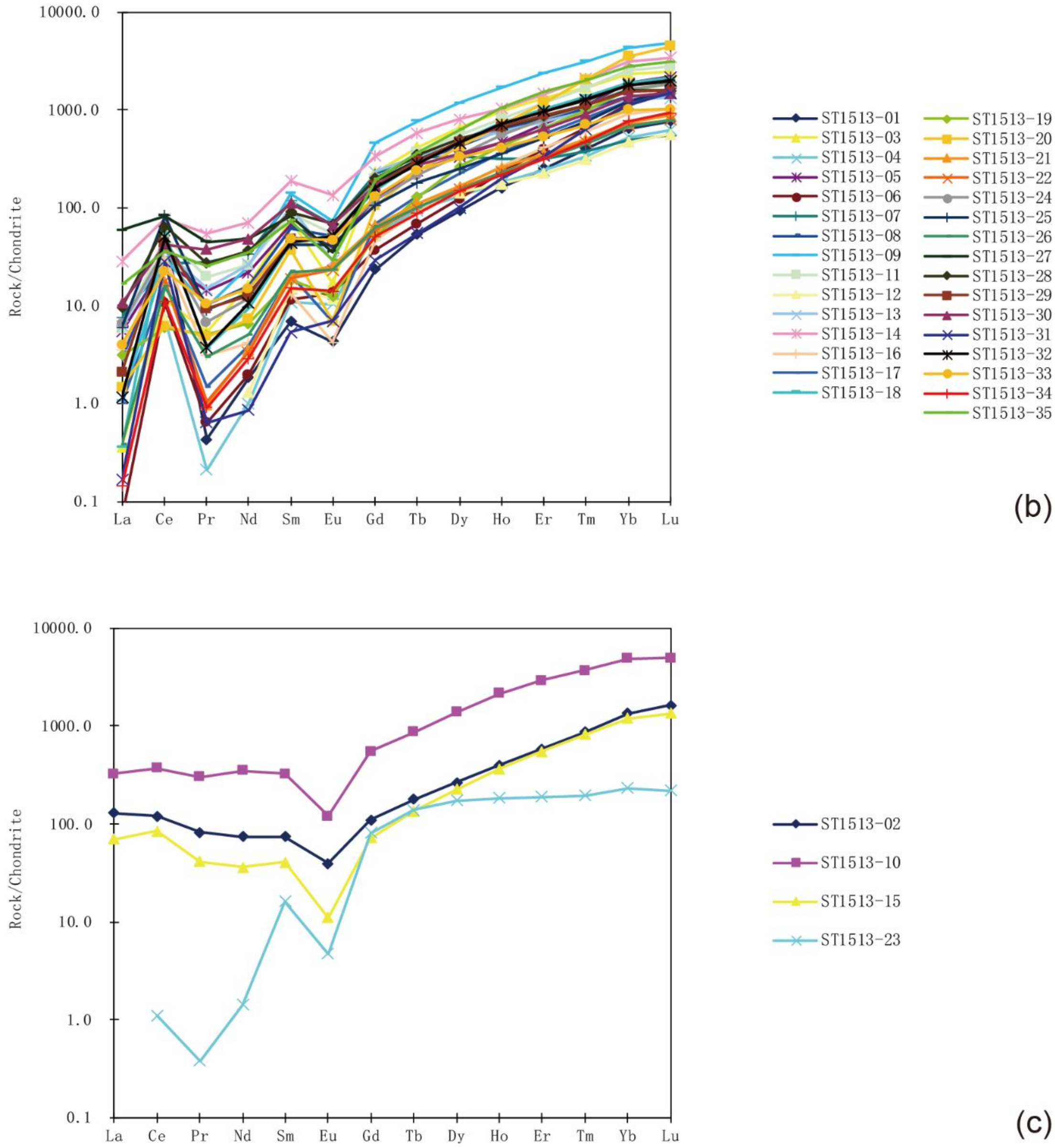

Figure E10 CL images and the REE pattern of ST1513.

The concordant magmatic ages fall into the following groups: 2485.3~2484.8Ma (2 analyses, Spot No.01, 16); 970.4~940.1Ma (2 analyses, Spot No.06, 09); 443.1±7.34Ma (1 analysis, Spot No.26); 425.6~403.3Ma (6 analyses, Spot No.08, 21, 22, 24, 25, 32).

ST1512 and ST1513 are two samples from a granitoid body. The weighted mean average magmatic ages of youngest groups in ST1512 and ST1513 are 424.9±2.2Ma and 417±11Ma, respectively (Fig.E11). The formation of this granitoid body corresponds to the early Paleozoic granitoids in the north Qinling belt.

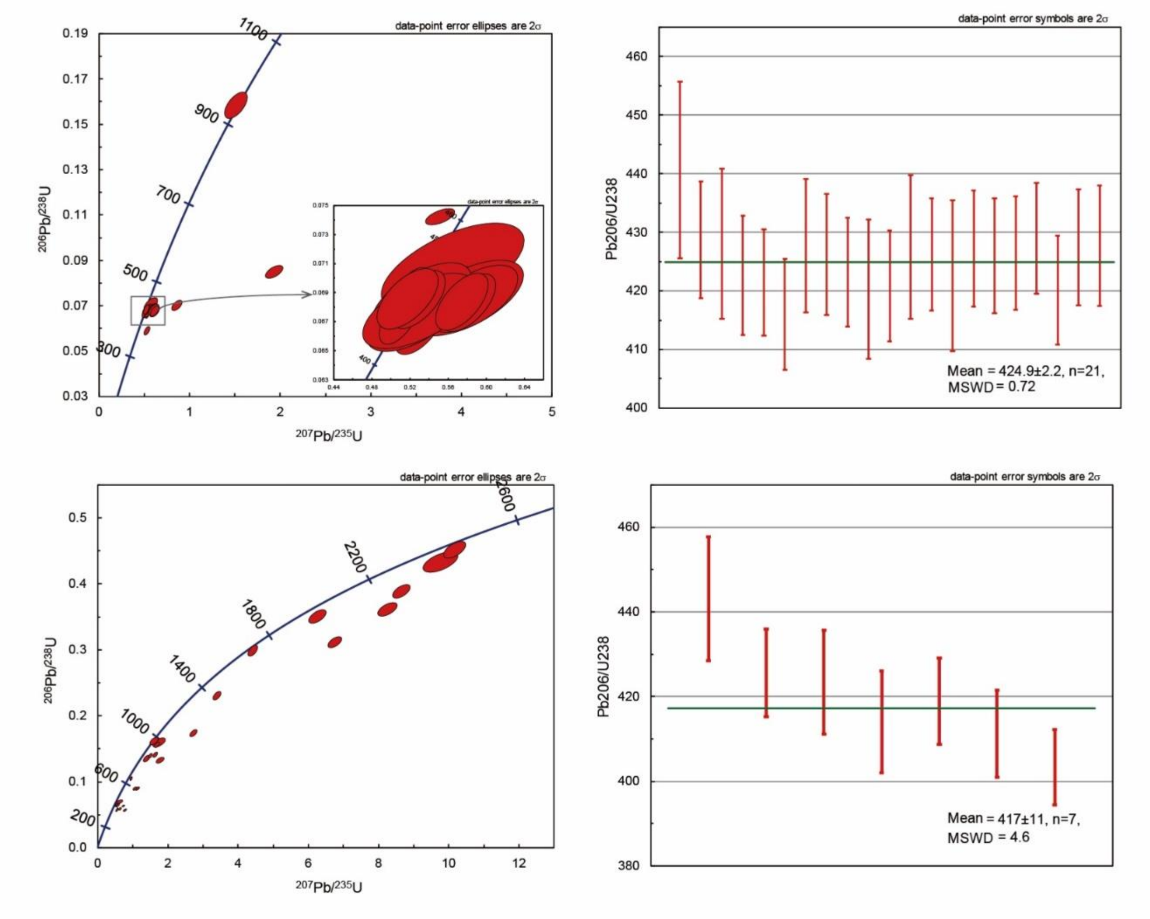

Figure E11 Concordia diagrams and weighted mean ages of TS1512 and TS1513, respectively.

3. Results from the Xinyang area
   (1) XY1605

Zircons in XY1605 vary in size, and the size ranges from 20μm to 150μm (Fig.E12a). Some grains are subhedral and euhedral prismatic (e.g., Spot No.07, 08, 10, 11, 15), and some are equant forms (e.g., Spot No.23, 26, 27, 28), and some are fragments (e.g., Spot No.04, 20, 25, 37). Some zircons show igneous zoning (e.g., Spot No.01, 10, 11, 12), and others show blurred zoning or no zoning (Spot No.06, 17-19, 30, 32, 34, 35, 38-42, 44-46, 48, 51-54).

Th/U ratios are between 5.37 and 0.03. Spot No.32, 42, 51, 52 have Th/U ratios < 0.1.

Spot No.02, 32, 34, 42, 46, 48, 50, 52 show abnormal patterns. Spot No.02, 34, 50 are abundant in LREE, and Spot No.32, 42, 46, 52 are depleted in HREE, and Spot No.48 shows a positive Eu-anomaly instead of a negative one (Figs.E12b,c).

In summary, metamorphic ages are Spot No.02, 06, 17-19, 30, 32, 34, 35, 38-42, 44-46, 48, 50-54. The concordant ages fall into several groups: 2185.1±36.45Ma (1 analysis, Spot No.44); 1952.7±50.07Ma (1 analysis, Spot No.19); 1148.3±12.49Ma (1 analysis, Spot No.41); 997.1~888.8Ma (4 analyses, Spot No.17, 30, 35, 45); 509.8~504.7Ma (3 analyses, Spot No.48, 51, 52); 499.2~484.7Ma (4 analyses, Spot No.32, 39, 40, 42); 455.1±5.59Ma (1 analysis, Spot No.38); 439.3±6.05Ma (1 analysis, Spot Mo.53).

The concordant magmatic ages can be divided into the following groups: 1769.8±39.99Ma (1 analysis, Spot No.24); 1501.9Ma (1 analysis, Spot No.05); 1089.8~1002 (3 analyses, Spot No.01, 07, 14); 999.5~882.6Ma (3 analyses, Spot No.04, 29, 49); 844.9~604.1 (3 analyses, Spot No.16, 25, 26); 490.3±7.03Ma (1 analysis, Spot No.47); 467.1~462.8 (2 analyses, Spot No.55, 56); 451~447.6Ma (3

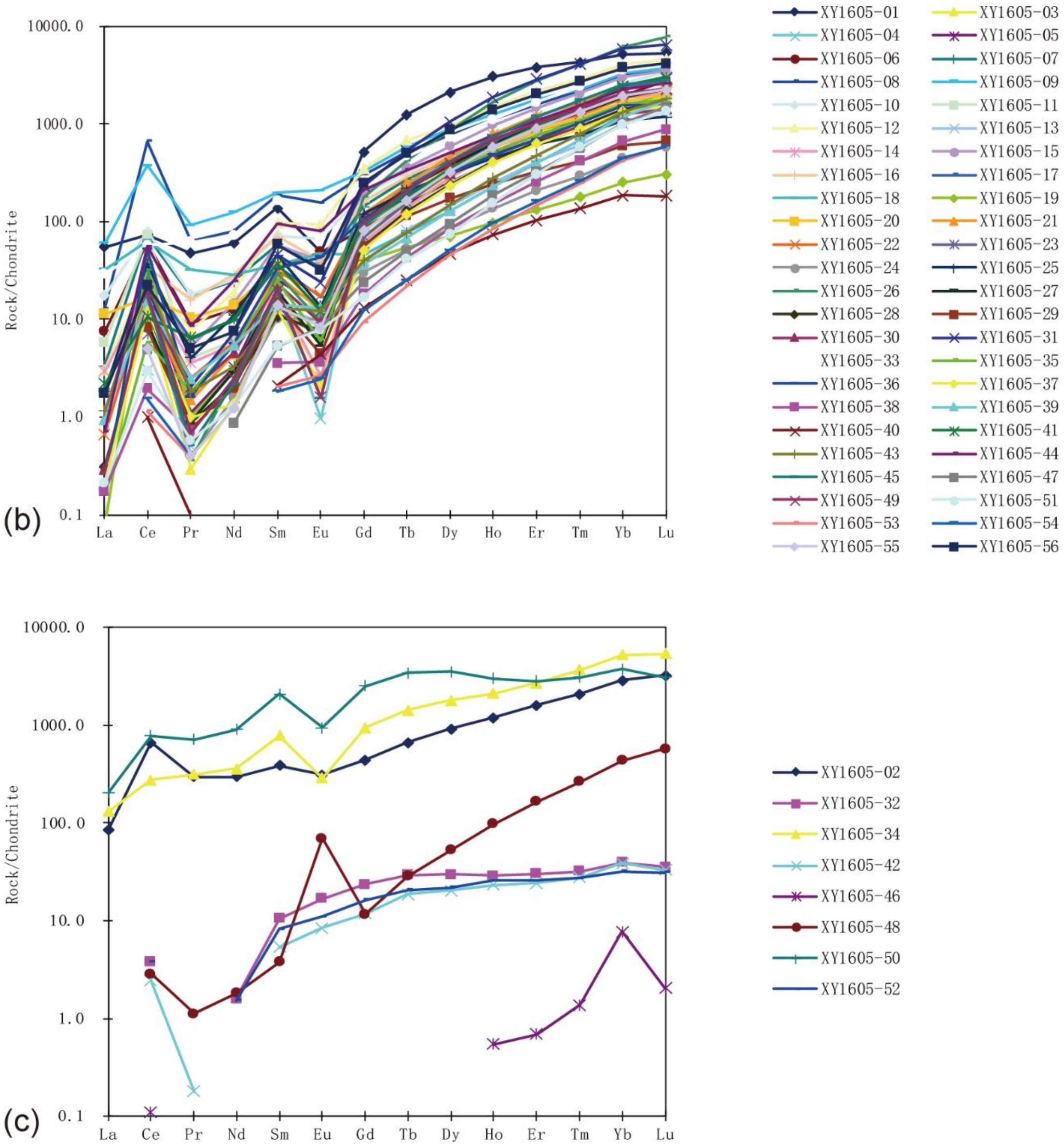

Figure E12 CL images and the REE patterns of XY1605.

analyses, Spot No.13, 21, 22); 441.6±4.02Ma (1 analysis, Spot No.23); 423.3±4.89Ma (1 analysis, Spot No.33); 408.1~405.5 (2 analyses, Spot No.31, 37); 374.6±4.7Ma (1 analysis, Spot No.03); 357.9±4.53Ma (1 analysis, Spot No.37); 234.5±2.98Ma (1 analysis, Spot No.15); 212.5±2.12Ma (1 analysis, Spot No.11); 201.8±2Ma (1 analysis, Spot No.10). The youngest age may indicate the crystallization age of this dyke (i.e., 201.8±2Ma).

(2) XY1601A

The shape and size of zircon grains in XY1601A are variable (Fig.E13a). The size ranges from 20μm to 150μm. Some are subhedral and euhedral prismatic in shape with variable length-to-width ratios. For example, Spot No.17 is needle-shaped, while Spot No.01 is equant, and Spot No.22 lies in the middle. Some are fragments (e.g., Spot No.05, 06, 11). There is no well-developed oscillatory zoning in these grains. Spot No.01, 07, 18 show weak zoning, and others show blurred zoning or homogenous domain.

Th/U ratios are between 1.71 and 0.01. Spot No.01, 10, 28 and 31 have Th/U ratios < 0.1.

Spot No.01, 04, 08, 10, 17, 20, 26 and 31 display abnormal REE patterns. Spot No.08, 17 are abundant in LREE, while Spot No.01, 04, 20, 26 are depleted in HREE, and Spot No.10 does not show positive Ce-anomaly and negative Eu-anomaly, and Spot No.31 does not show positive Ce-anomaly (Figs.E13b,c).

The concordant metamorphic ages can be divided into the following groups: 865.4±9.39Ma (1 analysis, Spot No.03); 1624.4~1412.5Ma (3 analyses, Spot No.15, 16, 22); 524.3~520.2Ma (2 analyses, Spot No.06, 20); 503.3~479Ma (4 analyses, Spot No.05, 24, 27, 30); 471.2~470.4Ma (3 analyses, Spot No.11, 19, 21); 454.4~453.9Ma (2 analyses, Spot No.10, 32); 432.8±5.96Ma (1 analysis, Spot No.09); 344.3±5.77Ma

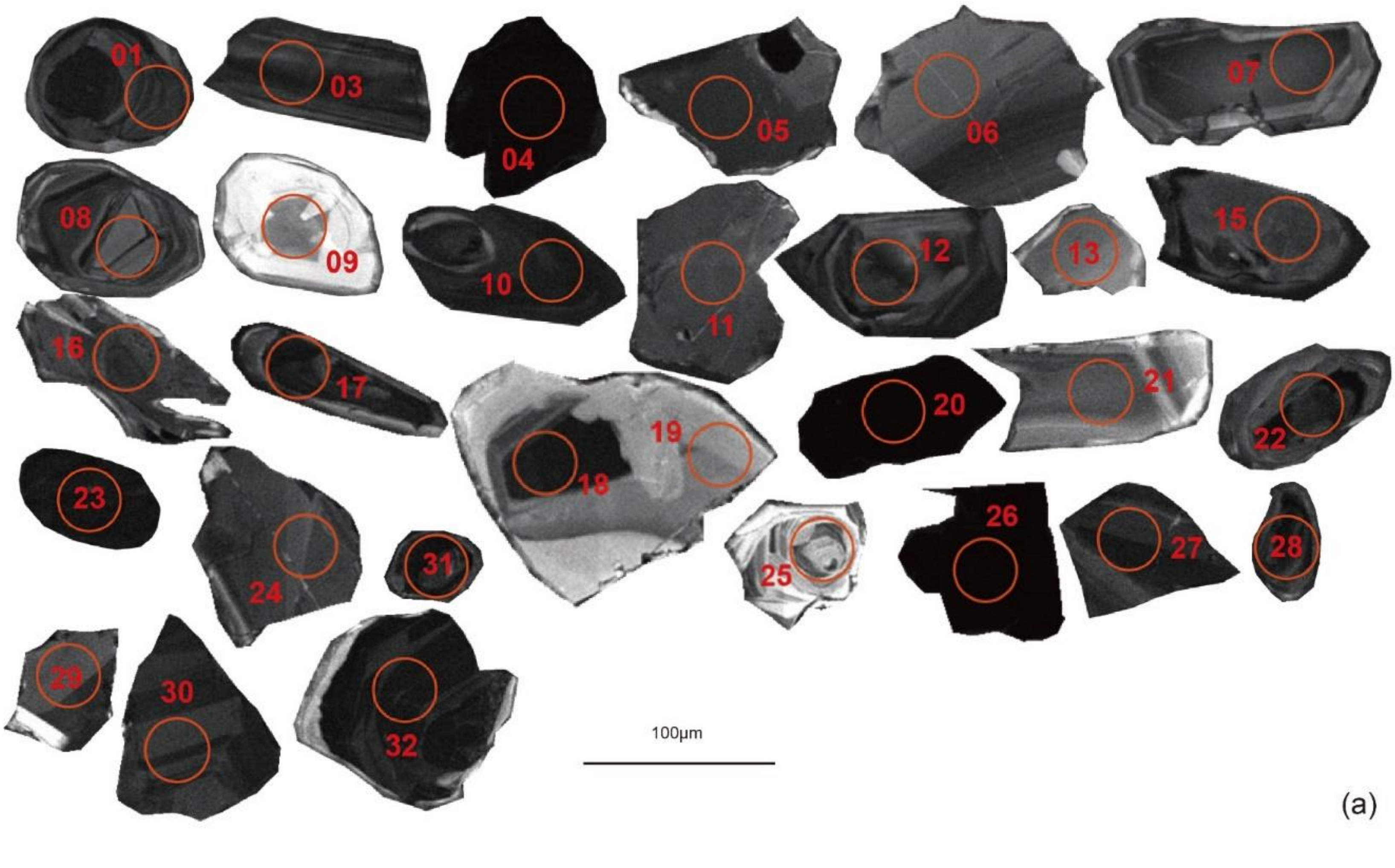
01
03
04
05
06
07
08
09
10
11
12
13
15
16
17
18
19
20
21
22
23
24
25
26
27
28
29
30
31
32
100μm
(a)

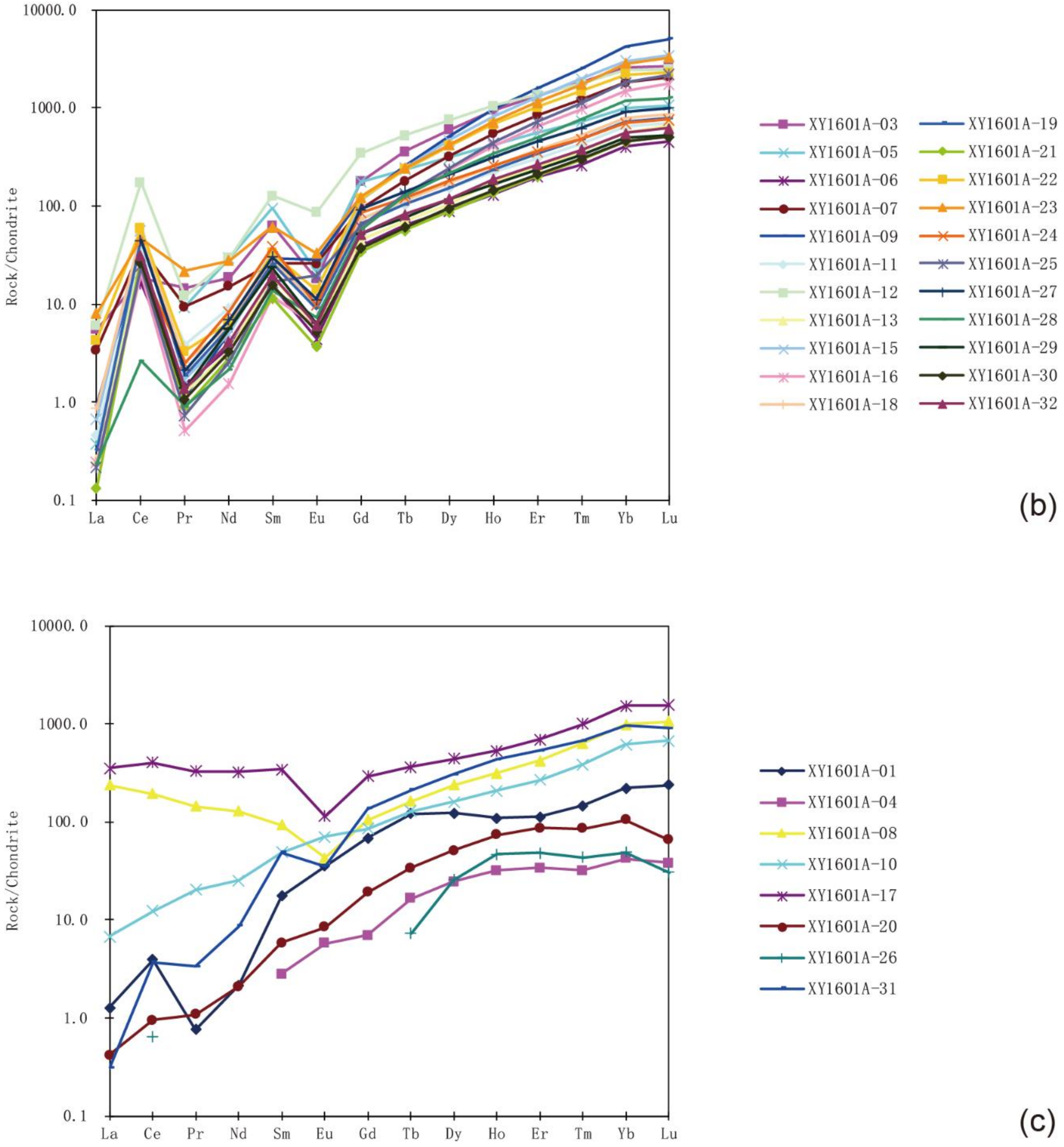

Figure E13 CL images and the REE patterns of XY1601A.

(1 analysis, Spot No.25); 228.8±2.9Ma (1 analysis, Spot No.12). There is only one concordant magmatic age: 470.8±5.2Ma (Spot No.18). This age is probably a xenocrystic age.

(3) XY1601B

Zircons from XY1601B range from 40μm to 130μm in size (Fig.E14a). Some are prismatic (e.g., Spot No.09, 11), and some are equant (e.g., Spot No.02, 04). Only Spot No.03 shows weak zoning, and others show blurred zoning or homogenous domain.

Th/U ratios are between 0.08 and 0.79. Spot No. 04 has Th/U ratio (=0.08) < 0.1.

Most of REE patterns show positive Ce-anomalies, negative Eu-anomalies and steeply slopes from LREE to HREE (Fig.E14b). Spot No.06, 07, 16 show different patterns. Spot No.06&07 are depleted in HREE and do not show positive Ce-anomaly, and Spot No.16 is depleted in HREE, and do not show positive Ce-anomaly and negative Eu-anomaly (Fig.E14c).

In summary, the concordant metamorphic ages can be divided into the following groups: 1025.8±12.39Ma (1 analysis, Spot No.11); 966.8~879.3Ma (6 analyses, Spot No.02, 08, 10, 13, 14, 15); 801.2±8.65Ma (1 analysis, Spot No.12); 716.2±8.15Ma (1 analysis, Spot No.04); 121.7±1.54Ma (1 analysis, Spot No.18).

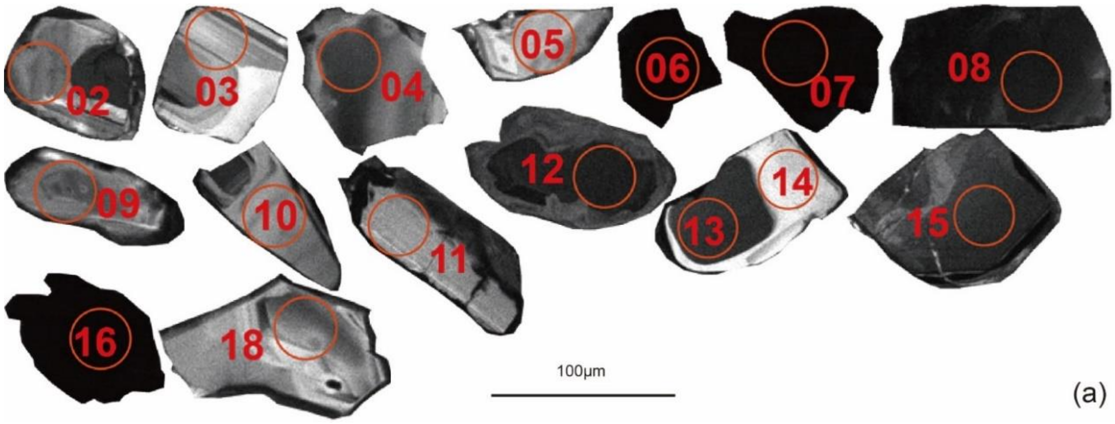

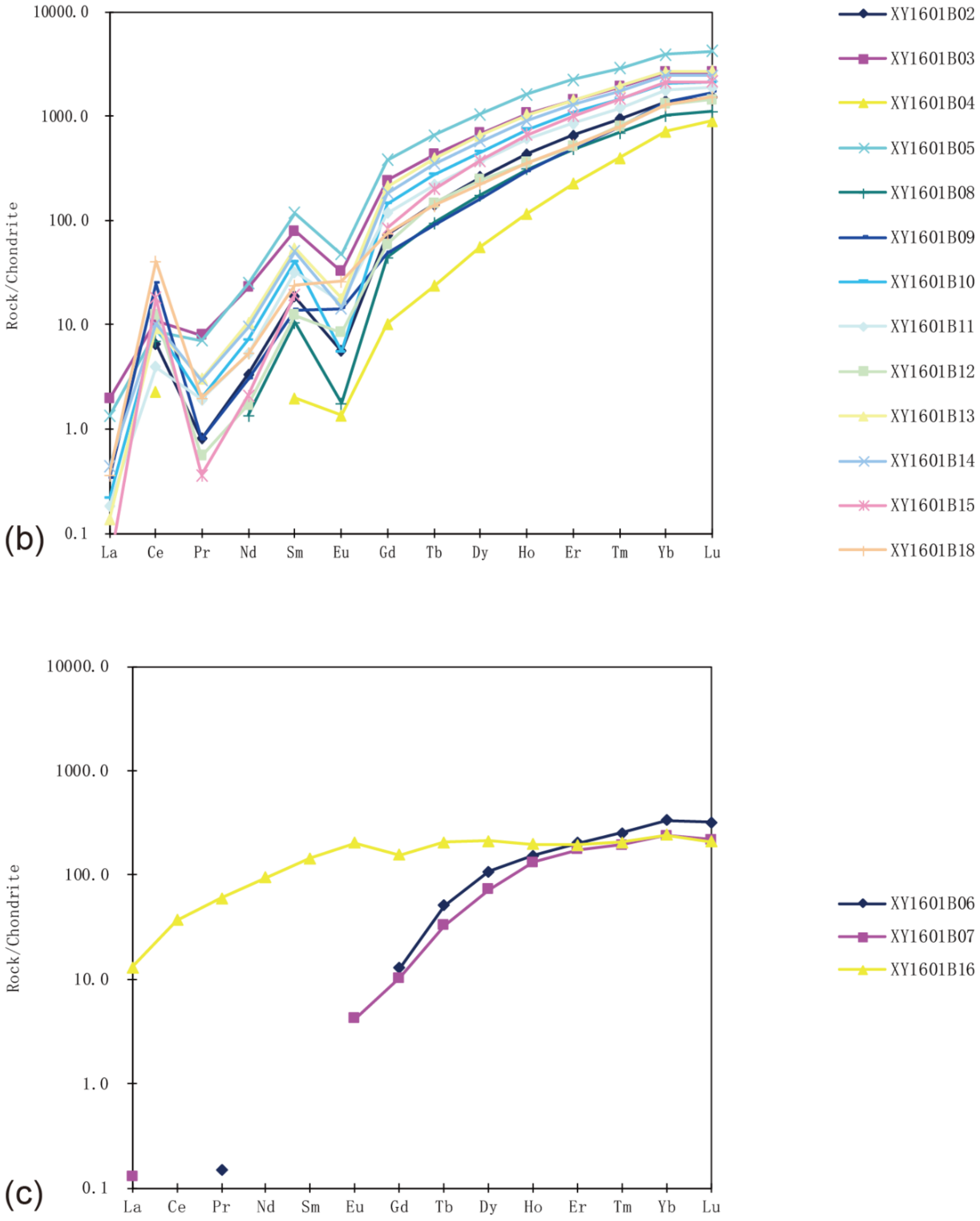

Figure E14 CL images and the REE patterns of XY1601B.

There is only one concordant magmatic age: 859±13.38Ma (Spot No.03). This is a xenocrystic age.

(4) XY1602

The size of zircons in XY1602 is in the range of 40~140μm (Fig.E15a). Some are prismatic (e.g., Spot No.14, 24), and some are equant (e.g., Spot No.05, 17, 19), and some are ellipsoidal (e.g., Spot No.03, 18, 22). Some spots show weak zoning (Spot No.01, 02, 14, 15), and others show blurred zoning or homogenous domain.

Th/U ratios are in the range of 0.02~0.95. Spot No.07, 09, 19, 23 and 24 have Th/U ratios < 0.1.

Most of REE patterns show positive Ce-anomalies, negative Eu-anomalies and steeply slopes from LREE to HREE (Fig.E15b). Spot No.04, 06, 19, 23, 24 show different patterns. Instead of a negative Eu-anomaly, Spot No.23 and 24 show positive Eu-anomalies. Spot No.19 is relatively depleted in HREE, while Spot No.04, 06 and 24 are relatively abundant in LREE (Fig.E15c).

The metamorphic concordant ages can be divided into the following groups: 2365±23.76Ma (1 analysis, Spot No.12); 1458.4~1408.8Ma (4 analyses, Spot No.09, 10, 13, 20); 1247.1~1203.5Ma (2 analyses, Spot No.03, 08); 1082.3~1000.9Ma (2 analyses, Spot No.17, 18); 920.3±10.03Ma (1 analysis, Spot No.16); 792.1±9.12Ma (1 analysis, Spot No.05); 491.5±5.54Ma (1 analysis, Spot No.19); 447.9±5.86Ma (1 analysis, Spot No.21); 354.3±4Ma (1 analysis, Spot No.24).

There are only two concordant magmatic ages: 1462.8±18.8Ma (Spot No.15) and 1131.9±12.57Ma (Spot No.14).


01
02
03
04
05
06
07
08
09
10
11
12
13
14
15
16
17
18
19
20
21
22
23
24
100μm
(a)

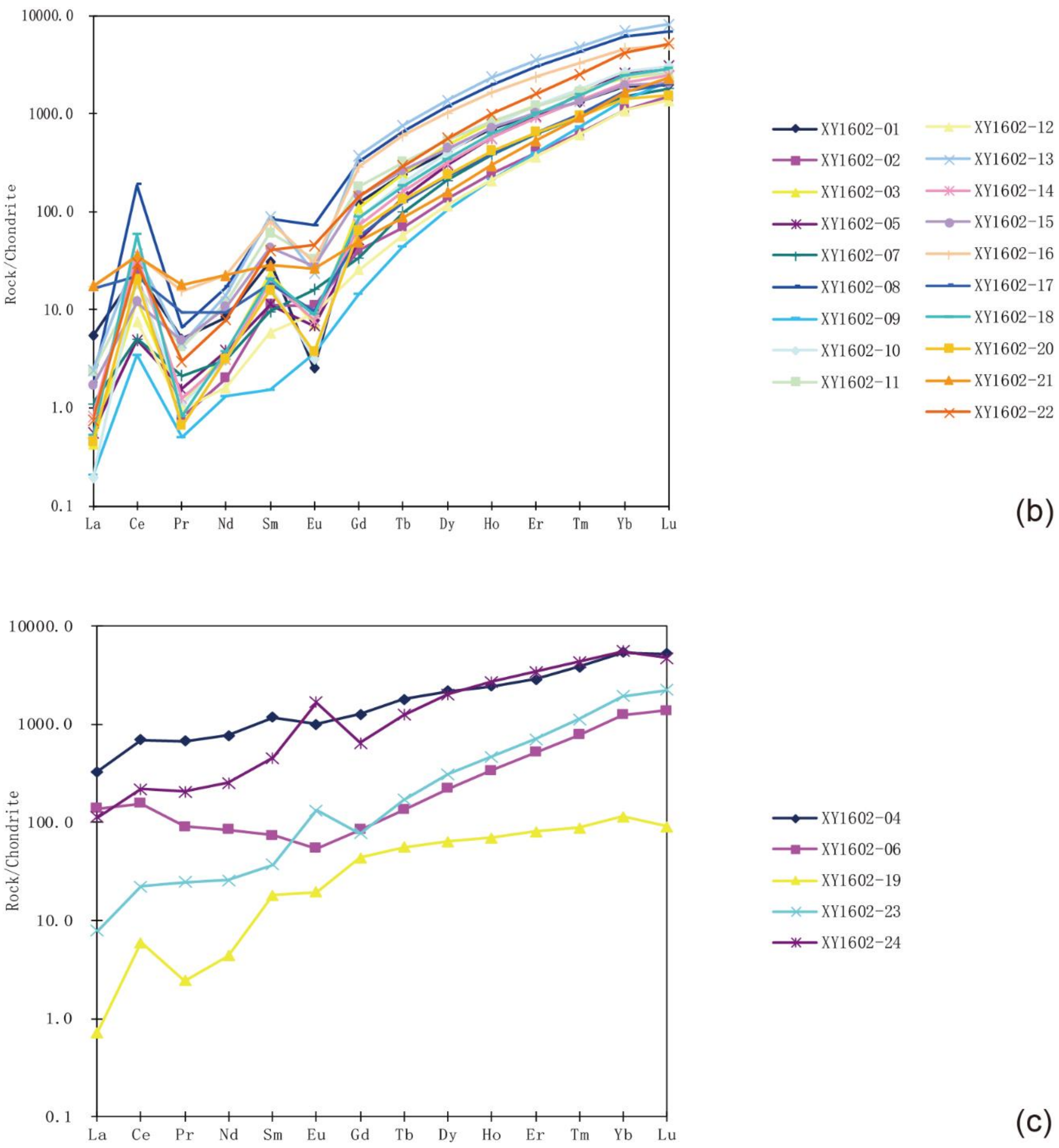

Figure E15 CL images and the REE patterns of XY1602.

References:

Corfu, F., Hanchar, J.M., Hoskin, P.W. and Kinny, P., 2003. Atlas of zircon textures. Reviews in Mineralogy and Geochemistry, 53(1), pp.469-500.

Hoskin, P.W. and Schaltegger, U., 2003. The composition of zircon and igneous and metamorphic petrogenesis. Reviews in Mineralogy and Geochemistry, 53(1), pp.27-62.

Curriculum Vitae

Name: Mengmeng Qu

Education Background:

- **01/2014 ~ 06/2018:** PhD Student, Department of Earth Sciences, Western University
- **09/2012 ~ 12/2013:** MSc Student (upgrade to Ph.D. program), Department of Earth Sciences, Western University
- **09/2008 ~ 07/2012:** BSc, Department of Geology, Northwest University, Xi'an, China

Work Experience:

- **01/2018 ~ 04/2018, 05/2016 ~ 08/2016, 05/2015 ~ 08/2015, 05/2014 ~ 08/2014, 05/2013 ~ 08/2013:**
  Research assistant at Laboratory for Structural Geology & Tectonics, Department of Earth Sciences, Western University
- **01/2016 ~ 04/2016:**
  Instructor of Structural Geology, Department of Earth Sciences, Western University
- **09/2016 ~ 04/2017, 09/2015 ~ 12/2015, 09/2014 ~ 04/2015, 09/2013 ~ 04/2014, 09/2012 ~ 04/2013:**
  Teaching assistant for the different courses in the Earth Sciences, Department of Earth Sciences, Western University

Publication:

- **Qu, M.**, Jiang, D., Lu, L.X., 2016. An optimal scheme for numerical evaluation of Eshelby tensors and its implementation in a MATLAB package for simulating the motion of viscous ellipsoids in slow flows. Computers & Geosciences 96 (2016): 98-108.
- Dang, B., Zhao, H., **Qu, M.**, Wang, T., Mi, W., Guo, X., Fan, J. and Liu, P., 2018. Distribution characteristics, genesis analyses, and research significance of Triassic regional structural fractures in the Ordos Basin, Central China. Geological Journal, 53, pp.212-224.

Conferences:

- Jiang, D., Qu, M., Shi, J., Li, Y., Lu, L.X., 2017. Triassic transpressional deformation along the Shangdan tectonic zone and the tectonics of the Qinling Orogenic Belt in China (ORAL PRESENTATION). In the Development of Accretionary Orogens session at Kingston in GAC-MAC annual meeting.

- **Qu, M.,** Jiang, D., Lu, L.X., Baker, I.R., Moser, D.E., 2016. A comparison between multiscale simulation results of quartz lattice preferred orientations and EBSD data from the Shangdan tectonic zone of the Qinling orogenic belt, China (POSTER). In Cananda Tectonic Group Meeting at Muskoka.

- **Qu, M.,** Jiang, D., 2014. A multiscale approach for analyzing the Wushan-Xinyang-Yuanlong shear zone in West Qinling, China (ORAL PRESENTATION). In the development of structures session at Sudbury in Canadian Tectonic Group Meeting.

- **Qu, M.,** Jiang, D., 2014. Multiscale simulation of quartz lattice preferred orientations from the Shangdan tectonic zone of the Central Orogenic Belt, China (ORAL PRESENTATION). In the structural geology general session at Frederiction in GAC-MAC annual meeting.

- Zhao, T., Jiang, D., Zhu, G., **Qu, M.,** 2014. Origin and tectonic nature of the Zhangbaling metamorphic rocks in the Tan-Lu Fault Zone, China: Insights from protolith ages and deformation mechanisms (POSTER). In the structural geology general session at Frederiction in GAC-MAC annual meeting.